X-ray Observations of Accreting Compact Objects

Röntgenbeobachtungen akkretierender kompakter Objekte

Der Naturwissenschaftlichen Fakultät
der
Friedrich-Alexander-Universität Erlangen-Nürnberg

zur
Erlangung des Doktorgrades
dr. rer. nat.

vorgelegt von
Ole König
aus Hannover

Als Dissertation genehmigt
von der Naturwissenschaftlichen Fakultät
der Friedrich-Alexander-Universität Erlangen-Nürnberg

Tag der mündlichen Prüfung:	01.03.2024
Gutachter:	Prof. Dr. Jörn Wilms
Gutachter:	Prof. Dr. Thomas J. Maccarone

TO MY FAMILY

Zusammenfassung

In meiner Dissertation untersuche ich die Physik akkretierender kompakter Objekte in Doppelsternsystemen. Die Akkretion von Materie eines Begleitsterns führt zu der Bildung einer turbulenten Scheibe um das kompakte Objekt, die effizient gravitative potenzielle Energie in Strahlung umwandelt. In Schwarzlochdoppelsternen kann stark variable Röntgenstrahlung mit weltraumbasierten Teleskopen detektiert werden. Sie entsteht durch Comptonisierung in direkter Nähe des Schwarzen Lochs. Die genaue Geometrie dieser Region ist jedoch umstritten. Bereits kurz nach der Entdeckung des ersten Schwarzen Lochs, Cygnus X-1, wurde erkannt, dass die Variabilität im harten Röntgenwellenlängenbereich genutzt werden kann um Aussagen über die Struktur der innersten Region des Systems zu treffen. Wie sich jedoch die Variabilität der Akkretionsscheibe auf das generelle Verhalten der Quelle auswirkt, kann nur zuverlässig in der weichen Röntgenstrahlung betrachtet werden. Diese Studien sind in den letzten Jahren durch eine neue Röntgenmission möglich geworden.
Cygnus X-1 zeigt Übergänge zwischen einem spektral harten Zustand, der von comptonisierter Emission dominiert ist, und einem weichen Zustand, in dem die Strahlung der Akkretionscheibe dominiert. In meiner Arbeit untersuche ich zum ersten Mal die Variabilität von Cygnus X-1 bei Energien $\lesssim$1 keV in diesen Zuständen anhand der Neutron Star Interior Composition Explorer (*NICER*) Beobachtungskampagne. Ich untersuche die Verbindung der Variabilität zwischen niedrigen und hohen Energien, welche sehr kohärent im harten Spektralzustand ist. Die hohe Kohärenz zeigt, dass es einen Prozess gibt, der die Variabilität verbindet, was stark vermuten lässt, dass es einen kausalen physikalischen Zusammenhang zwischen den Fluktuationen der Akkretionsscheibe und der Variabilität in der comptonisierenden Region gibt. Ich zeige, dass sich dieser Prozess im weichen Spektralzustand fundamental ändert, da die Variabilität inkohärent wird.
Im harten Spektralzustand können zwei etablierte Variabilitätskomponenten identifiziert werden. Ich zeige, dass diese Komponenten vermutlich individuellen physikalischen Prozessen in der Akkretionsscheibe und der comptonisierenden Region zugeordnet werden können. Ich entdecke ein neues Variabilitätsphänomen, das klar zwischen diesen beiden Variabilitätskomponenten lokalisiert und nur bei niedrigen Energien zu sehen ist. Es kann charakterisiert werden durch eine abrupte Änderung in den Ankunftszeiten der harten ($\gtrsim$2 keV) und weichen ($\lesssim$1,5 keV) Photonen, zusammen mit einer Reduktion der Kohärenz. Das Phänomen ist fundamental mit den Variabilitätskomponenten verbunden und folgt ihrer wohlbekannten Verschiebung zu höheren Frequenzen wenn Cygnus X-1 weicher wird. Ich zeige, dass das Phänomen nicht nur eine Eigenschaft von Cygnus X-1 ist, sondern auch im harten Spektralzustand von transienten Röntgendoppelsternen zu sehen ist, was die Entdeckung einer neuen generellen Eigenschaft akkretierender Schwarzer Löcher in Doppelsternsystemen suggeriert.

Im zweiten Teil meiner Dissertation betrachte ich einen Nova Ausbruch eines akkretierenden Weißen Zwerges. In Doppelsternsystemen mit einem Spenderstern sammelt sich wasserstoffreiche Materie in einer Hülle auf der Oberfläche des Weißen Zwerges. Sobald die Hülle eine kritische Masse erreicht hat, startet eine instabile thermonukleare Explosion, wodurch die Hülle abrupt expandiert und ihre meiste Masse verliert. Dieser Ausbruch wird Nova genannt. Seit über 30 Jahren sagt die Novatheorie die Existenz einer „Feuerball“ Phase voraus, die direkt der Kettenreaktion folgt. Diese Phase sollte als weicher, heller und kurzer Röntgenblitz zu sehen sein, bevor die Nova im optischen Licht sichtbar wird. Der Blitz ist jedoch schwierig zu detektieren, da Novae normalerweise durch ihren Helligkeitsanstieg im sichtbaren Licht entdeckt werden. Zu diesem Zeitpunkt ist der Röntgenblitz schon vorbei.
Ich präsentiere die klare Detektion eines extrem hellen und sehr weichen Röntgenblitzes von der klassischen galaktischen Nova YZ Reticuli, beobachtet mit dem extended ROentgen Survey with an Imaging Telescope Array (*eROSITA*) Weltraumteleskop. Der Blitz fand 11 Stunden vor dem 9 Magnituden starken Anstieg im optischen Licht statt und hatte eine maximale Helligkeit von 3,7 Magnituden. Auf der Südhalbkugel war die Quelle für etwa fünf Tage mit dem bloßen Auge sichtbar. Vier Stunden vor und nach dem Ereignis wurde keine Röntgenquelle detektiert, wodurch die Dauer des Blitzes auf unter acht Stunden begrenzt werden konnte. Diese Detektion kann eindeutig der Feuerballphase von YZ Reticuli zugeordnet werden.
Die Hauptherausforderung der Analyse ist die extreme Helligkeit der Quelle, die zu schwerwiegender Übersättigung im Detektor führte. Ein detailliertes Verständnis der physikalischen Prozesse im Halbleitermaterial ist notwendig, um die resultierenden Verzerrungen des Spektrums zu verstehen. Der Simulator Sixte ist in der Lage, diese komplexen Detektoreffekte zu modellieren. Mithilfe eines simulationsbasierten Minimierungsprozesses kann ich so die physikalischen Parameter der Quelle rekonstruieren, insbesondere die Temperatur, Leuchtkraft und Absorption der Photosphäre. In Übereinstimmung mit theoretischen Vorhersagen kann das Spektrum der Quelle mit einem Schwarzkörper einer Temperatur von $3{,}27^{+0{,}11}_{-0{,}33} \times 10^5$ K ($28{,}2^{+0{,}9}_{-2{,}8}$ eV), oder eines Atmosphärenmodells, modelliert werden. Die Photosphäre emittiert mit der Eddington-Leuchtkraft und ist nur etwas größer als ein Weißer Zwerg. Diese Detektion einer expandierenden Photosphäre eines Weißen Zwergs vor der Abstoßung der Hülle bildet das letzte Verbindungsstück des vorhergesagten photosphärischen Lichtkurvenverlaufs und eröffnet neue Möglichkeiten, um die gesamte Energetik der Nova zu vermessen.

Abstract

In my dissertation, I study the physics of accreting compact objects in binary systems. Accretion of matter from a stellar companion leads to the formation of a turbulent disk around the compact object, which efficiently converts gravitational potential energy into radiation. In black hole binaries, strongly variable X-rays can be detected with space-based telescopes. This radiation originates from Comptonization in a region of disputed geometry in the direct vicinity of the black hole. Already shortly after the discovery of the first black hole, Cygnus X-1, it was realized that the hard X-ray variability can be used to probe the innermost region of the system. How the variability of the accretion disk impacts the general behavior of the source, however, can only be reliably studied in the soft X-ray regime. In recent years, these studies have become possible with a new X-ray mission.

Cygnus X-1 shows transitions between a spectrally hard state, where the emission is dominated by Comptonization, and a soft state, where the accretion disk dominates the radiation. For the first time, I study the variability properties of Cygnus X-1 at soft X-rays $\lesssim$1 keV in these spectral states using the monitoring campaign of the Neutron Star Interior Composition Explorer (*NICER*). I study the connection of the variability at low and high energies, which is highly coherent in the hard state. The high coherence shows that there is a process at work which links the variability, providing evidence for a causal physical connection between the fluctuations from the accretion disk and the variability of the Comptonized emission. I show that this process fundamentally changes in the soft state, where the variability becomes incoherent.

In the hard state, two well-known variability components can be identified. I show that these components likely represent individual physical processes associated with the disk and Comptonized emission. I discover a new variability phenomenon that is prominently seen in between the two variability components, and only emerges at low energies. It can be characterized by an abrupt change of the arrival times of hard ($\gtrsim$2 keV) and soft ($\lesssim$1.5 keV) photons, together with a coherence drop. This feature is fundamentally connected to the variability components, and follows their well-known shift to higher frequencies as Cygnus X-1 softens. I show that the feature is not only a property of Cygnus X-1 but is also clearly detected in the hard state of transient low-mass X-ray binaries, suggesting a new general property of accreting black hole binaries.

In the second part of my thesis, I study a nova outburst of an accreting white dwarf system. In a binary system with a donor star, hydrogen-rich material accumulates in an envelope on the surface of the white dwarf. Once the envelope has reached critical mass, the system undergoes runaway thermonuclear burning, which results in the envelope to expand rapidly and to eject most of its mass. This outburst is called a nova. For more than 30 years, nova theory has predicted

the existence of a "fireball" phase following directly on from the runaway fusion, which should be observable as a short, bright, and soft X-ray flash before the nova becomes visible in the optical. This flash is difficult to observe because novae are usually discovered when the source rises in the visual light. At this time, the X-ray flash has, however, already ceased.

I present the unequivocal detection of an extremely bright and very soft X-ray flash of the classical Galactic nova YZ Reticuli observed with the extended ROentgen Survey with an Imaging Telescope Array (*eROSITA*) space telescope. The flash occurred 11 hours before its 9 mag optical brightening. The source had a peak brightness of 3.7 mag, and was visible to the naked eye in the southern hemisphere for about five days. No X-ray source was detected 4 hours before and after the event, constraining the duration of the flash to shorter than 8 hours. The detection can be clearly associated with the fireball phase in YZ Reticuli.

The main challenge of this analysis is the extreme brightness of the source, which led to severe pile-up in the detector. A detailed understanding of the physical processes in the semiconductor detector is necessary to understand the resulting spectral distortions. The simulator SIXTE is capable of modeling these complex detector effects. Using a simulation-based fitting approach, I could reconstruct the physical parameters of the source, in particular, the temperature, luminosity, and absorption of the photosphere.

In agreement with theoretical predictions, the source's spectral shape is consistent with a black body of $3.27^{+0.11}_{-0.33} \times 10^5$ K ($28.2^{+0.9}_{-2.8}$ eV) radiating at the Eddington luminosity, with a photosphere that is only slightly larger than a typical white dwarf. This detection of the expanding white dwarf photosphere before the ejection of the envelope provides the last link of the predicted photospheric lightcurve evolution and opens a new window to measure the total nova energetics.

Contents

Chapter 1

Aim of this Thesis

My research focuses on the physics of accreting compact objects. I investigate these sources by analyzing the X-ray radiation they emit, which can be detected with space-based telescopes. To comprehend what happens to matter in the vicinity of compact objects, it is necessary to understand how they form, what they are made of, how their radiation mechanisms work, and how they are classified observationally. Therefore, the general physics of these objects is introduced in Ch. 2. Chapter 3 introduces how X-rays can be detected with space-based telescopes.

Part I In accreting black hole binaries, a highly variable source of X-rays, called corona, is located close to the black hole. In recent years, the quality of space-based X-ray data has made it possible to analyze the spectroscopic properties of the accretion stream on very short time scales. This spectral-timing analysis proved to be a compelling method to study the location of the X-ray emitting region. However, the complex nature of these systems leads to a degeneracy in possible interpretations and a multitude of geometric models are actively discussed in the community. This debate shows that we still do not know the exact physics of the accretion stream around black holes, which motivates the first central physical question of my thesis:

1. What is the structure of the accretion flow in the vicinity of a stellar-mass black hole?

In order to address this question, I study the X-ray variability properties of the archetypical black hole binary Cygnus X-1. In Ch. 4, I first outline general observational characteristics of black hole X-ray binaries, specifically focusing on state transitions and their variability properties. Chapter 5 analyzes data of the *NICER* telescope to investigate how particularly the soft X-ray variability constrains the innermost region in Cygnus X-1.

Part II X-ray flashes in novae, called the "fireball phase", originate from the white dwarf's photosphere directly after the thermonuclear runaway. They have been predicted since the early 1990s but have, thus far, not been observed. Theoretically, the photosphere during this phase should emit soft thermal X-rays and should be located still close to the white dwarf. In July 2020, the *eROSITA* X-ray telescope detected a bright flash of X-rays associated with the fireball phase in

nova YZ Reticuli. The discovery of the X-ray flash with *eROSITA* motivates my second central question:

2. What are the physical properties of the photosphere during the fireball phase of a nova?

Typically, the energy spectrum is used to derive these physical parameters. However, the brightness of YZ Reticuli led to severe pile-up effects in the *eROSITA* detectors, which distorted the spectrum. Scientific simulations can help understand the source and the detection process and, therefore, facilitate a physical interpretation. This synergy of observations and simulations motivates the introduction of the SIXTE simulation software in Ch. 6, where I show its applicability using three example simulations. Chapter 7 presents the simulation-based analysis of the X-ray flash in YZ Reticuli and derives the physical properties of the photosphere.
In the last chapter of the thesis (Ch. 8), I conclude and give an outlook on open questions and possible next steps.

Chapter 2

Compact Objects

Dies ist die Geschichte von Paul[a]*. Paul ist ein Energiequantum. Entstanden ist er vor 13,8 Milliarden Jahren und schwirrt nun in Gestalt eines Röntgenteilchens im All umher.*

[a]Some sections of my thesis are accompanied by my story "The Adventures of Paul, the X-ray photon". Paul's encounter of a black hole begins in Ch. 2.4. His adventure in a thermonuclear fusion starts in Ch. 2.6. Comments and scientific considerations of the story are made in Appendix B. The story is written in German, my native language.

To be continued in Sect. 2.4.

Compact objects comprise the most extreme conditions of matter that we currently know to exist in our Universe. The scale of physical parameters inside or near compact objects, such as gravity and the resulting density and pressure, magnetic field strength, or the velocity of particles in their vicinity, is larger than any value achievable on Earth[1]. These properties make compact objects prime targets to explore fundamental physics and how matter behaves in strong gravitational fields. Shapiro & Teukolsky (1983, p. xii) classify three types of objects as compact: white dwarfs, neutron stars, and black holes[2]. These objects are not comprised of ordinary atomic matter and are, thus, called *compact* due to their high mass relative to their radius.

Two fundamental theories explore the limits of physics in these systems: The macroscopic effects of their gravitation is described by the theory of general relativity (Einstein, 1916), while the microscopic effects near or inside the object are characterized by the laws of quantum mechanics. More specifically, quantum electrodynamics is needed to describe, for instance, the consequences of

[1]Pressures in laboratory measurements of laser-induced shock waves can reach up to 4.5×10^8 bars (Kritcher et al., 2020). For reference, Earth's central pressure is at around 3.6×10^6 bars (Dziewonski & Anderson, 1981), while the pressure inside of a white dwarf surpasses 10^{17} bars (Carroll & Ostlie, 2017, Eq. 16.1). The inner crust of a neutron star exhibits a pressure of 3×10^{26} bars, which increases to roughly 3×10^{29} bars in the core (Özel & Freire, 2016, Fig. 7).

[2]A fourth class of compact objects hypothesizes that degenerate quark matter in so-called "exotic stars" can exert higher pressure than ordinary matter, such as neutrons, leading to even heavier stars than neutron stars without having an event horizon (Haensel et al., 1986). These objects have, however, not yet been found (see, e.g., Slane et al. 2002).

the strong magnetic field on matter falling onto neutron stars (Trümper et al., 1978), quantum chromodynamics is used to describe the quark matter postulated for neutron star cores (e.g., Haensel et al., 2007) and cosmic rays emerging from the vicinity of compact objects (e.g., Amenomori et al., 2019). Magnetohydro-, thermodynamics, and computer physics are utilized to describe the flow of matter around compact objects (Shakura & Sunyaev, 1973; Liska et al., 2018), solid state physics and laser physics are necessary to detect the radiation from these objects (Knoll, 2010; Amaro-Seoane et al., 2017), and (perhaps) a yet unknown theory of quantum gravity may be necessary to describe the true nature of black holes (e.g., Susskind & Uglum, 1994). Without doubt, it can be said that studying these extraordinary objects requires combining most, if not all, physical theories.
In this introduction chapter of my thesis, I describe the physics of X-ray emitting binary systems containing a compact object. The standard picture of the formation of such an X-ray binary involves two gravitationally bound stars. I will begin this chapter by introducing the basics of stellar evolution in Sect. 2.1, followed by a description of white dwarfs, neutron stars, and black holes in Sect. 2.2. Section 2.3 deals with the evolution of close binary stars and the formation of X-ray binaries. The accretion physics behind the X-ray emission is explained in Sect. 2.4 and the classification of X-ray binaries in Sect. 2.5. Finally, I will describe the nova phenomenon occurring on a white dwarf in Sect. 2.6.

2.1 Stellar Evolution

Compact objects that are observed in the mass range from 0.17 to roughly 21 solar masses[3] ($M_\odot$; see Kilic et al. 2007; Miller-Jones et al. 2021) are the end points of stellar evolution. In the following, I will first describe the evolution of low and intermediate mass stars to explain how white dwarfs form. Then, I will treat high-mass stars, supernova explosions and the formation of neutron stars and black holes.

2.1.1 Low- and Intermediate Mass Stars

Main sequence stars undergo nuclear fusion in their cores where hydrogen is burned to helium (Iben, 2012a,b). The burning happens dominantly via the proton-proton chain for stars like our Sun (Eddington, 1920; Bethe, 1939) and via the carbon-nitrogen-oxygen (CNO) cycle for stars with a mass larger than $\sim 1.5\,M_\odot$ (von Weizsäcker, 1937; Bethe, 1939). I will explain their evolution based on the tracks in the Hertzsprung-Russell diagram (HRD), calculated with the *Modules for Experiments in Stellar Astrophysics* (MESA; Paxton et al. 2011), and shown in Fig. 2.1.
At the end of the main sequence, when a star around $1\,M_\odot$ depleted the hydrogen in the core, nuclear burning continues in a thick hydrogen shell around a helium core. The core cannot counteract the gravitational pressure of the material above it through gas pressure any more and contracts (Schönberg & Chandrasekhar, 1942). The star moves away from the main sequence onto the

[3] Here, I explicitly exclude gravitational wave measurements of black hole mergers, where masses up to $85\,M_\odot$ have been proposed (Abbott et al., 2020a). Black holes of such high masses are not compatible with standard stellar evolution theory and are believed to be a consequence of a not yet understood merging evolution of multiple black holes.

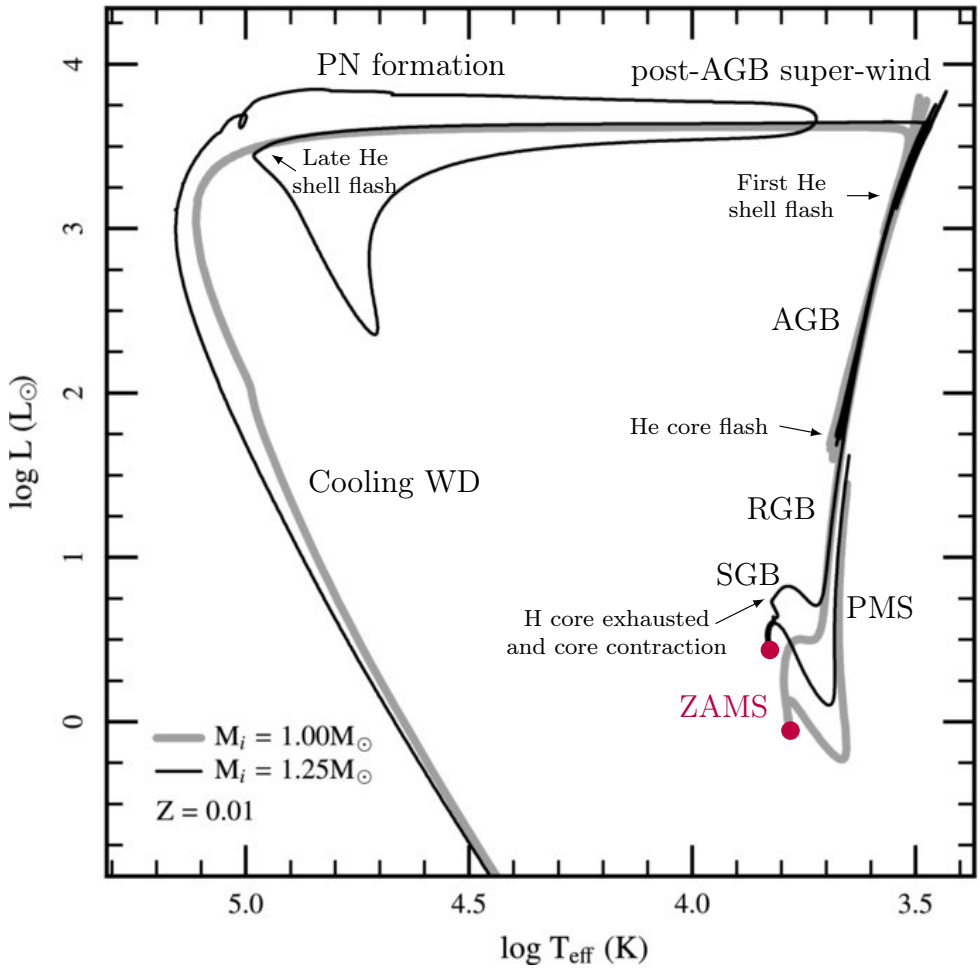

Figure 2.1: Hertzsprung-Russell diagram of low-mass stars evolving from the pre-main sequence (PMS) to a cooling white dwarf calculated with the MESA code (modified after Fig. 13 of Paxton et al. 2011). The metallicity, Z, is close to the solar value. The zero-age main sequence (ZAMS) is denoted as a red dot. ©AAS. Reproduced with permission.

sub-giant branch (SGB) and expands its envelope as the gravitational potential energy of the material in the core is released. While the star on the main sequence transported its energy outwards mainly through radiation, with only a thin convective layer on the surface, the convection zone expands. The star moves along the red giant branch (RGB) with an almost fully convective envelope, increasing in luminosity as the envelope expands further. Stars with a mass less than $1.8\,M_\odot$ develop a strongly electron-degenerate core[4] during the RGB phase. This stabilizes the core

[4]The high density in the core means that the electrons are strongly localized. Due to the quantum mechanical uncertainty principle (Heisenberg, 1927), the strong localization implies a large momentum of the particles. Furthermore, electrons, which are fermions, are subject to the Pauli exclusion principle (Pauli, 1925), which states

from further contraction. Non-nuclear neutrinos, which are created through bremsstrahlung and pair-production processes, escape from the denser center of the core and carry energy away (Chiu & Stabler, 1961). Thus, although the equation of state of the core is independent of the temperature (the heat conductivity of degenerate electron matter is very efficient), this *neutrino cooling* leads to a slight temperature inversion of the otherwise isothermal core.
The onset of helium burning is called the helium flash. This occurs when the temperature in the stellar core is high enough that the strongly temperature-dependent triple-α process fuses helium to carbon and oxygen (Salpeter, 1952; Hoyle, 1946, 1954; Burbidge et al., 1957). Due to the neutrino cooling, the helium burning first ignites in a shell around the center of the star. The energy released from the helium flash lifts the electron-degeneracy again (this lifting will also become relevant when I introduce novae in Sect. 2.6) and remaining energy mostly dissipates in the overlying envelope. The core then successively burns helium from the outside to the inside, undergoing multiple helium flashes, until the whole core fuses helium and an carbon/oxygen core is created. The region in the HRD which is explained by this He core burning is called the horizontal branch.
The asymptotic giant branch (AGB; Iben & Renzini 1983) begins when the helium core is depleted. The star develops "onion-like" shells, which burn the ashes of previous fusion processes, starting with an outer hydrogen shell, an inner helium shell and the inert carbon/oxygen core that is stabilized through electron degeneracy pressure. In stars with masses below approximately 8–10 $M_\odot$ (Woosley & Heger, 2015) the nucleosynthesis stops at oxygen (leaving a C-O core) for masses below 4 $M_\odot$, or neon (ONeMg core) for masses between 4–8 $M_\odot$.
Due to the increased energy output from the helium shell burning, post-AGB stars lose a significant fraction of their H-rich envelope through a so-called *super-wind*, which can have a mass loss rate as high as $10^{-4}\,M_\odot\,yr^{-1}$ and which lasts for roughly 100 000 years (Tanabé et al., 1997). The expelled envelope of the star becomes observable as a *planetary nebula* when the temperature of the remnant star becomes hot enough to ionize the material at $T_{\text{eff}} \gtrsim 20\,000\,K$ (e.g., Frew & Parker, 2010). The degenerate core cools and becomes a white dwarf, a stellar remnant located in the faint, hot strip below the main sequence of the Hertzsprung-Russell diagram (Miller Bertolami, 2016).

2.1.2 Massive Stars

Stars more massive than roughly 8 $M_\odot$ have an inner convective non-degenerate core and an outer radiative envelope. After the main sequence they begin burning helium more smoothly, without undergoing a flash. The temperature in the core becomes sufficiently high such that nuclear burning continues up to the elements with the highest nuclear binding energy, that is, iron and nickel (Woosley et al., 2002). Stars of masses between 10–20 $M_\odot$ become red or blue supergiants (Massey, 2003, p. 34). O-type stars with masses above roughly 20 $M_\odot$ become Wolf-Rayet (WR) stars[5] or

that fermions have to differ in at least one of four quantum numbers (location, momentum, angular momentum, and spin). Thus, the mechanical phase space is filled up to the Fermi energy, which leads to a degeneracy pressure $P \propto m_e^{-1}(N/V)^{5/3} \propto \rho^{5/3}$ for an ideal non-relativistic Fermi gas at zero temperature (Fowler, 1926, p. 121), where N denotes the number of particles, V is the volume, and ρ is the density, supporting the core from gravitational collapse.

[5]Wolf-Rayet stars exhibit surface temperatures of 35 000 to 150 000 K and are mainly powered by burning helium and heavier elements in the core (Crowther, 2007). They have initial masses of 25–75 $M_\odot$ and lose a large part of their mass, $>10^{-5}\,M_\odot\,yr^{-1}$, by a stellar wind, which may lead to a complete loss of the hydrogen envelope (Vanbeveren

luminous blue variables[6] for the most extreme end ($>85\,M_\odot$), both of which are characterized by very strong stellar winds, and a high temperature and luminosity.
The temperature and density evolution of two example stars of 15 and $30\,M_\odot$ is depicted in Fig. 2.2.
The evolution of massive stars at the end of their lifetime is a relatively short period of only a few millions of years. The helium burning stage of a $25\,M_\odot$ star lasts for about 800 000 yr. As the nucleosynthesis of elements closer to the iron peak produces less and less energy per unit mass of fuel, the next burning stages become increasingly shorter. Carbon burning lasts for ∼500 yr, neon burning for ∼10 months, oxygen burning for ∼5 months, and the final stage of silicon burning that fuses elements up to iron and nickel only takes ∼17 hours (Woosley et al., 2002, Table 1). The iron core builds up and is stabilized by electron degeneracy pressure. There is no more source of nuclear energy available that can counteract the gravitational pressure. When the mass of the iron core has almost grown to the Chandrasekhar limit of roughly $1.4\,M_\odot$ (Chandrasekhar, 1931), the star undergoes catastrophic core-collapse.
At the end of silicon burning the core has reached a temperature of roughly 8×10^9 K, which is high enough that photons disintegrate iron nuclei into neutrons and protons, initiating the collapse of the core. During the collapse, the protons react with free electrons and produce neutrons and neutrinos through electron capture (neutronization), leading to several 10^{53} erg being radiated away by neutrinos (Janka et al., 2012). In a runaway process the electron degeneracy pressure is reduced, speeding up the collapse. Within less than a second the inner core has collapsed in nearly free-fall from Earth-size to roughly 50 km. The gravitational collapse is halted when the density surpasses the nuclear saturation mass density ($2.7 \times 10^{14}\,g\,cm^{-3}$; Janka 2011). At this density, the strong nuclear force between the neutrons becomes repulsive due to the Pauli exclusion principle. The resulting neutron degeneracy pressure prevents further collapse (for the moment) and a ∼50–100 km large proto-neutron star forms.
Janka (2011) summarizes what happens in the milliseconds after the formation of the proto-neutron star. As its equilibrium density is slightly higher than what prevailed when it formed, the stellar core bounces back into equilibrium. This sends an outwards directed shock front through the supersonicly infalling material. The shock front travels through the outer core of iron and nickel and heats the plasma. This produces γ-rays, which dissociate the iron nuclei, and extract around 8.8 MeV per nucleon from the shock front. The shock begins to stall. A further effect is that electron capture produces a large number of electron neutrinos. When the shock reaches the outer layers of the iron core, these neutrinos escape in a short burst. As a result, the shock front stalls after 1–2 ms at a radius of 100–200 km and transforms into an accretion front. Thus, the "prompt" explosion mechanism of the outwards travelling shock front does not work to describe the observed explosion of the star.
The precise functioning of the resulting *core-collapse supernova*[7] explosion is still not fully understood

et al., 1998; Crowther, 2007). Consequently, the atmospheres of WR stars are composed of helium and nitrogen (WN-type) or helium and carbon (WC-type). Some even have lost their helium envelope and exhibit an atmosphere dominated by oxygen.

[6] Luminous blue variables (LBVs), such as η Carinae or P Cygni, are extremely luminous and blue (hot) stars that show strong outbursts and eruptions on timescales of decades or centuries, coupled to periods of pronounced mass loss. LBVs can have a luminosity of millions of times that of the Sun, making them the most luminous type of stars. During eruptions the stars can have a mass-loss rate of up to $0.1\,M_\odot\,year^{-1}$ (Massey, 2003).

[7] For completeness, I note that there exist also other types of physical processes initiating the supernova, sensitively

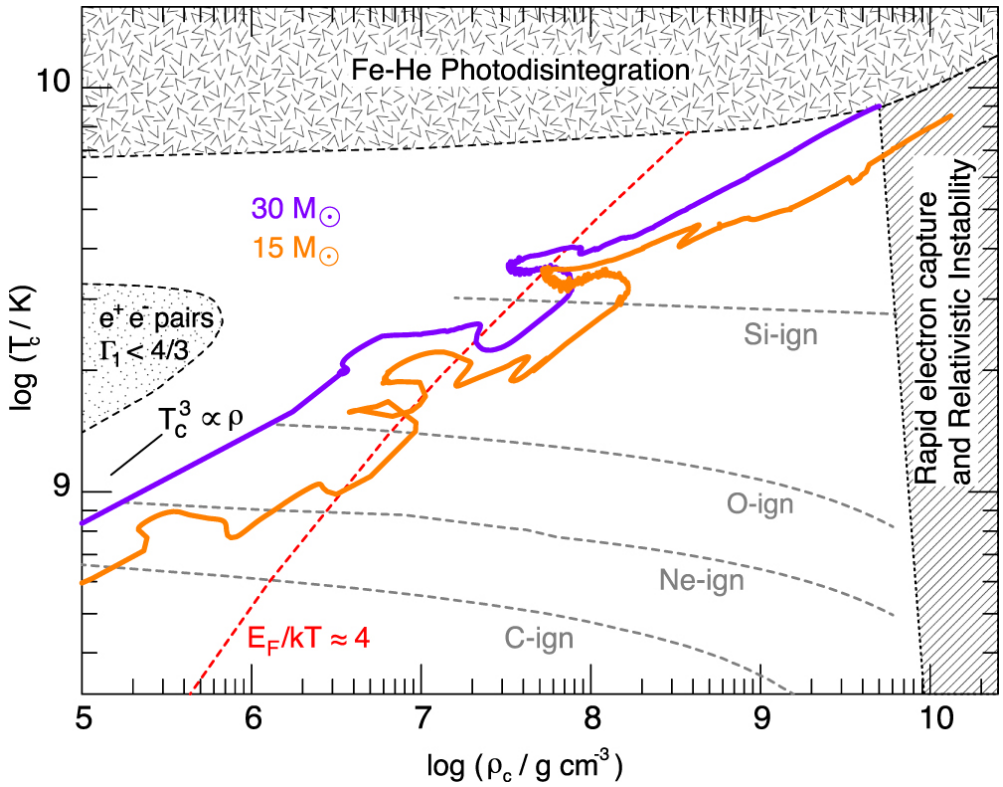

Figure 2.2: Temperature and density evolution of massive stars calculated with the MESA code (Fig. 24 from Paxton et al., 2015). The stars evolves from the bottom left to the top right. Ignitions of a more massive element are seen as tracks towards lower density at roughly constant temperature. The line $T_c^3 \propto \rho_c$ represents the condition where the gas pressure of an ideal gas equals the radiation pressure and, thus, separates the radiation pressure dominated (above) and gas pressure dominated regime (below). The evolutionary curves are flatter than this correlation due to the partial electron degeneracy of the core. The $E_{\mathrm{Fermi}}/k_{\mathrm{B}}T \approx 4$ curve separates the region where the core can be described by an ideal gas (above) and degenerate gas (below), respectively. Shaded areas indicate the regime, where the stellar core is unstable and collapses. The dotted region with an adiabatic index $\Gamma_1 = d\log P/d\log\rho < 4/3$ denotes the regime where the temperature is high enough such that electron-positron pairs are created, which leads to a pair-instability supernova. ©AAS. Reproduced with permission.

depending on the mass, metallicity, and rotation of the progenitor star. Stars in the mass range of 8–10 $\mathrm{M}_\odot$ are believed to undergo an electron-capture supernova. Hereby, nuclei in the ONeMg core capture electrons, which leads to a rapid decrease of the electron degeneracy pressure and a collapse of the core, producing a neutron star (theoretically predicted by Miyaji et al. 1980 and Nomoto 1984, 1987 and observed by Hiramatsu et al. 2021). Extremely massive stars in the mass range of 140–250 $\mathrm{M}_\odot$ are thought to explode in a pair-instability supernova (Fraley, 1968; Fryer et al., 2001). The γ-rays produced in the core at the final stage of very massive stars are energetic enough to create electron-positron pairs. This leads to a decrease of the radiation pressure that supports the core, which shrinks and heats up further. This produces even more electron-positron pairs through pair-production in a

but it is believed that the neutrinos play a major role in re-accelerating the shock front (Chiu, 1964; Colgate & White, 1966; Arnett, 1977; Bethe & Wilson, 1985; Burrows & Vartanyan, 2021). Although these particles have a very small interaction cross-section (e.g., Formaggio & Zeller, 2012), the outer core is dense enough ($\gtrsim 10^{12}\,\mathrm{g\,cm^{-3}}$) that the neutrinos deposit around 5% of their energy into the material. This process is called neutrino heating. The primary driver are electron neutrinos but bremsstrahlung and pair-production of tau and muon neutrinos in the cooling process of the proto-neutron star also contribute (e.g., Keil et al. 2003 or Janka 2011, their Fig. 3.17). The result of the neutrino heating is a violent explosion of the outer core and envelope of the star. The total gravitational binding energy released in the collapse amounts to around 10% of the total rest mass energy of the star's core ($\approx 3 \times 10^{53}\,\mathrm{erg}$; Lattimer & Prakash 2004). At this point the star has a luminosity of roughly $10^9\,\mathrm{L_\odot}$, which is comparable to the brightness of the entire galaxy.
The stellar core remains as a compact object. A neutron star forms if the mass is lower than the Tolman-Oppenheimer-Volkoff limit of around 2.2–2.9 $\mathrm{M_\odot}$ (Tolman, 1939; Oppenheimer & Volkoff, 1939; Kalogera & Baym, 1996). There is no stable form of matter known that sustains the gravity above this threshold. If more material is accreted in the brief time frame after the formation of the proto-neutron star, the stellar core collapses further into a black hole (Oppenheimer & Snyder, 1939).

2.2 White Dwarfs, Neutron Stars, and Black Holes

In the last section, I showed that stellar-mass compact objects are the end points of stellar evolution. In what follows, I will describe the physical parameters of these sources.

White Dwarfs

White dwarfs are the most abundant class of compact objects. It is estimated that 97% of all stars, including our Sun, will end their lives as white dwarfs (Fontaine et al., 2001). The closest known solitary white dwarf *van Maanen's Star* is at a distance of 4.31 pc (Sion et al., 2014, Table 1) and was discovered by van Maanen (1917, albeit he did not know it was a white dwarf).
White dwarfs form with a temperature of approximately $10^7\,\mathrm{K}$ and emit thermal radiation in the ultraviolet (UV), soft X-ray (Heise, 1985), and optical wavelengths. Radiative cooling is an inefficient mechanism to shed energy from the surface and, thus, white dwarfs have very long lifetimes (Mestel, 1952) that can exceed the current age of the Universe (e.g., Chabrier et al., 2000, their Fig. 2). A typical white dwarf takes approximately $10^{10}\,\mathrm{yr}$ to reduce its effective temperature from 10 000 K to 5000 K (Kepler et al., 2016).
Most known white dwarfs are composed of carbon and oxygen (CO). Oxygen/neon/magnesium (ONeMg) white dwarfs should also exist, although these sources have only been observed through their ejecta in nova outbursts (e.g., Vanlandingham et al., 1996, and see Sect. 2.6). In addition, white dwarfs with a helium core can be produced through binary evolution channels (e.g., Althaus & Benvenuto, 1997). All white dwarfs are extremely dense (10^5–$10^8\,\mathrm{g\,cm^{-3}}$; Rotondo et al. 2011,

runaway process. The resulting supernova disrupts the complete star and leaves no remnant behind. Therefore, it is postulated that there exists an *upper mass gap* where no black holes formed from the core-collapse of massive stars should be possible (Farmer et al., 2019).

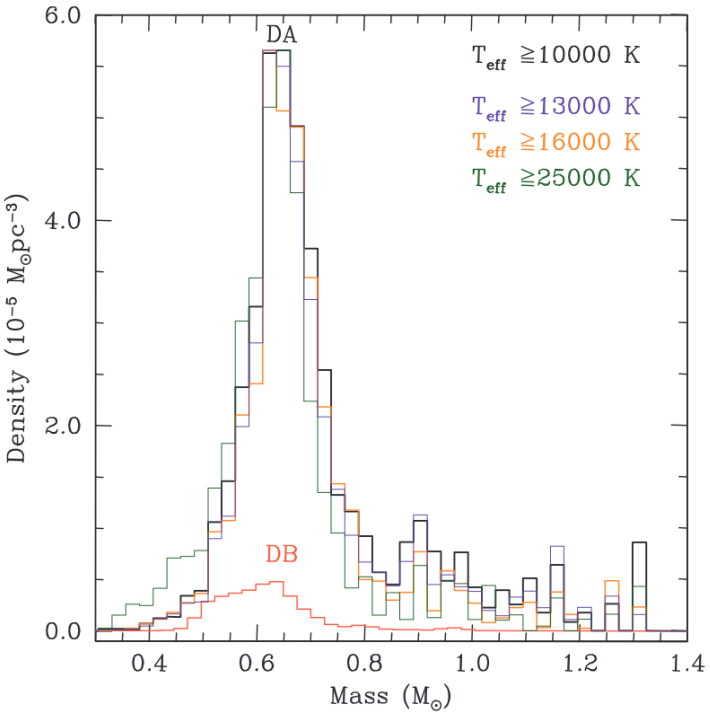

Figure 2.3: Mass distribution of white dwarfs from the Sloan Digital Sky Survey (Fig. 2 from Kepler et al., 2017).

their Fig. 3) and counteract the gravitational pressure by degenerate electron gas pressure, imposed by the Pauli principle. Due to the quantum-mechanical properties of the degenerate gas, the radius of a white dwarf is inversely proportional to the cubic root of the mass, which means that more massive white dwarfs are smaller than less massive ones. Measured radii of white dwarfs range from 3 500 to 18 000 km (Bédard et al., 2017) and the observed mass distribution is shown in Fig. 2.3. This distribution distinguishes between DA white dwarfs, which show hydrogen in their optical spectrum, and DB white dwarfs, which have a helium dominated atmosphere. Both histograms peak at approximately 0.62 $M_\odot$ but also depend on temperature and chemical composition (Kepler et al., 2016).

Neutron Stars

If the gravitational pressure inside the core of a massive star surpasses electron degeneracy pressure (Chandrasekhar, 1931), it becomes high enough that protons and electrons combine to produce neutrons. The core collapses until it is halted by neutron degeneracy pressure, which restores equilibrium. The collapsed core is called a neutron star.
Neutron stars have a radius of approximately 13 km (Miller et al., 2019) and a mass in the range of 0.77–2.3 $M_\odot$ (Doroshenko et al., 2022; Romani et al., 2022). These objects can spin extremely fast and some neutron stars exhibit a surface rotational speed that reaches a value close to the break-up speed of 0.25 c (e.g., Hessels et al., 2006). Neutron stars also exhibit the highest magnetic fields measured in the Universe (10^8 up to 10^{15} G, see Kaspi & Beloborodov 2017). For comparison, Earth's magnetic field is on the order of 10^{-1} G (Finlay et al., 2010). The classic way to explain

the spin and magnetic fields is angular momentum and magnetic field conservation during the supernova explosion. Due to the neutron star's much smaller radius, the spin and magnetic field of the progenitor star are strongly amplified. However, there are difficulties in explaining the high end of magnetic field values observed, suggesting that other processes are also important (see Sokolova-Lapa 2023, Sect. 2.1.4, and references therein).
34 years after Walter Baade and Fritz Zwicky proposed the existence of neutron stars (Baade & Zwicky, 1934), Jocelyn Bell Burnell discovered a pulsating radio source, which turned out to be an isolated neutron star (Hewish et al., 1968). The discovery of the first X-ray pulsar, Cen X-3 (Giacconi et al., 1971), established that neutron stars are often located in binary systems with main sequence stars. Strongly magnetized neutron stars accrete matter from the companion star along the field lines onto the magnetic poles of the star (Caballero & Wilms, 2012, and references therein). The X-ray radiation – which mainly emerges from inverse Compton scattering in an accretion column above the poles – can be detected by space-based X-ray telescopes and allows deducing the physical properties of the neutron stars, such as the magnetic field (Staubert et al., 2019, and references therein). As neutron stars are not the topic of this thesis, I direct the reader to numerous available review articles on neutron stars for further information, for instance, Lattimer & Prakash (2004), Harding & Lai (2006), Belloni et al. (2020), and the PhD thesis by Sokolova-Lapa (2023, and references therein).

Black Holes

The two types of compact objects described so far, white dwarfs and neutron stars, are stabilized by degeneracy pressure of electrons and neutrons, respectively. No stable form of matter is known to exist that can counteract a gravitational pressure surpassing neutron degeneracy pressure. White dwarfs and neutron stars are understood to have a surface. The third type, black holes, does not have this property and is described in this section.
The concept of objects so heavy that a "diminution of the velocity of their light" bends light rays back to the "dark star's" surface had already been thought of almost 240 years ago by John Michell (Michell, 1784). A few years later, Pierre-Simon Laplace independently proposed and "proved" (Laplace, 1796, 1799) the idea that "the attractive force of a heavenly body could be so large, that light could not flow out of it"[8]. This interpretation was based on Isaac Newton's corpuscular theory of light (Newton, 1704) and attributes light to having a variable speed (note that Ole Rømer demonstrated in 1676 that light has a finite speed). While it was clearly revolutionary to think of such an abstract object, the notion of light trying to escape, slowing down, and falling back onto the star's surface, is incorrect.
Black holes are understood as a region of infinite space-time curvature described by the theory of general relativity (Einstein, 1916). In 1916, Karl Schwarzschild found a solution to Einstein's field equations for a non-rotating, spherically symmetric object in vacuum, called the Schwarzschild metric (Schwarzschild, 1916). At the Schwarzschild radius $R_S = 2GM/c^2$, the metric diverges in Schwarzschild coordinates (Misner, Thorne, Wheeler, 1973, p. 820ff). For an observer in a reference frame far away from the object, the (coordinate) time of a particle falling into the black hole

[8]The translation of the original work by Laplace 1799 can be found in Hawking & Ellis 1973, appendix A, see also Montgomery et al. 2009 for a paper on the history of the black hole concept.

becomes infinite at R_S, called the *event horizon*. More laxly spoken, time "freezes" and nothing can ever be observed to fall through the event horizon. Even the surface of the star whose core collapsed into the black hole will never reach the event horizon as seen from a distant reference frame. In addition, any light emitted from an object close to the black hole is shifted in energy as it moves through the gravitational potential well. From the point of a distant observer, light from an object falling into a Schwarzschild black hole becomes more and more redshifted until it is too dim to observe it (Oppenheimer & Snyder, 1939).

The fact that no particle can reach the event horizon is, however, only observed from far away from the black hole. In the reference frame of the particle (e.g., in Kruskal-Szekeres coordinates; Kruskal 1960), the metric has no singularity at R_S and the particle can safely cross the event horizon within finite (proper) time. Once inside the event horizon, any particle or light ray will definitely end up in the singularity as all paths are warped such that they lead further into the black hole[9]. In other words, "that unseen power of the world which drags everyone forward willy-nilly from age twenty to forty and from forty to eighty also drags the [particle] in." (Misner, Thorne, Wheeler, 1973, p. 823). Therefore, objects, in which a particle that passes the event horizon will not be possible to escape any more, are called *black holes*.

From an astrophysical point of view, black holes only have two properties: Mass and angular momentum, also called *spin*. A rotating black hole is described by the Kerr metric (Kerr, 1963). The no-hair theorems (Hawking, 1976) state that the electrical charge is a third property. However, in an astrophysical black hole any charge different from zero will quickly be neutralized by the interaction with surrounding matter.

The solution of Schwarzschild was seen as a curious mathematical property of Einstein's new theory at first. Almost 50 years later, at the advent of X-ray astronomy, a bright X-ray emitting source was found in the constellation of Cygnus (Bowyer et al., 1965). Sub-second X-ray variability was detected (Oda et al., 1971), indicating a turbulent flow of matter within a radius of 100 km around a compact object (Rothschild et al., 1974), much less than the radius of a white dwarf. The X-ray source could be associated with a massive star called HDE 226868, which by itself cannot account for the detected X-ray emission, suggesting that the source is in a binary system. Bolton (1972) and Webster & Murdin (1972) used radial velocity measurements to determine the orbit parameters of the binary. Given a mass estimate of the companion star, the derived orbital period constrained the mass of the compact object, from where the X-ray emission originates, to be larger than what could be explained by a neutron star. This led to the widely accepted interpretation that the compact object is a black hole.

Although this source, Cygnus X-1 (abbreviated as Cyg X-1 from now on), is one of the most thoroughly studied X-ray sources[10], the connection of its emission and variability behavior is still

[9] For a particle inside the event horizon, $r \leq R_S$, the time and space coordinates of the Schwarzschild metric reverse roles, that is, the time coordinate becomes space-like and the space coordinate becomes time-like. Space-like paths are not possible for massive particles as they would have to move faster than the speed of light. Thus, particles cannot be at rest inside the event horizon. In other words, before a particle crosses the event horizon it could still change the direction of motion from a decreasing radius (in-falling) to increasing radius (escaping). Inside the event horizon, a decrease in radius means the passage of time. The particle would have to travel back in time in order to escape from the black hole. As time always continues in the local reference frame, the particle will definitely end up at the singularity (see Misner, Thorne, Wheeler 1973 p. 823ff, or Carroll & Ostlie 2017 p. 634f).

[10] At the time of writing a query of the Astrophysics Data System (`https://ui.adsabs.harvard.edu/`) yields

not sufficiently understood. The motivation behind Ch. 5, where I report on a variability analysis of Cyg X-1 using a modern space-based telescope, is to study what happens in the direct vicinity of the black hole from where the X-rays originate.

It is the general scientific opinion that black holes are ubiquitous in our Universe (Celotti et al. 1999, but see also Skenderis & Taylor 2008, Kovács et al. 2009 for alternative proposals in some mass ranges)[11]. Given the observation of few 10^4 O stars and taking into account the age of our Galaxy, it is estimated that there exist over 10^7 stellar mass black holes in the Milky Way (El-Badry et al., 2023a). Isolated black holes are certainly the most difficult type of compact objects to detect. They do not emit radiation except for Hawking radiation (Hawking, 1975), which is, however, unlikely to be discovered any time soon. Searches therefore rely on indirect methods, for instance, on the magnification of light from stars that is bent around the black hole, called micro-lensing (Sahu et al. 2022; Andrews & Kalogera 2022, and references therein). If the black hole is embedded in gas from the interstellar medium, it might also be detectable using radio observations (Maccarone, 2005). The fact that there might be a large population of undetected isolated black holes, among them hypothetical *primordial* black holes which could have formed shortly after the big bang (Zel'dovich & Novikov, 1966; Hawking, 1971), make them an interesting candidate for dark matter (e.g., Frampton et al., 2010).

Many of the black holes in our Galaxy should be situated in binary systems. If the system has a large orbital separation, in rare cases, the black hole can be detected in the optical wavelengths by measuring the movement of the star in the binary system around the common center-of-mass. Using this method, El-Badry et al. (2023b) recently found a black hole at a distance of roughly 480 pc, the closest distance of such an object, yet. Black holes in our Galaxy are much easier to detect if they are in close binary systems, as is the case for Cyg X-1. In the next section, I will describe how such binary systems form.

2.3 Binary Evolution

Many decades of research have led to a detailed understanding of the physics of single stars. However, this is not the case for close binary stars, where the interaction via tidal forces, mass exchange, stellar winds, and gravitational wave radiation link the evolution of the partner stars. A significant fraction of the stars in the Milky Way are in fact binary or multiple systems. Roughly 44% of Sun-like stars and more than 80% of O-stars are believed to be in multiple systems (Table 1 of Duchêne & Kraus 2013, see also Duquennoy & Mayor 1991; Lada 2006).

Before I begin this section, the concept of the Roche lobe needs to be introduced. In a binary system with point masses, the Roche lobe is defined as the equipotential surface where material remains gravitationally bound to each object. It has a teardrop shape and the point where the Roche lobes of both stars touch (and the gravitational and centrifugal forces are in equilibrium) is

643 refereed papers with Cyg X-1 in its name, while the next most studied confirmed black hole X-ray binaries, GRS 1915+105, GX 339−4, V404 Cyg, or GRO J1655−40, have around half the number of refereed papers.

[11] Next to stellar mass black holes, super-massive black holes (SMBHs) exist with masses of 10^5–$10^{10}\,M_\odot$. A relationship between the luminosity of galaxies (particularly, the velocity dispersion of stars in the galactic bulges) and the mass of the central object implies that most, if not all, regular galaxies harbor a central SMBH (Kormendy & Richstone, 1995; Magorrian et al., 1998; Ferrarese & Merritt, 2000), also the Milky Way (Schödel et al., 2002).

called the *inner* or *first Lagrange point*. If a star fills its Roche lobe, matter flows over through the inner Lagrange point onto the other star (Kuiper, 1941; Paczyński, 1971).

Stars in a binary system are typically formed from the same interstellar molecular cloud. Binary systems are ideal laboratories to study stellar evolution because, while the stars are roughly born at the same time and with similar initial chemical composition, they do not have the same mass and lifetime. During the parallel evolution, the more massive star typically evolves faster, leading to a variety of possible systems of stars at different evolution stages (see Paczyński 1971, Ivanova et al. 2013, Postnov & Yungelson 2014, or Belloni & Schreiber 2023 for reviews). Mass exchange during their life on the main sequence also impacts their evolution[12]. In the following, I will concentrate on close binaries, that is, on systems that are sufficiently close that they exchange or will exchange mass at some point of their evolution (in contrast to wide binaries, which only interact gravitationally; see also the classification scheme of binary stars into detached, semi-detached, and contact systems by Kopal 1955). An overview of binary evolution is shown in Fig. 2.4.

The fate of stars in binary systems largely depends on the masses of the components. When the more massive star, called the donor, reaches the end of its lifetime and enters the giant phase, it expands its envelope, either as a red giant or through a wind if the star has a high mass. An expansion of the star beyond its Roche lobe leads to matter flowing through the inner Lagrangian point onto the companion star, called the accretor. Continuous mass transfer can take place if the star expands faster than it loses material, or if the system sheds off angular momentum[13]. In close binaries the time scale of the mass transfer is too short for the mass-receiving star to adjust thermally to the gas. A disk forms from which the star gains mass, which likely also changes its evolutionary path. After some time the accretor also fills its Roche lobe and both stars become engulfed in a common envelope (CE; Paczyński 1976; Iben & Livio 1993; Ivanova et al. 2013; Ohlmann et al. 2016). The CE phase occurs preferentially if the stars have a large mass ratio and this step is essential to understand binary systems with hours or days long orbital period and separations much closer than the size of a star.

The common envelope is not co-rotating with the stellar core of the donor and accretor star. Thus, drag due to friction with the envelope gas leads to angular momentum loss and a rapid in-spiral. The orbit of the two stars shrinks by a factor of 100–1000 (El-Badry et al., 2023a). The CE phase either ends with a merging of the two stars or with the ejection of the envelope when sufficient gravitational potential energy is released (see Ivanova et al., 2013, and references therein). Assuming that the two stars do not merge, there is a variety of evolutions possible from here, sensitively depending on the mass ratio of the stars, the mass transfer rate, and the orbital separation.

If the donor star has insufficient mass to explode in a core-collapse supernova, a white dwarf binary is formed. Black hole and neutron star binaries develop if the donor star is of O- or B-type and has sufficient mass to explode in a core-collapse supernova. The natal kick that such a supernova imposes can disrupt the binary, which potentially leads to high-velocity runaway stars (Blaauw, 1961; Hoogerwerf et al., 2000). If the system remains bound and sufficiently close, matter flows

[12]The mass exchange can lead to a situation where the evolved and originally more massive star loses so much mass to its companion that it becomes the less massive object in the binary. This is sometimes referred to as the *Algol paradox*.

[13]In principle, the mass transfer also highly depends on the evolutionary stage of the donor. In case of a white dwarf donor, the inverse mass-radius relationship leads to a runaway process of mass loss.

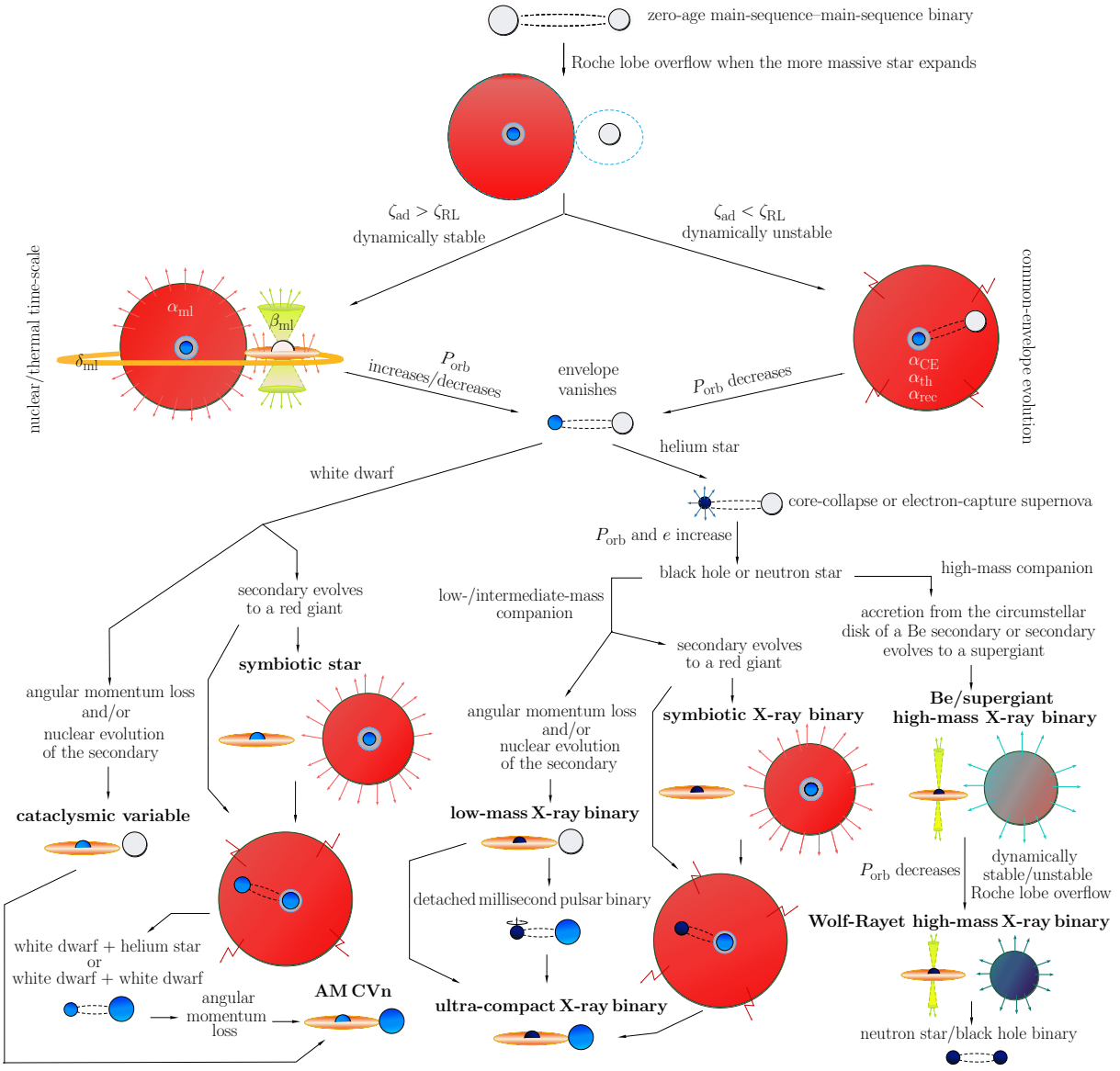

Figure 2.4: Binary evolution channels leading to the formation of accreting compact objects (Fig. 3 from Belloni & Schreiber, 2023). One of two zero-age main sequence stars depletes the hydrogen in its core and expands its envelope. If the initial separation of the two stars is less than roughly 1 astronomical unit, this leads to Roche lobe overflow to the accretor star. If the donor star cannot adjust its interior profile on the mass loss, i.e., the adiabatic exponent ζ_{ad} is smaller than the Roche lobe mass-radius exponent ζ_{RL}, the mass transfer is dynamically unstable and a common envelope forms, leading to a reduction in orbital period P_{orb}. After ejection of the envelope, a close binary is formed. A high-mass core explodes in a supernova after a few million years and the core collapses into a neutron star or black hole. Unless the natal kick from the supernova disrupts the binary, the compact object accretes mass from the donor star, and the system emerges as an X-ray binary. If the companion star has less mass, an accreting white dwarf system forms. Reproduced with permission from Springer Nature.

from the donor star to the compact object (note that the donor star was the accretor before the CE phase). The potential energy of the accreted matter is converted to X-ray radiation in the vicinity of the compact object. Studying the X-ray emission during this evolutionary stage is the main topic of this thesis. In order to understand the resulting "classification zoo" of accreting compact objects, one needs to understand how the X-ray are produced. Thus, I will explain the physics behind this process in the next section.
I conclude this section with the final evolution stages of binary systems. At some point the donor star will also become a compact object, potentially forming a binary system with two compact objects. They can be classified as double white dwarf systems (Nelemans et al., 2001a,b; Napiwotzki et al., 2020), ultra-compact X-ray binaries, where a neutron star or black hole accretes from a white dwarf (Nelemans & Jonker, 2010), or double neutron star/black hole systems. If the compact object is a white dwarf, it may accrete enough material to come close to the Chandrasekhar limit. This leads to a supernova type Ia, which disrupts the white dwarf completely and leaves no compact object behind (e.g., Gutierrez et al., 1996; Hillebrandt & Niemeyer, 2000). In general, the orbits of double compact object systems are very short and they continuously loose angular momentum though gravitational waves. Finally, the two compact objects merge, which can be studied using laser interferometry gravitational wave experiments (Abbott et al., 2016). In the case of two merging neutron stars the event is called a kilonova and the gravitation wave signature is accompanied by an electromagnetic signal (Abbott et al., 2017a,b).

2.4 Accretion Physics

Pauls Begegnung mit einem Schwarzen Loch

Als Wasserstoffatom wird Paul von seinem derzeitigen Heimatstern HDE 226868 aus der Atmosphäre gepustet, zusammen mit vielen anderen Wasserstoff-, Eisen- und anderen Atomen. Zwei weitere Energiequanten in diesem Gasstrom stellen sich ihm als Emilia und Peter vor – Paul wird ihnen später nochmals begegnen. Alle spüren sie das schwache Ziehen eines fremden Körpers. Die Atome lassen die Anziehungskraft des Sterns hinter sich und schießen durch einen engen Strom aus heißem Gas. Paul fühlt sich hier kurzzeitig völlig frei von den Anziehungskräften, doch er ist zu schnell, als dass er hier stoppen könnte. Turbulent geht es in eine strudelnde Scheibe hinein, herum um das zentrale Objekt der Schwerkraft. Peter bleibt etwas zurück, manche seiner Freunde werden sogar ganz nach außen getragen, während sich Paul und Emilia langsam dem Objekt nähern. Es sieht schwarz aus, sehr schwarz. Paul nennt es deswegen ein „Schwarzes Loch".

To be continued in Sect. 2.4.1.

As we have seen in the previous section, binary evolution theory predicts the existence of systems containing a compact accretor and a donor star. If the binary system is sufficiently close, mass flows from the donor star onto the compact object, either through Roche lobe overflow or as a stellar wind (the mass transfer mechanism is one way to classify X-ray binaries, as I will explain in Sect. 2.5). This process is called *accretion*. After the discovery of the first Galactic X-ray sources, accretion of gas from a companion star onto a compact object was proposed to be the mechanism by which X-rays are produced (Shklovsky, 1967). For stellar mass compact objects, accretion was

studied in detail by Pringle & Rees (1972), Novikov & Thorne (1973), and the seminal paper by Shakura & Sunyaev (1973). Reviews on accretion physics can be found in Pringle (1981) or Frank et al. (2002).

Accretion is a very efficient process to convert gravitational potential energy of matter into radiation (the accretion onto a canonical neutron star, for instance, is roughly 20 times more efficient than nuclear fusion, see Frank et al. 2002, p. 1). If the potential energy of the material falling from infinity to the surface of a compact object, R_*, is completely converted into radiation, the *accretion luminosity* can be calculated by (Frank et al., 2002, Eq. 1.5)

$$L_{\rm acc} = \frac{GM\dot{M}}{R_*} \quad , \tag{2.1}$$

where G is the gravitational constant, $\dot{M}$ the mass accretion rate, and M the mass of the compact object. Thus, the more compact an accreting object is (large M/R_*), the greater the amount of emitted radiation[14].

Equation 2.1 shows that the accretion luminosity is directly proportional to the mass accretion rate. However, $L_{\rm acc}$ cannot become arbitrarily large if $\dot{M}$ is scaled up, as the radiation interacts with the accreted matter and exerts pressure on it. The *Eddington luminosity* is defined as the maximal luminosity of an object (such as a star or accreting black hole) in hydrostatic equilibrium, that is, where the outward radiation pressure equals the gravitational force. The classical Eddington luminosity is defined under the assumption of spherical accretion of fully ionized pure hydrogen gas. It is given by (Frank et al., 2002, Eq. 1.3–1.4)

$$L_{\rm Edd} = \frac{2\pi GMcm_p}{\sigma_T} \approx 1.3 \times 10^{38} \left(\frac{M}{M_\odot}\right) \,{\rm erg\,s^{-1}} = 3.2 \times 10^4 \left(\frac{M}{M_\odot}\right) L_\odot \quad , \tag{2.2}$$

where c is the speed of light, m_p the mass of the proton, σ_T the Thomson electron scattering cross-section, and $L_\odot$ the solar luminosity.

How exactly does the material fall towards the compact object? In binary systems, the in-falling matter has non-zero angular momentum (the particle does not follow a straight line onto the compact object). In the case of Roche lobe overflow, particles would follow an elliptical orbit around the compact object in the plane of the binary system. This elliptical orbit precesses due to the presence of the donor star (Frank et al., 2002, p. 60). Therefore, the particle orbits from the continuous in-flowing stream intersect. Dissipative processes between the particles, such as collisions of gas elements, heating by shock waves, or radiative cooling, lead to a *circularization* of the orbits, resulting in the formation of a ring of matter. The particles in this ring move on a Keplerian orbit with angular velocity

$$\Omega_K(R) = \left(\frac{GM}{R^3}\right)^{1/2} \tag{2.3}$$

[14] Note that black holes do not exhibit a surface and energy can disappear within the event horizon. This effect is parameterized by introducing the *accretion efficiency* in Eq. 2.1, which becomes $L_{\rm acc} = 2\eta GM\dot{M}/R_* = \eta\dot{M}c^2$, with η having typical values of 0.1 for black holes, 0.15 for neutron stars, and 0.007 for nuclear fusion of hydrogen to helium (Frank et al., 2002, p. 4).

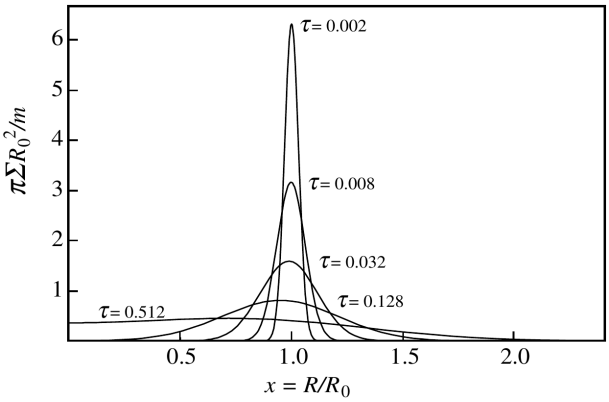

Figure 2.5: Formation of an accretion disk from a ring of matter due to the influence of viscous torques (Fig. 5.1 from Frank et al., 2002). A ring of matter with mass m is placed in a Keplerian orbit at $R = R_0$. The plot shows the surface density Σ as a function of radius, parameterized by $x = R/R_0$. The dimensionless time variable $\tau = 12\nu t R_0^{-2}$ parameterizes the time evolution of the ring, with ν denoting a constant viscosity parameter. Reproduced with permission of Cambridge University Press through PLSclear.

and circular velocity $v_\phi = R\Omega_K = (GM/R)^{1/2}$. This implies that gas elements rotate *differentially*, meaning that particles on a lower orbit move with greater angular velocity than particles on a higher orbit.

Viscous dissipation converts energy from the orbital motion into heat, which is radiated away. Due to this loss of energy, the gas must move to an orbit deeper in the gravitational well. A central question in accretion physics is, however, how the gas can get rid of its angular momentum[15]. Some of the angular momentum has to be transported outwards by internal torques. It is understood that turbulent viscosity is responsible for the angular momentum transport (what physical process causes the turbulent viscosity is, however, less clear – the current interpretation for viscous transport of angular momentum is *magneto-rotational instability*, see Balbus & Hawley 1991). This process leads to the formation of an *accretion disk* (Frank et al., 2002, their Sect. 4.5).

In order to understand the radial disk structure, one has to introduce the conservation equations of mass and angular momentum (Frank et al., 2002, Eq. 5.3–5.4). The mass conservation equation is

$$R\frac{\partial \Sigma}{\partial t} + \frac{\partial}{\partial R}(R \cdot \Sigma \cdot v_R) = 0 \quad , \tag{2.4}$$

where v_R is the *radial drift velocity*, that is, how fast the matter is in-falling, and Σ is the *surface density*, which gives the mass per unit surface area. The conservation equation of angular momentum reads

$$R\frac{\partial}{\partial t}(\Sigma R^2\Omega) + \frac{\partial}{\partial R}(R\Sigma v_R R^2\Omega) = \frac{1}{2\pi}\frac{\partial G}{\partial R} \quad , \tag{2.5}$$

where $G(R,t)$ is the viscous torque. The parameters Σ, v_R, and G depend on an unknown viscosity parameter ν (see Frank et al. 2002, Eq. 5.5, 5.8, and 5.12).

The ramification of these equations on the radial disk structure becomes evident by solving for the temporal variation of $\Sigma(R,t)$, called the *diffusion equation* (Frank et al., 2002, Eq. 5.8 and

[15]The necessity of angular momentum transport was already well understood by the 1920s. In the context of the formation of the solar system, Jeffreys (1929, p. 58) wrote: "The fast-moving interior will tend to drag forward the slower-moving exterior, and thus will increase its energy and make it recede from the sun. Thus the outer parts will be slowly expelled from the system. The inner parts, on the other hand, will have their motion delayed, and will therefore gradually fall into the sun" (see also the brief historical discussion in Pringle 1981, p. 141).

p. 81–84). The solution is shown in Fig. 2.5. One realizes that the radial velocity is *positive* for the outer part of the matter distribution and *negative* for the inner part. This means that the action of viscosity *spreads the ring of matter into a disk*. The majority of the mass spirals inwards, while a small amount of matter moves outwards carrying away the angular momentum.

2.4.1 Soft X-rays from an Accretion Disk around Compact Objects

Es wird eng in der Scheibe, in der sich Paul nun befindet. Er reibt ständig an den anderen Atomen, die sich etwas näher an dem Schwarzen Loch befinden und sich schneller darum herumbewegen. Durch diese Reibung wird es Paul so langsam wirklich heiß und er fängt an wie wild hin und herzuhüpfen. Sein Begleitelektron ist auch schon fort gehüpft. Durch diese zufälligen Richtungsänderungen strahlt Paul immer mehr Energie ab und verändert schließlich seine Gestalt – es ist so heiß, dass Paul zu einem weichen thermischen *Röntgenteilchen wird.*

To be continued in Sect. 2.4.2.

In the following, I will describe the emerging disk spectrum using the *thin disk* approximation, which means that the scale-height, H, is much smaller than the radius, R. This assumption, $H \ll R$, is justified for accretion rates where the radiation pressure of the disk can be neglected at $L_{\rm disk} < L_{\rm Edd}$, that is, where the disk forms a steady-state in hydrostatic equilibrium (Frank et al., 2002, their Sect. 5.3). As we will see later, this *standard model*, proposed by Shakura & Sunyaev (1973), has shown some remarkable agreement with observational data.
Using the thin disk assumption and the conservation laws in steady-state ($\partial/\partial t = 0$ in Eq. 2.4–2.5), one can derive the viscous dissipation rate per unit disc face area as (Frank et al., 2002, Eq. 5.20)

$$D(R) = \frac{3GM\dot{M}}{8\pi R^3}\left[1 - \left(\frac{R_*}{R}\right)^{1/2}\right] \quad . \tag{2.6}$$

This parameter determines the energy that is lost due to viscosity in the turbulent flow and radiated away on the two faces of the disk. Importantly, $D(R)$ is *independent* of the unknown viscosity parameter. This means that one can constrain the energy flux through a thin disk using observational parameters. Assuming that the disk is optically thick in the z-direction, the radiation at each radius is emitted as a local black body, following the Stefan-Boltzmann law $\sigma T^4(R) = D(R)$. Inserting $D(R)$ from Eq. 2.6, the radial temperature profile is obtained as

$$T(R) = \left(\frac{3GM\dot{M}}{8\pi R^3\sigma}\left[1 - \left(\frac{R_*}{R}\right)^{1/2}\right]\right)^{1/4} \propto \dot{M}^{1/4}\, R^{-3/4} \quad . \tag{2.7}$$

This equation shows that the temperature rises with decreasing radius. Around stellar mass black holes, the disk can extend to the innermost stable circular orbit (ISCO), which is at six gravitational radii, $r_g = GM/c^2$, for a non-rotating, and $\sim$1.2 r_g for a maximally progradely spinning black hole (Bardeen et al., 1972). The accreted matter in this innermost region is heated to temperatures of $\sim 10^7$ K and the resulting thermal radiation is emitted in the soft X-rays, peaking at a few 100 eV.

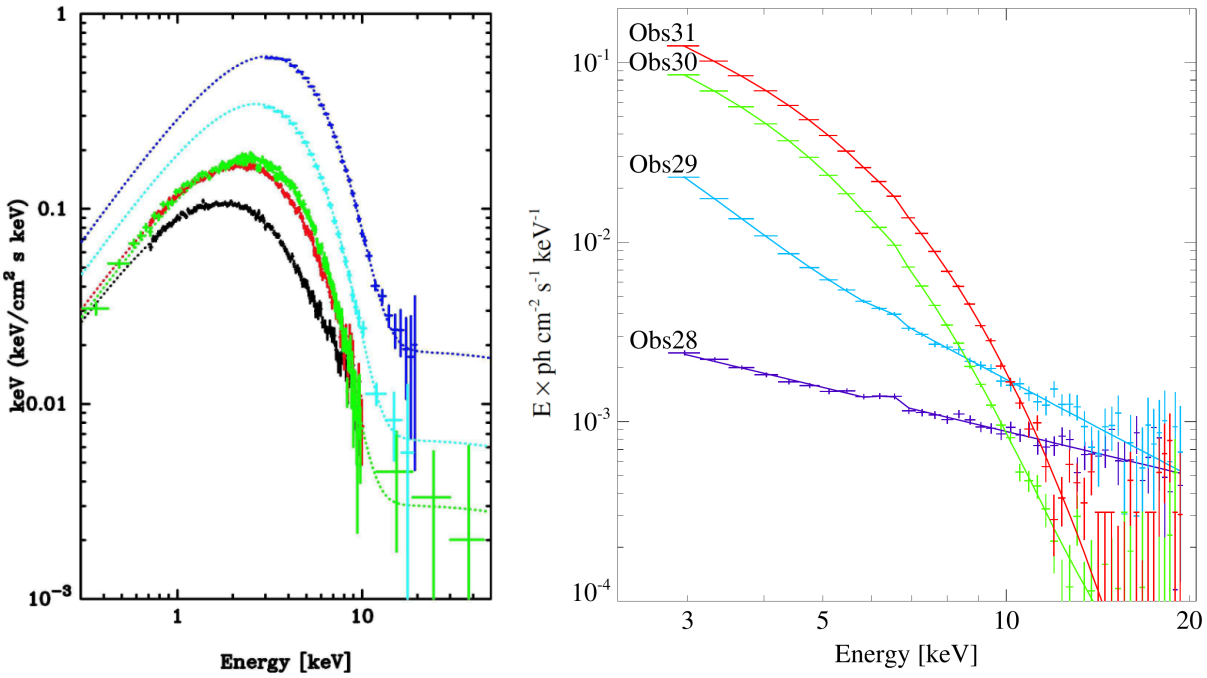

Figure 2.6: Unfolded spectra of the black hole X-ray binary LMC X-3 at different flux levels. *Left:* Data taken with *ASCA* (black and red), *BeppoSAX* (green), and *RXTE*/PCA (cyan and blue) during the soft state (Fig. 15 from Done et al., 2007). The dashed line denotes a multi-temperature disk black body model. Reproduced with permission from Springer Nature. *Right: RXTE* data of LMC X-3 (Fig. 4 from Wilms et al., 2001). At low luminosity ("Obs28"), hard X-rays in a power law component are seen, extending to energies above 10 keV.

In order to obtain an estimate of the total emitted spectrum, one can insert Eq. 2.7 into the Planck spectrum and integrate it over the whole disk. This yields a function that looks like a stretched-out black body. Figure 2.6 (*left*) compares this theoretically predicted multi-temperature disk black body to an observed X-ray spectrum of the accreting black hole binary LMC X-3. It can be seen that the spectrum is well approximated by the model. The figure also shows the source for different flux levels. From Eq. 2.1 and Eq. 2.7 it can be seen that a higher mass accretion rate leads to an increase in luminosity and temperature of the disk, thus shifting the spectrum up and to higher energies.

2.4.2 Hard X-rays from Comptonization in Black Hole X-ray Binaries

Als weiches Röntgenteilchen fliegt Paul weg von der Scheibe und trifft in direkter Nähe auf eine Wolke aus Gas. Sie ist deutlich durchsichtiger als die Scheibe zuvor, doch dafür ist es hier noch heißer. Es ist unmöglich, den springenden Elektronen auszuweichen, die sich hier befinden. Sie schubsen Paul immer weiter vorwärts, er bekommt mehr und mehr Energie. Hier trifft Paul auch Emilia wieder und zusammen erreichen sie den Rand der Wolke. Durch die ständige Stoßerei haben sie nun deutlich mehr Energie, als noch beim Eintreten in die Wolke hatten. Sie sind jetzt harte *Röntgenteilchen.*

To be continued in Sect. 2.4.3.

In the previous section, I introduced how the accretion of matter onto a compact object leads to the formation of an optically thick, geometrically thin accretion disk aligned with the binary plane, which radiates in the soft X-rays for accreting stellar mass black holes. In addition to these soft photons, hard X-rays are also detected in black hole X-ray binaries[16], which can be seen in Fig. 2.6 (*right*, see curve labeled "Obs28").

Early models often considered the hard X-rays to be produced by Compton up-scattering (Compton, 1923) of soft thermal photons from the disk in a hot ($kT_e \approx 100\,\mathrm{keV}$) plasma close to the black hole, which is heated by some kind of magneto-hydrodynamic effect such as magnetic reconnection (Thorne & Price, 1975; Sunyaev & Trümper, 1979). Analogous to the Sun, the source of the hard X-rays is therefore often called the *corona* (Liang & Price, 1977). The observed power law with exponential cut-off is widely considered to originate from this region and the energy of the cut-off is believed to roughly correspond to the temperature of the electrons in the corona. However, although the existence of the corona is widely accepted, its location and shape remains unclear, and an active debate is present in the literature (e.g., Kara et al., 2019; Zdziarski et al., 2021; Marino et al., 2021). Models for the corona place it either around the black hole inside a truncated accretion disk (Sunyaev & Titarchuk, 1980; Narayan & Yi, 1995; Esin et al., 1997; Done et al., 2007; Marcel et al., 2019; Mahmoud et al., 2019), in a slab geometry above and below the accretion disk (sandwich model; Haardt & Maraschi 1991; Churazov et al. 2001), spherically around the black hole (Dove et al., 1997), as a compact source on the rotational axis above the black hole (lamppost model; Matt et al. 1991; Martocchia & Matt 1996; Dauser et al. 2013), or as an outflowing plasma (Beloborodov, 1999; Markoff et al., 2005). Sketches of these geometrical interpretations are shown in Fig. 2.7.

Apart from X-rays, synchrotron radio emission from a large scale jet can sometimes be observed (Fender et al., 2004). Blobs of material are emitted perpendicular to the accretion disk with velocities very close to the speed of light, sometimes even exhibiting super-luminal motion (Mirabel & Rodríguez, 1994). The acceleration of particles to such relativistic velocities can only be powered by the innermost region around the black hole, either through extraction of angular momentum from the rotating black hole (Blandford & Znajek, 1977) or from the accretion disk (Blandford & Payne, 1982). Motivated by the spatial vicinity of the corona and jet base, Markoff et al. (2005) show that the radio and X-ray data can be explained if the outflowing base of the jet subsumes the role of the corona (jet base model) similar to a lamppost, radiating in the hard X-rays and

[16] The fraction of soft and hard X-rays depends on the *state* of the source, which I will explain in Sect. 4.1.

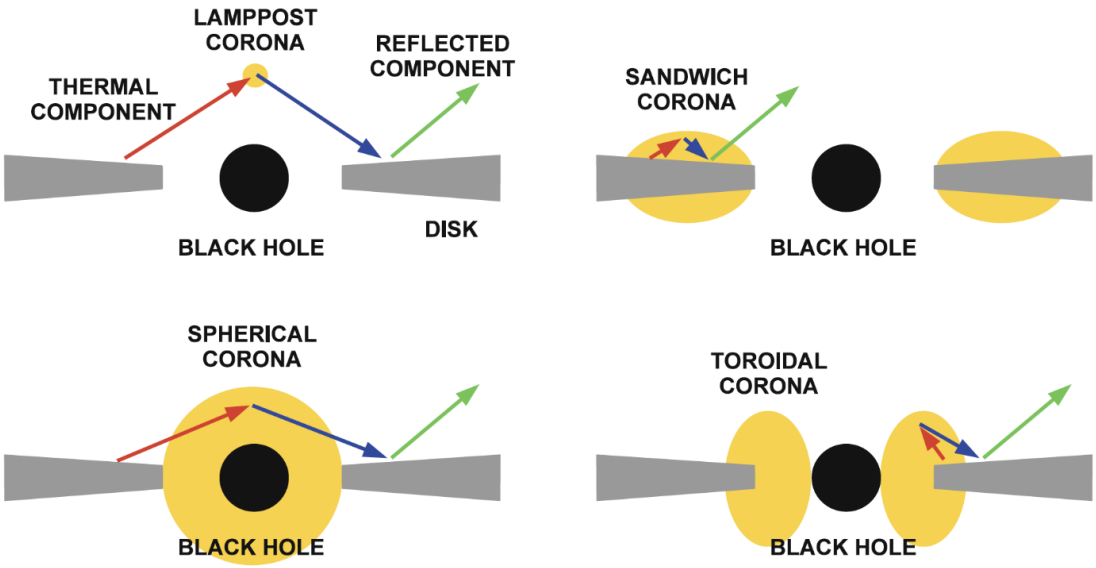

Figure 2.7: Examples of possible interpretations for the geometry of an accreting black hole (Fig. 3 from Bambi et al., 2021). The Comptonizing plasma could be located on the rotational axis of the black hole (lamppost), on top of the accretion disk (sandwich), spherically around the black hole, or as a hot flow inside of a truncated disk (toroidal). Thermal seed photons are indicated by a red arrow. In all four cases, some of the Comptonized X-rays impinge the accretion disk and are reprocessed (blue and green arrows). Reproduced with permission from Springer Nature.

illuminating the disk.

2.4.3 Reflected X-rays from the Accretion Disk

Einmal draußen aus der Wolke scheint es Paul zunächst, als wäre er auf dem Weg fort von dem Schwarzen Loch. Doch der direkteste Weg führt ihn nicht in den freien Weltraum. Obwohl er nur geradeaus fliegt, zieht es ihn von außen betrachtet im Bogen um das schwarze Loch herum, direkt auf die Scheibe zu, aus der er eben noch gekommen ist. „Achtung“, ruft Paul, als er auf Peter zurauscht, ein großer Eisenatomkern, der noch einige Begleitelektronen bei sich hat. Doch da schlägt er schon eines der inneren Elektronen von Peter weg, überträgt seine Energie, und nimmt eine Elektronengestalt auf einer höheren Bahn um Peter herum an. „Anregender Ausblick hier oben“, denkt er sich noch, doch da fällt er schon wieder hinab auf Peter zu und wird als leuchtendes Lichtteilchen weggestrahlt. Nun muss er noch der Anziehung des Schwarzen Lochs entkommen. Peinlich, dass ihm das so schwierig fällt, er errötet ein wenig und verliert nochmals etwas an Energie.

To be continued in Ch. 3.

The strong space-time curvature around the black hole bends some of the X-ray radiation from the corona towards the accretion disk. The light is reprocessed in the atmosphere of the disk, that is,

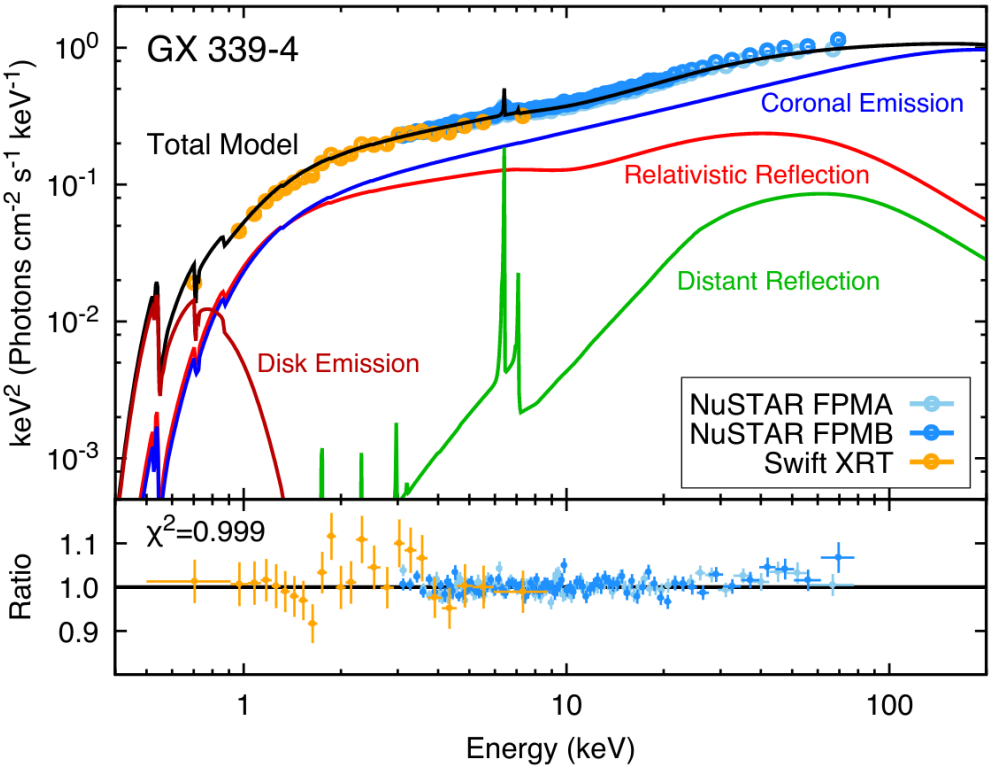

Figure 2.8: X-ray reflection spectrum from the black hole binary GX 339-4 measured with the *Swift*/XRT and *NuSTAR* and fitted with the RELXILL model (Fig. 4 from Ray et al., 2019). *Top:* Thermal seed photons emitted from the accretion disk are shown as dark red curve. The Comptonized emission is modeled as a power law with a high-energy cut-off (blue, note that the spectrum is shown as $E \times F_E$). The reflection spectrum with a broadened iron line at 4–8 keV and a Compton hump at ∼30 keV is shown in red. In addition, a *distant reflector* is included (green line). This component is attributed to an absorbing cloud of material far away from the black hole, leading to more narrow emission lines compared to the relativistic reflection. *Bottom:* Ratio of the data with respect to the best fit model.

it is scattered, absorbed, and re-emitted, which imprints the disk's chemical composition on the radiation (Guilbert & Rees, 1988; White et al., 1988; Lightman & White, 1988). Observationally, this can be detected as emission lines in the X-ray spectrum (Fabian et al., 1989; George & Fabian, 1991; García et al., 2015). Although the accretion disk mostly consists of hydrogen, the dominant feature in the spectrum is iron due to its large fluorescence yield (García & Kallman, 2010). The reprocessing occurs in the innermost disk region and the iron fluorescence lines at around 6.4–7.1 keV are relativistically broadened due to the rapid orbital motion of the disk, and skewed due to the gravitational redshift and Doppler boosting. Furthermore, often a broad feature at 10–40 keV, named the *Compton hump*, is seen (Lightman & White, 1988; Matt et al., 1991; Done et al., 1992), which provides further evidence for the reprocessing in the accretion disk.

The parameters of the black hole (spin) and the accretion flow (location of the inner edge, inclination, ionization, density, and iron abundance of the disk) therefore influence the spectrum of the reprocessed radiation. Physical models have been developed which describe the accretion flow and the black hole in relativistic space-time, often referred to as *relativistic reflection* models. RELXILL (Dauser et al., 2013) or REFLIONX (Ross & Fabian, 2005) include relevant relativistic effects and the atomic physics taking place in the accretion disk during the reprocessing. In the case of RELXILL, the reprocessing in the disk atmosphere is calculated with the XILLVER code (García et al., 2013). An illustrative reflection spectrum is shown in Fig. 2.8.
By carefully modeling the underlying broad-band continuum, the broadened iron line and Compton hump and, ideally, the soft excess at low X-ray energies, it is possible to infer the system parameters. Distances, such as the inner disk radius or height of the corona in a lamppost geometry, are given in dimensionless units, usually in r_g. Thus, the standard RELXILL modeling does not depend on the mass of the black hole. It is also important to emphasize that RELXILL is valid for arbitrary geometries (represented by the so-called emissivity profile) and not only for the lamppost geometry depicted in Fig. 2.7.

2.5 Classification of Accreting Compact Objects

There are two ways to classify the multitude of possible accreting compact object binaries that emerge from binary evolution (Sect. 2.3). The system can be classified by the donor star, thereby emphasizing the mass transfer mechanism, or by the compact object, focusing on how the potential energy of the matter is converted into radiation.

2.5.1 Classification by Donor

X-ray binaries are characterized as low- or high-mass X-ray binary (L-/HMXB) depending on the mass of the donor star. LMXBs have a donor star that has less mass than the compact object, typically a main sequence star, a sub-giant or red giant branch star. These objects comprise a complex class of sources with many sub-classifications based on their X-ray spectrum, variability and brightness, arising from the nature of the companion star and compact object, and the configuration of the binary orbit (see Bahramian & Degenaar 2022 for a recent review).
The orbital period of LMXBs is usually on the order of hours to few days (Bahramian & Degenaar, 2022, their Fig. 10) and the separation is small enough such that the donor star fills its Roche lobe. Matter flows over to the compact object and is accreted, as described in Sect. 2.4. The mass accretion rate, $\dot{M}$, sensitively depends on the orbit parameters, particularly the eccentricity and period of the orbit, the separation of the two bodies, and the exact type of the donor star. As a result, LMXBs can show strong variations in $\dot{M}$, which directly impacts the emitted X-ray flux (see Eq. 2.1). Thus, the luminosity of the LMXB can change by a factor of $\gtrsim$1000, or 0.01–0.5 L_{Edd} in terms of the Eddington luminosity (Eq. 2.2), on timescales of weeks to months with long intervals of quiescence at $\lesssim 10^{-5}\, L_{\mathrm{Edd}}$ in between (Bahramian & Degenaar, 2022). This behavior is called a *transient outburst*. Due to the fact that the spectrum at the peak of the outburst is dominated by soft X-rays, the term *soft X-ray transient* is also sometimes used. Historically, these systems are

also called *X-ray novae* due to there sudden appearance in the sky[17].
HMXBs contain O- or B-stars and are much rarer, mainly due to the shorter lifetime of the donor stars. These stars have a strong ($\dot{M} \gtrsim 10^{-5}$–$10^{-7}\,\mathrm{M}_\odot\,\mathrm{yr}^{-1}$; Martínez-Núñez et al. 2017), fast (up to $2500\,\mathrm{km\,s}^{-1}$; e.g., Grinberg et al. 2015), and clumpy (clump sizes of roughly 1% of the stellar radius; El Mellah et al. 2018; Sundqvist et al. 2018; Hirsch et al. 2019) stellar wind. The wind is driven by radiative line scatterings, which means that the momentum of the continuum photons from the star is transferred to the gas through scattering in atomic lines (Castor et al., 1975; Owocki et al., 1988). The wind is constantly accreted onto the compact object (very roughly approximated by spherical Bondi-Hoyle-Lyttleton accretion; Hoyle & Lyttleton 1939; Bondi & Hoyle 1944; Edgar 2004), leading to *persistent* X-ray emission. These sources typically have no quiescence state.
HMXBs are further sub-divided into Be/X-ray binaries (BeXRBs; Rappaport et al. 1978)[18], and those where the donor is a supergiant of O- or B-type (SGXBs). Roughly 60% of the HMXBs in the Milky Way are BeXRBs (Reig, 2011), and 32% are supergiant X-ray binaries (Liu et al., 2006), accompanied by some less common types, such as supergiant fast X-ray transients (Negueruela et al., 2006). Among the BeXRBs, almost all systems harbor a neutron star accretor, consistent with predictions from evolutionary models (Belczynski & Ziolkowski 2009, see also Casares et al. 2014 for the observational discovery of a Be black hole binary candidate). Based on the observational properties of the system, there are further sub-classifications possible, such as microquasars (Mirabel & Rodríguez, 1998) or γ-ray binaries (Dubus et al., 2017). Ultra-luminous X-ray sources (ULXs) are likely also HMXBs, which are further classified as pulsar ULXs if they show pulsations. Whether all ULXs have neutron star accretors is, however, an active area of research (see King et al. 2023 for a review on ULXs). For further details on the sub-classifications of HMXBs, I refer to the recent review by Fornasini et al. (2023).

2.5.2 Classification by Accretor

In the following, I will discuss the classification of accreting black holes, neutron stars, and white dwarfs. The identification of the accreting compact object is often not trivial. For HMXBs it is sometimes possible to determine the mass function of the system using radial velocity measurements and, thus, get a mass estimate of the compact object. In LMXBs, however, the optical companion is usually too dim to be observed. Therefore, the observable X-ray properties are used to determine the nature of the compact object. This includes the X-ray spectrum and variability properties, as well as the multi-wavelength appearance of the source.

Black Hole Accretors Historically, black hole systems are called *black hole candidates* until a confirmation from an optical dynamical mass measurement is available. This strict naming convention appears to change in recent years, likely because the differentiation between black holes and neutron star systems has become easier due to higher data quality and better knowledge of their

[17]The term *nova* is usually not used for accreting black holes or neutron stars any more, but rather for the thermonuclear explosions on the surface of white dwarfs, which I describe in Sect. 2.6.

[18]A Be star is a B-star that shows hydrogen emission lines in the optical spectrum. Be stars are rapidly rotating and exhibit gaseous decretion disks around their equator formed from material ejected by the star (Struve, 1931; Hanuschik, 1996; Rivinius et al., 2013).

populations. Black hole X-ray binaries are a rare consequence of binary evolution. Evolutionary models estimate that only 1% of LMXBs harbor black holes, with the rest containing neutron stars (Portegies Zwart et al., 1997). In the Milky Way, a total number of ∼1300 black hole X-ray binaries are predicted to exist with ∼70 being observed (Corral-Santana et al., 2016). Most of LMXB are transient with two examples being GX 339−4 (Belloni et al., 2005) and MAXI J1820+070 (Torres et al., 2019). There exist, however, also persistent ones, for instance 4U 1957+11 (Barillier et al., 2023). V4641 Sgr has an evolved B-type star of roughly $3\,M_\odot$ as companion, which is the heaviest companion known in the class of LMXB black holes (MacDonald et al., 2014).
There is only one confirmed HMXB black hole known in our Galaxy, namely Cyg X-1. There are, however, some further candidates such as GRS 1758−258 or 1E 1740.7−2942 (Smith et al., 1997), and the potential ULX source SS 433 (Fabrika, 2004). Cyg X-3 is another peculiar X-ray binary in the Milky Way. It has a Wolf-Rayet star as a companion and the mass of the central object is estimated to $2.4^{+2.1}_{-1.1}\,M_\odot$ (Zdziarski et al., 2013), making it another HMXB black hole candidate although a neutron star compact object and even a ULX nature cannot be excluded (Veledina et al., 2023). In nearby galaxies, LMC X-1 (Nowak et al., 2001), LMC X-3 (Wilms et al., 2001), and M33 X-7 (Orosz et al., 2007) are confirmed HMXB black holes and IC 10 X-1 (Prestwich et al., 2007) and NGC 300 X-1 (Carpano et al., 2007) are further candidates. In total, there are currently around 69 transient and around 10 persistent black hole X-ray binaries known out of which around 30% are dynamically confirmed (see Tetarenko et al. 2016 or the BlackCAT catalog[19] by Corral-Santana et al. 2016 for comprehensive lists).
Masses of accreting stellar black holes discovered in the X-ray wavelengths are observed to be in the range 4.6–21 $M_\odot$ (Barillier et al., 2023; Miller-Jones et al., 2021) with the peak of the distribution between 5–10 $M_\odot$ (Corral-Santana et al., 2016). Non-accreting binary systems, which can be detected with radial velocity measurements in optical wavelengths, lower this bound to $3.3\,M_\odot$ (Thompson et al., 2019). Including extra-galactic sources increases the measured masses to $\sim 33\,M_\odot$ (Prestwich et al., 2007). The mass range is further expanded by gravitational wave measurements, which observe sources with ∼2.6–85 $M_\odot$ (Abbott et al., 2020a,b) although some of the lower mass objects could also be neutron stars. If these are indeed black holes, this places them in the mass gap between neutron stars and black holes, which would challenge the standard stellar evolution models outlined in Sect. 2.1.

Neutron Star Accretors A unique way to distinguish a black hole from a neutron star X-ray binary is the detection of pulsations, which arise due to the misalignment of the star's rotational axis and the region of its magnetic poles from where the X-ray radiation originates. Another way to identify neutron stars is the presence of short, bright X-ray bursts, which originates from thermonuclear burning on the surface of the neutron star (e.g., Lewin et al., 1993). As neutron stars are not topic of this thesis, I refer the interested reader to the PhD thesis by Sokolova-Lapa (2023, and references therein) for further information.

White Dwarf Accretors Close binary systems formed by a dwarf main sequence star and an accreting white dwarf are called cataclysmic variables (CVs; Mukai 2017). Systems where the donor

[19] https://www.astro.puc.cl/BlackCAT/

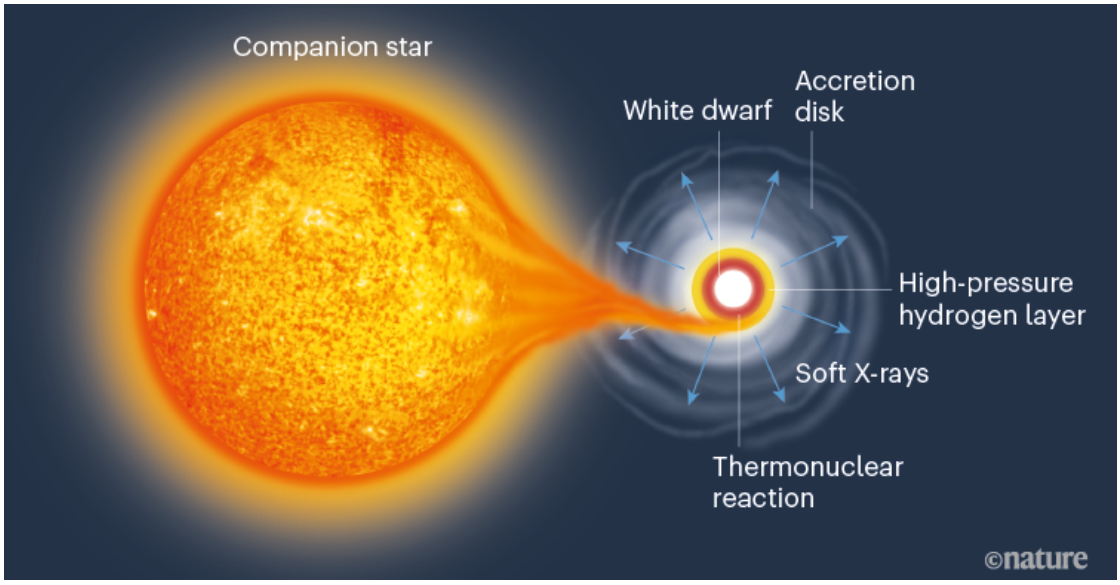

Figure 2.9: Sketch of a cataclysmic variable undergoing an X-ray flash during the early stage of a nova outburst (Fig. 1 from Walter, 2022). Reproduced with permission from Springer Nature.

star is a red giant typically accrete via a stellar wind and are called symbiotic binaries (Kenyon, 1986). The donor star can also be a hydrogen-deficit star (these are called AM CVn stars; Solheim 2010) or a hot subdwarf (Heber, 2009; Kupfer et al., 2020). Accreting white dwarfs are formally not classified as low- or high X-ray binaries because their accretion disk emission peaks in the UV and because the mass of the donor star and white dwarf are typically very similar (a massive star would have exploded in a supernova long before the white dwarf is formed). Their evolution is mainly determined by angular momentum loss through gravitational radiation and magnetic braking[20], which can lead to a very close binary separation (Mukai, 2017). Thus, CVs and symbiotic binaries typically have short orbital periods on the order of 80 minutes to 10 hours (however, this is not a necessity – the system RS Oph, for instance, has an orbital period of 454 days; Brandi et al. 2009). AM CVn stars can even show periods as short as 5 minutes (Roelofs et al., 2010).
As for LMXBs, Roche lobe overflow from the donor star leads to the formation of an accretion disk (see Fig. 2.9). Thus, CVs and symbiotic binaries can be strong emitters of X-ray radiation (10^{31}–10^{34} erg s^{-1}; Mukai 2017). Non-magnetic CVs emit X-rays from the boundary layer between the white dwarf and the accretion disk (Patterson & Raymond, 1985a,b), while magnetic CVs, so-called polars, funnel the accretion stream onto the magnetic poles, which produces X-rays mainly through bremsstrahlung (Mukai, 2017). In both cases, hydrogen-rich material accumulates in a shell around the white dwarf. The material can undergo stable continuous nuclear burning, leading to supersoft X-ray sources such as Cal 87 (van den Heuvel et al., 1992), or it ignites in a nova

[20] Magnetic braking is a mechanism for angular momentum loss of stars. In case of a single star the ionized material in the stellar wind couples to the magnetic field of the star. As the material is expelled while co-rotating with the star, angular momentum is shed from the system. In binary systems the stellar wind of the donor star couples to the magnetic field of the other star, leading to angular momentum loss (e.g., Rappaport et al., 1983).

eruption when a critical threshold for hydrogen burning is reached. The latter type of event is characterized in the following section.

2.6 Classical Novae

Pauls Abenteuer in einer Kernfusion

Paul hat während seiner vielen Abenteuer auch die Bekanntschaft mit einem Weißen Zwerg gemacht. Hier möchte sein Abenteuer in einer Kernfusion erzählt werden. Das war jedoch zunächst gar nicht so spannend. Schon seit 1000 Jahren sitzt er als Elektron auf der Oberfläche dieses Weißen Zwerges, dicht gedrängt an seine Elektronen- und Protonenfreunden. Es ist so eng, er weiß schon gar nicht mehr, ob er jetzt nicht doch den Platz mit dem Elektron Emilia getauscht hat. „Ich fühle mich ganz verschwommen!", ruft sie (oder hat er das gerade selbst gesagt?).

To be continued in Sect. 2.6.1.

The first reported observations of *stella novae*, "new stars" appearing on the night sky for a limited period of time, were made by Chinese imperial astrologers more than 2000 years ago (Duerbeck, 2008). The understanding of novae advanced significantly when researchers realized that these events occur in binary systems (Walker, 1954) containing a white dwarf (Kraft, 1959). The companion star can be a main sequence, sub-giant or red giant donor star (Darnley et al., 2012), transferring matter to the white dwarf via Roche lobe overflow (Crawford & Kraft, 1956). Usually, the mass accretion rate in these systems is too low, between 10^{-11} to $10^{-8}\,\mathrm{M_\odot\,yr^{-1}}$ (Prialnik & Kovetz, 1992; Townsley & Bildsten, 2004), to produce detectable X-ray radiation, making them undetectable in quiescence with current instruments.

The low mass accretion rate instead gives rise to a sudden thermonuclear explosion[21] on the surface of the white dwarf once a critial mass threshold of around 10^{-7}–$10^{-3}\,\mathrm{M_\odot}$ is accreted (Chomiuk et al., 2021). In the following, I will explain the outburst theory of *classical* novae. These are systems observed to explode once, as opposed to *recurrent* novae, which undergo multiple eruptions[22]. Throughout this section, I will use the evolution points in the Hertzsprung-Russell diagram, shown in Fig. 2.10, to describe the nova outburst. For theoretical modeling of novae and further information, I refer the reader to Starrfield et al. (1972), Prialnik et al. (1978), Prialnik & Kovetz (1992), Fujimoto & Iben (1992), José & Hernanz (1998), Townsley & Bildsten (2004), Hillman et al. (2014), Kato et al. (2017), and the reviews by Starrfield et al. (2016), and Chomiuk et al. (2021).

[21] In fact, already Rosseland (1946) speculated that nuclear processes were at work and that "the cause of the nova ourburst [...] might be connected with an atomic bomb explosion" (Pottasch, 1959), which was the reason that the latter author drew a "ball of fire" analogy.

[22] Typical recurrence times range from one (e.g. Darnley et al., 2016) to about 100 years, where the upper boundary is strongly biased due to the small amount of systematic all-sky observations performed before the 20th century. In principle, all classical novae should be recurrent on timescales of 10^3–10^6 yr (Truran & Livio, 1986).

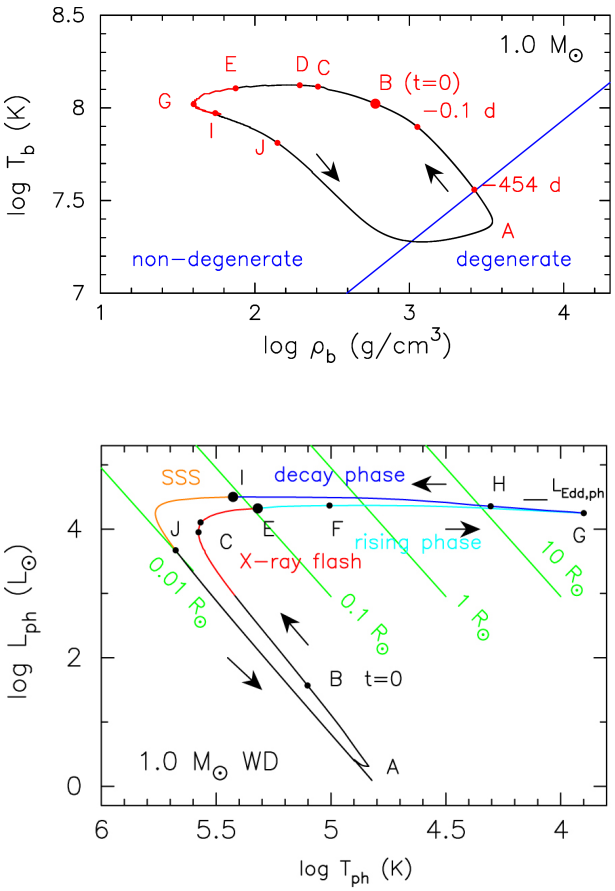

Figure 2.10: Model of a full nova cycle. *Top:* Temperature and density at the bottom of the envelope (Fig. 5a from Kato et al., 2022b). *Bottom:* Evolution in the Hertzsprung-Russell diagram (Fig. 8 from Hachisu & Kato, 2023). Point A represents the quiescent accretion phase where the electrons at the bottom of the envelope are degenerate. When the TNR begins, the source rapidly moves to higher temperature and luminosity, while the radius stays constant. At B, maximal nuclear luminosity is reached. The X-ray flash begins when the energy is transported to the surface. At C, the photospheric temperature is maximal during the rising phase. The envelope expands and the temperature decreases. An optically thick wind is emitted at point E. The photosphere has its maximal extent and maximal wind mass loss at point G, after which it recedes again, leading to an increase in temperature. When the photosphere has receded almost to the surface of the white dwarf, and the wind terminates (I), residual nuclear burning becomes visible as a supersoft source (I–J). When fusion ceases, the white dwarf cools down and returns to A. The Eddington limit is indicated as a horizontal line in the top right corner and the photospheric radius as green lines. ©AAS. Reproduced with permission.

2.6.1 First Signatures of the Thermonuclear Runaway: The X-ray Ignition Flash

Die Enge wird immer gewaltiger bis, endlich, etwas passiert. Paul und Emilia sehen, wie sich vier der dicken Protonen so nahe kommen, dass ihre Körper verschmelzen[i]*. Es gibt einen gewaltigen Blitz und Paul wird in einer Feuerwand mitgerissen und blubbert bis an die Oberfläche. Er kann nun sehen, dass der Weiße Zwerg ein riesiger, heiß glühender Feuerball ist. Die gesamte Hülle steckt in Brand und löst sich von der Oberfläche. Paul jagt vor ihr hinfort. Aufgrund der hohen Temperatur ist er zu einem weichen Röntgenteilchen geworden (was ihn freut, denn das Röntgenteilchen ist seine Lieblingsgestalt).*

To be continued in Sect. 2.6.2.

Accreted hydrogen-rich material from the donor star accumulates in an envelope on the surface of the white dwarf, which grows to a thickness of several hundred kilometers (Starrfield et al., 1972; José & Hernanz, 1998). The density and temperature at the base of the envelope steadily increase due to compression and nuclear burning via the proton-proton chain and cold CNO cycle (José & Hernanz, 1998; Wiescher et al., 2010). In classical novae, the electrons at the bottom of the envelope are degenerate[23] (Fig. 2.10, *top*). As for the helium flash in low-mass stars (Sect. 2.1.1), the degeneracy decouples density and temperature of the matter and the temperature increases without thermal expansion. When the temperature rises to the Fermi level at roughly 7×10^7 K (Starrfield et al., 2016), the coupling is recovered, meaning that the matter can expand. At this point, however, the temperature and energy output from fusion via the hot CNO cycle increases so rapidly that a thermonuclear runaway (TNR) occurs (Starrfield et al., 1972, 2016). The temperature at the bottom of the envelope rises to a peak of several 10^8 K within a few tens of seconds (José & Hernanz, 1998). Convection cells emerge, which range from the bottom to the top of the envelope (e.g., Fujimoto & Iben, 1992, their Fig. 1), and the energy is transported efficiently to the surface within 5–10 minutes (G. Sala, priv. comm.). Eventually, the thermal energy of the particles in the envelope becomes higher than the gravitational binding energy, such that the envelope expands rapidly.

Radiation is emitted from the shell where the material becomes optically thin, called the *photosphere* of the nova. An *effective temperature* is associated with the photosphere based on the approximation that the spectral energy distribution can be described by the Stefan-Boltzmann law, that is, it is "black body-like" (Baschek et al., 1991).

When the envelope ignites (point A–B in Fig. 2.10), the effective temperature of the photosphere rises rapidly from roughly 10^5 K to 10^6 K (Fig. 2.11, *left*), which is so high that the emitted thermal radiation peaks in the extreme ultraviolet (UV) or soft X-ray regime. The luminosity increases by several orders of magnitude and reaches the Eddington limit (Eq. 2.2) when the envelope starts expanding (point C). For more than 30 years, theory has therefore predicted that the photosphere right after the TNR should emit a short-lived flash of soft thermal X-rays (Starrfield et al., 1990), which has been labelled the "fireball phase" (Pottasch, 1959; Krautter, 2008).

The duration of the flash correlates to the mass of the white dwarf: the higher the mass, the higher the gravitational binding energy because the radius of degenerate white dwarfs scales inversely with mass. Therefore, pressure and temperature in the envelope increase with the mass and, thus, the amount of accreted material necessary to trigger a TNR decreases with the mass. The duration of the flash, which mainly depends on the amount of available burning material, scales inversely with the mass of the white dwarf (see Fig. 2.11, *right*). Theoretical models predict that an X-ray flash should last only a few hours for a white dwarf near the Chandrasekhar limit, while the flash of a white dwarf with $\lesssim 1\,M_\odot$ can last several days and peaks in the UV (Hillman et al., 2014; Kato et al., 2016).

While UV emission has been detected for a few novae (Cao et al., 2012; Pietsch et al., 2007), searches

[23] Note that the degeneracy is not a requirement for a nova. In recurrent nova with a mass accretion rate above roughly $3 \times 10^{-9}\,M_\odot\,yr^{-1}$, the TNR can also occur under ideal gas conditions due to the much stronger coupling of the nuclear burning rates to the temperature than the density (energy production $\epsilon_{CNO}(T) \propto T^{18}$, while $\epsilon_{CNO}(\rho) \propto \rho$, see Wiescher et al. 2010, p. 385 and Eq. 5 and also Sect. 2.1.1 of Chomiuk et al. 2021 and Sect. 3.3 in Kato et al. 2022b).

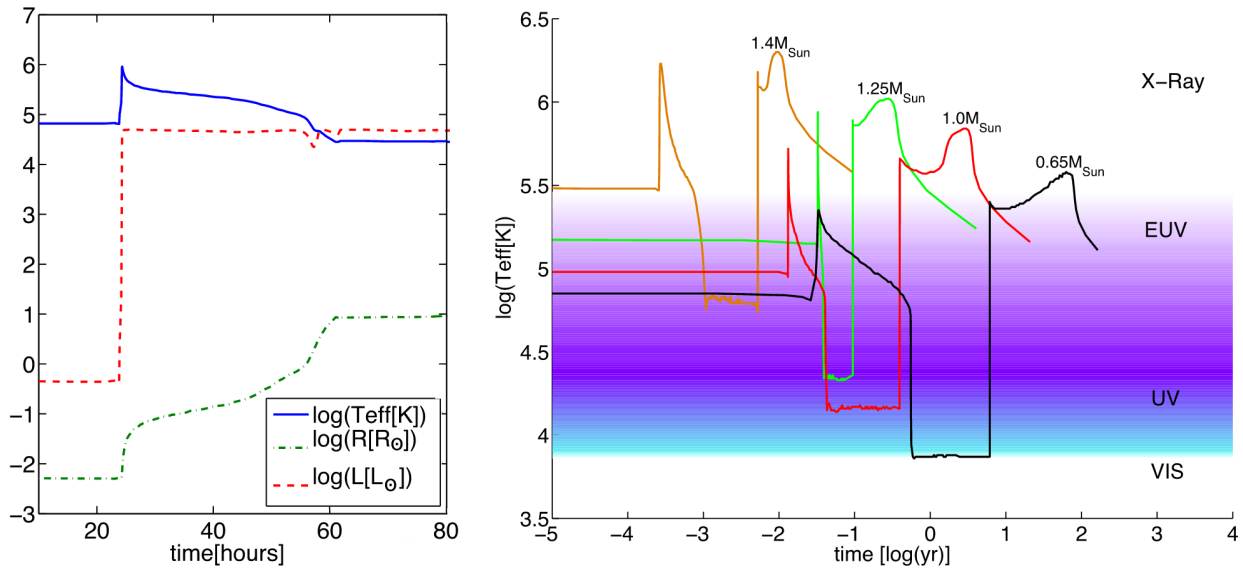

Figure 2.11: Evolution of physical parameters during a nova outburst. *Left:* Short-term photospheric evolution of a 1.25 $M_\odot$ white dwarf (modified after Hillman et al., 2014, Fig. 2). The X-ray flash begins at $t = 25$ h when the temperature rises to 10^6 K and the luminosity increases to the Eddington limit. The photosphere expands at constant luminosity, which results in a drop of the temperature after only a few hours. *Right:* Temperature evolution of a complete nova cycle for white dwarfs of different masses (Fig. 3 from Hillman et al., 2014). The first spike in the curve represents the initial UV/X-ray flash, while the second peak denotes the supersoft source phase (note that the x-axis is logarithmic).

for the X-ray flash have so far been unsuccessful (Morii et al., 2016; Kato et al., 2016). Morii et al. (2013) reported of a short X-ray flare in MAXI J0158−744, an atypical nova in a binary that consists of a Be-star and a white dwarf. The authors inferred a super-Eddington luminosity and very high temperature above 5×10^6 K. In combination with a relatively small ejection mass, the observation required a white dwarf mass near or even above the Chandrasekhar limit with a high magnetic field ($\sim 5 \times 10^{11}$ G) to explain the X-ray flash. These flare properties, in particular the super-Eddington luminosity and high-energy emission, differ from those predicted for the fireball phase and this event is likely attributable to interaction of the nova with the donor's stellar wind (Li et al., 2012; Kato et al., 2016). Morii et al. (2016) performed a systematic search using the Monitor of X-ray Image (*MAXI*; Kawamuro et al. 2018) but the luminosity limit was significantly above that expected from nova theory due to its low energy threshold of 2 keV. Another promising search that was conducted, was the *Swift* monitoring of the recurrent nova M31N 2008-12A by Kato et al. (2016). The search was optimized for a nova with an hours-long X-ray flash but the authors could not detect a flash 8 days prior to the optical detection (see also Henze et al., 2015, and references therein). Due to the 6.3 h cadence of the observation and the large distance to the Andromeda galaxy, it is, however, well possible that a flash lasting for only a few hours was missed or that it occurred before the monitoring was started. This non-detection demonstrates how difficult it is to

detect the short phase of an unpredictable event.
In summary, the fireball phase of novae provides a clear observational radiation signature but it has never been detected until now. Apart from confirming more than 30 years of theoretical work on novae, observing this phenomenon is important for a variety of reasons. By constraining the onset and relative time delay with respect to the optical outburst, the timescales of the TNR can be constrained. The length of the flash serves as a handle on the mass of the white dwarf, a parameter that is usually difficult to constrain and typically comes out of complex modeling of later stages of the nova. By measuring the amount of absorption, the fireball phase also provides the possibility to study the amount of pre-existing circumbinary material and determine whether outflows and winds are present or not. Furthermore, determining the luminosity during the X-ray flash helps tracing the energy conservation by comparing it to the luminosity values at later stages of the outburst. The last point is particularly interesting, because some novae show super-Eddington luminosities (Duerbeck, 1981; Aydi et al., 2018), which "remain almost as much of a mystery as when they were first discovered" (Chomiuk et al., 2021, p. 434).
In addition to the X-ray flash, a further observational signature of the TNR should be the emission of γ-rays. The CNO burning emits positrons, which produce an annihilation line at 511 keV. The kinetic energy of the e^+/e^- pair shifts and Doppler-broadens the line (F. Aharonian, priv. comm.) and the Comptonization on lower-energy electrons produces a continuum down to ∼20 keV (Hernanz et al., 2002). Since the density in the envelope is high, the annihilation line is likely of fast, transient nature and has not yet been detected (Hernanz et al., 1999). Lastly, neutrinos are also expected from the nuclear burning, however, their energy is likely not sufficiently high to distinguish them from the cosmic neutrino background.

2.6.2 Signatures of the Nova Outburst

Emilia hingegen ist noch in einer tieferen Schicht der Hülle. Um zum Rand zu kommen, muss sie sich durch die dichte Materie kämpfen und verliert durch viele Streuprozesse einen Teil ihrer Energie. Sie erreicht den Rand der sich ausdehnenden Hülle als sichtbares Licht.

To be continued in Ch. 7.

The typical observational signatures of the nova begin to emerge when the whole envelope explodes and approximately 10^{-5}–$10^{-4}\,M_\odot$ of matter is ejected into the interstellar medium (Gehrz et al., 1998; Chomiuk et al., 2014). A sketch of a lightcurve showing the electromagnetic signals during the outburst is depicted in Fig. 2.12. In the following, the nova model assumes that, throughout the whole outburst, the luminosity of the thermonuclear burning on the surface of the white dwarf is at an approximately *constant*, Eddington-limited level (Bath & Shaviv, 1976). To first order, the electromagnetic signature from the optical to the X-ray wavelengths can be described with this simple model being the result of the expansion and contraction of the photosphere, which shifts the peak of the thermal spectral energy distribution back and forth in energy.
During the X-ray flash, the luminosity remains constant at the Eddington limit, while the photospheric radius increases. Therefore, the temperature of the photosphere drops and, thus, the thermal spectrum shifts to the optical wavelengths within a few hours after the initial TNR (point

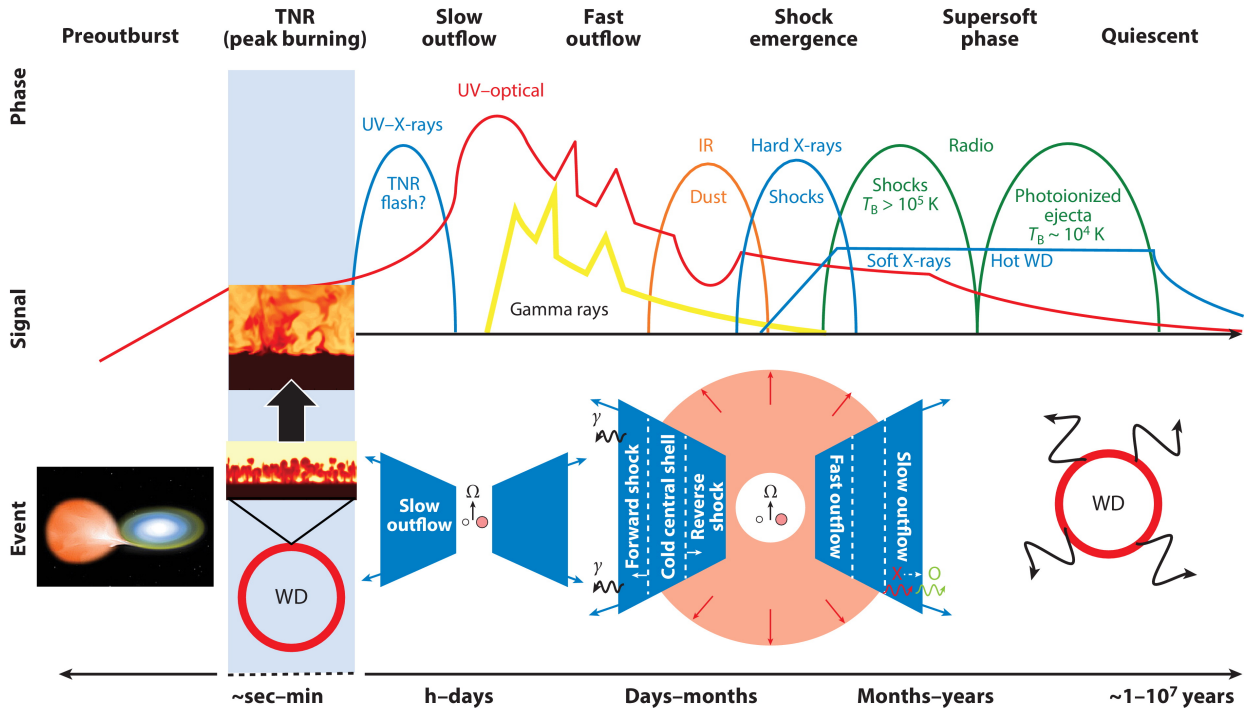

Chomiuk L, et al. 2021
Annu. Rev. Astron. Astrophys. 59:391–444

Figure 2.12: Timeline of a nova outburst (Fig. 1 from Chomiuk et al., 2021). The top curves show the electromagnetic signals emerging throughout the outburst, while the bottom sketches illustrate the main physical processes responsible for the emission. Used with permission of Annual Reviews, Inc., from Chomiuk et al. 2021, Annu. Rev. Astron. Astrophys. 59, 391; permission conveyed through Copyright Clearance Center, Inc.

E). This leads to a sudden brightening in the optical regime by up to 15 mag (factor 10^6; Chomiuk et al. 2021). Typically, novae are detected by this optical brightening. At this time, the initial X-ray flash has already ceased, which further illustrates the difficulties of observing it.

Several winds are thought to be launched during the nova outburst (Fig. 2.13 and Chomiuk et al. 2021). The first outflow is the ejection of the envelope that expands with a velocity of around $100\,\mathrm{km\,s^{-1}}$. Since the accretion disk is still located in the binary plane, the outflow propagates asymmetrically, probably as a torus-like structure. Secondary, much faster winds are successively launched from deep below the photosphere, which are driven by the radiation pressure from the continuously burning surface of the white dwarf (Bath & Shaviv, 1976). A few days after the onset of the TNR, these winds slam into the slower outflow with velocities of several $1000\,\mathrm{km\,s^{-1}}$ (Aydi et al., 2020a). The shock front can accelerate particles, which leads to γ-ray emission (Abdo et al., 2010; Metzger et al., 2015; Sokolovsky et al., 2022) reaching energies as high as a few TeV (H. E. S. S. Collaboration, et al., 2022). Due to the heating of the gas in the shocks to 10^7–10^8 K, thermally emitted hard X-rays can also emerge at this stage (Chomiuk et al., 2021). At high

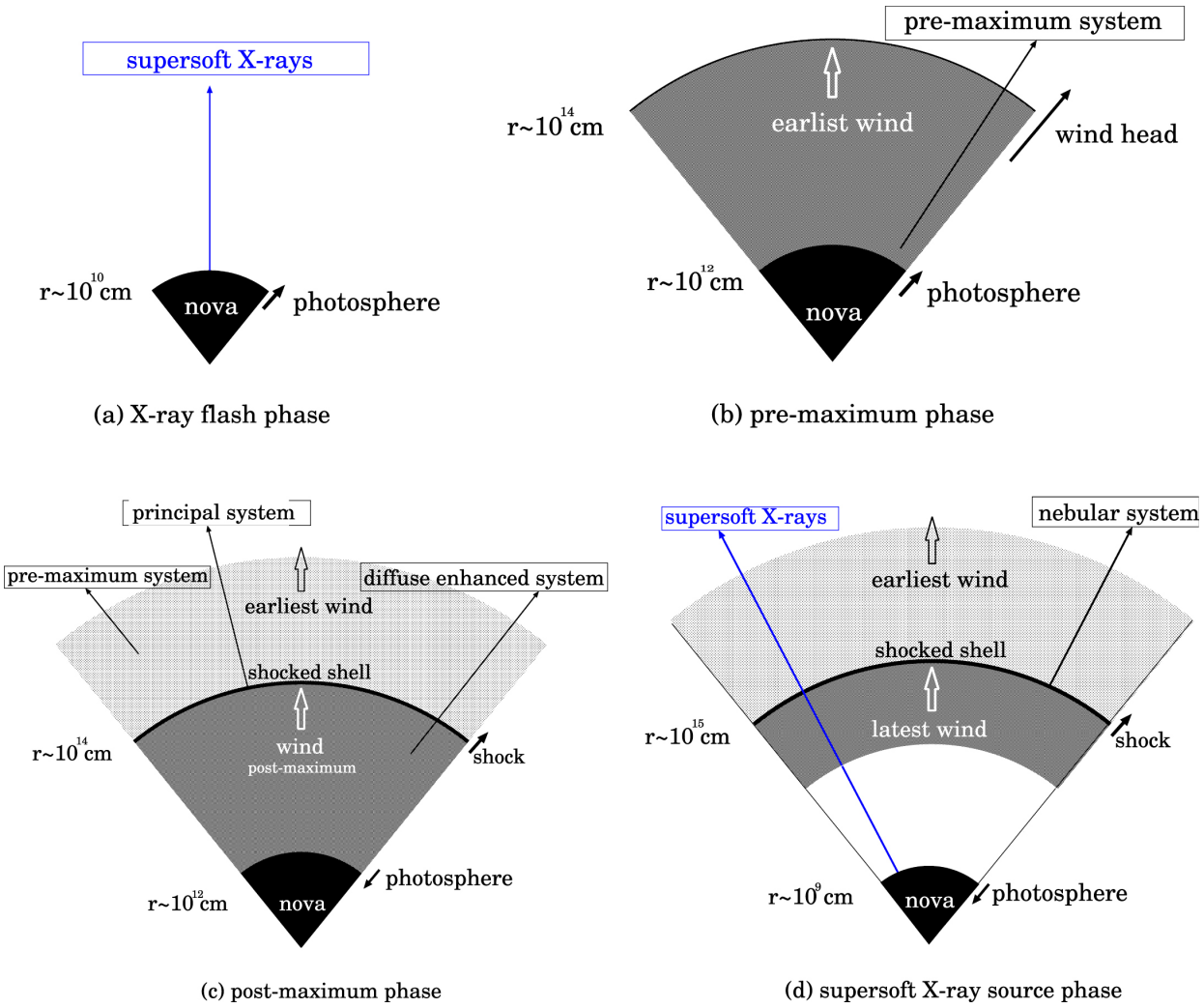

Figure 2.13: Cartoon of the wind model during a nova outburst (Fig. 2 from Hachisu & Kato, 2023). **a)** Soft X-ray flash from the surface of the white dwarf during initial expansion. **b)** The optically thin expanding envelope is the earliest wind blown off and has moderate velocity. Optically thick winds are accelerated from the photosphere with high velocity. **c)** After optical maximum, the photosphere recedes again, and a shock front forms between the optically thick wind and the expanding envelope, emitting hard X-rays and γ-rays. **d)** The optically thick wind stops and supersoft X-rays from the hot contracted photosphere escape the system. ©AAS. Reproduced with permission.

densities re-processing of the X-rays to lower wavelengths can lead to additional shock-powered optical flares (Li et al., 2017; Aydi et al., 2020a).

When the photosphere recedes (point G), the temperature increases again, and the peak of the spectral energy distribution shifts back to the X-rays. After a few weeks to months (the development

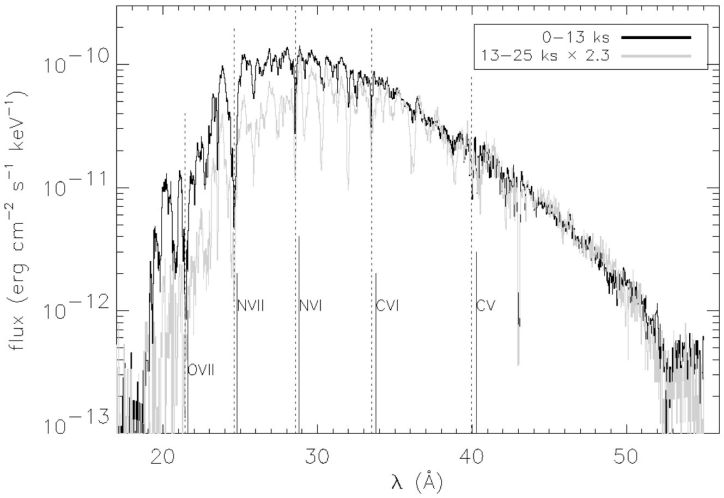

Figure 2.14: Supersoft source phase of Nova V4743 Sagittarii observed with *Chandra*/LETG (Fig. 3 from Ness et al., 2003). Absorption lines of carbon, nitrogen, and oxygen (dotted vertical lines) are blue-shifted with respect to their rest frame energies (solid vertical lines). ©AAS. Reproduced with permission.

is faster for heavier white dwarfs), the optically thick wind stops (point I) and the nova emerges as a supersoft X-ray source (SSS; e.g., Oegelman et al. 1984; van den Heuvel et al. 1992; Kahabka & van den Heuvel 1997; Ness et al. 2007). Quasi-stable hydrogen burning of the material remaining on the white dwarf's surface emits a thermal ("black body-like") spectrum of 30–50 eV. Due to the optically thick ejecta, this radiation is completely absorbed during the earlier outburst (except for the fireball phase) but when the material becomes optically thin, the X-rays shine through. If this phase is observed with an instrument with sufficient spectral resolution, the absorption in the remaining gas can become visible as absorption lines of elements that were created during the TNR. An example of such a SSS spectrum is shown in Fig. 2.14. Absorption lines of carbon, nitrogen, and oxygen can be seen, blue-shifted by a Doppler velocity of $-2400\,\mathrm{km\,s^{-1}}$.

The optical light curve has been seen plateauing until the end of the SSS phase (point J) and reduces in intensity only once nuclear burning turns off (e.g., Hachisu et al., 2007, their Fig. 3). The turn-on and turn-off times of the SSS can be used to estimate the mass of the white dwarf (Hachisu & Kato, 2006; Aydi et al., 2018, and reference therein), while the radiation during the SSS is important to derive the effective temperature of the white dwarf (which, in turn, can also be used to estimate the mass; Werner et al. 2012; Suleimanov et al. 2013). Finally, accretion sets back in and, when the thermonuclear burning ceases, the nova fades into quiescence (point A) until enough matter is accumulated for the next nova cycle.

How often is such a cycle observed? Recent estimates of the Galactic nova rate are at around $43.7^{+19.5}_{-8.7}$ novae year^{-1} (De et al., 2021, and references therein). However, only a fraction of this number is actually observed, around 5–10 per year (De et al., 2021). Approximately 250 novae

have been observed from 1900–2015 in the Milky Way (Shafter, 2017)[24]. The discrepancy of the predicted Galactic nova rate and the number of actually observed novae is most likely due to dust obscuration, preventing the optical discovery of many novae due to absorption. Since most novae are discovered and characterized using optical observations, the detection of an X-ray flash alone, without an optical counterpart, would require a very careful analysis to distinguish the event from other types of soft X-ray transients, such as tidal disruption events. Dust extinction, therefore, further diminishes the chances of direct searches to discover the fireball phase of novae.

[24]Comprehensive and up-to-date lists of Galactic novae are compiled, for instance, by Koji Mukai (https://asd.gsfc.nasa.gov/Koji.Mukai/novae/novae.html) and Bill Gray (https://projectpluto.com/galnovae/galnovae.htm).

Chapter 3

Detection of X-rays with Space-based Telescopes

Und so kommen wir wieder zum Anfang der Geschichte – seit 7200 Jahren ist Paul nun schon unterwegs[ii]*. „Oh, wow, was ist das denn für eine schöne blaue Murme...“, will er noch sagen, doch RUMMS kracht er in ein ihm bisher recht unbekanntes Material. Nanu, sah dieses Ding nicht aus wie eine Waschmaschine*[iii]*?*

To be continued in Sect. 3.1.

Photo-electric absorption of X-ray radiation on atoms in Earth's atmosphere requires experiments in the upper atmosphere layers, such as balloon missions, sounding rockets, or space-based satellites in order to detect extraterrestrial X-rays (e.g., Giacconi, 2009; Santangelo et al., 2023). In this chapter I will describe the technology that is necessary to observe extraterrestrial X-rays. Modern X-ray missions built with the goal of deep surveys often employ a focussing telescope, which is described in Sect. 3.1. In Sect. 3.2, I will introduce the main types of semiconductor-based X-ray detectors. Section 3.3 describes the X-ray missions which were used in this thesis. Lastly, I will describe typical analysis techniques used in X-ray astronomy (Sect. 3.4).

3.1 Focussing X-ray Telescopes: Optics and Mirror Design

Pauls Reise als leuchtendes Eisenlichtteilchen wird abrupt gestoppt. Er hat einen kleinen blauen Planeten erreicht, um den ein Gebilde kreist, mit vielen glitzerndes Sonnenpanelen, Schleusen, und einem waschmaschinenartigen Weltraumteleskop. Dort ist ein Spiegel angebracht, auf den er haarscharf aufprallt. Er kann jedoch nur wenige Nanometer in das Material eindringen und wird reflektiert. „Total krass!“, denkt er sich[iv]*. Hinter dem Spiegel ist ein Siliziumblock in das Paul einschlägt, wo seine Reise als Röntgenteilchen nun gänzlich gestoppt wird.*

To be continued in Sect. 3.2.

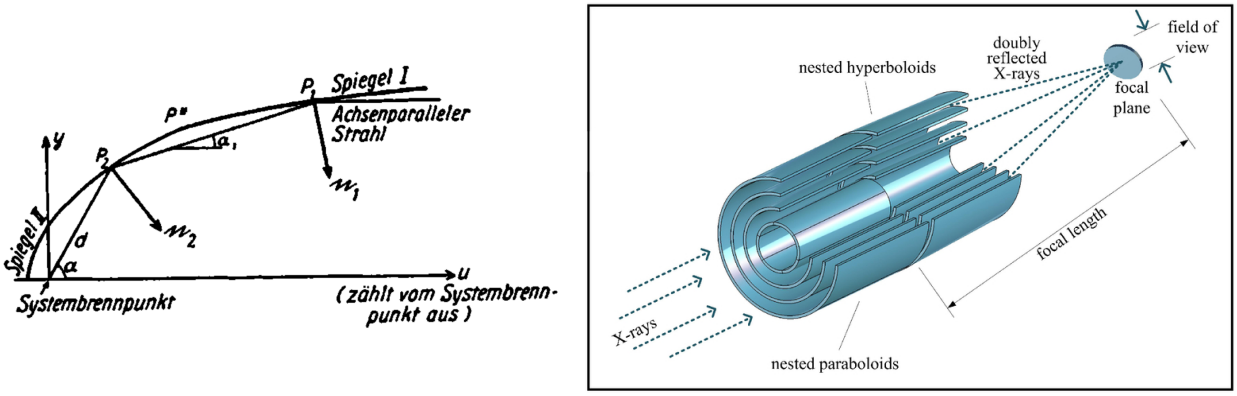

Figure 3.1: Mirror design of grazing incidence X-ray optics. *Left:* Original design of an X-ray microscope by Wolter (1952b, Fig. 1). *Right:* Wolter-I optics with four concentric nested shells (Fig. 2 from Döhring et al., 2015).

The refractive index of all materials is close to unity for X-rays (Spiller, 2015). While optical light can be re-directed using lenses, the high refractive index and Snell's law implies that X-ray photons do not change the direction much when passing through a material. Instead, they are absorbed after a short distance – for beryllium, for instance, the absorption length of a 1 keV photon is only 0.01 mm (Spiller, 2015, Fig. 1). Total reflection is only possible under small angles, typically below one degree (Parratt, 1954; Giacconi et al., 1979). Telescopes that use mirrors under total reflection are, thus, called *grazing incidence optics* (Pivovaroff & Okajima, 2022). Hans Wolter found that by using two conical mirror sections, e.g., a hyperboloid and a paraboloid called Wolter-I optics, one can focus X-ray with two reflections onto a focal plane (Wolter, 1952a,b; Giacconi & Rossi, 1960). In practice, multiple mirror shells are nested into each other in order to increase the photon collecting area of the telescope (*effective area*, Fig. 3.1). Due to the small reflection angle, the focal length of X-ray telescopes has to be relatively large, typically in the range of 1–12 m (Giacconi et al., 1979; Nandra et al., 2013; Okajima et al., 2016; Predehl et al., 2021).

3.2 X-rays Detectors

Paul dringt einige Mikrometer in das Halbleitermaterial ein und wird von einem Siliziumatom absorbiert. Er überträgt einen Teil seiner Energie an das Atom und flitzt als Elektron weiter durch das Material, stößt und ruckelt an den Atomen und hinterlässt eine wahre Wolke an freien Elektronen. „I want to break freeee", schmettert Paul, als er zu einer etwa 500 Nanometer großen Ladungswolke wird[v]. Er spürt ein elektrisches Feld, das ihn zum Rand des Detektors zieht[vi]. Ein wenig dicker und flacher erreicht er die Auslese, wird als Radiowelle zu dem blauen Planeten heruntergeschickt und landet schlussendlich auf dem Rechner eines Menschen. „Vielleicht möchte der ja herausfinden, wo ich herkomme? Ich kann viel erzählen", denkt er sich.

To be continued in Sect. 4.2.

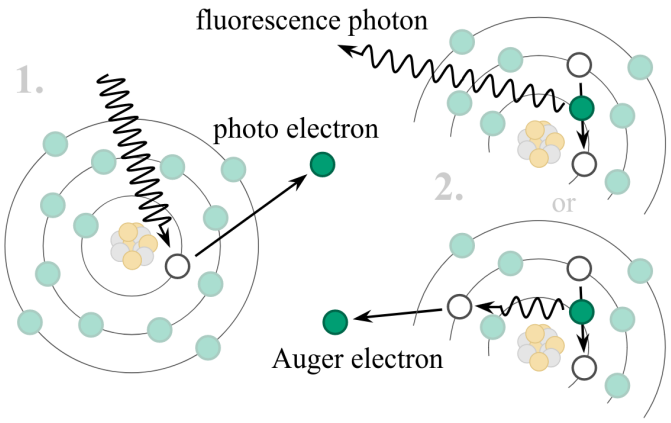

Figure 3.2: First most probable interactions of an X-ray photon with a silicon atom (Fig. 2 from Meidinger & Müller-Seidlitz, 2022). *1.* Initial photo-electric absorption of the X-ray photon produces a photo-electron and an ionized atom. *2.* The atom de-excites through the emission of a fluorescence photon or, if the photon is directly absorbed again, the emission of an Auger electron. Reproduced with permission from Springer Nature.

3.2.1 Detector Types

The first extraterrestrial X-ray source, the Sun, was observed in 1949 with a Geiger counter on-board a German "Vergeltungswaffe 2" rocket (Friedman et al., 1951). Also Giacconi et al. (1962) used Geiger counters on their sounding rocket experiments to detect extrasolar X-rays. Such a detector contains a gas that is ionized when a high-energy photon impacts, which results in the measurement of a current (e.g., Knoll, 2010, p. 159ff). The energy resolution of these early types of detectors was approximately 1 keV at energies of a few keV (Janesick et al., 1988). Beginning with the *ASCA* satellite in the early 1990s (Tanaka et al., 1994), semiconductor-based detectors were used, which provided a far better energy resolution.

Charge-coupled devices (CCD; Boyle & Smith 1970, see review by Janesick 2001) are among the most widely used detectors in X-ray astronomy (e.g., Strüder et al., 2001; Weisskopf et al., 2002; Predehl et al., 2021). CCDs are doped semiconductors that employ a p-n junction to convert a photon into an electronic signal. In the energy range of soft X-rays, the photon interacts with the semiconductor material through photo-electric absorption[1] (Einstein, 1905). When an X-ray of energy below a few tens of keV is absorbed, an electron from the inner shell is removed and the atom becomes ionized, creating an electron-hole pair (Fig. 3.2). The emitted photo-electron scatters through the bulk material and produces a further cascade of excitations. Ionized atoms de-excite either by the transition of an electron from an upper shell, which emits a fluorescence photon, or through the emission of an Auger electron when the fluorescence photon is directly absorbed again by the same atom leaving an excited ion behind. Thus, the energy of the X-ray dissipates in the detector through a cascade of interactions, forming a number of electron-hole pairs proportional to the energy of the X-ray photon. The extent of the interaction region where charge carriers are created is called the *charge cloud*. When an electric field is applied, the electron-hole pairs are separated and the charge can be accumulated in a potential well.

The band gap of silicon is 1.14 eV and it takes roughly 3.65 eV to produce an electron-hole pair (Janesick et al., 1988). X-rays have significantly more energy, which means that CCDs can measure the energy of single X-ray photons. As said above, the amount of collected charge is roughly

[1] In silicon, photo-electric absorption is the main effect in the soft X-ray energy range. Compton scattering (Compton, 1923) and pair-production (Blackett & Occhialini, 1933) become dominant for photon energies >50 keV.

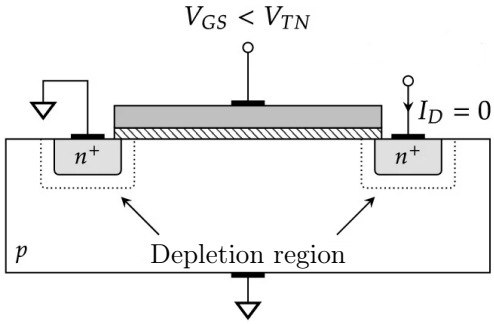

(a) Reverse-biased regime

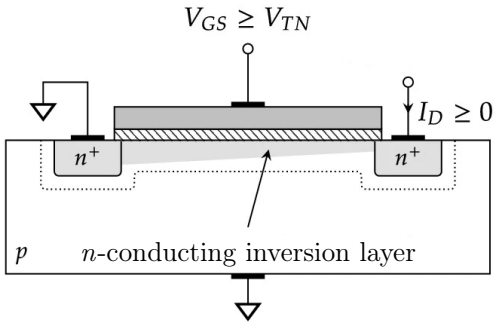

(b) Linear operating regime

Figure 3.3: Basic working principle of an n-MOSFET (modified after Momeni 2021, Fig. 5.9). **a)** MOSFET with "closed gate". The voltage between gate and source (V_{GS}) is below the threshold voltage (V_{TH}). No current is flowing from source to drain. **b)** When sufficient voltage is applied, an inversion layer is created below the oxide layer in the body semiconductor material and a conduction channel is formed. Reproduced with permission from Springer Nature.

proportional to the energy of the photon, E, however, not all energy is converted into electron-hole pairs. A small amount is transferred to the silicon lattice, giving rise to statistical fluctuations in the reconstructed energy, called *Fano noise*. The noise is described by the Fano factor (Fano, 1947), $F \approx 0.1$ for silicon, which determines the minimum possible energy resolution as (Janesick, 2001, Eq. 2.39)

$$\Delta E_{\mathrm{Fano}} = 2.355\sqrt{F \cdot E \cdot 3.65\,\mathrm{eV}} \quad . \tag{3.1}$$

Modern CCDs used in X-ray astronomy typically achieve a near Fano-limited energy resolution of around 70 eV at 1 keV (Predehl et al., 2021).

The pixels on a CCD are arranged in a grid, which is read out line-wise. By periodically clocking the voltage applied to the pixels, the charge is shifted to the readout electronics. The signal is then amplified and measured. This way, the impact position of the photon can be detected. In summary, in combination with a focussing telescope, a CCD enables spatially-resolved spectroscopy.

The next generation of semiconductor-based detectors used in X-ray astronomy is the depleted p-channel field effect transistor (DePFET; Kemmer & Lutz 1987). A field effect transistor (FET; Lilienfeld 1926; Heil 1935) uses an electric field to control the current through the semiconductor. It has three terminals, source, gate, and drain. When a voltage is applied to the gate an inversion layer is created in the semiconductor material (p-n junction) and charge carriers can flow from the source to the drain contact. An example of a metal oxide semiconductor FET (MOSFET; Atalla et al. 1959; Kahng 1960) is shown in Fig. 3.3.

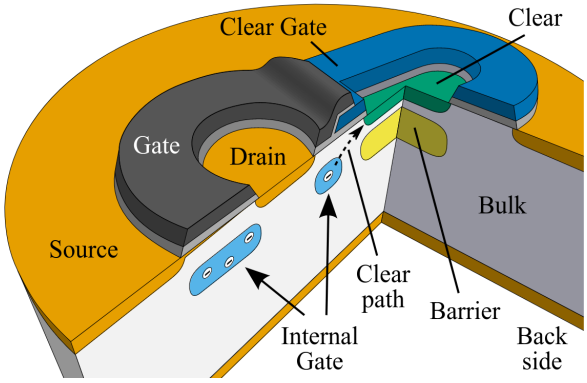

Figure 3.4: Schematic view of a DePFET pixel (Fig. 1 from Meidinger & Müller-Seidlitz, 2022). Reproduced with permission from Springer Nature.

A DePFET is a device which allows the direct amplification and measurement of the signal without the need of shifting the charge to the edge of the detector (see Meidinger & Müller-Seidlitz 2022 for a review). They are therefore also called *active pixel sensors* (see Fig. 3.4). When an X-ray photon impacts the pixel, electron-hole pairs are created in the fully depleted bulk material through the same processes as outlined above. Holes drift to the back contact, while the electrons are collected and amplified in an internal gate, which is placed below a FET. After the integration time the FET is switched on. The amount of charge collected in the internal gate influences the resistance between the source and drain contact. By measuring the conductivity between the two terminals, the amount of charge can be measured and the energy of the photon can be reconstructed. One advantage of the DePFET compared to CCDs is that the signal can be read multiple times, since the charge is not removed. In addition, having no readout of the signal at the edge of the detector saves power and, because there is no need for charge shifting and electric connections between detector and readout electronics, reduces noise. The detector noise is, thus, only limited by Fano noise. Finally, the charge can be cleared from the internal gate through a positively charged contact that can be switched on using a FET at the clear gate.

Another type of detector is the silicon drift detector (SDD; Gatti & Rehak 1984), which consists of a depleted silicon bulk where, as before, a charge cloud of electrons is produced by photo-absorption of an incident X-ray. The difference to a CCD or DePFET is that the electric field is applied parallel to the detector surface to transport the charge to collecting anodes. SDDs can be built with large sensitive areas and have good energy resolution of approximately 80–160 eV in the 0.5–8 keV range (e.g., Prigozhin et al., 2016, their Fig. 13). However, the main benefit of SDDs is an extremely high count rate capability above 100 000 counts per second (Lechner et al., 2001). This type of detector is, therefore, advantageous if high timing resolution with a large detection area is needed but good spatial resolution can be neglected.

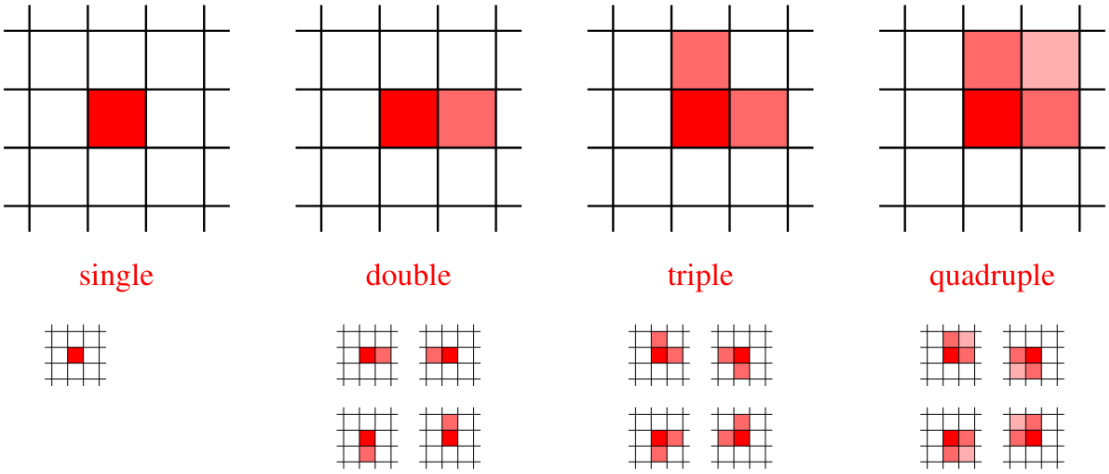

Figure 3.5: Valid pattern types of pixelized X-ray detectors (Fig. 2.19a from Schmid, 2012). All patterns are created by one photon impacting the detector and splitting its charge cloud into one to four pixels (which means that the charge cloud is smaller than the pixel). Single patterns have only one configuration, while double, triples and quadruples have four possible pixel configurations. All other pixel patterns are considered invalid.

3.2.2 Patterns and Pile-up

Parts of the content of this section have been taken in verbatim from König et al., *X-ray detection of a nova in the fireball phase*, first published in Nature, Volume 605, Issue 7909, p. 248–250, 2022 by Springer Nature and reproduced with permission from Springer Nature. These parts are reproduced without direct reference.

The major complexity in the detection of bright X-ray sources is the so-called pile-up that is caused by the high photon flux of the source (Ballet, 1999; Davis, 2001; Dauser et al., 2019; Tamba et al., 2022). When an X-ray photon impacts a charge-coupled device it creates a cloud of electrons in the semiconductor. These electrons are then collected in one or multiple detector pixels, depending on the size of the charge cloud with respect to the pixel. In the following, we assume that the charge cloud is smaller than the pixel, which is the case for CCD and DePFET detectors. During detector readout, charge below a certain threshold is discarded. The initial step of the event reconstruction in the event processing pipelines reconstructs the events from the measured charge distribution. Depending on the number of pixels in which charge is detected during one readout cycle, events are classified into four patterns: singles, i.e., only one pixel contains charge, doubles, triples, and quadruples (see Fig. 3.5). Since the charge cloud size is energy-dependent, and because of thresholding effects, the relative fraction of each of these pattern types depends on energy.

Virtually all currently operating imaging X-ray telescopes are designed to operate in single-photon mode, which allows direct reconstruction of the energy of each incident photon. For a moderate photon rate, the processing algorithm can correctly identify the patterns and reconstruct the original photon energy from the summed charges. For bright sources, however, multiple photons can hit the same or neighboring pixels during one readout cycle (Fig. 3.6). In the extreme case, the illuminated

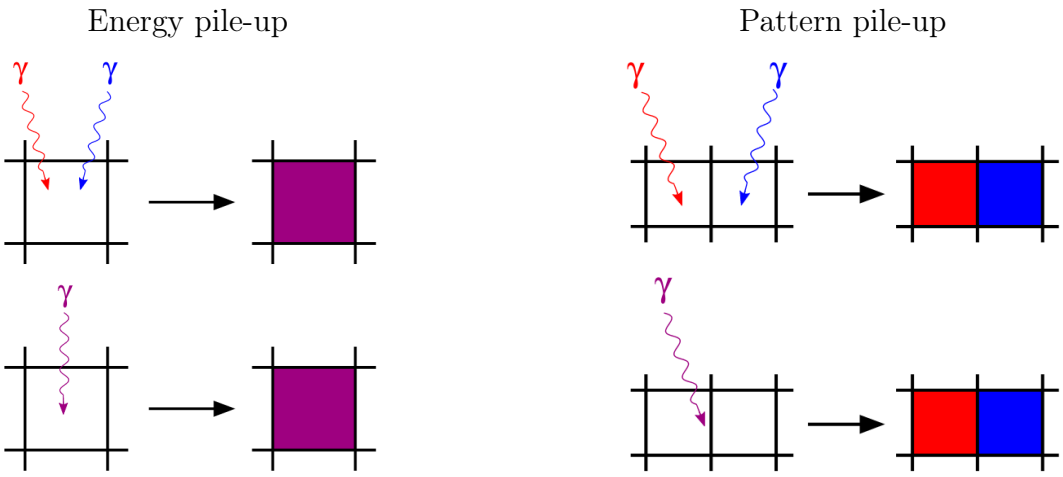

Figure 3.6: Illustration of energy and pattern pile-up (Fig. 2.20, 2.22 from Schmid, 2012). Energy pile-up occurs if two photons hit the same pixel during one integration period. The measured energy cannot be distinguished from a single photon with the summed energy. Pattern pile-up occurs if two or multiple photons hit adjacent pixels, which cannot be distinguished from a higher energy photon whose charge cloud spills into multiple pixels (two in this case).

pixels produce extended charge distributions (*pattern pile-up*) that can be discarded in the event reconstruction, leading to a complete loss of the signal, and a depression in brightness at the center of the source. For many other cases, however, the charge pattern deposited in the sensor by multiple photons cannot be distinguished from that deposited by a single photon that has a higher energy (*energy pile-up*; Ballet 1999; Davis 2001). As a result, the reconstructed count rate is reduced and the spectral shape is hardened. The ramification of these effects on the analysis of observations will be shown in Sect. 7 (in particular Fig. 7.1 for pattern pile-up and Fig. 7.5 for energy pile-up).

3.3 X-ray Observatories

After introducing the technology needed to detect X-rays with space-based telescopes, the next section describes three modern X-ray observatories. In this thesis, I analyze data from the *eROSITA* and *NICER* missions, described in Sect. 3.3.1 and 3.3.2, respectively, and perform simulations for the planned *Athena* observatory, presented in Sect. 3.3.3.

3.3.1 extended ROentgen Survey with an Imaging Telescope Array (*eROSITA*)

eROSITA (Predehl et al., 2021) is a German X-ray telescope on-board the Russian Spectrum-Roentgen-Gamma (SRG; Sunyaev et al. 2021) spacecraft, which was launched on 2019 July 13. The main scientific objective is to detect $\sim 10^5$ galaxy clusters out to a redshift $z > 1$ in order to constrain cosmological models of dark energy (Merloni et al., 2012). *eROSITA* is also an excellent instrument to study active galactic nuclei (AGN; e.g., Medvedev et al. 2020; Boller et al. 2021), Galactic and nearby X-ray sources, such as X-ray binaries (Schwope et al., 2022; Haberl et al., 2022),

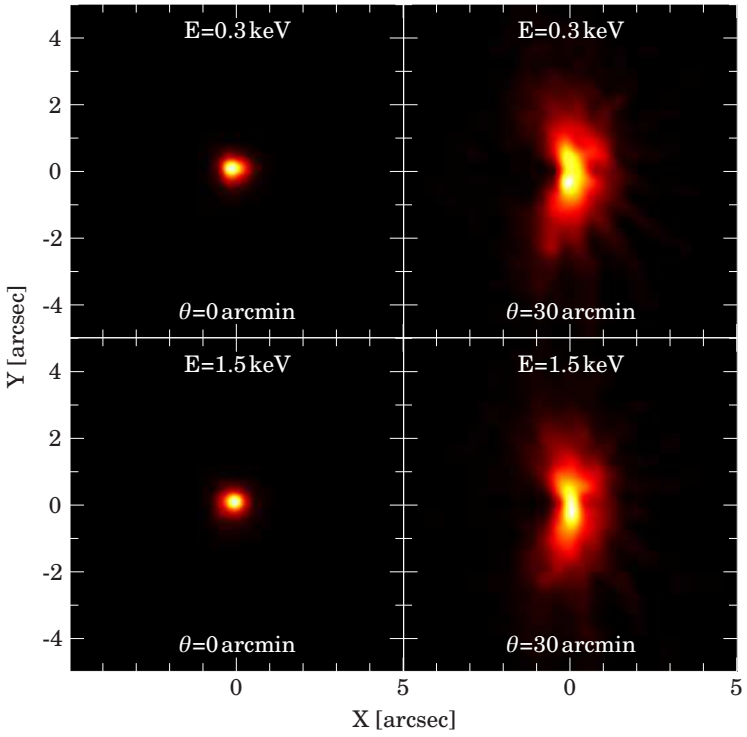

Figure 3.7: Point spread function of one *eROSITA* telescope module. Sources observed on-axis can be localized to within a few arcseconds, depending on the energy-distribution of the photons. Photons from larger off-axis angles are distributed more evenly across the detector plane and accumulate in a butterfly-like shape.

stars (Schneider et al., 2022), or supernova remnants (Becker et al., 2021), as well as time-domain astronomy, such as serendipitous observations of transient sources (e.g., Wilms et al., 2020; König et al., 2020a,b; Sazonov et al., 2021).

eROSITA consists of seven telescope modules (TMs). The Wolter type-I TMs have a focal length of 1.6 m and achieve a spatial resolution of 6–8″ full-width half maximum. The energy-dependent point spread function (PSF) of one TM can be seen in Fig. 3.7. Each TM is equipped with a backside-illuminated CCD, which provide a near Fano-noise limited energy resolution of 130–140 eV at 6.4 keV. The detectors of TM 1, 2, 3, 4, and 6 have an aluminum on-chip optical light filter, while TM 5 and 7 do not have such a filter. The CCD is read out every 50 ms by shifting the accumulated charge in the pixels to a frame store area next to the illuminated part of the CCD. The shift can be done within 0.115 ms and is read out in 9.18 ms. This significantly reduces the amount of out-of-time events. The low-energy threshold, below which no events are telemetered to Earth, is at around 50–60 eV for the cameras with on-chip filter, and 105–125 eV for TM 5 and 7 (Predehl et al., 2021). This increased threshold is due to a light leak that lets optical photons from the Sun pass through the telescope shielding (Predehl et al., 2021, their Sect. 9.2).

In order to achieve the mission's science goals, *eROSITA* was designed as an all-sky survey instrument.

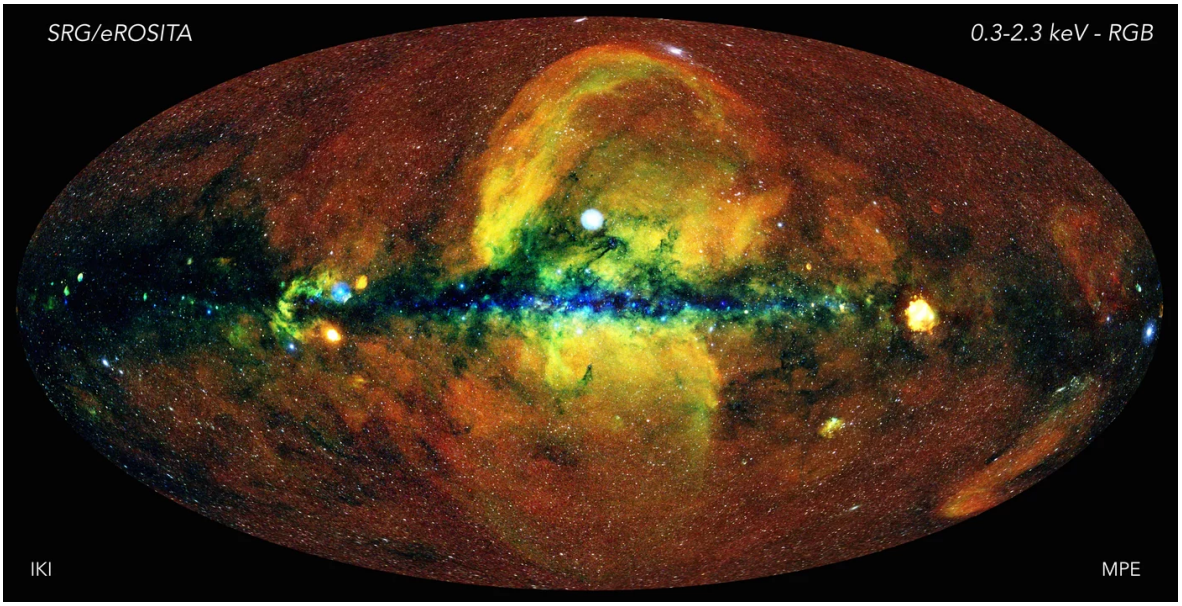

Figure 3.8: Map of the first *eROSITA* all-sky survey. In this Aitoff projection the Milky Way is in the vertical plane and the center is at the origin of the image. The red, green and blue colors correspond to the 0.3–0.6 keV, 0.6–1 keV, and 1–2.3 keV band. Credit: J. Sanders, H. Brunner and the eSASS team (MPE); E. Churazov, M. Gilfanov (on behalf of IKI).

SRG is located at the second Lagrange (L2) point and scans the sky in great circles with the rotational axis pointing to the Sun. The *scan rate* is $0.025^\circ\,\mathrm{s}^{-1}$. With a circular field-of-view (FoV) of 1.03°, sources are observed for up to $1.03^\circ/0.025^\circ\,\mathrm{s}^{-1} \approx 41\,\mathrm{s}$ every scan (if the source passes through the center of the FoV) and one revolution around its axis consequently takes 4 hours (called one *eroday*). While the spacecraft orbits the L2 point (Predehl et al., 2021, their Fig. 15), it also moves around the Sun with the same angular velocity as Earth. Therefore, the pointing of the spacecraft in the ecliptic plane changes by roughly $360^\circ/365.256\,\mathrm{days} \approx 1$ degree per day, called the *survey rate*. This results in a full scan of the sky within 182 days. Depending on the ecliptic latitude, *eROSITA* observes the source roughly 6 times, separated by 4 hours each. On the ecliptic equator this leads to effective exposure values of ∼100 s per eRASS. The exposure time at the ecliptic poles is much higher, larger than 10 000 s (Predehl et al., 2021), as the great circles always pass through the poles.

Following the *ROSAT* (Pfeffermann et al., 1987) all-sky survey (RASS; Voges et al. 1999) in the year 1990–91, the *eROSITA* all-sky survey (eRASS) is the most in-depth all-sky survey ever conducted with a 0.5–2 keV sensitivity threshold of $6.5 \times 10^{-15}\,\mathrm{erg\,cm^{-2}\,s^{-1}}$ (Brunner et al., 2022). The image of the first all-sky survey is shown in Fig. 3.8. The red diffuse emission is due to soft X-rays from hot gas in the local bubble close to Earth, while gas in the Milky Way absorbs soft X-rays and, thus, the Galactic plane appears blue. Next to the around one million point sources detected in this image (most of them being AGN), there are numerous extended sources, such as supernova remnants or the *eROSITA* bubbles (Predehl et al., 2020).

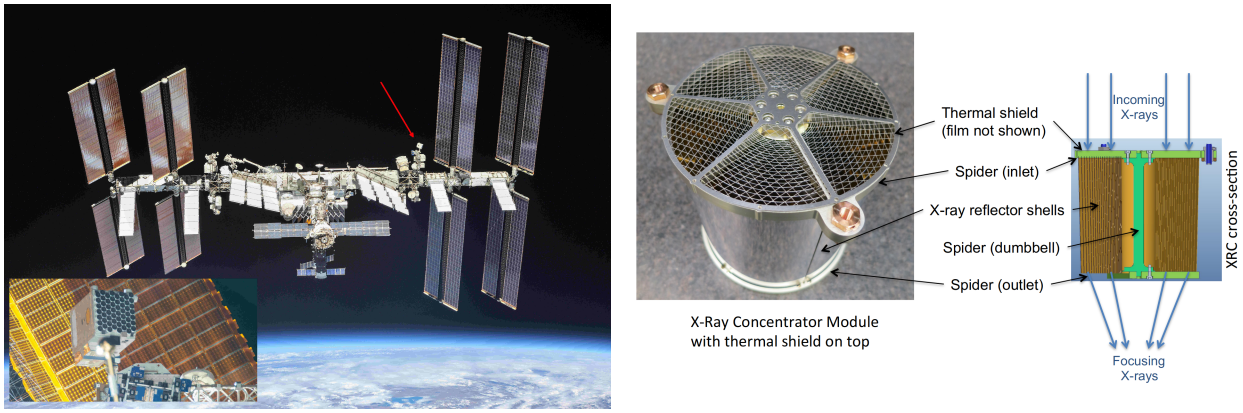

Figure 3.9: The *NICER* X-ray telescope on-board the International Space Station. *Left:* The position of *NICER* is marked by a red arrow. The 56 collimators, which focus the X-rays on the SDDs, can be seen in the inset (modified after HEASARC NICER Gallery). *Right:* Photo and cross-section of one of the 56 X-ray concentrators (Fig. 2 from Okajima et al., 2016).

3.3.2 Neutron star Interior Composition Explorer (*NICER*)

Depending on the science case, it is sometimes advantageous to wave the capability for spatial resolution and instead increase the photon collection area. *NICER* (Gendreau et al., 2016) is an X-ray telescope mounted on-board the International Space Station since June 2017 (Fig. 3.9). Its primary science target is the characterization of the neutron star equation of state (Riley et al., 2019). However, the unprecedented combination of timing and spectral resolution of *NICER* and its capability to perform long term monitoring campaigns with high cadence have proven extremely useful for other branches of astronomy, such as characterizing black hole binaries. One example is the outburst of MAXI J1820+070 that advanced the understanding of black hole transients significantly (e.g., Kara et al., 2019; Fabian et al., 2020; Wang et al., 2021; Zdziarski et al., 2021). *NICER* has 56 separate modules, out of which 52 are operative. Each module consists of an optic, called the X-ray concentrator, and a silicon drift detector (Okajima et al., 2016). The optics comprises 24 parabolic mirror shells. This design leads to a very high effective area compared to other X-ray missions, and thus, high count rates. For comparison, the *NICER* effective area is $>1700\,\mathrm{cm}^2$ at 1.5 keV (Okajima et al., 2016), while all seven *eROSITA* telescopes have a FoV-averaged area of $1237\,\mathrm{cm}^2$ at 1 keV (Predehl et al., 2021). The detectors are arranged in eight arrays, which are each processed by a measurement and power unit (MPU). Due to the SDDs, *NICER* is capable of observing sources brighter than 3.5 Crab[2] at a high throughput[3] and without

[2]The unit *Crab* is defined by the flux of the Crab nebula and the neutron star pulsar within it. In the 2–10 keV band 1 Crab equals roughly $2.20 \times 10^{-8}\,\mathrm{erg\,cm^{-2}\,s^{-1}}$ (Kirsch et al., 2005).

[3]The *throughput* describes the efficiency of a telescope system. It is defined as the number of detected valid events divided by the total number of photons entering the telescope. In a measurement it is generally unknown how many photons are lost in the optics and detector, so this term is somewhat used laxly in the literature. Simulations have an essential advantage as one can track all photons and knows how many are simulated and how many of them are detected.

suffering pile-up effects. For black hole binary science, the high count rate capability is important as these objects can easily reach such high fluxes during the soft state. Practically, this leads to lightcurves and spectra with extremely high signal-to-noise ratio. However, the downside of using single reflection mirrors and collimators is that it does not provide spatial resolution. Thus, background estimation proves more difficult than for other missions (Remillard et al., 2022), which can become problematic for weak sources. In addition, observations during passage of the South Atlantic Anomaly causes significant background and are, therefore, usually excluded.
NICER has an energy range of 0.2–12 keV with a resolution of 2.5% at 6 keV. The estimated error on the calibration of the energy channels is ∼5–10 eV [4]. Sometimes cross-calibration problems with respect to other missions, such as *NuSTAR* or *XMM-Newton*, emerge in the 3 keV region (e.g., Yao et al., 2022). For observations close to the Sun, Moon or Earth, the low-energy band $\lesssim$0.5 keV can be intruded by optical light, which leads to artificial flux at low energies. To ensure that no systematics affect the data analysis, I therefore constrain the energy range of the analysis on Cyg X-1 in Ch. 5 to 0.5–10 keV. Modeling the low-energy region sometimes also requires the addition of detector-related edges and absorption lines (e.g., Wang et al., 2021). Overall, the *NICER* instrument team, however, emphasizes that instrument residual artefacts from the ARF calibration are constrained to be below 2–3% (see *NICER* calibration memo[5] 20200202).
NICER has a time resolution of <100 ns (LaMarr et al., 2016), which is roughly 50 times better than the previous major timing mission, the Rossi X-ray Timing Explorer (*RXTE*). Generally, deadtime in *NICER* does not alter the Poisson noise level of power spectra significantly, even at high count rates (e.g., Stevens et al., 2018). The design of the instrument, therefore, allows researchers to perform variability studies on timescales of ms without pile-up or deadtime distortions, which has proven particularly useful for the spectral-timing analysis of black hole binaries (e.g., Stiele & Kong, 2018; Kara et al., 2019; Zhang et al., 2020; Wang et al., 2020a).

3.3.3 *Athena*

Athena is a large-class mission planned by the European Space Agency (ESA) to address the science theme of the hot and energetic Universe (Nandra et al., 2013). It strives to answer how ordinary matter assembles in the largest structures seen in the observable Universe (called the *cosmic web*), and how black holes grow and influence it. The necessity to observe galaxy clusters and AGN feedback at high redshifts drives the spectroscopic resolution requirements, as well as the survey capability, of the mission. Furthermore, *Athena* is designed to perform observatory science in a variety of branches of astrophysics. Examples include black hole spin measurements (Barret & Cappi, 2019), observations of γ-ray burst afterglows, obscured black holes at high redshift, accretion physics, abundance studies of galaxy clusters and the warm-hot intergalactic medium, and much more (Nandra et al., 2013).
At the time of writing, ESA performed a design-to-cost exercise to cut the costs of *Athena* from an estimated 1.9 billion to 1.3 billion Euros (Barret et al., 2023). After consolidation with a Science Redefinition Team, which was responsible for the characterization of the flagship character, the ESA Science Programme Committee endorsed a rescoped version of *Athena*, called *NewAthena*

[4] https://heasarc.gsfc.nasa.gov/docs/nicer/data_analysis/nicer_analysis_tips.html
[5] https://heasarc.gsfc.nasa.gov/docs/heasarc/caldb/nicer/docs/xti/NICER-Cal-Summit-ARF-2019.pdf

with an adoption expected in 2027 and launch planned for 2037[6]. As the final specifications of the instruments on *NewAthena* are not yet available, I will present the baseline of *Athena* as of Spring 2022.

Athena will contain two instruments. The X-ray Integral Field Unit (X-IFU; Barret et al. 2018) will provide spatially resolved X-ray spectroscopy with an unprecedented energy resolution of a few electron-volts (2.5 eV baseline), which can be achieved using micro-calorimeters (Moseley et al., 1984). The energy resolution of semiconductor-based detectors, such as CCDs, is constrained by Fano noise (Sect. 3.2.1). In micro-calorimeters the complete energy of the photon is thermalized within the absorber and deposited as heat, which enables a much higher energy resolution. The X-IFU uses a large array of molybdenum-gold transition edge sensors (TESs) coupled to absorbers of gold and bismuth. The TES is operated at the transition temperature between the super-conducting and normal-conducting regime. As the transition is below 0.1 K, the X-IFU implements a complex cooling chain to reach such low temperatures (the baseline is a TES temperature of 90 mK and a bath temperature of 50 mK). When an X-ray photon impacts the absorber, it deposits its heat and changes the resistance of the TES. Applying a constant voltage leads to a drop in the current. The current is measured by induction using a super-conducting quantum interference device (SQUID) and the shape of the pulse is used to reconstruct the energy of the photon. As the X-IFU is not the main emphasis of this thesis, I refer to Smith et al. (2016) and Barret et al. (2018) for more details on the instrument and Lorenz et al. (2022) and Kirsch et al. (2022) for a simulation-based characterization.

The Wide Field Imager (WFI; Rau et al. 2013) makes use of the excellent spatial resolution (5″ baseline) and large effective area to provide survey capabilities at high throughput and count rates with a 40′ field-of-view. The WFI Large Detector Array consists of four 512×512 DePFET pixel arrays with small chip gaps in between (Müller-Seidlitz et al., 2016). The aim point of the telescope can be shifted to an additional 64×64 pixel Fast Detector that is read out to both sides and thus achieves a time resolution of only 80 μs. The Fast Detector is placed 35 mm behind the focal plane. The PSF at this position covers almost the entire chip and, thus, photons are distributed evenly across the sensor. The defocusing results in the possibility to observe much brighter sources without drastic pile-up effects compared to the Large Detector. Simulation-based estimates[7] show that the Fast Detector is able to observe a Crab-like source up to a flux of 2 Crab, while the Large Detector suffers significant pile-up effects above 0.2 mCrab in full-frame mode and 1 mCrab in window-mode. In addition, the Fast Detector has a beryllium filter that attenuates soft energy X-rays and can be used to observe sources at fluxes up to 15 Crab. Thus, the design of the WFI comfortably allows researchers to observe the brightest X-ray sources. However, the WFI consortium has not yet converged on the actual thickness of the beryllium filter. In Sect. 6.2, I present a study to recommend what thickness is best used to study black hole X-ray binaries.

[6] https://www.esa.int/Science_Exploration/Space_Science/Final_three_for_ESA_s_next_medium_science_mission

[7] See the document WFI-ECAP-TNO-10-001_i1.11_Bright_Source_Report by the Sixte team.

3.4 Analysis Techniques

In this section, I explain the standard analysis techniques used for spectroscopic data and variability studies in X-ray astronomy. For more information on spectral fitting and χ^2-statistics, I refer the reader to Gorenstein et al. (1968), Davis (2001), and Arnaud et al. (2011), as well as the theses by Hanke (2007, 2011). A pedagogical introduction was also given by M. Nowak during the 2010 *2nd School on Multiwavelength Astronomy* in Amsterdam[8].

3.4.1 Spectroscopic Analysis

An X-ray instrument measures photons by accumulating counts in its detector channels within a certain exposure time. The detection is a counting process and the counts per time interval are Poisson-distributed. The physical information of an observed source is given by a photon flux density $F(E)$. In the absence of non-linear affects, such as pile-up, the number of counts N in detector channel c within an exposure time T is given by (Davis, 2001, Eq. 1)

$$N(c) = T \int_0^\infty \mathrm{RMF}(c, E) \cdot \mathrm{ARF}(E) \cdot F(E)\, dE \tag{3.2}$$

$$\approx T \sum_{i=0}^{N_\mathrm{chan}} \mathrm{RMF}(c, E_i) \cdot \mathrm{ARF}(E_i) \cdot F(E_i) \Delta E_i \quad , \tag{3.3}$$

where in the second step the integral is approximated by a discrete sum. This discretization is based on the finite energy resolution of the detector, where N_chan is the number and ΔE_i the width of the energy channels i, respectively. X-ray astronomical data typically uses two standard calibration files to describe the instrument. The *ancillary response file*, $\mathrm{ARF}(E)$, encodes the effective area of the optics in units of cm^2 and typically includes the detector quantum efficiency (Davis, 2001, Eq. 5). The unit-less *redistribution matrix file*, $\mathrm{RMF}(c, E)$, describes the detector response and represents the probability density that a detected photon of energy E is assigned to a channel c. In addition, background counts, B, contribute to the total number of measured counts N. In order to obtain the source counts, S, one has to perform a background correction. The background is usually estimated and added to the right-hand-side of Eq. 3.2 (it can also be included in the model $F(E)$ and then folded through the response). The estimated number of source counts is then $\tilde{S}(c) = N(c) - B(c)$ where the tilde refers to an estimate of a parameter whose precise value is not known. The source counts have a measurement uncertainty given by Poisson statistics,

$$\sigma_{\tilde{S}}(c) = \sqrt{\sigma_N(c)^2 + \sigma_B(c)^2} = \sqrt{N(c) + B(c)} \tag{3.4}$$

plus systematic uncertainties from the calibration. The physically interesting quantity of Eq. 3.2 is $F(E)$, which has the unit photons $\mathrm{cm}^{-2}\,\mathrm{s}^{-1}\,\mathrm{keV}^{-1}$. However, Eq. 3.2 is generally not invertible (e.g., Lampton et al., 1976; Kahn & Blissett, 1980). Spectral analysis, therefore, uses some kind of forward folding process to estimate the photon flux density. For a given spectral model the source counts are predicted using Eq. 3.2 assuming a certain background rate and detector description. An

[8] www.black-hole.eu/media/summerschool2/X-ray_Spectra_Part_I.pdf and X-ray_Spectra_Part_II.pdf

appropriate fit statistic is used to measure the goodness-of-fit. This fit statistic is then minimized such that the deviation between the predicted counts from the model and the measured data is minimal.
The most widely used fit statistic in X-ray astronomy is the χ^2-statistic (Arnaud et al., 2011, Eq. 7.12)

$$\chi^2(\mathbf{x}) = \sum_c \frac{(\tilde{S}(c) - M(c;\mathbf{x}))^2}{\sigma_{\tilde{S}}(c)^2} \quad , \tag{3.5}$$

where $M(c;\mathbf{x})$ is the tested model, having a set $\mathbf{x}$ of unknown parameters. It can be applied if the counts in each bin are normal-distributed and if the bins are independent with respect to each other. In X-ray astronomy, it is common practice to apply the χ^2-statistic when each bin contains at least 20 counts per bin, that is, where the Poisson distribution begins to approximate a normal distribution. For measurements with fewer counts, the Cash statistic (Cash, 1979) is often used, which takes the Poisson distribution of the counts into account according to

$$C(\mathbf{x}) = 2\sum_c \Big(M(c;\mathbf{x}) - \tilde{S}(c)\ln M(c;\mathbf{x})\Big) \quad . \tag{3.6}$$

3.4.2 Fourier Analysis

Many types of accreting compact objects, such as black hole X-ray binaries, are sources of extreme variability on a wide range of timescales, from sub-seconds to years (see Sect. 4.1). Fourier analysis has become the main technique to analyze their variability properties. This section introduces the most important concepts of Fourier analysis. In particular, I focus on a simple (albeit physically unrealistic) scenario of correlating two perfect sine waves. I will describe some peculiarities of the Fourier analysis based on this example. For further information, I refer the reader to the standard textbook on random time series by Bendat & Piersol (2010, first published in 1971). X-ray astronomy-related reviews can be found in van der Klis (1989), Nowak et al. (1999a), Pottschmidt (2002), Vaughan et al. (2003), Uttley et al. (2014), and Belloni & Bhattacharya (2022).
The Fourier transformation of a continuous time series $x(t)$ is[9]

$$\mathfrak{F}(\nu) = \int_{-\infty}^{\infty} x(t) e^{2\pi i t\nu} dt \quad . \tag{3.7}$$

However, a physical measurement cannot capture a signal with infinite resolution but always discretely *samples* the observable. Thus, a measured time series of length T has N data points x_k ($k = 0, \ldots, N-1$) with a width given by the time resolution $\Delta T = T/N$. In order to calculate the Fourier products, one can approximate the integral in Eq. 3.7 by its Riemann sum (cf. Bendat & Piersol, 2010, Eq. 11.36), which then reads

$$\mathfrak{F}(\nu_j) \approx \sum_{k=0}^{N-1} x_k e^{2\pi i t_k \nu_j} \Delta T = \sum_{k=0}^{N-1} x_k e^{2\pi i k \Delta T \nu_j} \Delta T = \sum_{k=0}^{N-1} x_k e^{2\pi i jk/N} \Delta T \quad . \tag{3.8}$$

[9] Here, the convention is used to have a + sign for the transform into Fourier space and a − sign for the inverse transform which also includes the $1/\sqrt{2\pi}$ pre-factor.

$\nu_j = j/(N\Delta T)$ are the Fourier frequencies from $j = -N/2, \ldots, N/2-1$ and $t_k = t_0 + k\Delta T$, where $t_0 = 0$ is set without loss of generality. We can now define the discrete Fourier transform (DFT) as (e.g., van der Klis, 1989, Eq. 2.4a)

$$X_j = \sum_{k=0}^{N-1} x_k e^{2\pi i j k/N} \quad . \tag{3.9}$$

Typically, the power spectral density (PSD) is used to analyze the variability behavior. It is calculated as

$$|X_j|^2 = X_j^* X_j \quad , \tag{3.10}$$

where * denotes the complex conjugate. The PSD is then normalized. To understand the normalization, one needs to introduce the term *root mean square* (RMS), which can be defined as the square root of the lightcurve variance (Vaughan et al., 2003, Eq. 6)

$$\sigma_{\mathrm{RMS}} = \sqrt{\frac{1}{N-1}\sum_{k=0}^{N-1}(x_k - \bar{x})^2} \quad . \tag{3.11}$$

Equation 3.11 is called the *absolute* RMS variability amplitude. The *fractional* RMS of a time series can be obtained by the standard deviation of the time series divided by the mean count rate, $\sigma_{\mathrm{frac\,RMS}} = \sigma_{\mathrm{RMS}}/\bar{x}$, where $\bar{x} = 1/N \sum_{k=0}^{N-1} x_k$. In astronomy, the PSD is usually normalized to fractional RMS per Hertz (Belloni & Hasinger, 1990; Miyamoto et al., 1992; van der Klis, 1997). The PSD in this normalization is given by (Vaughan et al., 2003, Appendix A)

$$P_j = \frac{2\Delta T}{\bar{x}_{\mathrm{sig}}^2 N}|X_j|^2 \tag{3.12}$$

where $\bar{x}_{\mathrm{sig}}$ is the mean background-corrected count rate. In this normalization, the PSD has the unit (RMS/mean)^2/Hz. It is used to study sources where background noise is relevant and to compare the absolute shape of the PSD at different count rates (fractional RMS is independent of brightness due to the division by the mean count rate).
Using the theorem of Parseval (1806), the fractional RMS can be directly obtained by summing over the Fourier frequencies[10] (Vaughan et al., 2003, Eq. 5)

$$\sigma_{\mathrm{frac\,RMS}}^2 = \sum_{j=0}^{N/2-1} P_j \Delta\nu \quad , \tag{3.13}$$

where $\Delta\nu = 1/T$ is the frequency resolution of the DFT grid. If one constrains the summation over a certain frequency interval $[\nu_1, \nu_2]$, one obtains the contribution to the fractional RMS squared variability on timescales from ν_2^{-1} to ν_1^{-1} (Uttley et al., 2002). Note, however, that this depends on the binning of the Fourier grid, that is, if ν_1 and ν_2 do not match Fourier frequencies, the RMS is

[10] Note that the sum only goes over positive Fourier frequencies.

slightly underestimated (in practice this usually has a negligible effect, as one integrates over many Fourier frequencies).
Another normalization sometimes used is the *Leahy normalization* (Leahy et al., 1983) given by

$$P_{j,\mathrm{Leahy}} = \frac{2\Delta T}{\bar{x}N} \cdot |X_j|^2 \quad . \tag{3.14}$$

The PSD then yields the variance of the time series per frequency interval ($\mathrm{RMS}^2\,\mathrm{Hz}^{-1}$) and this normalization is typically used when the relative shape at varying source brightness is compared.
In order to give an example of the PSD, consider a sine wave $\sin(2\pi\nu_{\mathrm{sine}}t)$ which oscillates with a frequency ν_{sine}. The continuous Fourier transform of a sine wave is a δ-peak. However, the fact that we have a discretely sampled time series of finite length leads to further effects in the Fourier products (which may appear somewhat unintuitive at first). Most likely, the frequency of the sinusoid does not exactly match the frequencies of the DFT. Since the true period lies in between two DFT bins, the power is spread across multiple Fourier bins and the PSD shows a symmetrically broadened peak. This effect is due to *spectral leakage* and is illustrated in Fig. 3.10 (see also van der Klis, 1989, their Fig. 6.1a and Eq. 6.3). As the spacing of the Fourier bins is given by the inverse window length, the amount of leakage depends on the size (and shape) of the measurement window. The longer the window, the lower is the spectral leakage. In summary, spectral leakage can lead to a broadening of narrow features in the PSD[11].

Source-intrinsic and Detector Noise

Lightcurves of astrophysical objects do not show pure sinusoidal signals but are subject to noise, which can be source-intrinsic or originate from the detection process. If source-intrinsic variability extends over a wide frequency range, it is often referred to as *broad band noise*. This type of noise gives information on the physical processes in the source. On top one sometimes sees periodic or quasi-periodic oscillations that emerge as more narrow, peaked variability components in the PSD (e.g., Ingram & Motta, 2019). Figure 3.10 shows different types of noise and the consequences on the power spectrum. The most common types of noise are (see also Press 1978):

- *Poisson noise*, also called shot noise, has a constant power spectrum over all frequencies. If the PSD is Leahy normalized, Poisson noise has a level of 2, independent of the source flux and variability (see blue PSD in Fig. 3.10). The fact that source and Poisson noise are uncorrelated implies that the constant Poisson noise can be subtracted off the PSD[12].

- Gaussian *white noise* is also frequency independent ($\propto \nu^0$) and emerges if the time series data consists of independently and identically distributed random variables. Due to the central

[11] For steep red noise power spectra, spectral leakage also leads to a flattening of the power spectrum as power from below ν_{min} is moved across the entire measured frequency range. For more information, I refer the reader to Uttley et al. (2002, their Sect. 3.3).

[12] While the Fourier transform is a linear function, the PSD (Eq. 3.10) is not linear. This means that, generally, the PSD of the sum of two signals is not the sum of the PSD of two signals but there is an additional cross-term (see Eq. 8 of Belloni & Bhattacharya 2022). In the case of Poisson noise, the source intrinsic and detector variability are uncorrelated and the cross-term is zero, meaning that a Poisson noise subtraction in the PSD is valid.

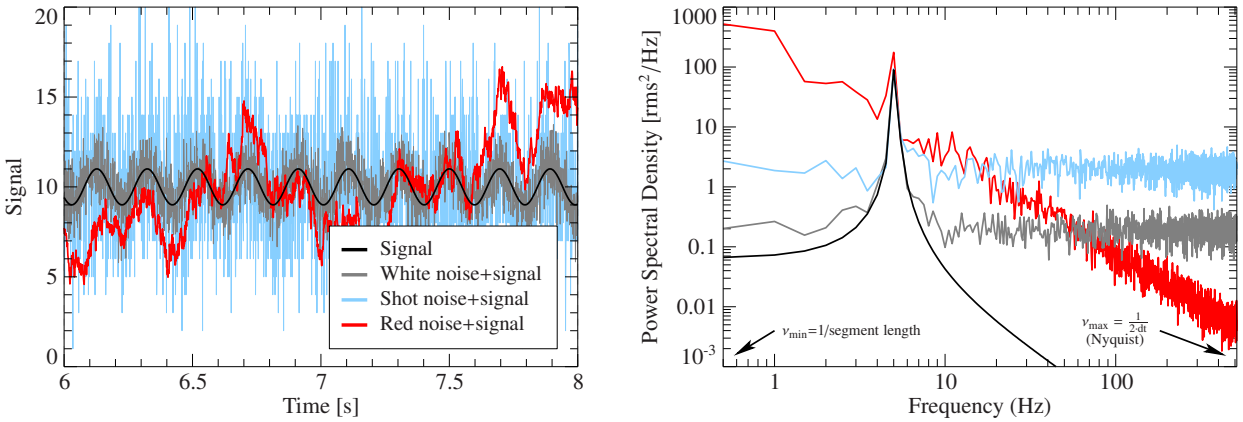

Figure 3.10: Sine wave and additional noise components. *Left:* Simulated time series with an underlying ∼5 Hz periodicity. The segmentation length (window) is 2 s, and, for clarity, only one of these segments is shown. *Right:* Corresponding PSDs in Leahy normalization. The PSD of the sine wave is not a δ-peak due to windowing effects, which smears out the power into neighboring frequency bins. Note that the PSD is shown on a double-logarithmic axis. The asymmetric appearance of the sine wave PSD is, thus, only a result of the logarithmic x-axis. The red noise curve has a slope of 1.7.

limit theorem, Poisson noise becomes white noise as the variance approaches N [13].

- Astrophysical sources can also show source-intrinsic *red noise*, which has a powerlaw-shaped frequency dependence. In the black hole binary community, red noise often refers to *any* power spectrum, which follows a power law $\propto 1/\nu^{\alpha}$ with $\alpha > 0$ (Vaughan, 2010). Some authors also constrain red noise to strictly follow $1/\nu^2$, while $1/\nu$ noise is called *flicker noise* (Press, 1978). $1/\nu^2$ red noise can be attributed to random walk processes and is therefore also called *Brownian noise* (Press, 1978). A simulated example using the Timmer & Koenig (1995) algorithm is shown in Fig. 3.10 (I refer to Fig. 5.2 for an astrophysical example). It should be noted that the RMS of a pure red noise PSD diverges if integrated from zero to any frequency. This is, obviously, not physical and astrophysical sources must have a turn-over at some frequency.

The timing analysis attempts to isolate the detector variability from the source-intrinsic variability. However, power spectra have a statistical uncertainty that is as high as the value itself[14]. In order

[13] The variance of the Poisson distribution equals the mean. If there are more than about 20 counts in each bin and one draws random numbers from a Poisson distribution, it is very similar to a normal distribution with a standard deviation of $\sqrt{N}$.

[14] For completeness, I note that the observed PSD can be modified by detector deadtime for instruments such as *RXTE*/PCA or *NuSTAR* (Jahoda et al., 2006; Usman & Patil, 2018; Bachetti & Huppenkothen, 2023). Paralyzable deadtime arises in an X-ray detector if the electronics become unresponsive after a photon impacted the detector. This effect distorts the power spectrum at high frequencies and can be corrected for using, for instance, the algorithm of Zhang et al. (1995) or by correlating lightcurves measured by simultaneously operating detectors (Bachetti et al., 2015). For the study performed in Ch. 5 using the *NICER* instrument, deadtime has, however, a negligible effect.

to reduce the statistical scatter, the PSD is averaged over multiple realizations, M, which is called *segmenting* (e.g., Uttley et al. 2014, Sect. 2.1.1, Pottschmidt 2002, Sect. 3.2.3). However, one has to make sure that the underlying variability is stationary, that is, it does not change over the segments (this can lead to a broadening of peaks in the PSD if the centroid frequency is non-stationary). In addition, one typically averages over a number of frequencies K. This process reduces the uncertainty of the PSD values by $1/\sqrt{K \cdot M}$.

Cross Power Spectral Density

Let us consider two time series, which may represent measurements in different X-ray energy bands. It is interesting to compare the two time series to each other, for example to find correlations of photons produced from different physical processes. In Fourier space, one derives this correlations from the *cross power spectral density* (CPD)

$$C(\nu) = X_1^*(\nu) \cdot X_2(\nu) = A(\nu)e^{i\phi(\nu)} \quad , \tag{3.15}$$

which is a complex quantity that has an amplitude, $A(\nu)$, and a phase between the two time series, $\phi(\nu)$. As for the PSD, the cross spectrum is typically averaged over multiple segments, M, to reduce the noise.
I will continue the example of sine waves and introduce a second sinusoid, $\sin(2\pi\nu_{\mathrm{sine}}(t+\tau))$, which is shifted with respect to the first one by a constant time lag of $\tau = 0.1\,\mathrm{s}$. This corresponds to a phase lag of $2\pi\nu_{\mathrm{sine}} \cdot \tau = 36° \approx 0.63\,\mathrm{rad}$. The vector of the cross spectrum in the complex plane can be seen in Fig. 3.11 (red). It is strongly localized at the expected phase angle of 36° (in fact, this peak is also slightly broadened due to windowing, as we will see in Fig. 3.12). If the two time series have identical Poisson noise, all frequencies (not only ν_{sine}) are shifted by 0.1 s. As the phase angle is proportional to the time lag and frequency, a constant time delay means that the phase angle changes linearly with frequency. In other words, the vector of the cross spectrum rotates with constant angular frequency in the complex plane while scattering around the mean amplitude.

Coherence

The coherence measures the degree of linear correlation between the two time series. The *raw* coherence is defined as (Pottschmidt, 2002, Eq. 3.33)

$$\gamma^2_{\mathrm{raw}}(\nu) = \frac{|C(\nu)|^2}{|X_1(\nu)|^2 \cdot |X_2(\nu)|^2} \quad . \tag{3.16}$$

As evident from the definition of the cross spectrum, the raw coherence is a quantity between zero and one. In the presence of measurement noise, all quantities have to be Poisson noise-corrected. The intrinsic coherence is then (Vaughan & Nowak, 1997, Eq. 8)

$$\gamma^2_{\mathrm{I}}(\nu) = \frac{|C(\nu)|^2 - n^2}{S_1(\nu) \cdot S_2(\nu)} \quad , \tag{3.17}$$

where n^2 is a bias term that gives the Poisson noise contribution of the (modulus squared) cross spectrum and $S_{1,2}$ is the Poisson noise-corrected, non-normalized power spectrum of time series

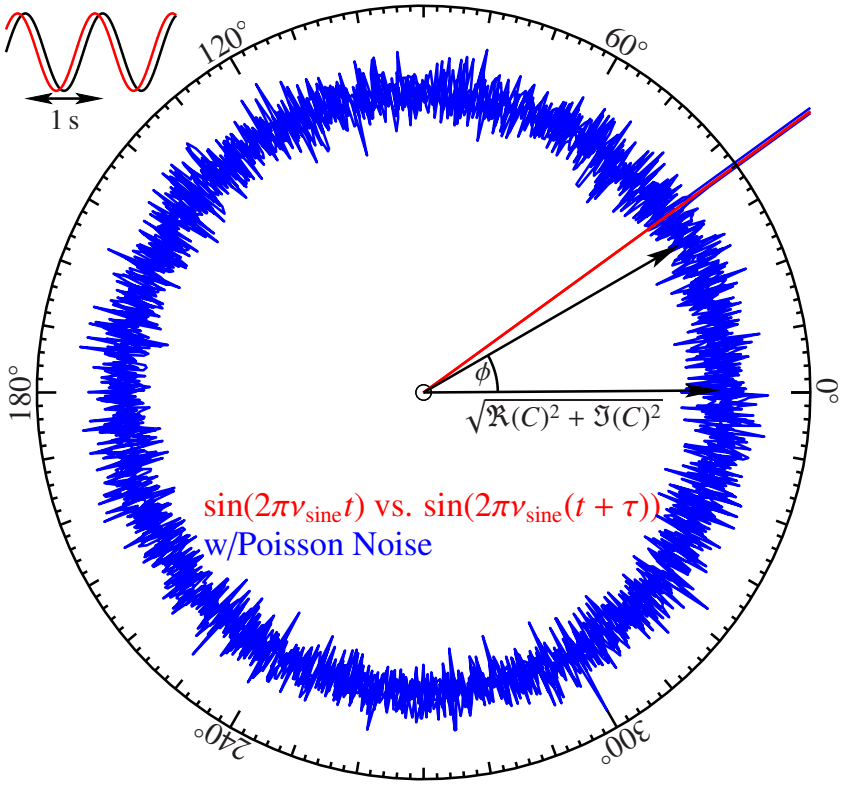

Figure 3.11: Cross power spectral density in the complex plane. In this polar plot, the radius denotes the amplitude of the cross vector and the angle denotes the phase. The red curve represents two identical sinusoids of 1 s periodicity that are shifted by a constant time lag of 0.1 s with respect to each other (top left inset). The cross vector is strongly localized at the corresponding phase angle of 36°. The blue curve shows the cross spectrum of the same two signals but with additional (identical) Poisson noise. Because all frequencies are now subject to the constant time lag, the complex vector rotates in the plane with a constant angular frequency.

1 and 2, respectively. I refer to Vaughan & Nowak (1997) for more details on the calculation of the uncertainty of the intrinsic coherence and for the explicit expression of the bias term. The estimated intrinsic coherence can become larger than unity if the noise causes the magnitude of the cross spectrum to be larger than the magnitude of the PSDs (see also Pottschmidt, 2002, p. 75)[15]. In the above example (Fig. 3.12), the coherence is unity across all frequencies for the two noisy time series, meaning they are perfectly linearly correlated. This makes sense, as the second time series is simply a shifted copy of the first time series. In the absence of noise, the coherence is unity only at ν_{sine}. However, it does not drop to zero for lower and higher frequencies. Again, this effect

[15] In fact, the intrinsic coherence estimate can also become negative if the bias term of the cross spectrum is larger than the signal (numerator is negative), or if the noise PSD is overestimated, leading to a negative signal PSD (denominator is negative). A negative coherence is, however, a sign for very low variability in the time series and the timing analysis is not meaningful in this case, anyways.

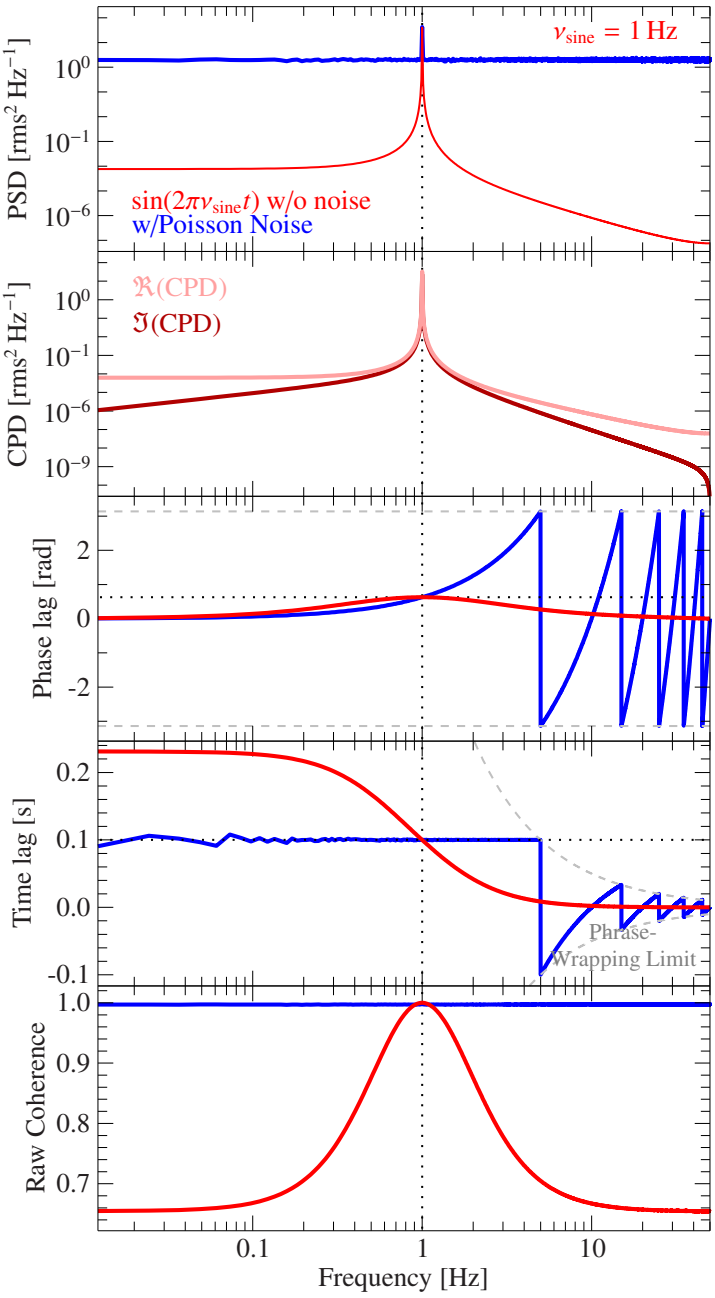

Figure 3.12: Example of the Fourier products of two correlated sine waves. Two sine waves with a frequency of 1 Hz are shifted by a time delay of 0.1 s. The Fourier products of the noiseless signals are shown in red, while a signal with Poisson noise is shown in blue. The correct phase lag is measured at the frequency of the sine waves (vertical dotted line). However, other effects are visible in the timing products at low and high frequencies, such as a larger time lag at low frequencies due to windowing. At high frequencies, phase wrapping due to the 2π periodicity of the phase in the CPD can be seen. Note that the CPD panel does not show the Poisson noise example because it oscillates periodically between positive and negative values, which cannot be displayed on a logarithmic axis (see Fig. 3.11 for a representation in the complex plane).

is due to windowing as it propagates through the cross spectra into the coherence.

If two time series show a coherence of unity, that is, they are perfectly linearly correlated, this gives a strong indication that the underlying variability processes are causally related. Thus, in principle, the coherence can be used to constrain the physical connection of variability processes. In practice, however, the physical implication of the coherence is very difficult to address (e.g., Nowak et al.,

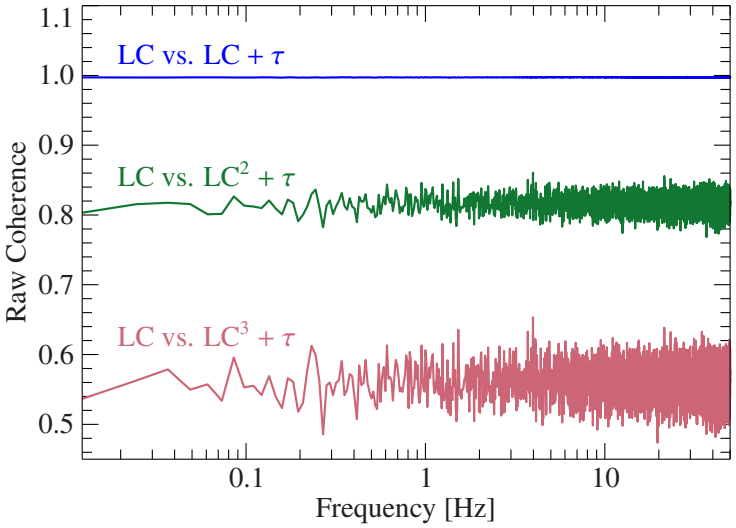

Figure 3.13: Coherence of two time series correlated by a non-linear transfer function. In the first example a random time series is shifted by a constant time lag (as in Fig. 3.12). This linear transformation has a coherence of unity. In the green and red curves, the shifted time series $x + \tau$ was changed to $x^2 + \tau$ and $x^3 + \tau$, respectively. The coherence drops due to this non-linearity.

1999b; Nowak, 2000) and some studies developing models of the variability processes assume an intrinsic coherence of unity due to the significant ease of mathematical complexity (e.g., Ingram et al., 2019). It needs to be emphasized, however, that this assumption is not always true, as I will show in Sect. 5.
In addition, γ^2 also only measures the degree of *linear* correlation and one has to be very careful attributing causality to time series with a coherence smaller than unity. It might be possible that the two time series are either completely uncorrelated or that there is a non-linear transfer function that couples the signals. In this case, γ^2 could be low although there is an underlying correlation between the time series. Such an example is given in Fig. 3.13. While a random time series shifted by a constant time lag has a coherence of unity, the coherence drops if the squared or tripled time series is shifted.

Time Lags

The phase of the complex cross spectrum gives information about the time relation of the two time series. In the case of two sinusoids shifted in time, this corresponds to a phase shift of $2\pi\nu_{\text{sine}} \cdot \tau$. The red curve of Fig. 3.12 shows that the phase lag of two correlated sine waves is indeed measured at the frequency ν_{sine}. Due to windowing, the phase lag is not only measured at ν_{sine} but "spills" into the neighboring Fourier bins. The phase shift corresponds to a time lag of

$$\tau(\nu) = \frac{\phi(\nu)}{2\pi\nu} \quad . \tag{3.18}$$

For the example of two sinusoids, the division by the frequency leads to an unintuitive effect in the time lag versus frequency spectrum (*lag-frequency spectrum*): The time lag at low frequencies is *larger* than the original time shift. This has nothing to do with the actual time shift, it is purely a mathematical consequence of the windowing. However, I want to emphasize that this shows that windowing does not only lead to spectral leakage in the power spectrum but also changes the time lag behavior of the signal.

In order to measure the constant time lag across all frequencies, we need to break up the periodicity in the signal, which can be easily done by introducing noise. Indeed, the introduction of noise in the blue curve of Fig. 3.12 leads to a clear lag-frequency spectrum that shows the expected constant time lag (note that windowing is still present, albeit less apparent). However, at higher frequencies, the phase lag oscillates and diverts from the true value (see also Fig. 20 of Uttley et al. 2014). This effect is called *phase wrapping*. Phase wraps occur whenever the phase lag is larger than π or smaller than $-\pi$ radians (it is the same effect as in movies where the wheels of a carriage have a beat with the shutter speed of the camera, leading to the appearance of backward spinning wheels). Therefore, such phase wraps are no intrinsic source property but are an artefact of the Fourier analysis.
Using the coherence, one can calculate the uncertainty of the time lag (Nowak et al., 1999a, Eq. 16) as

$$\Delta\tau(\nu) = \sqrt{\frac{1-\gamma^2_{\mathrm{raw}}(\nu)}{2\gamma^2_{\mathrm{raw}}(\nu)KM}} \cdot \frac{1}{2\pi\nu} \quad . \tag{3.19}$$

In practice, time series often have a certain degree of correlated variability. To give an astrophysical example, imagine two processes which create variability predominantly in two different energy ranges but also leak into the energy band of the other process. This leads to a reduction in phase lag at an increased coherence and is called *dilution* (see Uttley et al. 2014, Sect. 4, for more information). Dilution needs to be kept in mind if one interprets the absolute magnitude of a time lag.
In the sine wave example, I calculated the cross spectrum and the resulting time lag and coherence between *two* time series. In black hole timing analysis, the two time series represent photons from two broad energy bands. A spectral-timing analysis adds a further dimension, the energy, by investigating the relative time lag and coherence changes of different energy bands with respect to each other. The product calculated from the energy-dependent cross spectrum is called the *lag-energy spectrum*[16]. By extracting lightcurves in small energy bands, one can calculate the cross spectrum between the subject bands and a reference band (for "cookbook instructions" on the calculation, I refer to Sect. 2.2.2 of Uttley et al., 2014). Often, the reference band is calculated by summing the individual channels without the subject band in order to avoid having correlated Poisson noise in both time series (subject and reference band). This means that each subject band is cross-correlated with a slightly different reference band. Ingram et al. (2019) showed that one can also use the same reference band for all subject bands and subtract the Poisson noise contribution directly from the cross spectrum. This approach is valid for all values of intrinsic coherence. It is important to emphasize that the absolute level of the lag depends on the choice of the reference band (which can make it, in fact, difficult to interpret the data, as I will show in Sect. 5.4.2). The lag-energy spectrum is primarily used to detect relative changes in the time lag across energy.
To summarize, this section showed that the Fourier analysis of real measured periodicities and intrinsic noise is always subject to distortions and, as such, rather unintuitive. For the analysis of astrophysical sources, such as black hole binaries, it is important to carefully disentangle these effects from the actual intrinsic physical sources of variability.

[16] I implemented this calculation in the code base used throughout this thesis (ISISScripts). The function is named `lag_energy_spectrum`.

Part I:

Variability Processes in Accreting Black Holes

Chapter 4

Observational Characteristics of Black Hole X-ray Binaries

In the introduction of this thesis, I showed that stellar mass black holes are the evolution end points of massive stars (Sect. 2.1.2) and that they can be present in binary systems with main sequence donor stars (Sect. 2.5). After introducing the X-ray observatories used to detect radiation from these systems (Sect. 3.3) and describing the techniques to analyze their data (Sect. 3.4), I will proceed to describing the observational characteristics of black hole binaries. I will begin with the description of their spectral states (Sect. 4.1) followed by the interpretation of the variability properties, in particular, their time lag behavior (Sect. 4.2).

4.1 Outburst Characteristics and State Changes

The X-ray luminosity of black hole X-ray binaries is strongly coupled to the amount of material that is accreted onto the black hole (see Eq. 2.1). The emission of X-rays due to an increased mass accretion rate can be observed as extremely bright outbursts, where the luminosity increases by up to eight orders of magnitude (Kalemci et al., 2022). This makes them some of the brightest X-ray sources in the sky. Examples are the 2015 outburst of V404 Cyg (Segreto et al., 2015), which went up to 30 Crab, or the 50 Crab outburst of A 0620−00 in 1975 (Elvis et al., 1975).

In Fig. 4.1, I show long-term lightcurves of four black hole X-ray binaries. The sources GX 339−4 and MAXI J1820+070 are prototype transient LMXBs, showing distinct outbursts with extended periods of quiescence in between. GRS 1915+105 shows complex structured variability patterns (Belloni et al., 2000) and is classified as a quasi-persistent source (see Altamirano et al. 2011 for another source example). Since May 2018, GRS 1915+105 has dimmed, likely due to obscuration from failed disk winds (Miller et al., 2020). Black holes in HMXBs, such as Cyg X-1, accrete from a continuous (albeit strongly varying; see Grinberg et al. 2015) flow of matter from a supergiant companion star and are persistent sources.

During these flux changes, the sources show significant changes in their X-ray spectrum (Fig. 4.2),

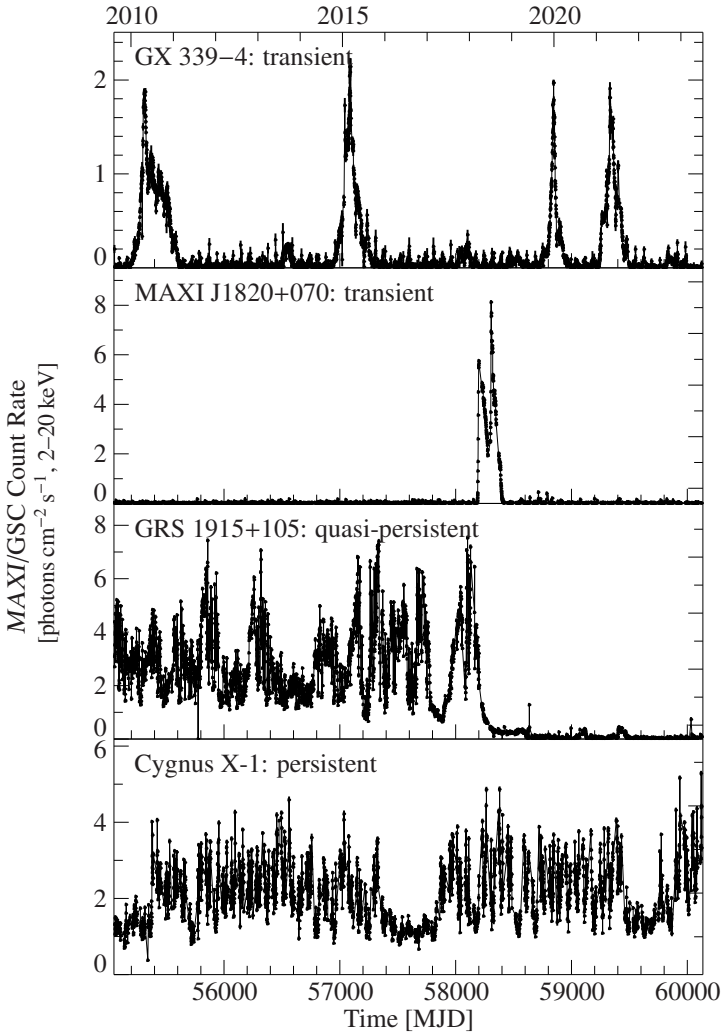

Figure 4.1: Long-term lightcurves of transient and persistent black hole X-ray binaries measured with the Gas Slit Camera (GSC) on-board *MAXI*. Transient LMXB black holes show strong, distinct accretion outbursts where the flux increases by several orders of magnitude. High-mass X-ray binary black holes usually emit persistently. All sources show a high level of short-term variability.

first observed in Cyg X-1 (Tananbaum et al., 1972)[1]. Based on the shape of the X-ray spectrum, variability, and the radio emission (Fender et al., 2004), black hole X-ray binaries are classified into multiple spectral *states*. Next to the long-term variations, the sources also show short-term variability on timescales of milliseconds to minutes. This variability can be studied using Fourier domain techniques, specifically the power spectral density (see Sect. 3.4.2). The appearance of the PSD is an important proxy for the state classification, as shown in Fig. 4.3, and will be described in detail in this section. For completeness, I note that also time domain techniques are used to analyze the variability (e.g., Priedhorsky et al., 1979; Maccarone et al., 2000; Omama et al., 2023).

[1]Due to its brightness, the early detection, and the status as first proposed black hole candidate, Cyg X-1 historically played an important role in the definition of spectral states. However, the source shows some distinctly different properties compared to transient LMXBs, which are mainly related to the mass transfer from the stellar wind. Therefore, I explain the general picture of transient LMXB outbursts here and describe the specialties of Cyg X-1 in Sect. 5.1.

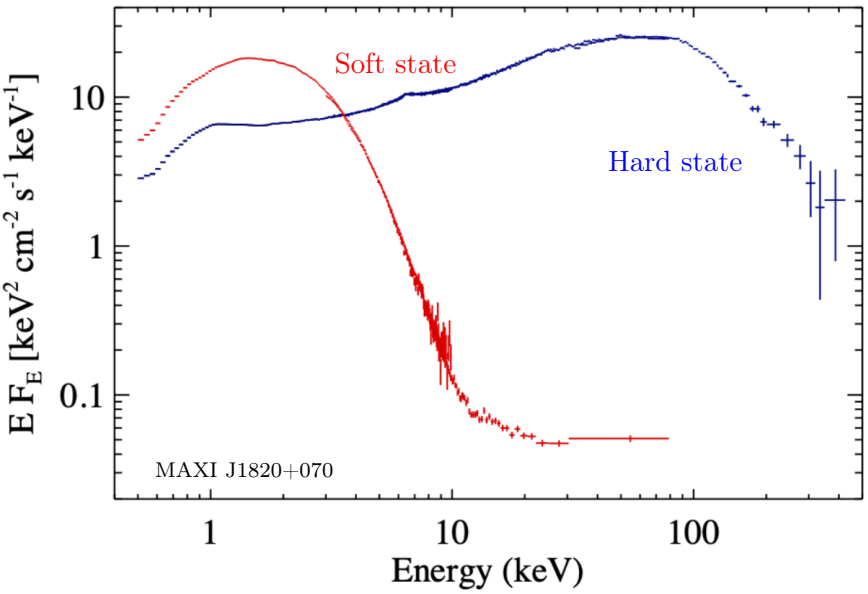

Figure 4.2: Canonical soft and hard spectral state of the black hole X-ray binary MAXI J1820+070 during the 2018 outburst using *NICER*, *NuSTAR*, and *Insight-HXMT* data (Fig. 3 from Kalemci et al., 2022). The soft state (red) shows prominent thermal emission from a multi-temperature accretion disk with a temperature at the inner disk radius of roughly 1 keV. The hard state (blue) is characterized by a cut-off power law that is formed by a ∼100 keV hot plasma which Comptonizes the seed photons of the accretion disk. Note that the spectra include absorption in the interstellar medium. Reproduced with permission from Springer Nature.

To classify the spectral state, one also correlates the spectral hardness of the source (typically defined as the ratio of soft and hard X-ray flux) with the intensity in the detector, called the *hardness-intensity diagram* (HID). For transient sources, this results in a q-shaped hysteresis pattern (Miyamoto et al., 1995). In order to be able to compare the data between different missions, rather than using the traditional HID, one can also use simple empirical spectral fits that describe the data well in a χ^2 sense and then display the luminosity in units of the Eddington luminosity as a function of the flux ratio. This way, the diagram is independent of the detector used and also permits the direct comparison of different sources (see Wilms et al., 2006; Barillier et al., 2023, and references therein). Figure 4.4 shows an example of such a color-luminosity diagram. The q-shaped hysteresis can be seen for the transient LMXB GX 339−4.

Physically motivated models describing the spectral-timing properties of accreting black holes have advanced significantly in recent years. The variability behavior has been interpreted with a variety of physical models, including magnetic flares (Poutanen & Fabian, 1999), propagating fluctuations (Lyubarskii, 1997; Kotov et al., 2001; Arévalo & Uttley, 2006; Ingram & van der Klis, 2013), reverberation (Campana & Stella, 1995; Reynolds et al., 1999; Uttley et al., 2014; Ingram et al., 2019), wave oscillations in the corona (Miyamoto et al., 1988; Cabanac et al., 2010), and

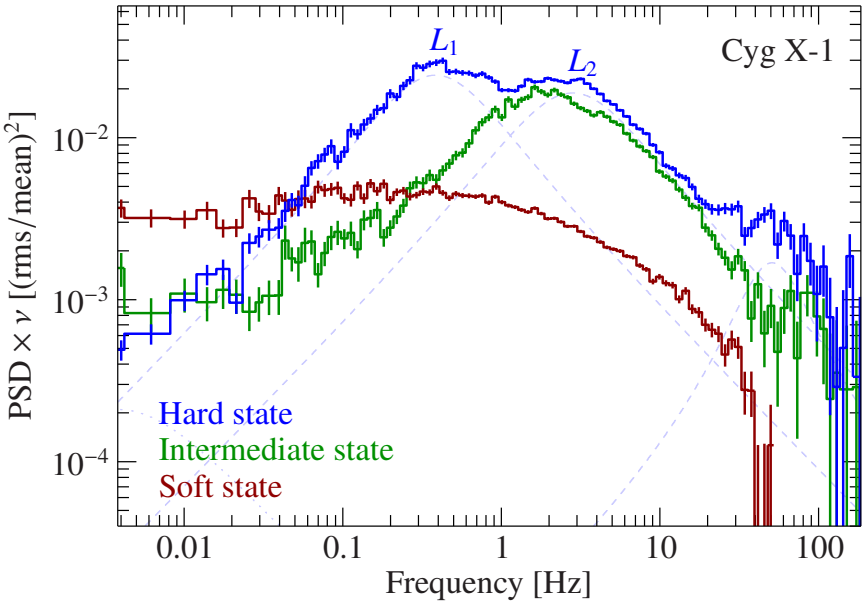

Figure 4.3: Representative power spectral densities of the hard, intermediate, and soft state of Cyg X-1 in the 2–10 keV band taken with *NICER*. The hard state (Obs. ID 2636010101) can be characterized by strong broad band noise that can be resolved into multiple Lorentzian components (blue dashed lines). The intermediate state observation (0100320110) exhibits roughly a single broad component and the soft state (1100320122) is red noise-like. Transient LMXBs show a lower level of red noise in the soft state.

geometrical misalignment of the accretion flow and black hole spin, leading to Lense-Thirring precession (Ingram et al., 2009, and references therein). Shot-noise models (Terrell, 1972; Belloni & Hasinger, 1990) can be tentatively ruled out as they cannot explain the full phenomenology in the timing regime (specifically, the RMS-flux relation; Uttley & McHardy 2001).
Generally, the complex observational outburst behavior is very difficult to model and interpret. Therefore, I will concentrate on the observational appearance in the following (some of the variability models will be explained in Sect. 4.2). I will also explain the overall physical picture that is commonly used to interpret the observations, albeit it needs to be stressed that many of the predictions of this outburst model, such as the location of the inner disk radius, have not yet been unambiguously proven. For reviews on the state behavior, I refer the reader to Remillard & McClintock (2006), Gilfanov (2010), Belloni (2010), Belloni & Motta (2016), and Kalemci et al. (2022).

4.1.1 Quiescence

In *quiescence*, the mass accretion rate onto the black hole is small. The disk is truncated at very high gravitational radii such that few material is present in the innermost region around the BH. The resulting X-ray luminosity is between 10^{30}–10^{33} erg s^{-1} (Kong et al., 2002) or $\lesssim 10^{-5}$ L_{Edd} in terms of Eddington luminosity (Plotkin et al., 2013) and most of the accreted energy likely goes

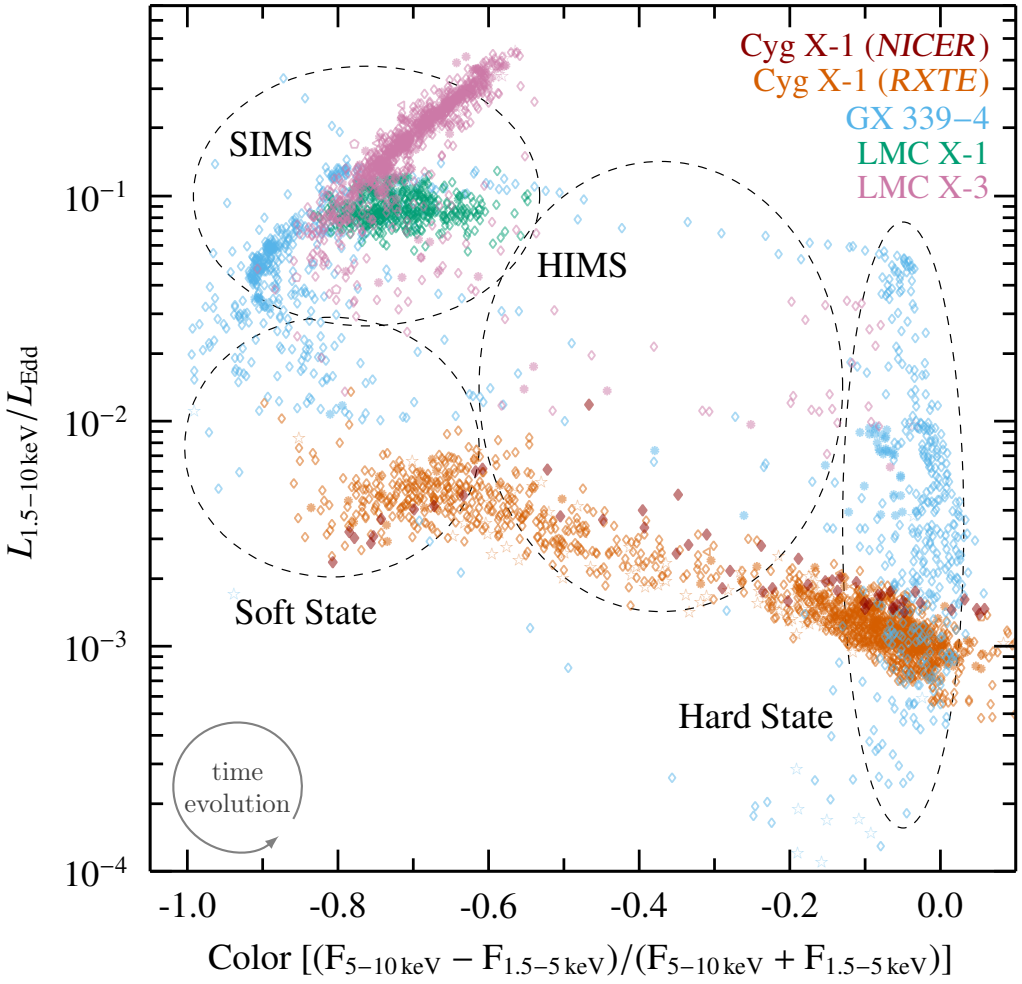

Figure 4.4: q-shaped color-luminosity diagram of black hole X-ray binaries from the *RXTE* and *NICER* archive. The color of 1.5–5 keV and 5–10 keV fluxes is shown as a function of luminosity, scaled to the Eddington value. Transient sources show a hysteresis during an outburst and cycle in a counter-clockwise direction through this diagram. The persistent source Cyg X-1 populates the lower branch. Dashed lines indicate the approximate state classifications of Belloni et al. (2005). The *RXTE* data points are reproduced based on work by Horn (2022).

into powering a steady, compact jet (Fender et al., 2003). The quiescence state is important for dynamical mass measurements from optical photometry, with which the mass of the black hole can be estimated (e.g., Orosz & Bailyn, 1997). Such a measurement is not possible if the source is in outburst because the optical light from the companion star is overshadowed by other effects, such as X-ray reprocessing in the cool outer accretion disk (van Paradijs & McClintock, 1994).

4.1.2 Hard State

The canonical outburst starts in the *faint hard state* when the inner edge of the accretion disk moves closer to the BH and more material is accreted (bottom right in the q-diagram). This may happen through a thermal-viscous instability in the highly truncated disk (Lasota, 2001), but how exactly the outburst is triggered remains unclear. Historically, this state is also called the *low state* because it shows a lower X-ray flux than what is observed at the peak of an outburst (Tananbaum et al., 1972).

The X-ray spectrum in the hard state is dominated by Comptonized emission, which can be observed as a power law with a high-energy cut-off at a photon index of $1.5 \lesssim \Gamma \lesssim 2.0$. Thermal contribution from the faint and cool accretion disk is low (the fraction of the flux coming from the disk is typically below 20% in the 2–20 keV band, see Remillard & McClintock 2006, Table 2) and the spectrum can show strong reflection features (García et al., 2015). In radio wavelengths, synchrotron radiation from a compact, steady, self-absorbed, and mildly relativistic radio jet is often observed (e.g., Fender et al., 2004). The intensity of this radio emission is correlated to the X-rays (Gallo et al., 2003; Wilms et al., 2007; Corbel et al., 2013) as the source becomes gradually brighter and moves to the *bright hard state* (top right of q-diagram).

The X-ray flux is also linearly correlated to strong broad band noise at >10% RMS (Uttley & McHardy, 2001), often even reaching 30–40% RMS (Miyamoto et al., 1991). The hard state power spectrum has a flat-topped shape (in PSD $\times \nu$) with a low and high-frequency break (Belloni & Hasinger, 1990). Historically, PSDs of X-ray binaries were modeled using broken power laws (Cui et al., 1997b; Nowak et al., 1999a). As the data quality increased, it became clear that the flat-topped part is *bumpy* (see Fig. 4.3) and a doubly-broken power law could not describe these data any more. Thus, particularly with the advent of *RXTE*, PSDs were modeled using individual Lorentzians (Miyamoto et al. 1991; Psaltis et al. 1999; Nowak 2000; Belloni et al. 2002). While this modeling is usually considered phenomenological, it is interesting to note that there is an underlying motivation behind choosing Lorentzians, which is that Lorentzians approximate *resonances* in physical systems[2] (Nowak, 2000; Psaltis & Norman, 2000; Körding & Falcke, 2004).

Empirically, the Lorentzian components are often interpreted as coming from physically distinct regions (Cui et al., 1997b; Nowak, 2000). However, due to the uncertainty in the geometry of the accretion flow outlined in Sect. 2.4.2, interpreting variability phenomena is rather intricate and the origin of the Lorentzians is still not completely clear. The broad Lorentzian at low frequencies is found to dominate the soft X-ray variability and, therefore, Wilkinson & Uttley (2009) propose that this component originates from instabilities in the accretion disk. Assuming the truncated disk model, Done et al. (2007) and Rapisarda et al. (2017) suggest that the higher frequency Lorentzian originates inside of a coronal hot inner flow.

In addition to power spectra, the phase of the cross power spectral density is used to study the arrival times of photons in different energy bands, so-called time lag spectra (see Sect. 3.4.2). Measuring such spectra is possible if the light curves in the two energy bands are sufficiently coherent (Vaughan & Nowak, 1997; Nowak et al., 1999a, and references therein). Throughout this thesis I denote high-energy photons lagging low-energy photons as *hard lags*, and measure them with a positive time delay. *Soft lags*, where the soft energy photons lag the high energy ones, will

[2]For instance, a Lorentzian describes the power spectrum of a damped driven harmonic oscillator.

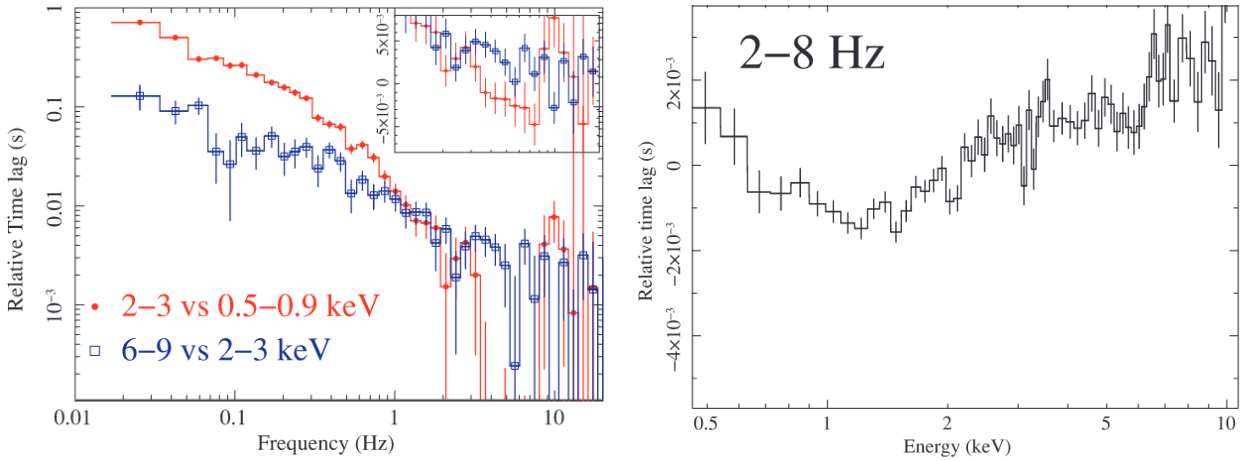

Figure 4.5: Detection of soft lags in the hard state of the LMXB black hole GX 339−4 using *XMM-Newton* EPIC-pn data (modified after Uttley et al., 2011, Fig. 1 and 2). *Left:* Hard time lags between moderate (2–3 keV) and high energy photons (6–9 keV) show roughly a power law-like behavior (blue curve). If soft X-ray energies are considered, the lag becomes negative above roughly 3 Hz (see red curve and inset). *Right:* Lag-energy spectrum with a 0.5–10 keV reference band. The soft lag can be seen as an up-turn at low energies. 0.5 keV photons arrive roughly 3 ms later than 1 keV photons with respect to the reference band. At energies $\gtrsim$1.5 keV, the source shows hard lags.

have a negative time delay.

Hard lags between photons in the 1.5–3 keV and 12–42 keV bands were first identified in Cyg X-1 by Priedhorsky et al. (1979). These hard lags are frequency dependent and, at energies $\gtrsim$2 keV, roughly follow a power law-like $\nu^{-0.7}$ shape (see blue curve in Fig. 4.5, *left*, and also Nowak et al. 1999a). The hard lag is also energy dependent and its amplitude increases approximately logarithmically with the separation of the energy bands, which can be shown using the lag-energy spectrum (Fig. 4.5, *right*, above 1.5 keV, see also Miyamoto & Kitamoto 1989). Furthermore, Nowak et al. (1999a,b) showed that there can be shelf-like structures in the time lag, roughly coinciding with the overlap region of the Lorentzians in the PSD. In the LMXB GX 339−4, these structures also coincide with drops in coherence by up to 10%. Therefore, Nowak et al. (1999b) argue that this behavior indicates that the Lorentzian components are likely incoherent with respect to each other.

During the last decade, X-ray timing missions with soft X-ray coverage allowed researchers to study the time lag phenomenology with respect to a low X-ray energy band. Uttley et al. (2011) found that at high frequencies the 0.5–0.9 keV photons lag behind 2–3 keV photons by several milliseconds, that is, low energies show soft instead of hard lags[3] (Fig. 4.5, *right*). During the rise of the hard

[3]The nomenclature "soft lags" in the lag-energy spectrum can appear confusing because it does not follow the strict "positive value = hard lag, negative value = soft lag" convention used in the lag-frequency spectrum. In this thesis (and generally in black hole timing analysis), soft lags always refer to low-energy photons arriving *after* high-energy photons. In Fig. 4.5 (*right*) an up-turn is seen at low energies. 0.5 keV photons arrive at approximately +2 ms and 1 keV photons arrive at −1 ms with respect to the reference band. This means that the 0.5 keV photons come roughly 3 ms after the 1 keV photons, that is, the soft band lags the hard band. The same lag can be measured

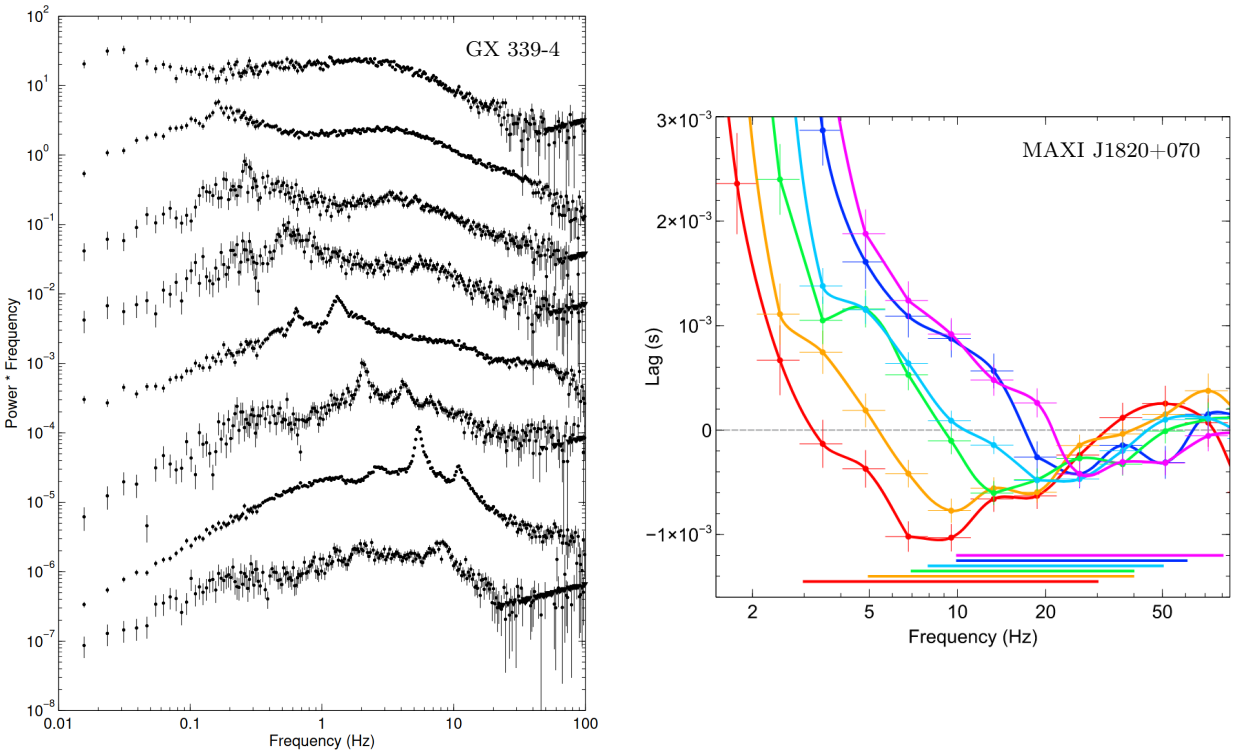

Figure 4.6: Timing behavior of two black hole binaries in the intermediate state. *Left:* Evolution of quasi-periodic oscillations in the power spectrum of GX 339−4 (Credit: Fig. 3 from Belloni et al. 2005, A&A 440, 207, reproduced with permission ©ESO). *Right:* Varying time lags in the state transition of MAXI J1820+070 (Fig. 2 from Kara et al., 2019). Colors indicate different observations ordered successively in time from red to pink. At low frequencies, hard (1–10 keV) photons lag soft (0.5–1 keV) photons, while at high frequencies soft lags hard. The frequency range of the soft lags (horizontal lines) increases as the source moves to the soft-intermediate state, while the amplitude decreases. Reproduced with permission from Springer Nature.

state, these high-frequency soft lags *decrease* in amplitude (De Marco et al., 2015). I will describe the interpretation of this lag behavior in detail in Sect. 4.2.

4.1.3 Intermediate State

Typically a few weeks into the outburst, transient black hole X-ray binaries transition into the *intermediate state* where the system becomes brighter due to an increased mass accretion rate. What exactly initiates this transition is unclear but it is thought that the inner edge of the accretion disk moves towards the ISCO at some point (although it is disputed whether this happens in the bright hard or intermediate state).

in the lag-frequency spectrum in the 2–8 Hz as a negative value if one chooses these energy bands.

As the inner disk edge approaches the black hole, the temperature and luminosity of the multi-temperature disk black body increases (see Eq. 2.7), while the power law component becomes steeper and weaker. Thus, the overall spectrum softens and the system moves to the left on the q-diagram at overall roughly constant X-ray luminosity (Maccarone, 2003). Typically, the transition lasts from only a few days to less than two weeks, both in the persistent HMXB Cyg X-1 (Grinberg et al., 2013), as well as in transient LMXBs (Belloni, 2010). *Failed* state transitions occur when the source goes directly back to the hard state after an initial softening (Pottschmidt et al., 2003). Due to this unstable nature of the intermediate state, it has been discovered much later than the canonical hard and soft state, first by Miyamoto & Kitamoto (1991, see also Miyamoto et al. 1993). Historically, this state is referred to as the *very high state*, as the X-ray flux of the outburst can peak at this stage (Miyamoto et al., 1991). Also the term *steep power law state* is sometimes used (Remillard & McClintock, 2006).

The characteristic frequencies of the variability components increase in the intermediate state. The Lorentzians in the power spectrum shift to higher frequencies, together with a drop in RMS (see, e.g., Pottschmidt et al. 2003, Fig. 7, for Cyg X-1, Belloni et al. 2005, Fig. 4, for GX 339−4, or Wang et al. 2020b, Fig. A1, for MAXI J1820+070). On top of the broad Lorentzians, transient black hole binaries also show more narrow variability components between roughly 3–20 Hz, called *quasi-periodic oscillations* (QPOs; see Wijnands et al. 1999 and Ingram & Motta 2019 for a review). In the intermediate state, these QPOs change in frequency and strength (Fig. 4.6, *left*). Based on their appearance, Belloni et al. (2005) established a further division into the hard and soft intermediate state (HIMS and SIMS, respectively). Coinciding with the transition of QPO types and typically the highest X-ray flux, a strong, optically thin radio flare is seen. Homan et al. (2020), for instance, detected a hard X-ray flare and the transition of one QPO type to the other, which occurred 2–2.5 h before a discrete radio flare in MAXI J1820+070.

The radio flare is due to the ejection of a ballistic jet displaying highly relativistic (sometimes even super-luminal) motion away from the radio core (Mirabel & Rodríguez, 1994; Hjellming & Rupen, 1995). The optically thin radio emission is believed to originate when the fast ejected blob shocks with the material from the slower steady jet emitting synchrotron radiation (Fender et al., 2004). It has been proposed that the ejected material is the corona, which expands vertically upwards (Vadawale et al., 2003; Fender et al., 2004). After the radio flare, the radio emission usually ceases and the jet is quenched. The border between these regimes is, therefore, called the *jet line* (Fender et al., 2004).

The time lags show a more complex behavior in the transition compared to the pure hard state. At high energies, Pottschmidt et al. (2000) found that hard lags increase in the transition of Cyg X-1, accompanied by a drop in coherence (Grinberg et al., 2014). This behavior was later found to be typical for black hole X-ray binaries and is seen also in transient sources in the HIMS (e.g., Belloni et al., 2005; Altamirano & Méndez, 2015; Wang et al., 2020b). The increase in hard lags in the transition is also connected to the radio flares and has been interpreted as an indication of a change in the size of the Comptonizing plasma (Cui et al., 1997b; Pottschmidt et al., 2000; Wilms et al., 2007). Similarly, amplitude and frequency changes of soft lags are also seen in a number of LMXB black holes. In the HIMS, Kara et al. (2019) found that the soft lags move to higher frequencies, while simultaneously reducing in amplitude (see Fig. 4.6, *right*). Before the transition to the SIMS, the time lags become longer again and move back to lower frequencies (Wang et al., 2021; De Marco

et al., 2021). This behavior has triggered an active debate about the geometrical interpretation, which I will discuss in Sect. 4.2.

4.1.4 Soft State

In the *soft state*, the flux of the source is dominated by thermal emission from the geometrically-thin, optically-thick accretion disk and can be modeled as a multi-temperature black body around ∼1 keV. This state is historically referred to as the *high state*. It is generally accepted that the inner disk reaches the ISCO in the soft state (Steiner et al., 2010) and that it is relatively stable (Churazov et al., 2001; Gierliński & Done, 2004). The contribution of the corona to the emitted flux is small (although there can still be strong reflection features detected, see Steiner et al. 2016) and the radio emission is quenched. There is usually no jet present in the system any more (Fender et al., 2004). Instead, high-resolution spectroscopy shows that there can be high-velocity equatorial disk winds present (Ponti et al., 2012).
The variability of LMXBs shows a strong drop in RMS in the soft state (e.g., Stiele & Kong, 2020, their Fig. 1). It is typically only a few percent and the PSD shows a smooth red noise-like power spectrum (e.g., Debnath et al., 2008, their Fig. 4b), sometimes with weak QPOs at frequencies >10 Hz (e.g., Nowak et al. 2008, their Fig. 14, or Homan et al. 2001, their Fig. 23). Due to the low RMS, time lags in the soft state usually cannot be constrained properly but comparisons to the persistent source Cyg X-1 indicates that they should have low amplitude (Altamirano & Méndez, 2015).
Then, the source transitions back into the hard state and subsequently into quiescence (e.g., Plotkin et al., 2013). In transient sources, this generally occurs at a lower luminosity level than the "forward" transition from hard to soft, leading to the hysteresis in the HID (Miyamoto et al., 1995).

4.2 Interpretation of Time Lags: Propagating Fluctuations and Reverberation Mapping

Auf dem Rechner des Menschen trifft Paul Emilia wieder, die ebenfalls von Cygnus X-1 kommt. „Teilchen, wir haben uns ja ewig nicht gesehen. Du bist kurz nach mir hier angekommen, oder? Ich bin direkt aus der Wolke hergekommen", wird Paul von Emilia gefragt. „Genau, ich musste noch den Umweg über die Scheibe nehmen", sagt Paul. „Da habe ich Peter wiedergesehen und bin als leuchtendes Eisenlichtteilchen hergekommen. Du hast ja noch viel mehr Energie, als ich." Die beiden finden heraus, dass sie nur im Abstand von wenigen Millisekunden getrennt voneinander in den Detektor geprallt sind.

To be continued in Ch. 5.

One major difficulty in characterizing the innermost environment of black holes binaries is that no telescope can spatially resolve the geometry of the accretion flow in the foreseeable future[4]. In fact,

[4] A black hole binary with an orbital separation and distance such as Cyg X-1 ($a \approx 0.244$ AU, $d \approx 2.22$ kpc; Miller-Jones et al. 2021) has an angular size of roughly 100 μas, a resolution that may be achievable with X-ray

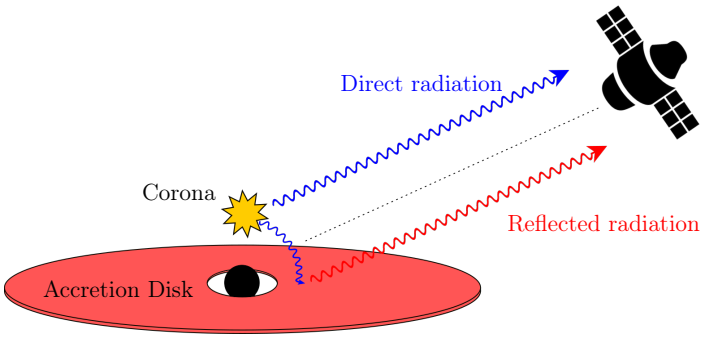

Figure 4.7: Sketch of an accreting black hole in the lamppost geometry. Reverberation lags occur because the reflected radiation has a longer light travel time with respect to the direct radiation.

the whole systems appears as a point source. In order to study the direct environment of black holes, it is necessary to employ different techniques. In the last section, I outlined that black hole X-ray binaries show characteristic time lags between photons of different energies. In this section, I will describe the interpretation of the Fourier time lags and how they can be used to estimate the geometry of the corona and accretion disk.

Reverberation mapping is a technique used to measure the mass of black holes. Classically, it has been applied using optical spectroscopy to study the light travel time between the BH and the broad line region of AGN (Peterson et al., 2004). X-ray reverberation mapping exploits the same principle. The physical scale of the system leads to different light travel times between the radiation coming from the corona and the accretion disk. Part of the X-rays originating in the corona propagate directly into our line-of-sight. These are observed as a power law continuum. X-rays that are reprocessed in the accretion disk have a longer distance to travel (see Fig. 4.7 for an example sketch in the lamppost geometry and Fig. 2.7 for alternative geometries). The light-crossing delay results in a measurable time lag of the reflected with respect to the continuum X-rays, which is called *reverberation lag* (see Uttley et al. 2014 for a review). In contrast to the typical hard lags, which have been known since the 1970s (Priedhorsky et al., 1979), reverberation lags emerge as soft lags, that is, the soft photons lag the hard photons.

Soft lags were first found in AGN using a soft band below 2 keV and a hard band typically between 2–10 keV[5] (McHardy et al., 2007; Fabian et al., 2009). Subsequently, Uttley et al. (2011) found soft lags in black hole X-ray binaries using similar bands (Fig. 4.5), and shortly later Zoghbi et al. (2012) detected the first Fe Kα photons lagging behind the continuum photons. It was also found that the amplitude of the lag is correlated to the mass of the black hole (De Marco et al., 2013), supporting the idea that all characteristic timescales become longer as the gravitational radius

interferometry (Uttley et al., 2021). However, the event horizon of Cyg X-1 (assuming maximal spin) is only 30 km large, which corresponds to an angular size of 10^{-4} μas. A multi-spacecraft X-ray interferometer may reach resolutions below 1 μas, which is, however, orders of magnitude larger than the innermost region that mainly produces the X-rays. I note, though, that AGN, which are thought to be scaled-up black hole X-ray binaries (McHardy et al., 2006), have an event horizon that is more reasonably resolvable with X-ray interferometry. For reference, the Event Horizon Telescope operating in the radio wavelengths has a resolution limit of $\sim$25 μas (Event Horizon Telescope Collaboration et al., 2019).

[5]Such soft lags can be seen in the lag-energy spectrum at low energies for a narrow (e.g., Kara et al., 2013a, using 0.3–0.8 keV in their Fig. 2), as well as a broad reference band (e.g., Kara et al., 2013b, using 0.3–10 keV in their Fig. 3).

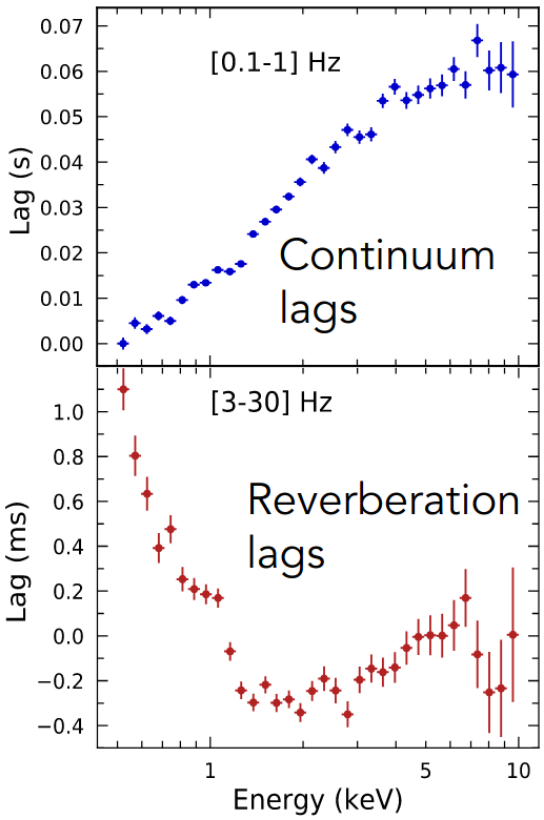

Figure 4.8: Example of reverberation lags seen in the LMXB MAXI J1820+070 in the hard intermediate state (Fig. 2 from Ingram 2023, originally published in Kara et al. 2019). *Top:* At low frequencies the lag-energy spectrum shows featureless hard continuum lags (the reference band is 0.5–10 keV with the subject band removed). *Bottom:* At high frequencies soft lags emerge, which trace the low energy soft excess and the broadened iron line that is seen in reflection spectra.

increases with mass (McHardy et al., 2006).

Often, a lag-energy spectrum is used to test the data for reverberation signatures (Fig. 4.8). Depending on the sampled frequencies, such spectra isolate different physical effects in the data. At low frequencies, hard lags are seen with an approximately log-linear energy dependency (Fig. 4.8, *top*). At first, it was postulated that these hard lags are due to the scattering timescales in the corona. However, these simple Comptonization models are not capable of explaining the long lag amplitudes at low frequencies (see Miyamoto et al. 1988 and, e.g., discussion in Nowak et al. 1999a,c). The standard interpretation of the hard lags is that fluctuations in the mass accretion rate propagate through the accretion disk into the corona (Lyubarskii, 1997; Kotov et al., 2001; Arévalo & Uttley, 2006; Ingram & van der Klis, 2013). This "propagating fluctuations" model has to explain two different time lag signatures seen in the data: The lag-frequency spectrum shows that low frequencies exhibit longer lags than higher frequencies (Fig. 4.5, *left*), while the lag-energy spectrum shows that high energies have a longer lag than low energies (Fig. 4.8, *top*).

The propagating fluctuations model is based on the fact that each disk radius emits variability driven by the viscous timescale due to instabilities in the disk. Furthermore, each radius has a temperature that corresponds to the local black body. Large disk radii produce fluctuations at longer timescales (lower frequencies) than smaller radii. The emitted variability is a product of the locally produced variability and the longer timescale variability that propagated inwards from larger

radii. Thus, the lag is "hard", simply because the inner radii have a higher temperature than outer radii. The variability that propagates all the way into the corona is emitted at the highest energy and exhibits the longest lags, explaining the lag-energy spectrum. Low frequencies have traveled the longest distance and, thus, have the largest time lag amplitude. At high frequencies the fluctuations are produced only at the smallest radii and the corresponding time lags are short, which explains the lag-frequency spectrum. It has been shown that this model can also quantitatively explain the broad Lorentzians in the hard state power spectrum (e.g., Psaltis & Norman, 2000; Rapisarda et al., 2017; Kawamura et al., 2022), although their modeling uses a common noise source for all variability timescales with a linear response, preserving unity coherence, which is, however, not observed at all frequencies, as I will show in Sect. 5.4.2.

The fact that the amplitude of these "continuum lags" decreases with increasing frequencies gives the opportunity to detect reverberation lags at high frequencies. The lag is, however, *smoothed* because different disk radii reflect light rays of different travel time, and *diluted* because each energy band contains some direct and some reflected photons (Ingram, 2023). This means that one cannot simply calculate a distance from the measured value of the time lag. The idea behind a general relativistic reverberation model, such as RELTRANS (Ingram et al., 2019; Mastroserio et al., 2021), is that the physical response of the system is modeled as an *impulse-response function*. It is calculated through ray-tracing and encodes the time delays from the light-crossing and the energy shift of photons coming from a point source above the black hole. The time-dependent reflection spectrum is then obtained by convolving the continuum flux from the corona with the impulse response (this is typically done using the convolution theorem) to predict the energy spectrum and time lags (see also Uttley et al., 2014; Bambi et al., 2021; Ingram, 2023). The resulting model for the cross-, lag-energy, and/or time-averaged energy spectra is then fitted to the observational data by varying the system parameters, such as black hole mass, height of the corona, inner disk radius, etc. This way, the spectral-timing signal can be used to estimate the geometry of the system under the assumption of a lamppost configuration.

How does the reverberation model relate to the observational detection of soft lags outlined in the last section? To recapitulate, there are two main observational characteristics of soft lags throughout the states: During the hard state and HIMS the soft lags *decrease* in amplitude and move to *higher* frequencies (De Marco et al., 2015; Kara et al., 2019), while in the SIMS the soft lags *increase* in amplitude and move to *lower* frequencies (De Marco et al., 2021; Wang et al., 2021). Shortly after this increase, a radio flare is seen, indicating a ballistic jet ejection (Bright et al., 2020), which has been associated with the corona (Fender et al., 2004). Similar to the interpretation of the increasing hard lags in the transition (Cui et al., 1997b; Pottschmidt et al., 2000; Wilms et al., 2007), it has been proposed that the increasing soft lag amplitude is due to longer light-travel times between the ejected corona and the accretion disk (De Marco et al., 2021; Wang et al., 2021). It is important to caution that the reverberation interpretation in black holes is not unique, particularly in the hard state. This discussion is closely related to another active debate on the position of the disk inner edge during the bright hard state. It is generally accepted that the corona is close to the black hole in the hard state but how the accretion geometry looks like exactly is unclear (see Sect. 2.4.2). Multiple studies have found that the disk reaches the ISCO during the bright hard state, consistent with a lamppost corona (e.g., Miller et al., 2006; García et al., 2015; Buisson et al., 2019), while other studies find that the disk is truncated at several tens of R_g with a

hot inner flow corona (Tomsick et al., 2009; De Marco et al., 2021; Axelsson & Veledina, 2021). Due to this inconsistency, the interpretation of the soft lags is also degenerate. As an example, using the same data of MAXI J1820+070, the soft time lag has been interpreted to be due to either a contraction of the coronal height in the lamppost geometry (Kara et al., 2019) or a reduction in the disk truncation radius in the inner hot flow geometry (Zdziarski et al., 2021).

Chapter 5

Long term variability of Cygnus X-1: A spectral-timing look at low energies with *NICER*

Paul und Emilia sind nicht die einzigen Röntgenteilchen, die von Cygnus X-1 kommen. Auch Peter kommt irgendwann an. Doch der Zeitpunkt, zu dem Peter ankommt, können die drei Energiequanten sich nicht so recht erklären. „Warum sind wir denn nun in dieser Reihenfolge angekommen?“

The End?

In Sect. 2.2, I outlined the historic relevance of Cyg X-1 as the first source accepted to harbor a black hole. It is also one of the best, if not the best, studied black hole binary, and its properties have been explored at almost all wavelengths. From early on, it has been realized that the X-ray variability can provide crucial information on the accretion flow near the compact object (Rothschild et al., 1974). In fact, the X-ray variability properties led to the speculation that the compact object in Cyg X-1 is a black hole (Oda et al., 1971) even before the (now considered) confirmation using dynamical mass measurements (Webster & Murdin, 1972; Bolton, 1972).

There is, however, a gap in the knowledge of Cyg X-1's variability behavior in the soft X-ray regime $\lesssim$2 keV where the emission of the accretion disk becomes important. Only recently, with the launch of *NICER* in 2017 (Sect. 3.3.2), it became possible to combine the spectral and timing regime in the soft X-ray range with high signal-to-noise data, high monitoring cadence, and no complications from pile-up or deadtime. The study presented in this chapter addresses this knowledge gap and, for the first time, allows us to study the variability properties of the accretion disk in detail. I begin this chapter with an introduction of the known variability properties of Cyg X-1, building on the state classification introduction in Sect. 4.

Large parts of the content of this chapter are taken in verbatim from the manuscript *Long term variability of Cygnus X-1. VIII. A spectral-timing look at low energies with NICER* by O. König, G. Mastroserio, T. Dauser, M. Méndez, J. Wang, J. García, J. Steiner, K. Pottschmidt, R. Ballhausen, R. Connors, F. García, V. Grinberg, D. Horn, A. Ingram, E. Kara, T. Kallman,

M. Lucchini, E. Nathan, M. Nowak, P. Thalhammer, M. van der Klis, and J. Wilms. These parts are reproduced without direct reference. The manuscript will be submitted to the journal Astronomy & Astrophysics.

5.1 X-ray Variability Properties of Cygnus X-1

Cyg X-1 (Bowyer et al., 1965) is a high-mass X-ray binary with a $(21.2 \pm 2.2)\,M_\odot$ (Miller-Jones et al., 2021), rapidly rotating black hole (e.g., Tomsick et al., 2014) that accretes matter from the stellar wind of the supergiant HDE 226868 (Walborn, 1973). Cyg X-1 is a persistent source that is located on the lower branch of the q-shaped HID (Belloni 2010; Nowak et al. 2012 and Fig. 5.4), where it transitions from a hard state to a softer state where still a power law component is seen at energies >10 keV (e.g., Wilms et al., 2006).
In Fig. 5.1, I show an overview of the known timing properties of Cyg X-1 in the hard state at X-ray energies above 2 keV. The PSD (Fig. 5.1a) is overall similar to transient LMXB black holes, introduced in Sect. 4.1.2, and can be decomposed into multiple broad Lorentzian components. The major difference is that there is no firm detection of a QPO in Cyg X-1 (although there have been various claims, see, e.g., Cui et al. 1997b, Rutledge et al. 1999, and the discussion in Nowak 2000). The lag-frequency spectrum between bands in the 2–4 keV and 4–10 keV range roughly follows a $\nu^{-0.7}$ shape (Fig. 5.1c). Sometimes shelf-like structures can be seen in frequency ranges coinciding with the Lorentzians (e.g., Fig. 10 of Nowak et al. 1999a, Fig. 11 of Grinberg et al. 2014, or Fig. 3 of Uttley et al. 2014). The coherence is close to unity in the 0.01–10 Hz range between these energy bands (Fig. 5.1d and Nowak et al. 1999a).
The soft state PSD of Cyg X-1 is red noise-like with an RMS at a much higher level than what is usually seen in LMXBs (Fig. 5.2). In fact, the RMS can even surpass the hard state variability above roughly 10 keV with values larger than 30% (see Pottschmidt et al. 2006, Grinberg et al. 2014, Fig. 4, and Zhou et al. 2022, Fig. 10). The source of this strong high-energy variability is likely the flux in the power law component that can be seen in the soft state energy spectrum of Cyg X-1 between approximately 4–100 keV (e.g., Wilms et al., 2006, their Fig. 12).
Cyg X-1 has been subject of decades-long efforts to characterize its spectral and timing properties. Since the launch of the *RXTE* satellite in 1995, roughly 13 refereed papers with Cyg X-1 in its title are published every year[1]. I do not attempt to give a comprehensive and complete overview of the source. Instead, I will concentrate on the "Long term variability of Cygnus X-1" paper series, which revealed a wealth of phenomena due to both the accretion flow and the interaction of its X-rays with the surrounding stellar wind. Thus far, seven papers have been published in this series mainly based on regular monitoring by *RXTE*, which accumulated 4.77 Ms of data on Cyg X-1 from 1996 to 2011. In the following, I will describe the main results of this paper series.

1. **X-ray spectral-temporal correlations in the hard state.** Pottschmidt et al. (2003) decomposed the PSDs into four broad Lorentzian components and studied their evolution throughout the 1998–2001 hard state. The authors found that the variability components systematically shift to higher frequencies as the source softens (which was later also confirmed

[1] https://ui.adsabs.harvard.edu/search/q=title%253A%22Cyg%20X-1%22%252C%20property%253Arefereed

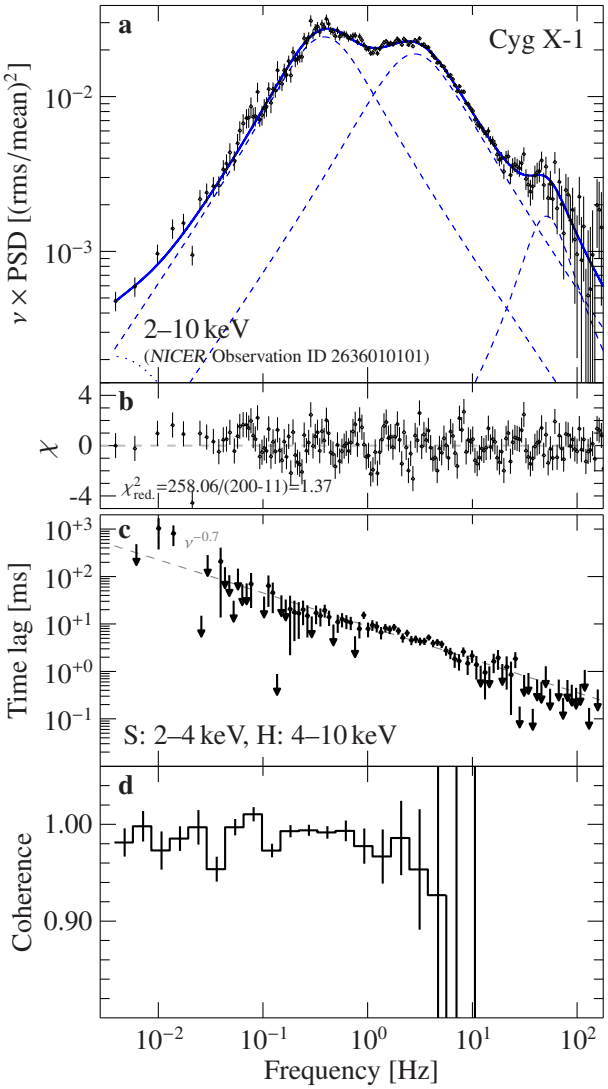

Figure 5.1: Timing behavior of the high-mass X-ray binary Cyg X-1 in the hard state as seen with *NICER*. **a)** The power spectral density shows strong variability (32.93 ± 0.18% RMS in 2–10 keV) that can be decomposed into multiple broad Lorentzian components (dotted lines). **b)** Residuals of a fit to the PSD with three Lorentzians plus one zero-centered Lorentzian. **c)** The lag-frequency spectrum with 2–4 keV as soft and 4–10 keV as hard band roughly follows a $\nu^{-0.7}$ shape (dashed line). **d)** The coherence between these energy bands is unity or close to unity. In this *NICER* observation, the coherence becomes unconstrained above roughly 5 Hz.

for LMXBs, e.g., Belloni et al. 2005, and Sect. 4.1), together with an increase of the hard time lags, indicating changes in the structure of the accretion flow such as a geometrical change of the Comptonizing medium. Interestingly, the third Lorentzian component at around 8 Hz dropped significantly in amplitude in 1998 and has not been detected since then (see also Fig. 5.1a–b).

2. **The RMS-flux relation.** Gleissner et al. (2004b) showed that there is a linear correlation between the RMS variability amplitude and the flux (see also Uttley & McHardy, 2001), which is valid across a wide range of time scales from seconds to months and in all states of Cyg X-1 (note that this is not the case for transient LMXB black holes as the RMS in their soft state drops).

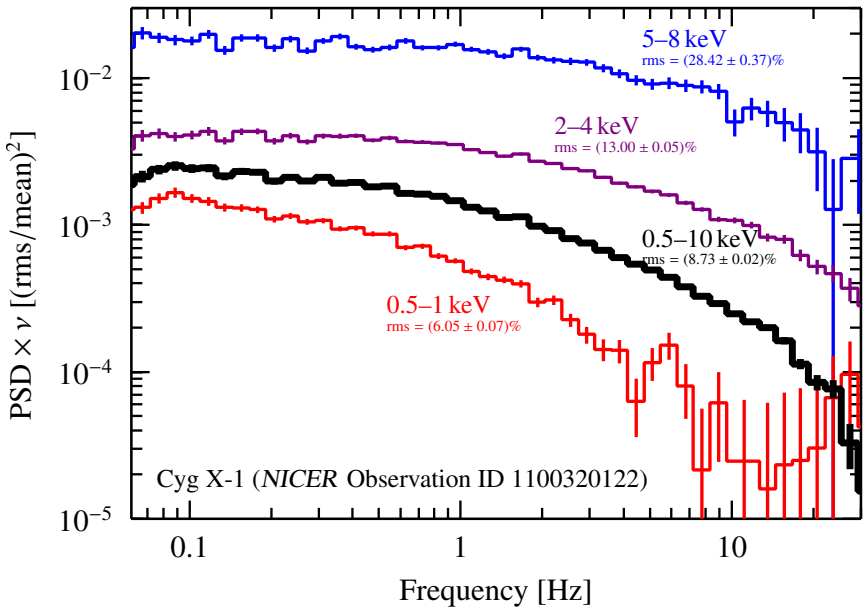

Figure 5.2: Soft state power spectral density of Cyg X-1 measured with *NICER*. The soft state is characterized by red noise and shows a strong energy dependence in its variability, with high variability in the hard and low variability in the soft X-rays. The fractional RMS values are derived by integrating the power spectrum from 0.06–30 Hz.

3. **Radio-X-ray correlations.** Gleissner et al. (2004a) find a correlation between radio emission from the jet of Cyg X-1 and hard X-rays from the Comptonization. Correlated flares are particularly strong in the intermediate state on timescales of days to months.

4. **Spectral evolution 1999–2004.** Wilms et al. (2006) model the *RXTE*/Proportional Counter Array (PCA) data using a broken power law to derive the spectral evolution of Cyg X-1. This phenomenological model was chosen to allow a straight-forward comparison of the low- to high-energy components without over-parameterizing the model. In particular, the modeling is simple enough that it can be mapped onto other sources. The authors find a correlation of the soft and hard photon index of the broken power law, representing a relationship of the black body luminosity and the Comptonized plasma (which was confirmed by *Insight-HXMT* data in Zhou et al. 2022, their Fig. 7).

5. **State definitions with all sky monitors.** Grinberg et al. (2013) find that the evolution of the spectral and timing properties of Cyg X-1 suggest a distinction into a hard state for $\Gamma_1 < 2.0$, intermediate state for $2.0 < \Gamma_1 < 2.5$, and soft state for $\Gamma_1 > 2.5$, where Γ_1 is the soft photon index of a broken power law fit to the *RXTE*/PCA data. The authors map this criterion to other monitoring missions (*RXTE*/ASM, *MAXI*, *Swift*/BAT, and *Fermi*/GBM) to provide easy-to-use criteria for the state classification of Cyg X-1. While it has been clear that the source has been predominantly in the hard state until approximately 2013, the

authors could systematically address the stability of the states, showing that the intermediate state is short-lived and Cyg X-1 transitions within 3 days in 50% of the time (some transitions can even be on the order of hours, as shown in Böck et al. 2011).

6. **Energy-resolved X-ray variability 1999–2011.** Grinberg et al. (2014) systematically address the energy dependence of the X-ray variability in Cyg X-1, which changes smoothly as a function of the continuum shape. Figure 5.3 (Fig. 8 of Grinberg et al. 2014) shows that the hard state is characterized by two main variability components, except for the hardest observations at $\Gamma_1 \lesssim 1.8$. The low-frequency Lorentzian dominates at low energies (2.1–4.5 keV), while the high-frequency Lorentzian is the prominent component at high energies ($\gtrsim$5.7 keV). These components shift to higher frequencies throughout the intermediate state until a clear change is visible when the source is in the soft state. At $\Gamma_1 \gtrsim 2.6$, the PSD becomes red noise-like with a very strong energy dependence in its variability. Most variability originates from energies $\gtrsim$5.7 keV.

7. **Orbital variability of the focussed wind in Cyg X-1/HDE 226868 system.** Grinberg et al. (2015) find that absorption in the stellar wind is most prominent at superior conjunction ($\phi_{\rm orb} = 0$) but is generally highly variable across the orbital phase, especially in the hard state. More recently, Lai et al. (2022) found that the stellar wind likely also has an influence on the time lags. The authors find long soft lags at low frequencies that could be due to scattering or recombination processes in the wind. This result shows that the interpretation of lags in Cyg X-1 is not straight-forward and that, importantly, soft lags are no unambiguous sign of reprocessing in the accretion disk (reverberation).

In this eighth paper of the series, we revisit the timing behavior of Cyg X-1 using *NICER*. The main emphasis is to characterize the variability of the accretion disk at low X-ray energies $\lesssim$2 keV and its connection to the Comptonized medium, as well as putting the timing phenomenology into context of the previous *RXTE* work. The chapter is organized as follows. Section 5.2 discusses our data reduction. In Sect. 5.3, we classify the spectral states and hardness evolution, emphasizing the extension of previous monitoring campaigns to low X-ray energies. Section 5.4 analyzes three representative hard, intermediate, and soft state observations, and reports of the discovery of previously unknown time lag and coherence phenomena, both in the hard and soft state. We discuss and interpret our results in Sect. 5.5 and summarize the paper in Sect. 5.6.

5.2 Data Reduction

Our *NICER* dataset of Cyg X-1 comprises 52 observations performed between 2017 June 13 and 2022 April 15 (see observation log in Table A.1). The data were reduced with HEASOFT 6.29c and NICERDAS 2021-08-31_V008c. We exclude data taken inside the South Atlantic Anomaly (`saafilt=YES`) and all data taken with detectors 14 and 34, which have exhibited anomalous behavior. We filter out data measured below an angle of 15° to the Earth's X-ray bright limb to avoid contamination from fluorescence in the atmosphere, as well as data taken below 30° with respect to Earth's horizon in case the surface is illuminated by the Sun to prevent optical loading

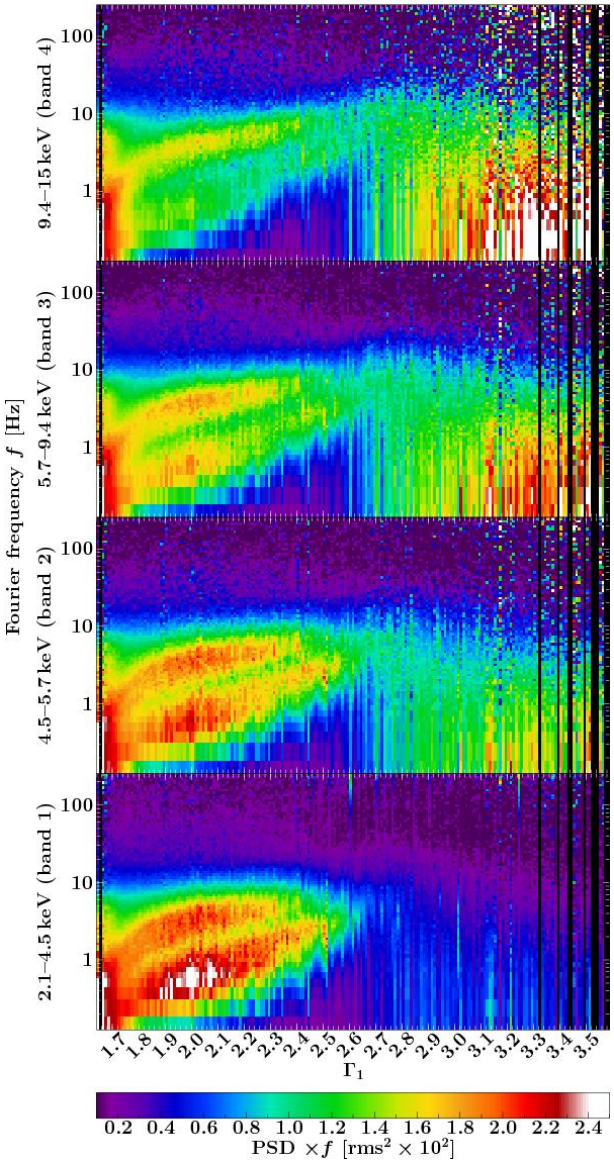

Figure 5.3: Evolution of the PSD with spectral shape for four different energy bands from 2.1–15 keV using *RXTE* data of Cyg X-1 (Credit: Fig. 8 from Grinberg et al. 2014, A&A 565, A1, reproduced with permission ©ESO).

by reflected optical light. We do not filter out all data taken during orbit day. Instead, we limit our analysis to observations which have a per-detector undershoot rate below 200 counts s^{-1}, as recommended by the *NICER* analysis guide[2]. Furthermore, to ensure that no low-energy noise intrudes the data products, we constrain our analysis to the energy range above 0.5 keV. Overshoots are constrained to the default range of less than 30 counts s^{-1} per detector to excludes periods of high particle background. We then extract lightcurves in multiple energy bands between 0.5–10 keV with a time resolution of 1 ms. These lightcurves have full-instrument count rates ranging from

[2] https://heasarc.gsfc.nasa.gov/docs/nicer/data_analysis/workshops/NICER-Workshop-Filtering-Markwardt-2021.pdf

500–30 000 counts s^{-1}, while typical background rates of *NICER* are estimated to be on the order of 1 count s^{-1} (Remillard et al., 2022). Given this brightness of Cyg X-1, no background correction is necessary. The data analysis is performed with ISIS 1.6.2-47 (Houck, 2002).
For the hardness diagrams in Sect. 5.3.2 and 5.3.3, we rebin the lightcurves to a time resolution of 100 s. For the Fourier analysis in Sect. 5.4, we compute the timing products by splitting the lightcurves into segments of 16.384 s and, in case of gaps, only include data that fully cover a segment to avoid aliasing. This approach rejects ∼5.6 ks of data, such that we remain with a total of ∼211 ks of exposure. We do not further subdivide the 52 observations based on breaks in the data which arise due to the orbit of the ISS ("good time intervals"). All PSDs in this study use the fractional RMS normalization (Belloni & Hasinger, 1990; Miyamoto et al., 1991). Generally, the impact of deadtime on the Fourier products in *NICER* is low, especially at low frequencies (e.g., Stevens et al., 2018). Since we concentrate on frequencies below 10 Hz in this study, we do not perform a deadtime correction. The coherence and its uncertainty are determined using Eqs. 2 and 8 of Vaughan & Nowak (1997)[3]. The RMS and its uncertainty are computed using Eqs. 5 and 11 of Vaughan et al. (2003)[4]. The uncertainty of the (segment-averaged) lags for each Fourier frequency is calculated from the coherence (Nowak et al., 1999a, their Eq. 16). Finally, we logarithmically rebin all timing products in frequency.

5.3 Evolution of the Flux and Hardness over all States

5.3.1 Position of Cyg X-1 in the q-diagram

We start our analysis by putting the *NICER* data into the context of previous monitoring campaigns of Cyg X-1 and other black hole binaries observed by *RXTE*, using a color-luminosity diagram (Fig. 5.4). To be able to compare the *NICER* and *RXTE* data, we derive the fluxes and hardnesses of each observation from simple empirical spectral fits rather than employing the traditional approach of showing a hardness intensity diagram in terms of mission-dependent count rates and hardness ratios.
To model the continuum, we use a power law plus disk black body. The absorption of this continuum in the stellar wind and the interstellar medium is described with `TBabs` (Wilms et al., 2000), the iron line is modeled with a broad Gaussian emission line (modeling the detailed shape of the relativistic line is not necessary). Two further narrow Gaussians are added at 6.4 keV and 7.1 keV, respectively, to model Fe Kα/β emission from neutral iron. As we are interested only in the behavior of the overall broad continuum components, we include a 5% systematic uncertainty to account for possible residuals due to calibration uncertainties of *NICER*[5] and the simplicity of the model. Furthermore, we fit the data only above 2.5 keV in order to be able to better compare it to the *RXTE* results. We then display the luminosity in units of the Eddington luminosity (assuming the black hole mass and distance estimate of Miller-Jones et al. 2021) as a function of the flux ratio for the 1.5–5 keV and

[3] We note that there is an incorrect factor γ^2 in the numerator of the intrinsic coherence calculation in Nowak et al. (1999a, Eq. 8), see Bendat & Piersol (1986, Eq. 79) and the text after Eq. 2 of Vaughan & Nowak (1997).
[4] For the uncertainty of the RMS we note that a number of slightly different definitions are also used, e.g., Uttley et al. (2014, Eq. 14) and Ingram et al. (2019, Eq. 22).
[5] `https://heasarc.gsfc.nasa.gov/docs/nicer/data_analysis/nicer_analysis_tips.html`

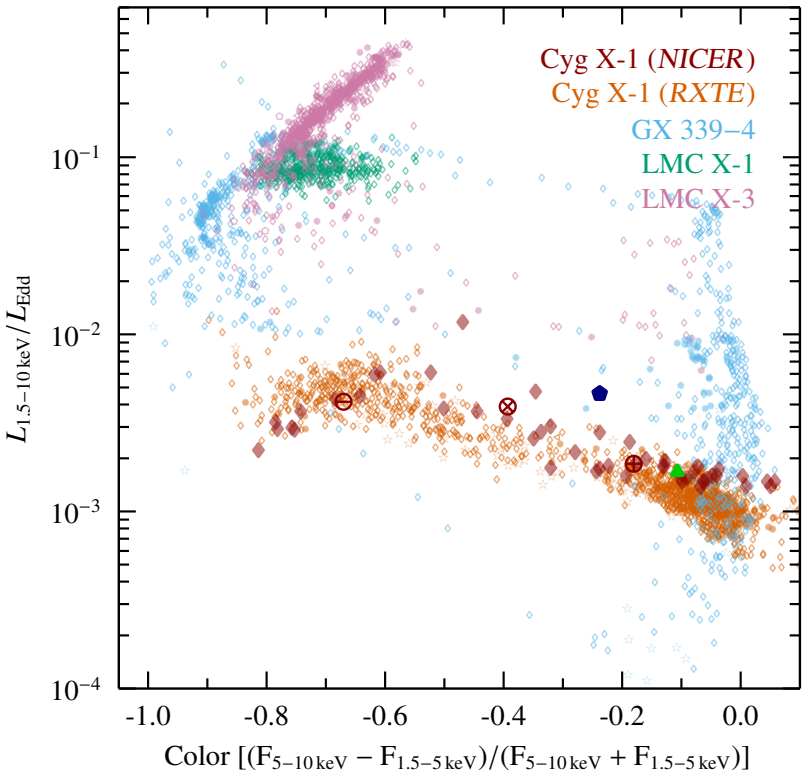

Figure 5.4: Color-luminosity diagram of Cyg X-1 and other black hole X-ray binaries from the *RXTE* archive. The transient source GX 339−4 shows a q-shaped pattern, while Cyg X-1 only populates the lower branch of the q. The soft and hard bands are 1.5–5 keV and 5–10 keV, respectively, and the color is derived from (absorbed) fluxes of phenomenological model fits. The *NICER* data (red diamonds) cover the entire color range seen in Cyg X-1 with *RXTE*. Red circles with a plus, times, and minus sign within it denote *NICER* observation 2636010101, 0100320110, and 1100320122 of Cyg X-1, respectively. The blue pentagon and green triangle denote *NICER* observations 1200120268 of MAXI J1820+070 and 2200530129 of MAXI J1348−630, respectively. The *RXTE* data points are reproduced based on work by Horn (2022).

the 5–10 keV bands. This way the diagram is independent of the detector used and also permits us to directly compare different sources (see Wilms et al., 2006; Barillier et al., 2023, and references therein).

Figure 5.4 shows that the *NICER* data cover the hard and soft state of Cyg X-1, connected by observations in the parameter space of the lower transition from the soft back to the hard state in transient black hole binaries. Contrary to the other sources, Cyg X-1 always remains on the lower horizontal track in this diagram. The *NICER*-measured luminosity is approximately 20% higher than that of *RXTE*, which is likely due to systematics in the flux calibration of *NICER* and *RXTE*/PCA data (Jahoda et al., 2006; Shaposhnikov et al., 2012; García et al., 2014). See Barillier et al. (2023) for a detailed discussion of the fitting approach of the *RXTE* data and a comparison

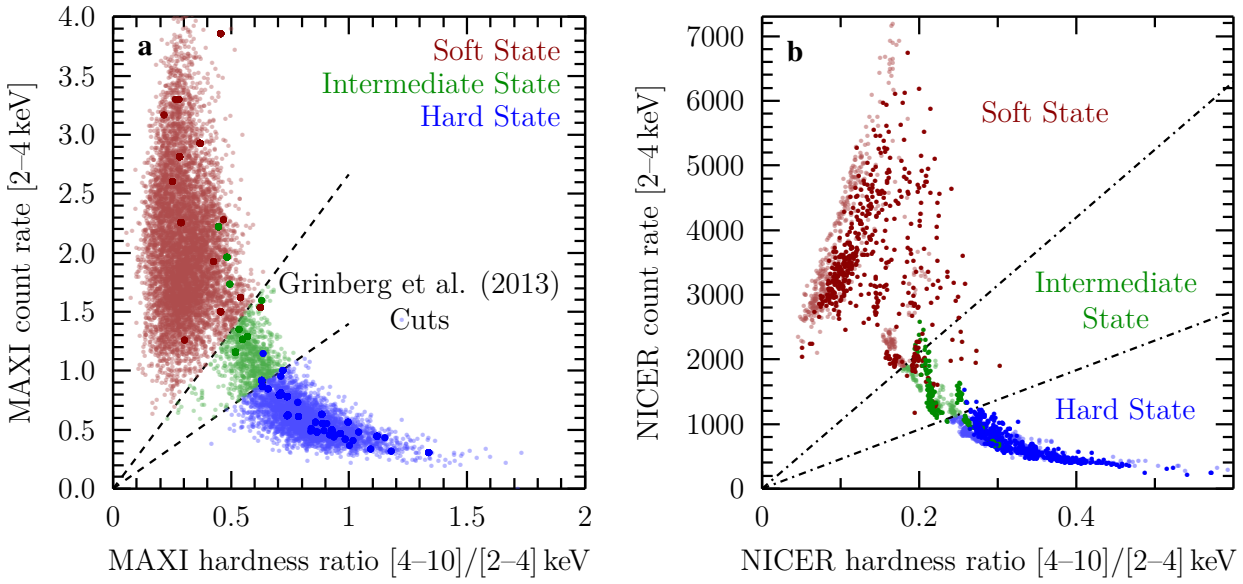

Figure 5.5: Hardness-intensity diagrams of Cyg X-1. **a)** HID using *MAXI* count rates from 6 h binned lightcurves. Light points are classified according to Grinberg et al. (2013, dashed line). Solid points denote *MAXI* time bins which have a *NICER* bin falling into the 6 h time frame, colored according to our *NICER* cuts. **b)** HID using *NICER* count rates from 100 s binned lightcurves. Light points are colored according to our *NICER* criterion. Solid points denote *NICER* time bins which fall into the 6 h *MAXI* time frame and are classified according to the *MAXI* cuts. The *NICER* cuts (dash-dotted line) are chosen such that the *MAXI* criterion is reproduced with minimal contamination.

of the different sources used in the preparation of the color-luminosity diagram.

5.3.2 State Classification and Long-Term Monitoring

In order to classify the *NICER* observations, we place them into the context of existing state classifications of Cyg X-1. Such spectral states were introduced to roughly characterize the *continuous* changes in brightness as well as the spectral and timing properties of black hole X-ray binaries (Tananbaum et al., 1972; Belloni, 2010). Specifically, we use the *MAXI* criteria given by Grinberg et al. (2013) to classify Cyg X-1 into a hard, intermediate, and soft state (Fig. 5.5a). For each observation, we assign a state based on those bins in 100 s resolved *NICER* lightcurves which are strictly simultaneous to the 6 h binned *MAXI* lightcurves[6]. In order to verify the precision of the mapping, we color strictly simultaneous time bins in the HIDs according to the state definition of the other mission. We define the cuts in the *NICER* HID (Fig. 5.5b) such that the *MAXI* criterion of Grinberg et al. (2013) is best reproduced. Specifically, we determine that Cyg X-1 is in the soft

[6] http://maxi.riken.jp/pubdata/v7lrkn/J1958+352/

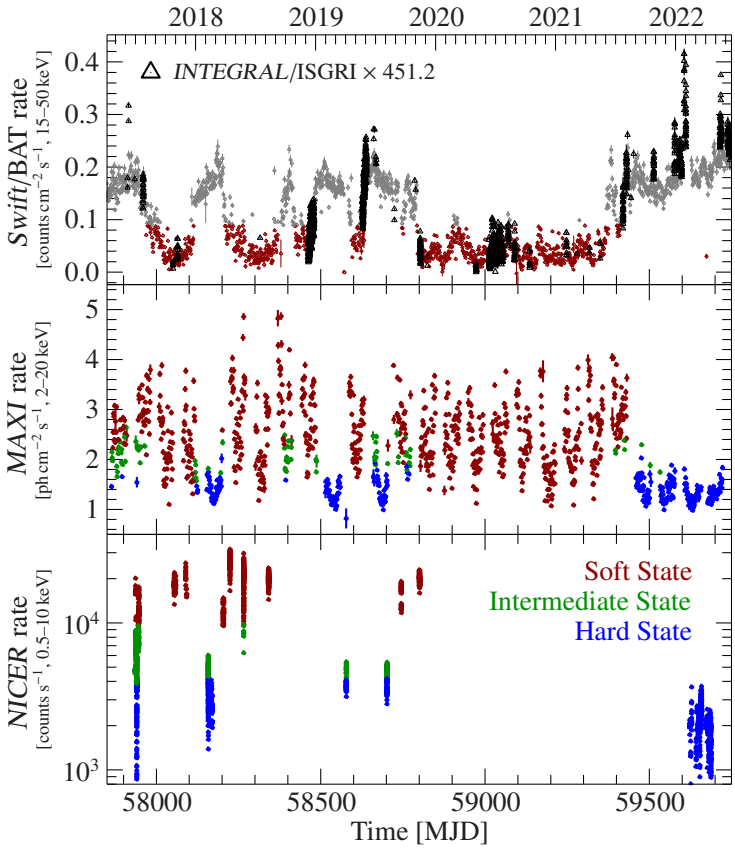

Figure 5.6: *Swift*/BAT, *INTEGRAL*/ISGRI (top panel), *MAXI* (center), and *NICER* (bottom) light curves of Cyg X-1. In the top panel, gray data points denote either the hard or intermediate state as *Swift*/BAT's energy range does not allow a further differentiation. Black triangles show *INTEGRAL*/ISGRI count rates in the 30–50 keV band, showing each science window as one data point. These data are scaled by the ratio of the average BAT and ISGRI count rates over the whole campaign in order to align them with the *Swift*/BAT data.

state for a 2–4 keV *NICER* count rate, R, that satisfies $R \geq 10500 \cdot h$ and is in the hard state for $R < 4580 \cdot h$, where h is the count rate ratio of the 4–10 keV to the 2–4 keV band.

The derived *NICER* criterion is then applied to all *NICER* data to classify the states in the HID. The overall behavior in the HID is similar to previous monitoring campaigns from *RXTE* (Grinberg et al., 2013) and *MAXI* (Sugimoto et al., 2016). Cyg X-1 exhibits a smooth transition from the hard to the intermediate state and shows a kink when the source is in the soft state.

We emphasize that the state definitions used so far follow the traditional names for the states of Cyg X-1, which are inconsistent with state designations used for other black hole binaries (see Sect. 5.1). In addition, state classifications in Cyg X-1 and other sources should only be taken to be approximate as they attempt to discretize a continuous source evolution. We therefore regard the photon index, Γ, inferred from our power law fits of Sect. 5.3.1, as the most salient property characterizing the observations, rather than the state designation.

Finally, in Fig. 5.6, we put the *NICER* data into perspective of the long-term evolution of Cyg X-1. We show the *NICER* and *MAXI* lightcurves and also add *Swift*/BAT data, using the state classification methodology of Grinberg et al. (2013), as well as *INTEGRAL*/ISGRI count rates (Thalhammer et al., to be submitted). The long-term lightcurves show that Cyg X-1 underwent several state transitions during the *NICER* observations.

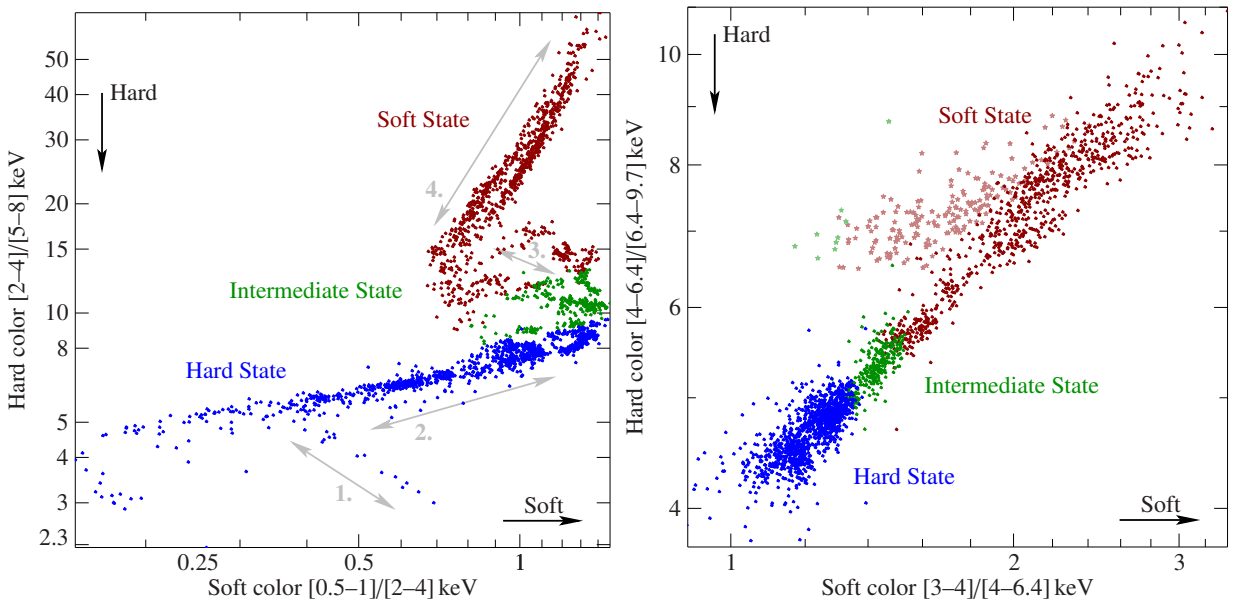

Figure 5.7: Color-color diagram of Cyg X-1. The diagram at soft energies (*left*) shows distinct regions where the source undergoes several turns. Numbered gray arrows indicate preferred tracks which Cyg X-1 follows when transitioning between the hard and the soft state. Some observations in the hard state show "nose"-shaped tracks where the color-color bends down towards a harder spectral shape ("1."), which is called dipping. When Cyg X-1 softens, the source shows large variations dominantly in soft color ("2."). As the source transitions through the intermediate into the soft state, it follows a distinct zig-zag shape driven by the soft color ("3."). When Cyg X-1 is in the pure soft state, it still ranges significantly in hard color ("4."). *Right:* Color-color diagram using higher energy bands as in Done & Gierliński (2003) and Zdziarski et al. (2016). Light stars denote observation 1100320121, which is the only observation that does not follow the straight line.

5.3.3 Color-Color Behavior throughout the Spectral States

The color-color diagram of the *NICER* observations is shown in Fig. 5.7 (*left*). The hard state follows a broad lower track which varies most strongly in soft color. The diagram shows at least two outlier tracks, which deviate from the straight line (gray arrow labeled "1."). These "nose"-shaped variations are well known and can be attributed to dipping events where absorption of soft X-rays in the clumps of the stellar wind leads to a hardening of the spectrum (Nowak et al., 2011; Hirsch et al., 2019; Grinberg et al., 2020; Lai et al., 2022).

When Cyg X-1 undergoes a full transition to the soft state, it first softens and moves rightward in the diagram, mainly changing in soft color ("2."). The track then bends around and the source hardens, again changing predominantly in the soft color ("3.")[7]. In the soft state, the track bends

[7]A two track-like structure can be seen in the color-color diagram, which is built up from four observations (for reference, I refer the reader to Figs. A.10, A.26, A.27, and A.35) with a total exposure of nearly 20 ks. I checked whether there is a correlation of these tracks with the flux evolution during these observations. I cannot find that

around again and softens, both in the soft and hard color ("4."). This overall behavior creates a zig-zag shape in the color-color diagram.
In summary, the *NICER* color-color diagram shows a rather complex pattern with a distinctive zig-zag shape in the transition that has not been seen from monitoring campaigns of Cyg X-1 limited to the hard X-ray regime (Done & Gierliński, 2003; Zdziarski et al., 2016)[8]. This shape disappears for the *NICER* data when we use the harder energy bands in the color-color diagram typical of previous campaigns (Fig. 5.7, *right*). The more complex soft behavior is therefore a property that only emerges at soft X-ray energies and is probably due to absorption and ionization effects in the foreground material and/or complex behavior of the accretion disk emission.
A further complication in the analysis of observations of the intrinsic spectral and timing properties of the accretion flow in Cyg X-1 is that HDE 226868 has a strong stellar wind which has an influence both on the observable spectral and the timing properties of Cyg X-1 (Hirsch et al., 2019; Lai et al., 2022, and references therein). It is especially strong at superior conjunction ($\phi_{\rm orb} = 0$), where the line of sight passes through regions of the wind that cause "dipping" by inhomogeneities in the wind (e.g., Bałucińska-Church et al., 2000; Grinberg et al., 2015, and references therein). While these observations are ideal to study dipping effects due to absorption in the stellar wind, they complicate the analysis of the intrinsic variability. While the *NICER* archive contains observations at almost all orbital phases (Fig. 5.8), many hard state observations cluster at superior/inferior conjunction ($\phi_{\rm orb} = 0/0.5$). We identify observations strongly affected by dipping through inspection of their color-color diagrams[9] and exclude them from the further analysis in Sect. 5.4 in order to reduce contamination of the variability behavior by foreground effects.

5.4 Spectral-Timing Analysis: Energy-resolved Timing Properties for each Spectral State

In order to illustrate the general behavior and emphasize the extension of the variability to low X-ray energies compared to the earlier *RXTE* work, we concentrate on three selected observations that are representative of the overall source behavior. To illustrate the behavior when the source spectral shape is hard, we choose observation 2636010101 at $\Gamma \sim 1.8$. This observation has an orbital phase of $\phi_{\rm orb} = 0.94$–0.04 but does not show prominent signatures of dipping in the lightcurve or color-color diagram. Observation 0100320110 ($\phi_{\rm orb} = 0.05$–0.21) is formally classified as soft state according to the *NICER* to *MAXI* mapping discussed in Sect. 5.3.2 but exhibits many properties of a transition between typical hard and soft state behavior, such as a photon index of $\Gamma \sim 2.3$. With $\Gamma \sim 3.1$, observation 1100320122 ($\phi_{\rm orb} = 0.61$–0.69) is characteristic of the classical soft state of Cyg X-1. These three observations are also marked in the q-diagram (Fig. 5.4).
In this section, we will first investigate the power spectra of these observations and connect them

the observations during rising or falling flux accumulate only on one of these branches. Therefore, I infer that this structure is most likely an observational bias, that is, the monitoring simply does not fill the complete color-color space.

[8]While many color-color diagrams of Cyg X-1 are widely available, also at softer energies, they often only cover individual spectral states and not the full transition cycle (e.g., Nowak et al., 2011; Grinberg et al., 2020).

[9]Examples are observation 0100320106 (Fig. A.6) and 4690010111 (Fig. A.43).

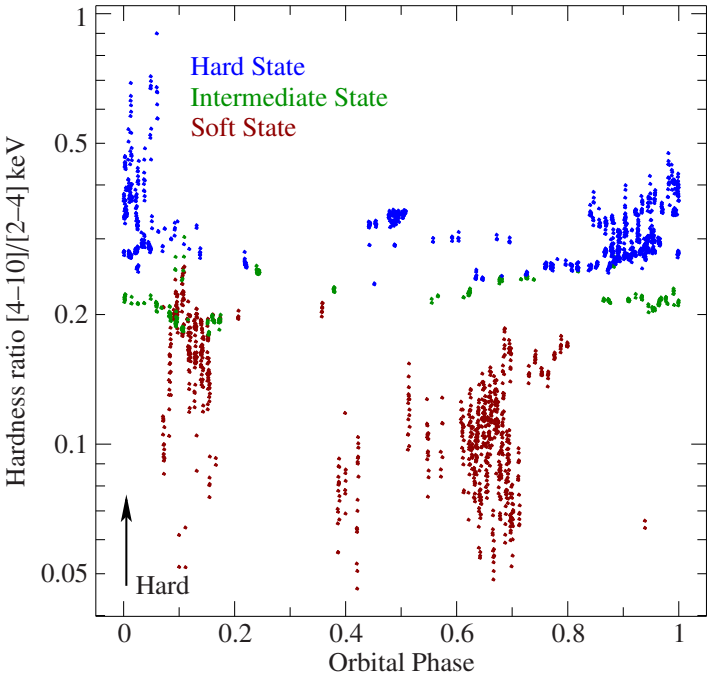

Figure 5.8: Orbital phase coverage in the *NICER* dataset of Cyg X-1.

to energy spectral components (Sect. 5.4.1). We then study the coherence to probe the linear correlation between low and high energies (Sect. 5.4.2), before we analyze the time lags (Sect. 5.4.3) as they can be reliably interpreted only for sufficiently high coherence (see, e.g., Nowak et al., 1999a).
For reference, we also show the energy-resolved PSDs, lag-frequency spectra, and coherence of all *NICER* observations studied here in Appendix A. These figures also include *NICER* products for the typical *RXTE* bands.

5.4.1 Power Spectral Density

Figure 4.3, shown in the introduction of this thesis part, displayed representative PSDs in the spectral states of Cyg X-1. Consistent with earlier work (e.g., Miyamoto & Kitamoto, 1989; Nowak et al., 1999a, and references therein), multiple broad components can be clearly identified in the hard state. As the source transits to the soft state, these components merge to a single-humped structure (e.g., Cui et al., 1997a; Pottschmidt et al., 2003; Grinberg et al., 2014). The PSD in the soft state is red noise-like (e.g., Cui et al., 1997a,b) with a 0.5–10 keV RMS of around 10%, which is much higher than what is seen in the soft state of LMXB black holes. As shown in Fig. 5.3 in the introduction of this chapter, the structure of the PSD is a function of the spectral continuum shape (and therefore state).
Following Nowak (2000) and Pottschmidt et al. (2003), we model the hard state PSD in the 0.06–20 Hz range with two individual Lorentzian functions peaking at roughly 0.2 Hz and 1.8 Hz, plus a zero-centered Lorentzian. Following earlier works we call the two lower frequency Lorentzians L_1 and L_2 in the following. Observation 2636010101 potentially shows an additional high-frequency

component at around 50 Hz, which has been seen before (Pottschmidt et al., 2003) and which is also included in the model fits shown in Fig. 4.3. Another Lorentzian, which was clearly visible at around 8 Hz in *RXTE* data taken before 1998 and then vanished (Pottschmidt et al., 2003) is still not significantly detected.

It is well known that the power spectra of all states are energy dependent (e.g., Nowak et al., 1999a; Grinberg et al., 2014; Zhou et al., 2022). In order to study this energy dependence, we calculate an energy-resolved power map for each observation (Fig. 5.9). These maps show the PSDs computed for narrow energy bands in a color coded way, such that we can study the relative contribution of each Lorentzian component.

In the hard state observation, the main components seen in the broad energy band PSDs (Fig. 4.3) can be well identified in the power map (Fig. 5.9, *top*) as yellow/orange peaks. While their peak frequencies do not change with energy, their strength strongly depends on the energy. At the lowest energies below ∼1.5 keV, L_1 dominates the variability, albeit with low amplitude. At energies $\gtrsim$1.5 keV, L_2 starts to become apparent. The strength of L_1 peaks at around 1.7 keV. It then decreases in amplitude at harder energies. On the other hand, at energies above ∼1.5 keV, the strength of L_2 remains fairly constant (for completeness, we show the RMS spectrum of L_1 and L_2 in Fig. 5.10). Integrating the power spectrum over all frequencies, (using Eq. 3.13) we derive a fractional RMS of (18.5 ± 0.4)% in 0.5–1 keV and (30.0 ± 1.7)% in 5–8 keV.

In the data taken during the transition between the soft and hard state ($\Gamma \sim 2.3$), the PSD is single-humped at a slightly lower RMS compared to the hard state (Fig. 5.9, *center*). The hump can be described by a broad Lorentzian peaking at around 1–2 Hz in frequency and 3–4 keV in energy space. The RMS at softer energies is significantly lower, but the overall shape of the PSD matches the high-energy data. Again, the position and width of the Lorentzian components does not depend on the energy.

The pure soft state observation ($\Gamma \sim 3.1$, Fig. 5.9, *bottom*) shows the typical red noise behavior reported previously for the spectrally softest observations of Cyg X-1. In this observation the variability increases drastically with energy, as also seen in, e.g., Grinberg et al. (2014) or Zhou et al. (2022), from (6.57 ± 0.21)% fractional RMS in 0.5–1 keV to (30.6 ± 1.2)% in 5–8 keV.

In order to understand the physical origin of the variability, we first consider physical processes underlying the dominant emission in the energy band where the variability is strongest. Therefore, we perform spectral fits to the time-averaged X-ray spectrum in the 0.5–10 keV range, to determine the contribution of the accretion disk emission and of Comptonization to each energy bin. For all states, the spectrum of Cyg X-1 can be approximately described as a combination of thermal emission from the accretion disk and a non-thermal component. We describe this spectral shape with a model consisting of emission from a multi-temperature accretion disk (`diskbb`), which is partly Compton-upscattered following (`simpl` model; Steiner et al., 2009). As before, we include a 5% systematic uncertainty to account for possible residuals due to absorption in the ionized stellar wind, calibration uncertainties of *NICER*, and the simplicity of the model.

To see whether the variability is due to the disk emission or due to effects related to the Comptonization of that radiation, for each energy we compute the ratio between the model counts of the accretion disk component $C(\texttt{diskbb})$, and the Comptonized model $C(\texttt{simpl} \otimes \texttt{diskbb})$. Note that at low energies this fraction can become larger than unity because Comptonization redistributes photons from lower to higher energies.

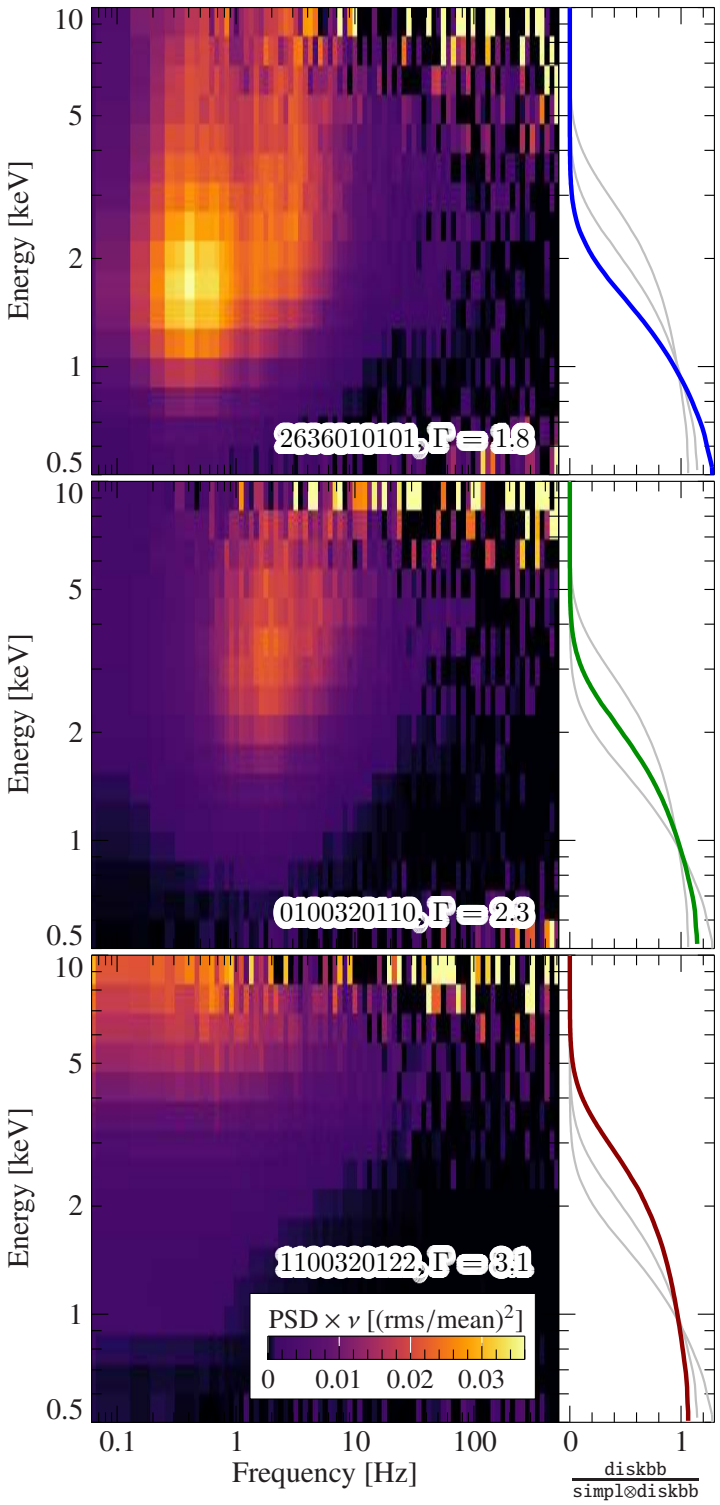

Figure 5.9: Energy-resolved PSDs for three representative observations at different hardness. The blue, green, and red thick lines in the side panels show the relative contribution from the accretion disk (that is, the quantity $C(\texttt{diskbb})/C(\texttt{simpl}\otimes\texttt{diskbb})$) for the hard ($\Gamma \sim 1.8$), intermediate ($\Gamma \sim 2.3$), and soft state ($\Gamma \sim 3.1$), respectively. The gray lines show the curves of the other states for comparison. *Top:* In the hard state, the power spectrum peaks at $\sim$2 keV. It is double-humped at energies $\gtrsim$1.5 keV while the second hump reduces in amplitude at lower energies. *Center:* At $\Gamma \sim 2.3$, the PSD has a single-humped structure that peaks at $\sim$4 keV. The variability peak shifts to higher frequencies compared to the hard state. *Bottom:* In the soft state, the PSD is red noise-like and is strongest at the highest energies covered by *NICER*.

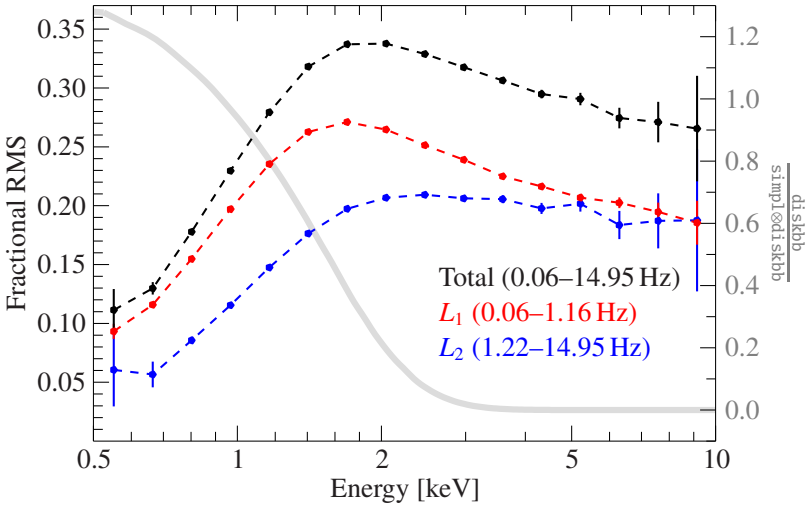

Figure 5.10: RMS spectrum of observation 2636010101 at $\Gamma \sim 1.8$. The black dashed line shows the total RMS averaged over the 0.06–15 Hz range, which peaks at around 2 keV. The low- (red) and high-frequency (blue dashed line) variability shows a bimodal behavior. The high-frequency variability from L_2 remains constant above ∼2 keV, while the RMS of L_1 drops off. Below roughly 1.5 keV, the variability drops at all frequencies. The remaining variability is dominated by L_1. The gray curve with the scale on the right axis measures the contribution from the accretion disk in the hard state. L_1 peaks at ∼1.7 keV where the disk contributes to ∼40% of the flux.

We display the energy-dependent disk fraction for the three example observations in the vertical side panels of Fig. 5.9. In general, and in line with more detailed spectral analyses (Nowak et al., 2011; Tomsick et al., 2014), the disk dominates the emission at low energies and becomes weaker at 1–3 keV, where the Comptonized emission begins to dominate. This transition region where the Comptonization starts to dominate shifts from ∼1.5 keV in the hard state to ∼2.5 keV in the soft state. Likewise, the variability shifts to higher energies. At $\Gamma \sim 2.3$, the disk fraction is below 10% at the peak of the variability around 3–4 keV and in the soft state ($\Gamma \sim 3.1$), the contribution of the disk is essentially zero in the energy range of the largest variability. This behavior clearly suggests that the variability is due to the behavior of the Comptonizing medium in the soft state.

In order to better quantify the peak energy of the two main variability components of the hard state, we use the RMS variability amplitude spectrum. Figure 5.10 shows the fractional RMS of lightcurves extracted in small energy bands, integrated over three frequency ranges that sample the total PSD (0.06–15 Hz), the low-frequency range of L_1 (0.06–1.16 Hz), and the high-frequency range of L_2 (1.22–15 Hz). Overall, most variability comes from ≥1.5 keV and the variability drops significantly at low energies (Fig. 5.9). We can constrain the energy where L_1 peaks to be at ∼1.7 keV and derive a disk fraction of roughly 40%. At higher energies, the RMS of L_1 declines, while the high-frequency variability covering L_2 stays constant above 2 keV. This behavior is consistent with *AstroSAT* data of Cyg X-1, shown in Misra et al. (2017, their Fig. 4), and *Insight-HXMT* data, shown in Feng et al. (2022, their Fig. 7).

5.4.2 Coherence

Figure 5.11 shows the energy-resolved intrinsic coherence, calculated between small energy bins and a reference band. In order to test the influence of the choice of the reference band on the behavior of the coherence function, we calculate maps with three different reference bands: A broad 0.5–10 keV reference band, following the typical procedure of the lag-energy spectrum calculation (Uttley et al., 2014), a 3.3–10 keV reference band, tracing the variability of the Comptonized emission, and 0.5–1.9 keV, which traces variability dominated by emission from the accretion disk. Figure 5.11 also shows the PSD map in the top row such that the amount of variability at the relevant energy can be directly related to the coherence.

Generally, in all *NICER* data of Cyg X-1, the coherence can only be constrained for frequencies up to ∼10 Hz for energies around 2 keV, beyond which the coherence begins to fluctuate wildly. At lower and higher energies, where the power is lower, the coherence becomes unconstrained earlier (in all states). For clarity, coherence values with fractional uncertainties larger than 50% are set to zero.

In the hard state observation, the coherence can be well constrained to near unity at almost all frequencies in the 0.06–10 Hz band. This behavior is largely independent of the chosen reference band. The coherence is reduced only in the 1–2 Hz band, which can be seen as a purple stripe at 0.5–1 keV in the map with the 3.3–10 keV reference band. This frequency band is the location where the two variability components in the PSD have an overlap. We will systematically characterize the implications of this coherence drop in Sect. 5.4.3.

For the data taken during an intermediate spectral shape, $\Gamma \sim 2.3$, similar to the hard state, the coherence is again close to unity at frequencies where the variability in the PSD map peaks, and also largely independent of the reference band (Fig. 5.11, *center-column*).

This behavior changes in the soft state observation ($\Gamma \sim 3.1$). Here, the global variability is strongly dominated by the hard X-rays above 5 keV (Sect. 5.4.1). However, looking at the coherence with respect to the low-energy reference band (Fig. 5.11 *upper-right*), the coherence of this variability with this lower energy band is very low. Note that the coherence with respect to the hard reference band (Fig. 5.11 middle-right) shows identical behavior, but in the converse. Namely, the measured coherence indicates that the low-energy variability is *incoherent* with respect to the high-energy reference band, i.e., the emission in both bands varies independently.

Figure 5.11 also shows that in the soft state the value of the coherence increases with frequency. In the coherence maps, this effect also depends on energy and the reference band but it occurs whenever bands between the soft ($\lesssim$2 keV) and hard X-rays ($\gtrsim$3 keV) are involved[10]. For instance, the coherence at 5 keV (0.5–1.9 keV reference band, Fig. 5.11, *upper-right*) increases from below 40% at 0.1 Hz to above 70% at 5 Hz. This shape traces the red noise variability seen in the PSD: The coherence with respect to soft X-rays is lowest at the energy and frequency bins where the variability is strongest. From this overall behavior we conclude that the red noise is not linearly correlated to the low-energy variability.

As we have seen above, especially in the soft state the choice of the reference band drastically

[10] For simplicity, we also refer to the corresponding coherence-frequency spectrum in Fig. A.31 in the appendix, where the increase is shown in the traditional one-dimensional way. We also note that the coherence can increase up to unity at high frequencies in other observations in the soft state (e.g., Fig. A.28).

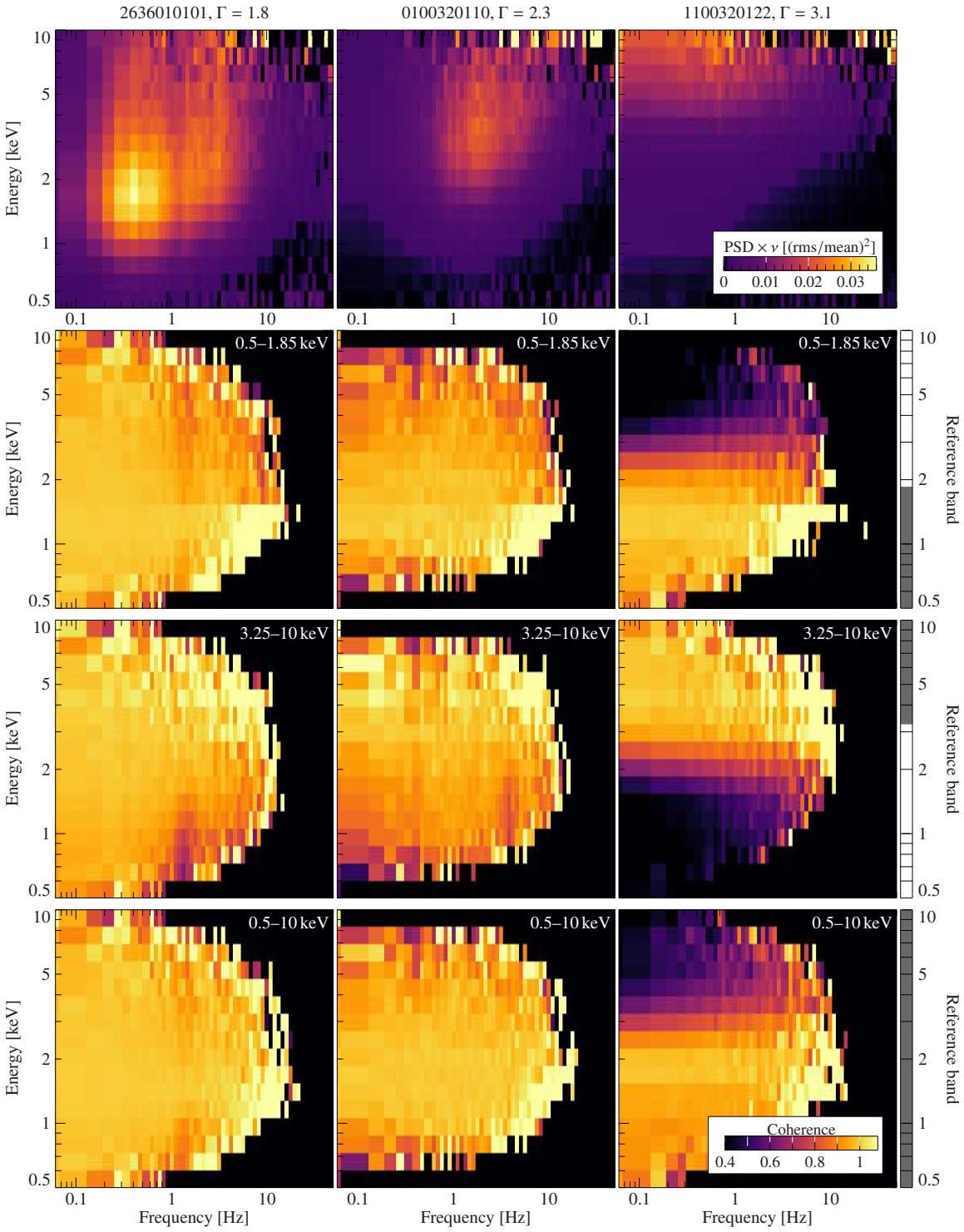

Figure 5.11: Energy-resolved coherence maps with respect to three different reference bands (written in the top right corner of each panel and indicated via the shaded gray region on the right). The power map for each observation is shown in the top row for reference. *Left column:* In the hard state, the coherence is generally close to unity in the probed frequency range, except for a drop between 1–2 Hz. *Center column:* When the PSD is single-humped at $\Gamma \sim 2.3$, the coherence is still close to unity. This behavior is largely indifferent to the chosen reference band. *Right column:* In the soft state, the high and low energy variability is incoherent with respect to each other. This can be isolated by choosing a low or high energy reference band. We emphasize that the choice of the reference band has a drastic influence on the derived coherence values for soft state.

influences the measured coherence values (Fig. 5.11, *right column*). While this is not surprising given that different physical processes are at play in different energy bands (this is the reason why studies like Nowak et al. 1999a or Kara et al. 2013a use a reference band with a small energy range), in order to increase the signal-to-noise ratio many studies of the coherence and other energy dependent quantities choose a broad reference band that often spans the entire range of the data (see, e.g., Uttley et al., 2011; Kara et al., 2019; De Marco et al., 2021). As can be seen in Fig. 5.11, in all three *NICER* observations, the coherence for such a broad reference band (0.5–10 keV) is very similar to the one for the low energy reference band (0.5–1.85 keV). The reason is that X-ray instruments tend to have a large effective area at low energies and that Cyg X-1 and other black hole X-ray binaries produce photon fluxes which decline precipitously with energy in the X-rays. Combining both effects means that taking a broad reference band biases the measurement towards the peak of the instrumental effective area – in reality, the reference band is not broad. As a consequence, the coherence and any quantities derived from variability with respect to a broad energy band (such as time lags) may be very difficult to interpret. It is only by specifically choosing reference bands such that either the accretion disk emission or Comptonization dominates (see previous section and Fig. 5.9), that we are able to test the connection of the variability between these physical processes.

5.4.3 Time Lags

In the previous section, we found that the low- and high-energy variability is highly coherent in the hard and intermediate states, while the coherence is broken up in the soft state. In this section, we analyze the time lags of the three example observations. In particular, we concentrate on the changes of the time lag phenomenology when the energy bands are extended to soft X-rays below 2 keV. We show the lag behavior of all observations in Appendix A, including lags between harder, *RXTE*-like, energy bands.

In the soft state observation at $\Gamma \sim 3.1$, time lags between bands chosen in the *NICER* energy range, including low energies below 2 keV, have low amplitude $\lesssim$10 ms. This is consistent with previous studies of Cyg X-1 above 2 keV (Grinberg et al., 2013, 2014) and shows that the behavior does not change significantly for lower energies. As shown in Sect. 5.4.2, the coherence of this observation is low and an interpretation of the time lags is, therefore, difficult. We do not discuss the lags in the soft state further.

Figure 5.12 shows the time lags of the transition observation with $\Gamma \sim 2.3$. We consider two pairs of energy bands, a high-energy pair of bands which resembles *RXTE* bands, and a lower-energy pair to explore behavior out of reach to *RXTE*. We show the corresponding coherence. Again, the time lags strongly depend on the reference band. The lag-frequency spectrum between the 5–8 keV and 2–4 keV bands shows the familiar, highly coherent power law-like hard lags (Cui et al., 1997b). At low energies (2–4 keV and 0.5–1 keV), there is a soft lag at most frequencies, albeit with low amplitude. In the 0.3–5 Hz range, the coherence is >0.9, while it drops to ∼80% at low frequencies where the power is reduced (see again the PSD map in Fig. 5.9). The time lag behavior is qualitatively similar to the phenomenology seen in the hard to soft transition of LMXB black holes (e.g., Wang et al. 2022, their Fig. 3f, and also Uttley et al. 2011, Kara et al. 2019, and De Marco et al. 2021), keeping in mind the different state terminology for these sources and the fact

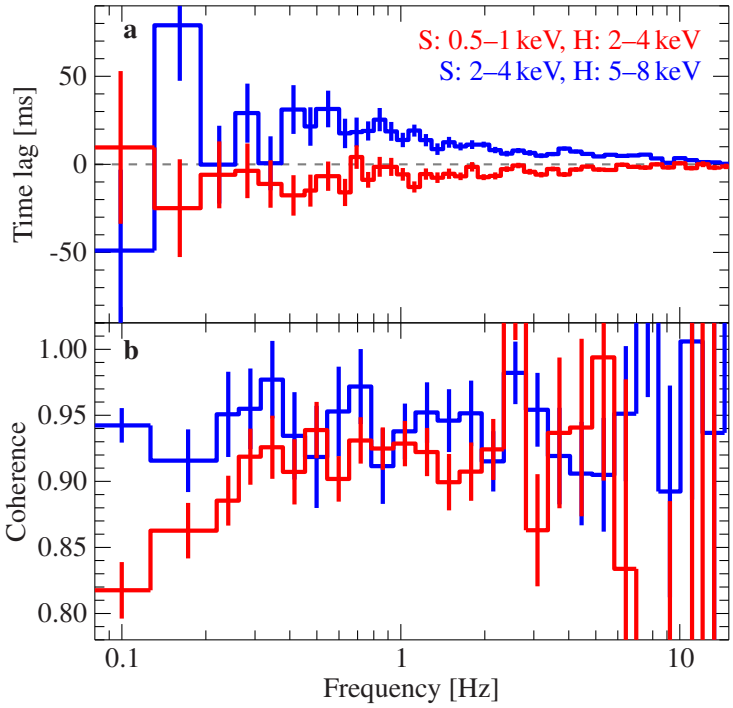

Figure 5.12: Time lag and coherence of observation 0100320110 at $\Gamma \sim 2.3$. Time lags at hard X-ray energies (blue) show power law-like hard lags at a high coherence. In soft X-rays (red), the time lags are predominantly soft with a relatively low amplitude at a coherence >0.9 in the 0.3–5 Hz range. At lower frequencies, the coherence is reduced.

that Cyg X-1 is on the lower branch of the q-diagram. A full interpretation of the soft lag involves complex modeling of the spectral-timing products (e.g., Ingram et al., 2019; Mastroserio et al., 2021; Kawamura et al., 2022), which is beyond the scope of this paper, and we concentrate on its empirical behavior here.

We show the time lags between different energy bands for the hard state observation with $\Gamma \sim 1.8$ in Fig. 5.13. For bands above 1.5 keV, highly coherent hard lags with the typical power law-like frequency dependence are seen, as has been extensively documented before (e.g., Nowak et al., 1999a). Moving to softer energies, the time lag drops towards or even below zero around 1 Hz, before it slightly increases again at lower frequencies. Interestingly, this feature appears simultaneously with a drop in coherence (see Fig. 5.13b) and increases in strength for softer energy bands. The frequency of the coherence drop coincides with the peak of the hard time lag around 1.6 Hz. Since the lag phenomenon is strongly correlated with the coherence, we avoid a naming that relates to the time lag only and refer to the whole structure as a *timing feature*. We focus the remainder of this section on the analysis of this timing feature in the hard state observation as this low-energy phenomenon has not previously been found in Cyg X-1.

To better understand the energy dependency of this timing feature, we show the lag-energy spectrum in Fig. 5.14. We choose frequency ranges according to the structure in the lag-frequency spectrum (Fig. 5.13a): the first frequency range (0.1–0.6 Hz) corresponds to the first peak, the second (0.6–1.2 Hz) covers the drop in time lag, and the third frequency range, (1.2–6 Hz), corresponds to the peak of the hard lag and the largest drop in coherence. Furthermore, the time lags are calculated for different reference bands. From the results found in Sect. 5.4.1, we choose bands dominated by accretion disk emission (0.5–1 keV), or by Comptonization (2–4 keV), as well as a broad reference

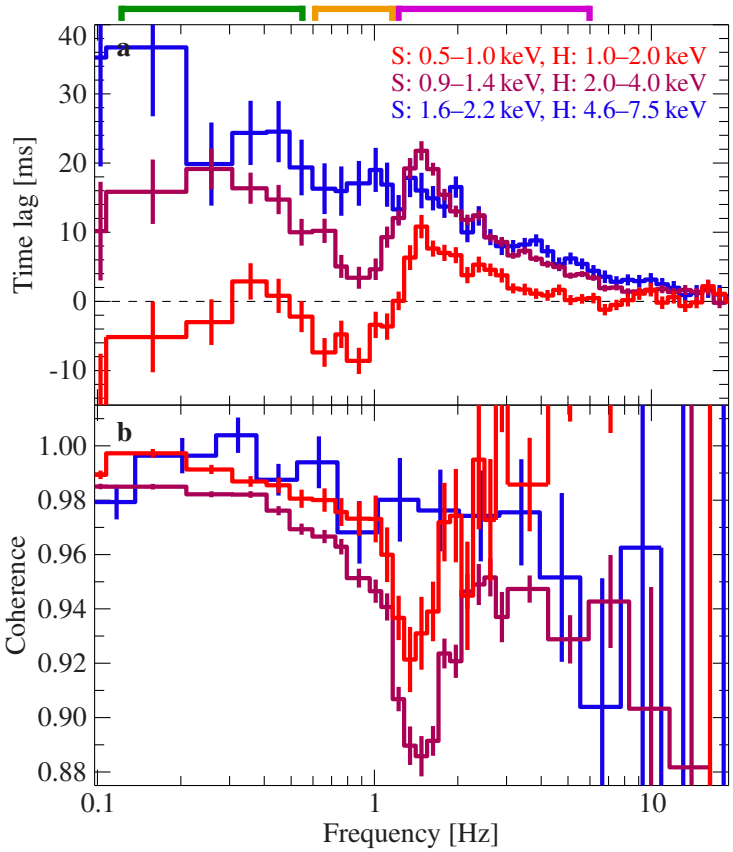

Figure 5.13: Lag-frequency and coherence spectra of observation 2636010101 in the hard state for various energy bands. **a)** Time lags between energy bands $\gtrsim$1.5 keV show the well-known power law-like behavior (blue line), while an abrupt change in time lag with soft X-ray data $\lesssim$1.5 keV is seen (red and purple lines). **b)** The coherence between high energy bands, when power law-like hard lags are seen, is close to unity. When the energy range is extended to below 1.5 keV, the coherence drops significantly between 1–2 Hz. Colored brackets on top denote the frequency ranges chosen for the lag-energy spectrum in Fig. 5.14.

band (0.5–10 keV).

The lag-energy spectrum in Fig. 5.14 shows hard lags at high energies in all three frequency bands. While the general behavior at these high energies is similar, the curvature of the hard lag changes for different frequencies. As in Kotov et al. (2001) or Mastroserio et al. (2019), we also do not detect a significant iron line lag feature. For each frequency band, we see that the overall shape of the lag-energy spectrum is very similar for the different reference bands and mainly the zero-crossing of the time lag changes.

Additionally, we detect soft lags at energies $\leq$1.5 keV, but only in the second frequency range (0.6–1.2 Hz). In the literature such low-energy soft lags are often referred to as "reverberation lags" and they are interpreted as light-crossing time delays between hard photons from the Comptonizing medium and soft photons from the accretion disk. A prediction for reverberation lags is that they are also present at higher frequencies (e.g., Ingram et al., 2019). This has also been seen, e.g., in observations of GX 339−4 (Uttley et al., 2011). (see also Ingram, 2023, and Sect. 4.2).uch a behavior is not found in the *NICER* observation with $\Gamma \sim 1.8$. Therefore, the low-energy soft lag in the 0.6–1.2 Hz range is likely not due to reverberation.

In Fig. 5.15, we show a two-dimensional map of the time lag depending on energy and frequency. Again, the maps are shown for the different reference bands and include the PSD map to allow for

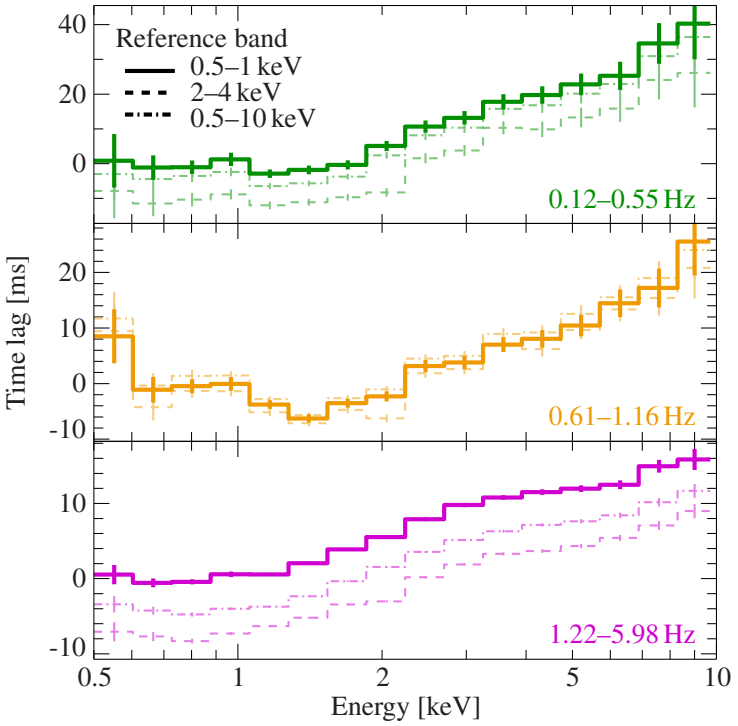

Figure 5.14: Lag-energy spectra of observation 2636010101 in the hard state. Frequency ranges are chosen which trace the timing feature (colored brackets in Fig. 5.13). The low-frequency range, 0.1–0.6 Hz, shows hard lags. The frequency range 0.6–1.2 Hz during the "dip" in the lag-frequency spectrum shows an upturn at low energies (soft lags). This upturn vanishes at higher frequencies, 1.2–6 Hz, which covers the peak of the timing feature. Solid, dashed, and dash-dotted lines denote spectra for a broad, and two narrow reference bands.

a better comparison. The time lag peak of the timing feature can be identified as a red or blue stripe-pattern at around 1.6 Hz, depending on if we use the low- or high-energy reference band. As can be seen in comparison with the PSD, its peak coincides with the frequency range where the two variability components L_1 and L_2 overlap and does not depend on energy. As mentioned previously, the peak of the feature is a hard lag, meaning the hard photons lag the soft reference band, and seen as a positive time lag when using a low-energy reference band (red stripe in Fig. 5.15, *bottom-right*). As expected, the sign of this lag changes to a negative lag if a high-energy reference band is used (blue stripe in Fig. 5.15, *bottom-left*), but still remains a hard lag (now the soft photons come before the hard reference band).

We note that lag maps can only be reliably interpreted when the time lags are well constrained and when the coherence is well constrained. Using the same approach as for the coherence map in Fig. 5.11, we set pixels to black where the relative uncertainty of the coherence is >50%. The coherence is $\gtrsim$70% in the frequency range of the timing feature (1–2 Hz) and near unity outside of this range.

For completeness, we also derive a time lag map for a broad reference band (0.5–10 keV; Fig. 5.15, *top-right*). As is also the case for the coherence map based on a broad reference band (Fig. 5.11, *bottom*), it is very similar to the time lag map for the low energy reference band, showing a positive time lag for the feature at high energies. In addition a negative lag at lower energies appears. As discussed in Sect. 5.4.2, this is an effect of the detector's effective area, which peaks near 1.5 keV. In case of the time lags, this peak of the effective area determines the energy of zero-crossing of the lag. We emphasize again that for the physical interpretation of the absolute value of the time lag,

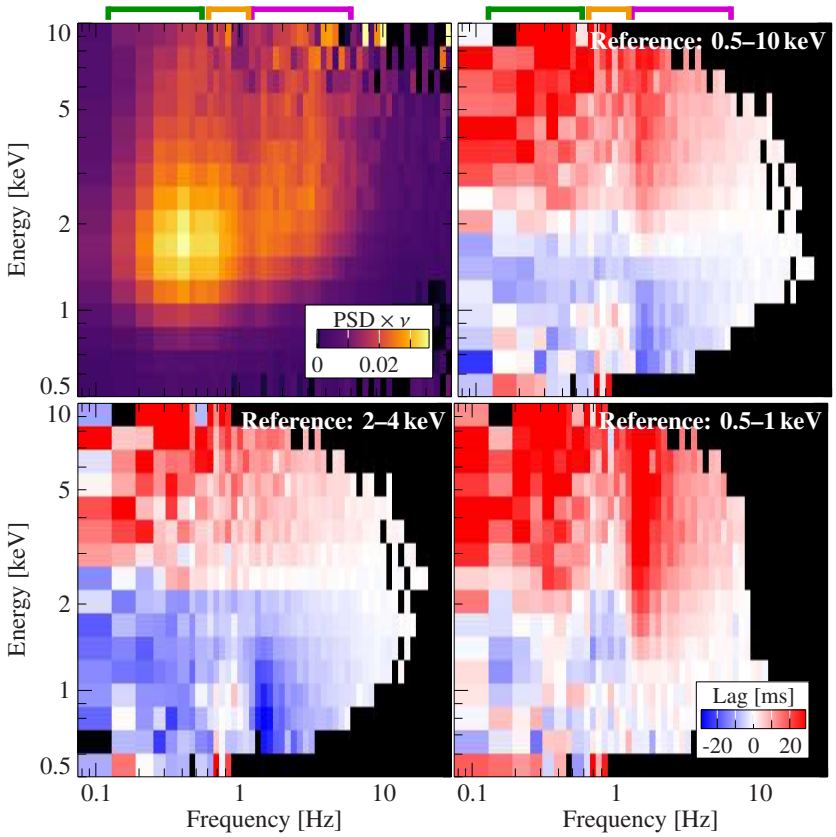

Figure 5.15: Energy-resolved time lag maps of observation 2636010101 in the hard state. The maps are calculated between small energy bins and three reference bands, written in the top right corner of each plot. For reference, we also show the power map in the top left panel. Pixels where the coherence has an uncertainty larger than 50% of its value are set to black. Colored brackets on top denote the frequency ranges chosen for the lag-energy spectrum in Fig. 5.14.

it is important to understand the variability process that dominates in the reference band. Due to the influence of the effective area, interpreting absolute time lag values using a broad reference band is particularly challenging when time lags are compared across different instruments, as the relative contribution of variability to the broad reference band changes. We will therefore focus our interpretation on the soft (0.5–1 keV) reference and hard (2–4 keV) subject bands, corresponding specifically to where the emission from the accretion disk and from the Comptonizing plasma, respectively, dominate.

In order to rule out an instrumental origin of the timing feature, we performed a number of detailed tests adopting different selection criteria, such as selecting only one continuous data segment (to exclude potential time shifts between good time intervals) obtained during International Space Station night with a low undershoot range. Even with the most conservative data extraction cuts, the timing feature is visible in the data. We therefore exclude an instrumental origin.

5.5 Discussion

Previous X-ray timing missions which performed monitoring campaigns of Cyg X-1 include *Ginga* (Miyamoto et al., 1988), *EXOSAT* (e.g., Belloni & Hasinger, 1990), *RXTE* (e.g., Cui et al., 1997b; Nowak et al., 1999a; Revnivtsev et al., 2000; Pottschmidt et al., 2003; Axelsson et al., 2005, 2006; Grinberg et al., 2014), *AstroSAT* (Misra et al., 2017; Maqbool et al., 2019), *XMM-Newton* (Lai et al., 2022), and *Insight-HXMT* (Zhou et al., 2022). Most of these missions have limited sensitivity to Cyg X-1's disk emission, being limited to the hard X-ray regime above 1.0–2.7 keV. The extension to softer X-rays provided, e.g., by *NICER* and *XMM-Newton* is, however, essential to understand the accretion disk variability, which contributes below ∼2 keV (see Sect. 5.4.1), and its connection to the Comptonizing plasma. However, due to the brightness of Cyg X-1, *XMM-Newton* observations can be affected by telemetry drop outs and suffer from pile-up. As a result, *XMM-Newton* spectral-timing studies with soft X-ray coverage is challenging and limited to Cyg X-1's fainter hard state[11]. Work with *XMM-Newton* has mainly concentrated on the timing effects introduced by the stellar wind (Lai et al., 2022).
The data from the *NICER* monitoring give a unique opportunity to analyze the general spectral-timing behavior of Cyg X-1 down to 0.5 keV for all spectral states for the first time. In the following, we discuss our spectral-timing results presented in the previous section and put them into context with previous monitoring campaigns. We start in Sect. 5.5.1 with a general overview of the variability behavior, followed by an overview of the the coherence behavior in Sect. 5.5.2 and a discussion of the time lags in Sect. 5.5.3.

5.5.1 Variability Components in the Power Spectrum

In the hard state, the high-energy PSDs of Cyg X-1 exhibit two or three prominent Lorentzians, which are well studied (see, e.g., Nowak, 2000; Grinberg et al., 2014, and references therein). The dominant variability component at around 2–6 keV is called L_1, while L_2 is dominant at energies $\gtrsim$10 keV (Grinberg et al., 2014). In order to be able to interpret the physical origin of these components, we need to understand the processes that are dominating the flux at each energy. In particular, by extending the energy band to below 2 keV, where the accretion disk emission dominates, we are able to study the contribution of the disk to the variability.
In Sect 5.4.1, we showed that the peak frequency of the L_1 and L_2 Lorentzians is independent of the energy. This result supports the interpretation that the Lorentzian components represent individual variability components each of which has a unique physical origin. The total variability seen is the superposition of these independent components. In the following, we show that the data are consistent with the interpretation that L_1 originates in the accretion disk and is then modulated by Comptonization, while L_2 can be directly associated with the Comptonized medium. For the strongest variability component in the *NICER* energy range, L_1, we find that it peaks around 1.7 keV in strength, while also contributing significantly to the variability above 3 keV. From our model fits (Fig. 5.9), we have seen that Comptonization dominates the emission above ∼1.5 keV. Together with the fact that L_1 is also strong above 3 keV, where the disk contribution to the flux

[11] For the brighter states of Cyg X-1, the only option is to use the modified timing mode of the EPIC-pn cameras (Duro et al., 2011), which, however, ignores data <2.8 keV.

is negligible, we conclude that this component has to be connected to the Comptonizing plasma. Below 1.7 keV, L_1 is the main source of variability, although it drops in strength. The peak strength of L_1 lies in the energy band where accretion disk emission and Comptonization both contribute roughly equally. This behavior suggests that at least part of the variability in the accretion disk contributes to L_1, in agreement with earlier work by Wilkinson & Uttley (2009), who proposed that the variability of the low-frequency Lorentzian, L_1, originates in an unstable accretion flow in the disk. A process such as propagating fluctuations, which connects the intrinsic disk variability with the emission of the Comptonizing plasma, may be a physical model to explain this behavior (see Lyubarskii 1997, Kotov et al. 2001, Ingram & van der Klis 2013, and Rapisarda et al. 2017 for an application to Cyg X-1).

In contrast, we have shown in Sect. 5.4.1 that the strength of L_2 decreases at energies below 2 keV and that it only contributes significantly above ∼1.5 keV. This suggests that L_2 is due to processes in the Comptonizing plasma. This interpretation is also consistent with *RXTE* data, which show that L_2 is the dominant component above 10 keV (Grinberg et al., 2014), and *Insight-HXMT* data shown by Zhou et al. (2022, their Fig. 11), where L_2 continues to be visible up to ∼90 keV.

In the soft state, the variability properties fundamentally change. Red noise dominates the PSD (see Fig. 4.3, and, e.g., Cui et al. 1997a; Gilfanov et al. 2000; Churazov et al. 2001; Axelsson et al. 2006) and the variability strongly increases with energy, peaking above 7–10 keV (see Sect. 5.4.1 and Grinberg et al. 2014; Zhou et al. 2022). At these energies, the soft state spectrum of Cyg X-1 shows a power law component, which is associated with non-thermal Comptonization (e.g., Wilms et al., 2006). As the contribution of the accretion disk is negligible at these energies, the variability in the soft state must be linked to the Comptonizing plasma. This is consistent with earlier work by Churazov et al. (2001) who linearly decomposed *RXTE* lightcurves into stable and variable components associated with the disk and Comptonizing plasma, respectively.

While the variability drops by almost a factor of 5 to around 6% rms at lower energies (0.5–1 keV), it is still significantly detected. At these energies, the fraction of the disk black body contributing to the spectrum is very high (see Fig. 5.9). Since only a low fraction of the soft emission is due to Comptonization, we propose that this low-energy variability in the soft state can also directly originate from fluctuations in the accretion disk. That the soft state has a lower level of RMS (∼6%) at low energies compared to the hard state (∼18%) would be consistent with the picture that a soft state disk is more stable than a hard state disk, as proposed by, e.g., Nowak (1995) and Churazov et al. (2001).

5.5.2 Coherence between Low and High Energies

The coherence of the variability of Cyg X-1 between energy bands above ∼2.5 keV has been investigated in detail with *RXTE*. The coherence is typically between 0.95 and 1.0 in the hard state (Nowak et al., 1999a; Grinberg et al., 2014). We find for all hard and intermediate state *NICER* observations in our sample that the 0.06 Hz to ∼10 Hz coherence is close to unity between bands chosen in the 2–10 keV range, consistent with these previous results.

With the *NICER* monitoring we can extend the coherence to the soft X-rays. This has not been studied before. As shown in Fig. 5.9, the low-energy ($\lesssim$1.5 keV) and high-energy bands ($\gtrsim$2 keV) can be identified with the accretion disk and Comptonizing plasma, respectively. For the $\Gamma \sim 1.8$

and $\Gamma \sim 2.3$ observations, we find that the coherence between these bands is close to unity (see Sect. 5.4.2), with the exception of a drop at 1–2 Hz, which we further discuss in the next section. The high coherence between the bands where disk emission and Comptonization dominate the flux strongly suggests a physical connection of the variability of these two components[12]. A model such as propagating fluctuations would explain such a connection. In the soft state ($\Gamma \sim 3.1$), the coherence map shows clearly that the high-energy variability, which we identified with Comptonization, is not coherent with respect to the variability at low energies any more. As there is significant RMS at a 6% level at 0.5–1 keV, the loss of coherence between low and high energies is statistically robust and not an effect of the low RMS. Therefore, regardless of the nature of the physical processes that produce the coherent variability in the hard state and the transition, this process changes in the soft state. Following the interpretation that the low- and high-energy variability is due to the disk and the Comptonizing medium, respectively, this result demonstrates that the variability from these regions is not linearly connected in the soft state. The variability information of the seed photons from the intrinsic disk fluctuations appears to be "washed out" in the process producing the red noise.

5.5.3 Evidence for an Abrupt Time Lag Change and Drop of Coherence in the Hard State

We measured time lags with respect to the soft energy band below 2 keV for three example observations at $\Gamma \sim 1.8$, 2.3, and 3.1 (Sect. 5.4.3). While the time lags of the $\Gamma \sim 2.3$ and 3.1 observations show overall consistent behavior with previous intermediate and soft state observations, respectively, in the hard state observation at $\Gamma \sim 1.8$, the time lags contain a strong feature around 1–2 Hz. That this feature has not been seen before is mainly due to the fact that, as a low-energy phenomenon, it was not accessible with *RXTE* and similar missions with hard X-ray timing capabilities. In our example observation (obs. ID 2636010101), the feature disappears when only taking into account photons above 1.5 keV (Fig. 5.13), where the well-known power law-like lag-frequency behavior is found instead (Nowak et al., 1999a). The feature is located at the frequency range where L_1 and L_2 overlap. It also coincides with a drop in coherence.

To further understand the origin of the feature, in the remainder of this section we will consistently use the 0.5–1 keV band as the reference band and the 2–4 keV band as the subject band. We note that these bands are mainly dominated by accretion disk emission, and Comptonized photons, respectively (see also Sect. 5.4.3).

We have systematically searched all *NICER* data of Cyg X-1 taken up to cycle 4 (until April 2022) to study the occurrence of the timing feature in detail. In general, the feature is not present in observations with soft spectra with $\Gamma \gtrsim 2.2$. In the following, we will show that observations with spectra harder than $\Gamma \sim 2.0$, on the other hand, show significantly different time lag behavior than

[12]The coherence only measures the degree of linear correlation and one has to be careful attributing causality based on it (Vaughan & Nowak, 1997). If the coherence is below unity, it is possible that the two time series are either uncorrelated (and have no physical connection) or that there is a non-linear transfer function which couples the signals. In the latter case, the coherence is low although there is an underlying correlation (see an example in Fig. 3.13). On the other hand, a coherence of unity does show that there is at least a linear correlation and we can make statements about causality.

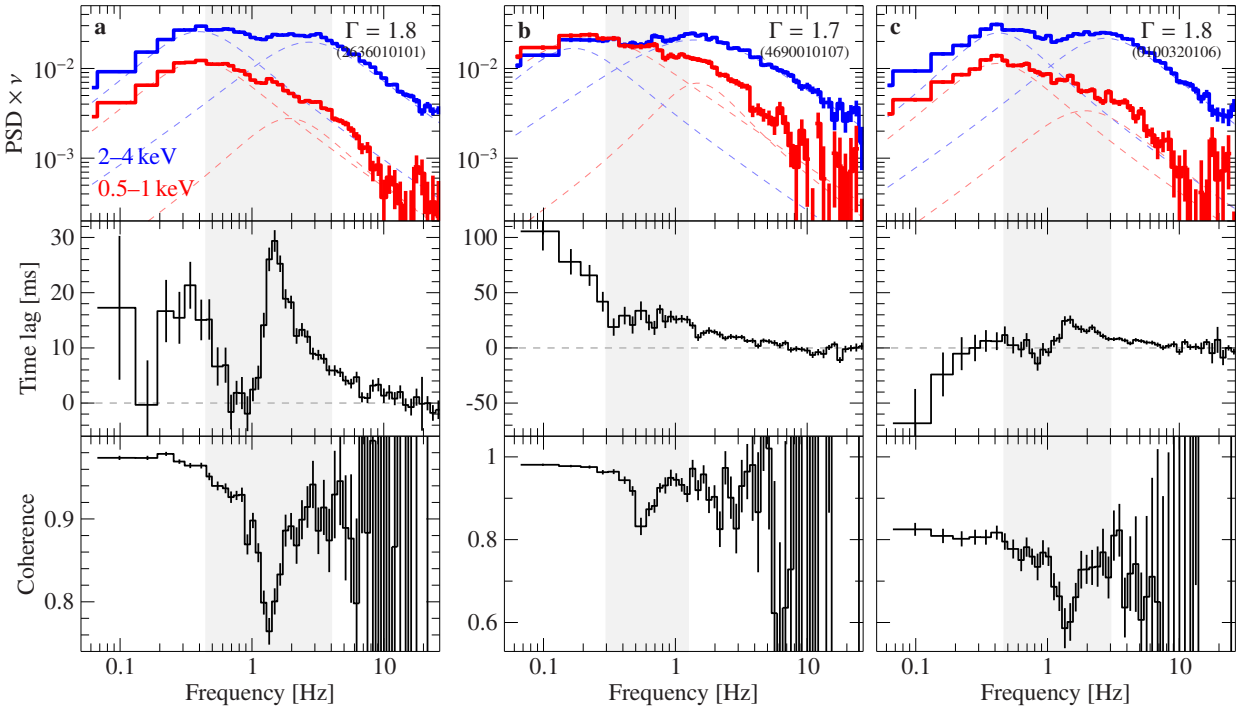

Figure 5.16: Timing behavior in the hard state of Cyg X-1. The time lag and coherence is calculated between the 2–4 keV and 0.5–1 keV bands. To guide the eye, the gray shaded region roughly indicates the frequency range of the feature, as indicated by the reduced coherence. **a)** Observation 2636010101 ($\Gamma \sim 1.8$) shows the clearest signature of the timing-feature in the *NICER* data. A localized ∼30 ms hard lag at ∼1.6 Hz is present at the overlap region of the L_1 and L_2 components. The amplitude of L_2 is reduced at soft energies. The coherence drops at the peak frequency of the timing feature's time lag, and appears asymmetric with respect to the time lag. **b)** Observation 4690010107 is slightly harder at $\Gamma \sim 1.7$ and shows coherent hard lags at low frequencies. At 0.5 Hz, a coherence drop indicates the presence of the timing-feature. The time lag shows a shelf-like structure at this frequency with an amplitude around 30 ms (note that the y-axis is different). **c)** Observation 0100320106 is affected by dipping and shows long soft lags at low frequencies at an overall reduced coherence. The timing-feature is blended into the lag spectrum with similar amplitude as in the other observations.

the softer ones, especially at frequencies $\lesssim$1 Hz.

In Fig. 5.16, we compare the power spectra, time lag, and coherence for three selected hard state observations and show that despite major differences in the lag-frequency spectra between those observations the feature occurs in all of them. All of the observations have in common that hard photons lag behind soft photons by approximately 30 ms at the frequency of the coherence drop. This drop in coherence is generally largest at the peak of the feature, albeit its shape is found to be different in these observations due to the low-frequency time lag behavior. In the hard state observation ($\Gamma \sim 1.8$) that we have shown in Sect. 5.4 and which represents the observation with

the strongest timing feature in the *NICER* data, the peak of the hard time lag and the strongest coherence drop is located at 1.6 Hz (Fig. 5.16a). The coherence drop appears asymmetric with respect to the time lag in the sense that the lag shows a sharp drop below the peak with a tail towards higher frequencies, while the coherence drop extends to lower frequencies.
The data shown in Fig. 5.16b (obs. ID 4690010107) were taken when Cyg X-1 was slightly harder ($\Gamma \sim 1.7$). Here, pronounced hard lags with a shelf-like structure are seen, resembling the shape found with *Ginga* (Miyamoto et al., 1992, their Fig. 1c) and *RXTE* (e.g., Nowak et al. 1999a or Grinberg et al. 2014, their Fig. 11). These structures are significantly less peaked compared to Fig. 5.16a. In the *NICER* data of Fig. 5.16b, a coherence drop can be seen at the frequency of the shelf, which is not apparent in the *RXTE* data of Cyg X-1 at higher energies (Grinberg et al., 2014, their Fig. 10). A similar coherence drop was found in GX 339−4 by Nowak et al. (1999b, their Fig. 6c–d), who used ∼2.5–3.9 keV and 10.8–21.9 keV bands. Due to the frequency match of the overlap region of L_1 and L_2, the lag shelf, and the coherence drop for Cyg X-1, the underlying process responsible for this shelf-like structure could be the same as for the timing-feature. We also note that the drop in coherence is at significantly lower frequency, roughly 0.5 Hz, compared to the previous observation and that, while the time lag shelf is rather broad, the absolute time lag is again around 30 ms.
Finally, Fig. 5.16c illustrates the variability behavior of one of the observations that shows strong "nose"-shaped color-color variations (obs. ID 0100320106, $\Gamma \sim 1.8$). As discussed in Sect. 5.3.3, these variations originate from absorption of X-rays in clumps of the stellar wind. During such absorption events, additional modulation of the X-ray variability by the absorbing foreground material imprints long soft lags at low frequencies and reduce the coherence (Lai et al., 2022). In Fig. 5.17 (*left*), we split the lightcurve of 0100320106 such that the color-color diagram of the observation is separated into a part covering the "nose" and a part that is not predominantly affected by dipping. Fig. 5.17 (*right*) confirms that dipping events produce very strong soft lags up to 200 ms at 0.1 Hz. In fact, this is a factor >5 longer than the ∼40 ms found by Lai et al. (2022). We can also confirm that these soft lags are more incoherent compared to the non-dipping part. The timing feature is prominently present in the non-dipping case. In this example, the timing feature blends with the time lag induced by the stellar wind, while its overall shape is very similar to Fig. 5.16a, again with a maximum hard lag of ∼30 ms.
Having established how the feature impacts the Cyg X-1 hard state data, we next quantify its frequency behavior for the different observations. By visually inspecting the *NICER* products for a peaked lag structure at the overlap region of the Lorentzians in combination with a coherence drop at the same frequency (see Appendix A for reference), we identify seven observations in the hard state ($\Gamma \lesssim 2.0$) where we confidently detect the feature. These observations are marked in Table A.1 and four example observations can be seen in Fig. 5.18. We then estimate the feature's frequency from the peak in the lag-frequency spectrum. As this is a manual process, we adopt a systematic uncertainty of 0.1 Hz. We find that the frequency of the feature is correlated with the peak frequencies of L_1 and L_2 (Fig. 5.19), with Pearson correlation coefficients of 0.95 and 0.99, respectively. Similar to the peak frequencies of the Lorentzians (Pottschmidt et al., 2003; Grinberg et al., 2014), the frequency of the feature increases as the spectral continuum softens (Fig. 5.20). These results indicate a connection between the feature and the two Lorentzians, which is also consistent with the fact that we do not find observations with a single-humped or red noise-like

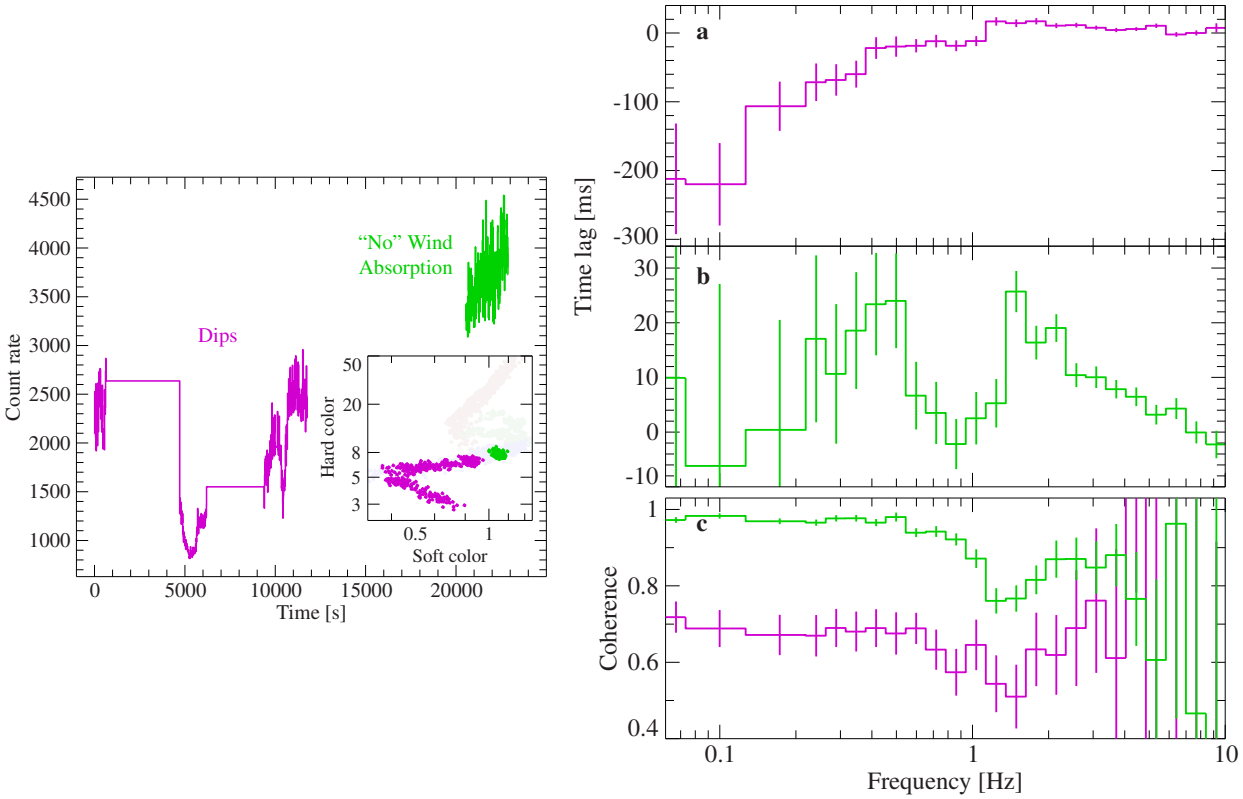

Figure 5.17: Separation of periods with and without dipping in observation 0100320106. *Left:* Lightcurve of the full observation colored by a cut that separates the color-color diagram (see inset, same bands as in Fig. 5.7, *left*) into a part that is strongly affected by dipping (magenta) and a non-dipping part (green). Colors were chosen to match Fig. 6 of Lai et al. (2022). *Right:* Lag-frequency spectra and coherence of Cyg X-1 between 0.5–1 keV and 2–4 keV. **a)** Data during dipping events show soft lags up to ∼200 ms. **b)** Data outside of dips, where wind absorption is low, show a strong change in time lag around 1–2 Hz. **c)** The coherence of the non-dipping data shows a dip at 1–2 keV. Data taken during dipping events shows an overall reduced coherence.

PSD where the feature is present.

In order to quantify this relationship between the timing feature and the Lorentzians further, we use the approach of Méndez et al. (2023, motivated by earlier work, e.g., Nowak et al. 1999b; Nowak 2000), who describe the variability of black hole candidates through the sum of incoherent multiple Lorentzian functions that have a constant phase lag $\Delta\phi(\nu)$ between the energy bands. In such a simple empirical model, we expect high coherence within the frequency band dominated by a single Lorentzian, and a decreased coherence in frequency bands where there are contributions by more than one variability component. We fit the data from observation 2636010101 using two broad and a zero-centered Lorentzians (Fig. 5.21). The model successfully reproduces the reduction in coherence in the overlap region of the L_1 and L_2 components (1–2 Hz). However, strong fit

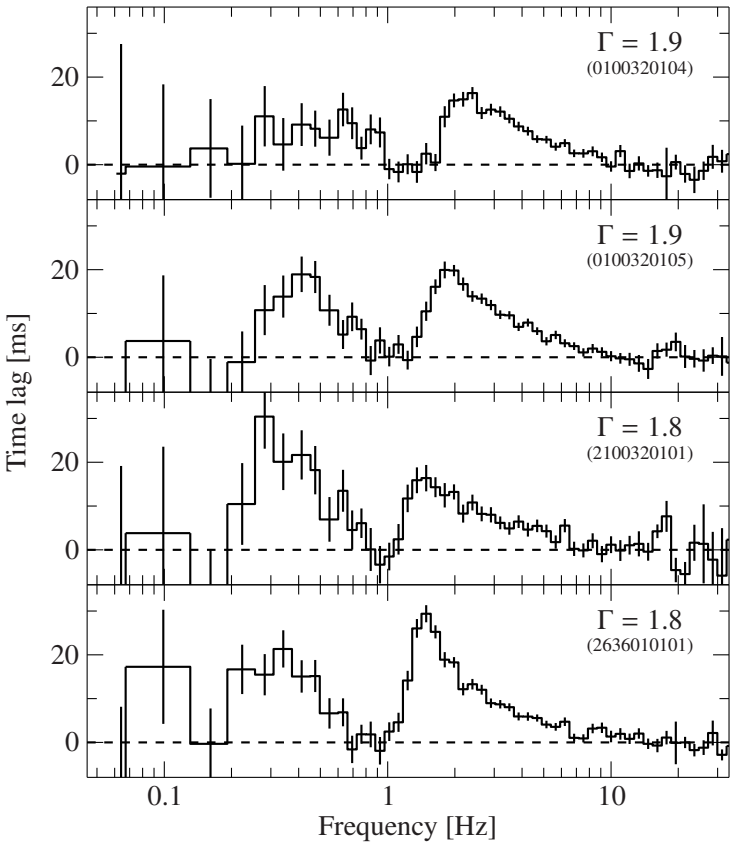

Figure 5.18: Evolution of the time lag with spectral hardness. The reference and subject bands are 0.5–1 keV and 2–4 keV, respectively. The spectra are ordered by photon index. The timing-feature at around 1–2 Hz increases in frequency as the source softens.

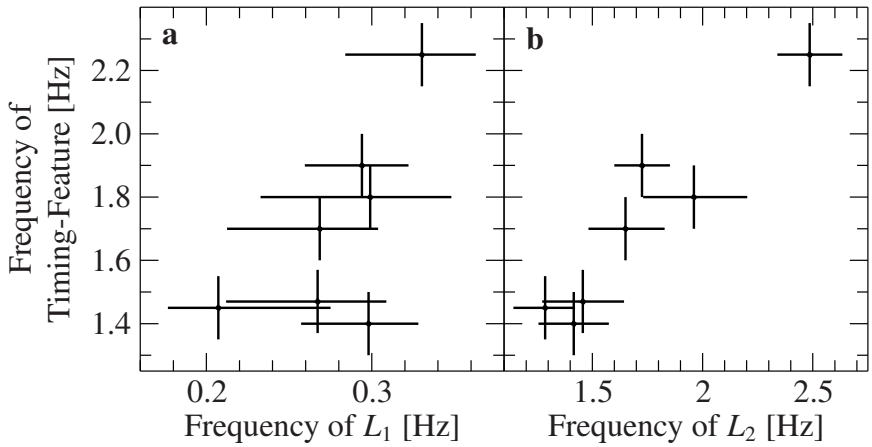

Figure 5.19: Frequency of the timing feature versus the peak frequencies of L_1 and L_2 for seven observations with a clear signature of the timing feature (marked in Table A.1). The frequency of the feature is defined as the time lag, we assume a systematic uncertainty of 0.1 Hz. Uncertainties on the Lorentzian frequencies and Γ are at the 90% confidence level. The frequency of the feature correlates positively with the position of the Lorentzians, which are known to increase in frequency as the source softens.

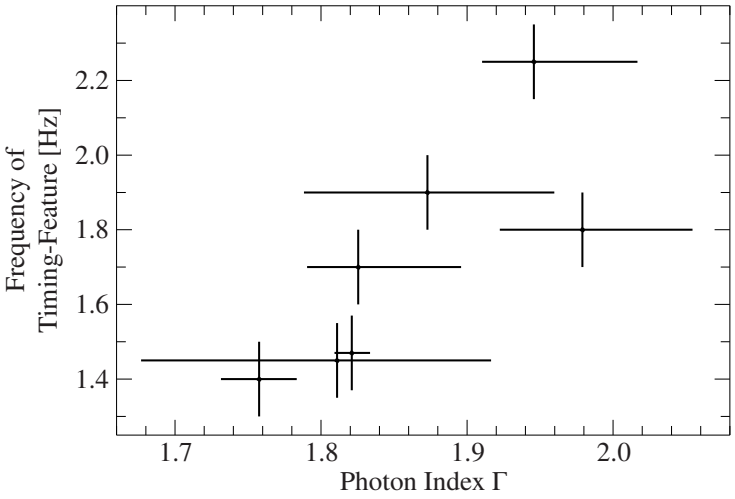

Figure 5.20: The frequency of the timing feature increases as Cyg X-1 softens.

residuals remain in the imaginary part of the cross spectrum and the 0.5–1 keV PSD at around 1–2 Hz and the fit is unable to describe the peaked lag feature (dashed line in Fig. 5.21d–e). Adding an additional Lorentzian component at 1.57 ± 0.04 Hz with a width of 0.703 ± 0.018 Hz improves the χ^2 from 1420 to 1066 while adding six free parameters (see Table A.2 for all parameters with uncertainties). The reduced χ^2 of our final model with four Lorentzians is 1.95 for 546 degrees of freedom. This model fits the imaginary part of the cross-spectrum better and, when evaluated on the lags, therefore also reproduces the abrupt lag change at 1–2 Hz.
Measuring all time lags with respect to L_1, i.e., setting $\Delta\phi(L_1) = 0$, we find that L_0 has a soft lag of $-7°$ (as this component is zero-centered, the phase lag cannot be transformed to a time lag). L_2 has a slight hard lag of $+11°$, which corresponds to 18 ms for the centroid frequency of L_2. In the additional narrow Lorentzian at 1.57 Hz, the 2–4 keV photons arrive with a long hard lag of roughly $+58°$ with respect to the 0.5–1 keV photons, corresponding to 103 ms. While this value may appear large, we re-iterate that the timing feature is most likely not due to reverberation (see Sect. 5.4.3) and that our phenomenological model assumes a constant phase relationship between L_1 and L_2. More realistic physical models are likely to impose more complex phase relationship between individual variability components. Such models may also explain the remaining residuals in the cross spectrum at around 0.4 Hz and 3 Hz that we do not attempt to fit here. Alternatively, the timing feature might also be a real, distinct physical feature, similar to the variability components discussed by Méndez et al. (2023), which were also only seen in the cross-spectrum but not in the PSD. It is, however, interesting to note that Rutledge et al. (1999) reported a QPO-like feature in the Cyg X-1 hard state power spectrum using *Ginga* data, which was also strongest at low energies, 2.3–4.6 keV, and had a quality factor of roughly 1, similar to what we find for the timing feature.

Time-series Modeling of the Timing Feature: Phase Wrapping Signature from a Low-Pass Filter?

The fact that the L_2 component becomes weaker relative to L_1 at low X-ray energies poses the question whether this attenuation can be due to a process acting as a low-pass filter. That such

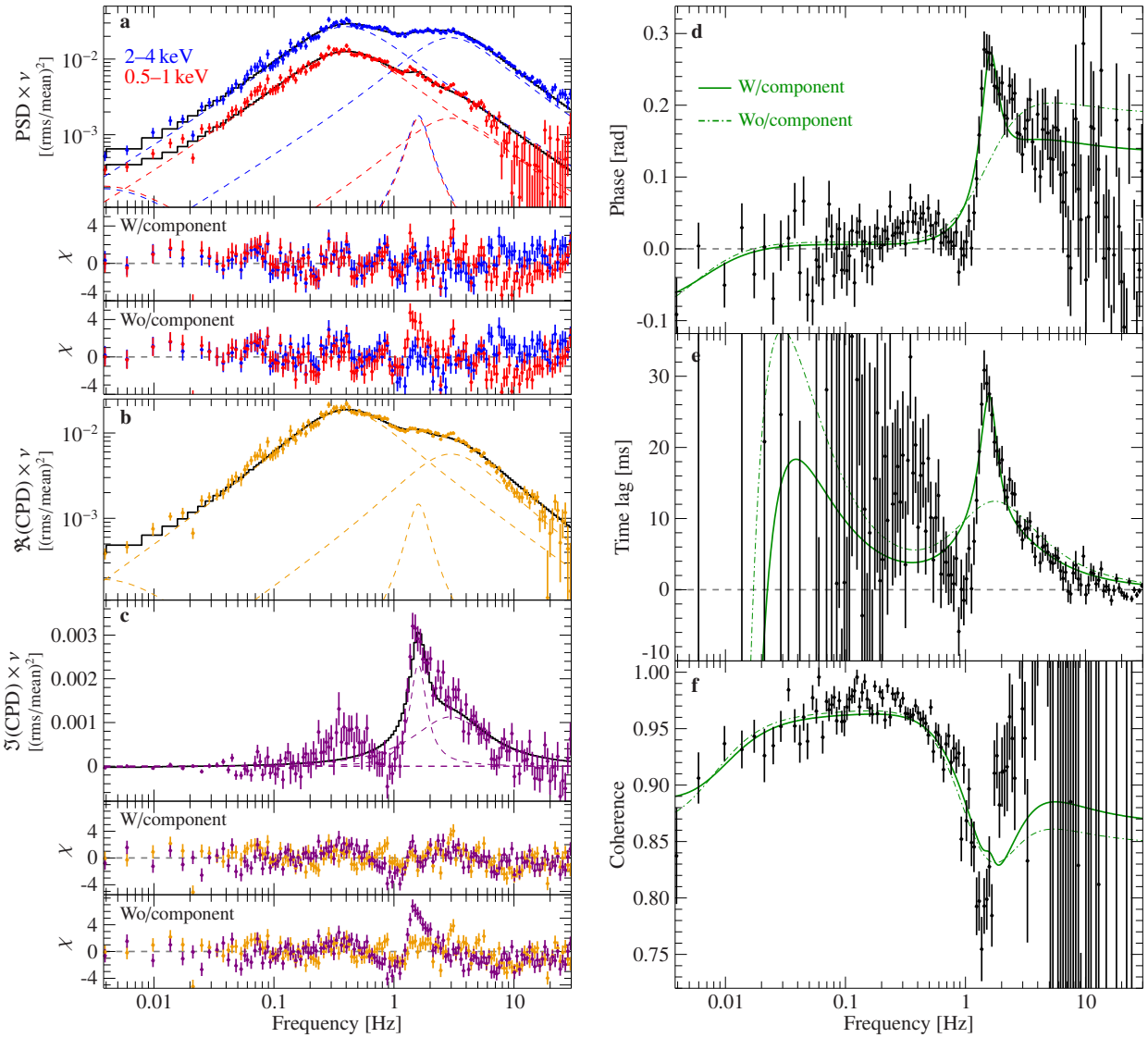

Figure 5.21: Simultaneous fit of power and cross spectra of Cyg X-1 for *NICER* observation 2636010101. The data can be modeled with three broad Lorentzians (one of them zero-centered) plus one narrow Lorentzian at 1.57 Hz (dashed lines). The total fit model is shown as a black line. The fit model with and without the narrow component evaluated on the lags and coherence is shown as a solid and dash-dotted green line, respectively. **a)** Power spectral density and fit residuals with and without the narrow component at 1.6 Hz. **b)–c)** Real and imaginary part of the cross spectrum (soft band: 0.5–1 keV, hard band: 2–4 keV). The additional Lorentzian is very significant in the imaginary part. **d)–e)** Model evaluated (not fitted) on the phase and time lag spectra. The model without the narrow component is shown as red dashed line. **f)** The coherence spectrum changes only slightly when including the narrow component. The dip at the overlap of L_1 and L_2 emerges because the Lorentzians are assumed to be incoherent with respect to each other.

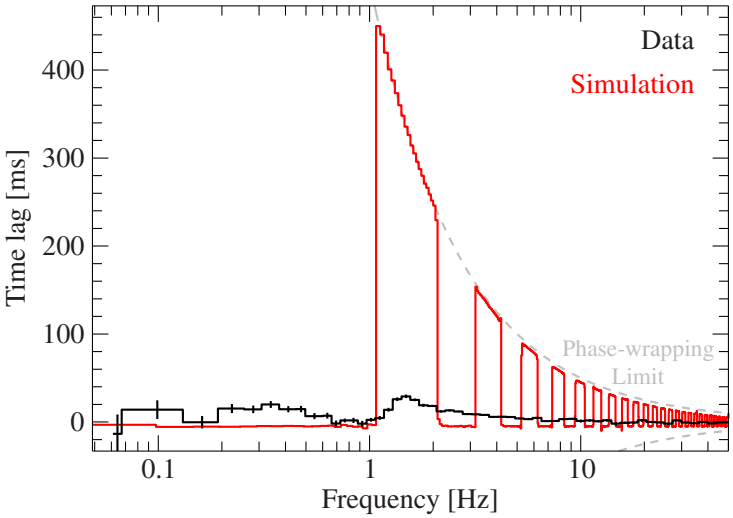

Figure 5.22: Timing response of an ideal moving average low-pass filter (top-hat function). The black histogram shows the data of Cyg X-1 from *NICER* observation 2636010101.

damping processes may be at work has been noted in multiple studies in the past. Kallman et al. (1987) propose that light travel and recombination time scales in winds can act as low-pass filters (see also Vrtilek et al., 2008) with the filter cut-off frequency indicating the size of the ionized region. Other studies attribute the Comptonized plasma to act as a low-pass filter (Cui et al., 1997a), determined by the viscous timescale of a hot inner flow in the last stable orbit, which may explain the drop in in the PSD at high frequencies (Done et al., 2007).

I will use the most simple example of a finite impulse response low-pass filter, the moving average, to simulate the data. Mathematically, it can be described as a rectangle function and is therefore also called a "boxcar" or "top-hat" filter. The transfer function of a moving average filter of length L is $H(\nu) = 1/L \cdot \sin(\pi\nu L\Delta t)/\sin(\pi\nu\Delta t)$. In general, all physical filters imprint a phase lag on the filtered signal. For the moving average, phase wraps occur at $H(\nu) = 0$, which is shown in Fig. 5.22.

To adapt this filter to our example hard state observation, I use the 2–4 keV PSD best-fit model to simulate the input of the low-pass filter using the Timmer & Koenig (1995) algorithm. This lightcurve represents the source-intrinsic high-energy signal and, therefore, no Poisson noise is added. The source-intrinsic low-energy lightcurve is then obtained by applying the low-pass filter on the input. By choosing a length of 96 bins, which equals roughly 1 s, I can move the first phase wrap to the position where we see the timing feature in the data. Since it has significantly lower amplitude (∼30 ms) than the phase wrapping limit (312 ms for 1.6 Hz), it is necessary to dilute the filter. Mixing 20% of the original lightcurve into the filtered lightcurve reduces the amplitude of the lag because this fraction of the variability has a time delay of zero.

Next, I simulate the detection process. I scale the count rate to match the ARF ratio of the 0.5–1 keV and 2–4 keV band, and re-normalize to match the lower RMS of the low-energy data. I then apply independent Poisson noise to both lightcurves. This is done by drawing Poisson distributed random numbers for each bin count (not count rate). Finally, I compute the timing products between the two simulated lightcurves.

Figure 5.23 shows that I can qualitatively and quantitatively reproduce the rising flank of the time lag. Also the dip in the coherence is reproduced by this approach. However, the low-energy

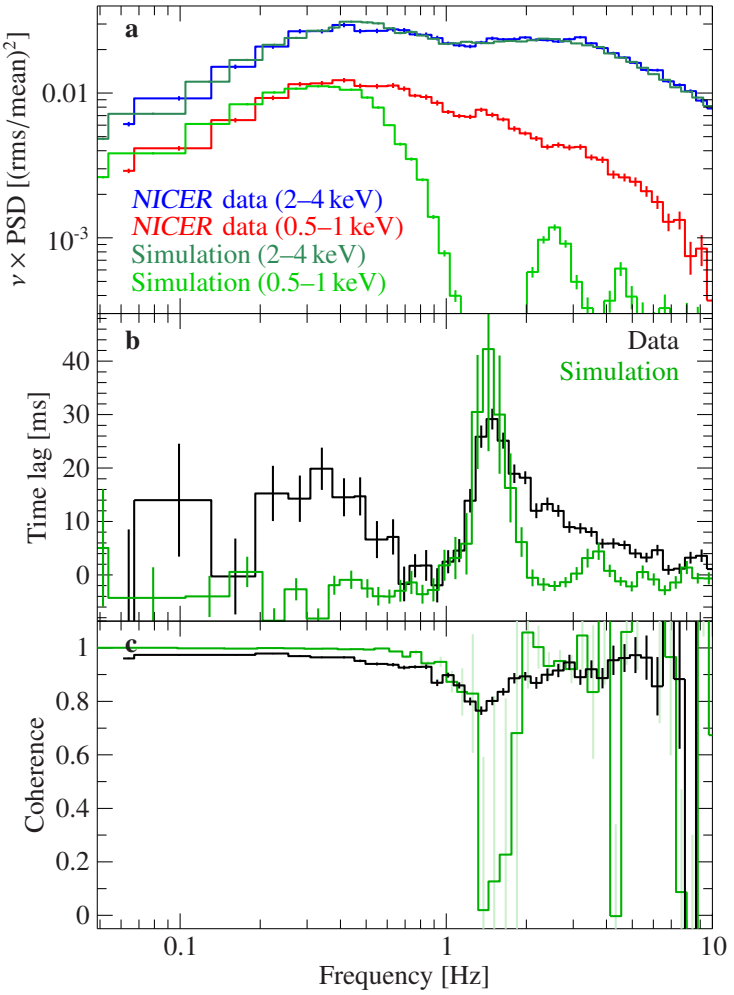

Figure 5.23: Timing response of a diluted moving average low-pass filter. **a)** Simulated and measured PSDs (observation 2636010101). The model fails to correctly predict the high frequency variability at low energies. The wiggles in the PSD of the 0.5–1 keV simulation are due to the wings of the sinc function that allow some frequencies to pass at a reduced magnitude. **b)** The filter process induces a phase wrap, which results in a time lag and a **c)** coherence drop, which is similar to our observed timing feature.

lightcurve misses significant power at high frequencies, which is a major drawback of this model. This might point to an additional variability source at high frequencies, which is not connected to the process that acts as a low-pass filter. It could also be possible that the boxcar filter is too simple, and a filter is needed which lets more high-frequency variability pass.

5.6 Summary and Conclusions

The second part of my thesis studied 211 ks of *NICER* data from Cyg X-1 across all spectral states to study the spectral-timing behavior below 1 keV. This energy range is important to understand the contribution of the accretion disk to the variability, however, it has not been comprehensively addressed in previous monitoring campaigns. We find that significantly more complex phenomenology emerges at soft X-rays compared to the harder X-ray bands. When investigating the overall state evolution, for instance, we find that the color-color diagram of

Cyg X-1 splits up into a zig-zag track when soft energies are included (Sect. 5.3.3).
The properties of the power spectrum are highly energy dependent (Sect. 5.4.1). Consistent with earlier results, the hard state PSD has two main variability components, which are commonly described with Lorentzian functions. The first Lorentzian, L_1, dominates the low energy variability where accretion disk emission contributes most photons, while the second Lorentzian, L_2, is the dominant component at high energies where Comptonization dominates the X-ray spectrum. The second component is suppressed at low energies.
We directly compare the variability with the disk contribution, as inferred from the energy spectrum, and show that the variability at low and high energies has dominant contribution from the disk and Comptonized plasma, respectively. The energy dependency of L_1 and L_2 is therefore consistent with an interpretation in which the low-frequency Lorentzian originates from fluctuations in the accretion disk being modulated by Comptonization, while the high-frequency Lorentzian is solely related to the Comptonized plasma.
Both components shift to higher frequencies as Cyg X-1 softens (Pottschmidt et al., 2003; Grinberg et al., 2014). The variability also shifts to higher energies in the state transition, clearly showing that the Comptonized emission becomes the main mechanism associated with the variability. The soft state of Cyg X-1 shows very strong red noise variability at high energies, with the flux exclusively coming from the Comptonized emission. At low energies, the source still shows a low but significant level of variability. We note that the fact that the low-energy variability likely comes directly from the accretion disk and has lower level of variability compared to the hard state is consistent with the picture that the soft state accretion disk is relatively stable.
Using energy-resolved coherence maps, in Sect. 5.4.2 we investigated the correlation of the variability between low and high energies. Overall, the hard and intermediate states each show a coherence of unity or close to unity. This changes in the soft state, where the high-energy red noise is incoherent with low-energy variability. In the propagating fluctuations paradigm, the physical process linking the accretion disk fluctuations and Comptonized emission in the hard and intermediate states is broken up in the soft state – the propagating fluctuations appear to not reach the emitted red noise variability from the Comptonized plasma in the Cyg X-1 soft state.
We also find a low-energy timing phenomenon in the hard state (Sect. 5.5.3), which can be characterized by (i) a sudden jump from a soft to a hard time lag at around 1–2 Hz, (ii) a drop in coherence at the peak frequency of this hard time lag, (iii) a position in between the two broad Lorentzians in the power spectrum, and (iv) a strong energy dependence as it vanishes when bands $\gtrsim$1.5 keV are considered. The feature increases in frequency as the source moves into the transition, together with the Lorentzians. If other sources of lags are present, such as the well-known power law-like hard lags, the feature is blended into the lag spectrum and emerges as a shelf-like structure. We do not find the feature in observations with a single-humped power spectrum softer than $\Gamma \gtrsim 2.3$.
We find that similar features are not only present in the variability of the HMXB Cyg X-1, but also in data from hard state observations of LMXB black holes. Figure 5.24 shows a comparison of the Cyg X-1 data to observations of MAXI J1820+070 (obs. ID 1200120268), MAXI J1348−630 (obs. ID 2200530129), and AT 2019wey (obs. ID 3201710115), identified using the products of Wang et al. (2022). These data show the exact same characteristics as the data from Cyg X-1, that is, a reduced amplitude of L_2 at low energies, a time lag in the overlap region of the Lorentzians, and a drop in coherence. This comparison provides evidence that the timing feature is a general property

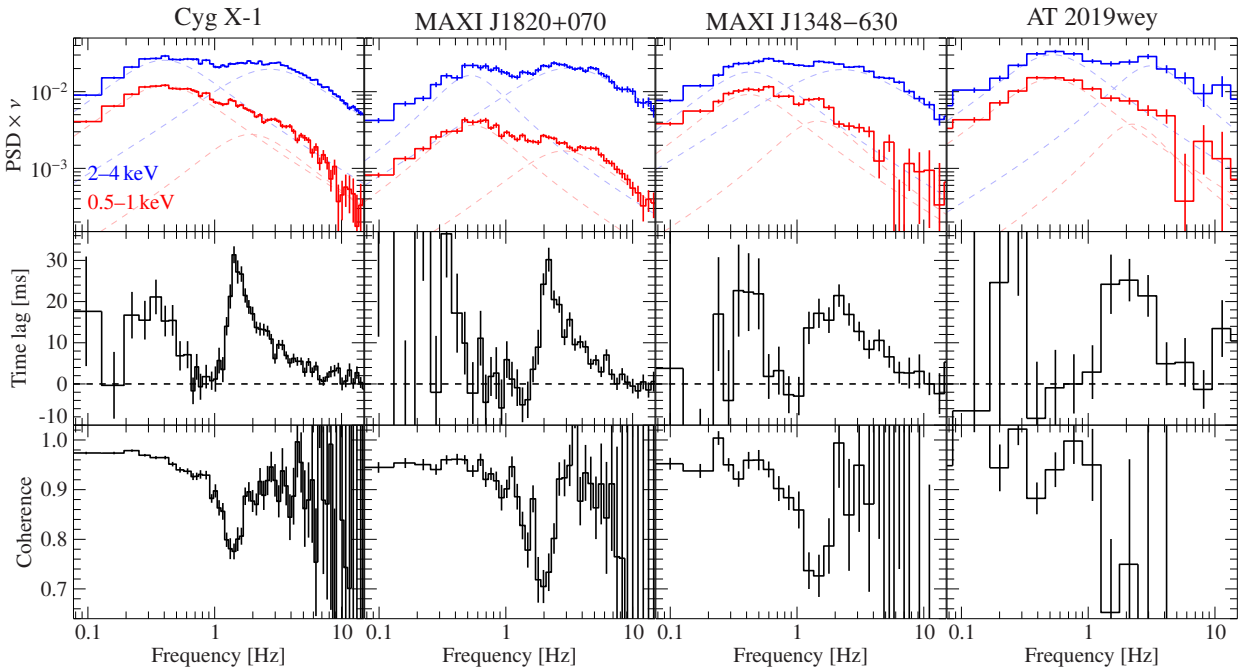

Figure 5.24: Comparison of the timing-feature in Cyg X-1 to similar data for the low-mass X-ray binaries MAXI J1820+070, MAXI J1348−630, and AT 2019wey. In all four observations, a reduction of L_2 at low energies, a time lag jump between soft (0.5–1 keV) and hard (2–4 keV) photons, and a coherence drop in the overlap region of the Lorentzians can be seen. The similarity of the data suggests that the timing-feature is a ubiquitous property of accreting black hole binaries.

intrinsic to both high- and low-mass X-ray binary black holes. It is interesting to note that for the sources where reliable mass and distance estimates are available, such that they can be placed on the q-diagram, the observations showing the feature appear to be located on the lower branch of the q-diagram (see blue pentagon and green triangle in Fig. 5.4). Further research is required to systematically study the occurrence of the feature in LMXBs.

Since this complex lag behavior is found in both HMXBs and LMXBs, the Lorentzian components and the feature are not due to effects from the interaction of the X-rays with the stellar wind. By simultaneously fitting the power and cross spectra (Sect. 5.5.3), we showed that the feature can be modeled as a relatively narrow Lorentzian component in between the two well-known Lorentzians constituting the broad band noise. While the simplified modeling in Sect. 5.5.3 did not assume any relationship between the Lorentzians, in reality these components show correlated behavior, e.g., they shift together in frequency when the source softens (Pottschmidt et al., 2003; Grinberg et al., 2014). However, they are not perfectly coupled, as a drop in coherence is observed in the overlap region (Nowak, 2000, and Sect. 5.4.2) and because the strength of each Lorentzian with energy is different between the components (Grinberg et al., 2014, and Sect. 5.4.1).

If the Lorentzians are sufficiently coupled, the timing feature might be due to a beat between the two broad Lorentzians, similar to, e.g., models invoked to describe kHz QPOs in accreting neutron

stars (e.g., Alpar & Shaham, 1985; Lamb et al., 1985; Ingram & Motta, 2019, and references therein), although we note that kHz QPOs show much higher quality factors than L_1 or L_2, and therefore physical models for them are likely not applicable to black hole candidates. The beat frequency is roughly given by the difference between the centroid frequencies of the two Lorentzians, that is, $\nu_{L_2} - \nu_{L_1}$. For our example hard state observation, the difference frequency of L_2 and L_1 matches the frequency of the Lorentzian representing the timing feature in Sect. 5.5.3. We emphasize that this beat would not necessarily mean the presence of a separate distinct physical process, such as an oscillation at a characteristic frequency, creating the feature. Instead, the beat arises from the interaction of the variability processes constituting L_1 and L_2.

It is beyond the scope of this chapter to develop a beat model that describes the observed coherence loss and lags in order to prove the beat frequency hypothesis. However, independent of the interpretation of the feature, the detection in both types of accreting stellar mass black holes X-ray binaries has intriguing implications. In particular, we stress that the soft lag at low energies associated with the timing feature cannot be interpreted as reverberation lags, as shown in Sect. 5.4.3. Instead, this detection requires a modification of the general picture on how soft lags can be created, at least for the observations which show this feature.

Part II:

The Synergy of Observations and Simulations

Chapter 6

Simulation of X-ray Telescopes

In Part I of this thesis, I analyzed the variability processes of Cyg X-1. The scientific analysis discussed there was primarily data-driven, with the goal of inferring the physical properties of the source from observations with an existing telescope. The second part my thesis is about the synergy of X-ray astronomical observations and the theoretical simulation-based modeling of the detection process. In this chapter, I emphasize the necessity to have a sophisticated simulator of X-ray telescopes available. In Ch. 7, I report on the discovery of an X-ray flash from a nova and show that simulations are highly complementary to a data analysis – in this case they are even necessary to infer the astrophysical parameters.

I outlined in Sect. 3.2 that X-ray telescopes and detectors have been developed since the 1950s, starting with early Geiger and proportional counters, to CCDs and microcalorimeters. In the past decades, computer technology has advanced rapidly (which has been popularized as "Moore's law", named after an observation by Moore 1965 on the increase of the number of components and reduction of overall costs of an integrated circuit). In order to give an example, a standard SIXTE simulation (introduced below) of the *Athena* WFI observing the Tycho supernova remnant for 1 ks requires around 10^8 floating point operations per second[1] (100 MFLOPS). In 1975, such a simulation would have needed a supercomputer, such as Cray-1 which achieved 138 MFLOPS (Russell, 1978). In 1999, a standard computer with an Intel Pentium III processor could deliver around 1 GFLOPS[2] (Diefendorff, 1999) and a basic simulation like this would have become feasible. Today, simulators offer an excellent opportunity to support the hardware development, the calibration, and ultimately also the operation of the mission, making the overall development easier and more cost-efficient. In this chapter, I will present three key application fields to show why simulators are an integral constituent and a significant investment in the budget of an X-ray mission.

First, simulators are vital during the *development* phase of an X-ray mission. As proposed missions are only funded if it can be proven that the scientific questions can be confidently answered, simulators are necessary to solidify the science case. Furthermore, simulations are needed to understand the impact of changes on the scientific capabilities of the mission. Changes in the detector, the

[1] The number of floating point operations was inferred with the `perf` tool (`fp_arith_inst_retired.scalar_single`, `fp_arith_inst_retired.scalar_double`) and yielded 6.8×10^9 operations taking 70 s on an Intel i5 CPU (1.6 GHz).

[2] 4 FLOPs per cycle at a clock speed of 450 MHz (Diefendorff, 1999).

mirrors, or the spacecraft have to be studied without building new hardware components for each configuration. With a sophisticated simulator one can study the impact of hardware changes on science observations efficiently and at low costs. In addition, simulated data are often needed to test data processing and analysis software pipelines during the development phase.

The second major application of simulators is to assist in the *calibration* of the sensors. On ground, X-ray telescopes and detectors are typically calibrated using X-ray beam lines (see, for instance, Freyberg et al. 2005 for the calibration of X-ray missions in the PANTER facility). Once in space, the calibration relies on on-board radioactive probes or relatively stable and well understood astrophysical sources. The flux calibration is often done using the Crab (Kirsch et al., 2005), while supernova remnants, such as N132D or 1E 0102.2−7219, are used for energy calibration due to their strong emission lines (Plucinsky et al., 2017). However, it is important to understand the calibration of an instrument already before launch, often even before a prototype is built, and a simulator can assist in that.

Third, simulators are used during the *operation* phase of a spacecraft. They are crucial for *proposal planning* to show the feasibility of the proposed science. They can be used for further calibration studies in case the space-based calibration differs from ground-based experiments. In addition, the complex functioning of the instrument, together with involved data reduction pipelines, often lead to a situation where it is not clear whether a feature in the data is due to the observed astrophysical source or effects from the instrument. Simulations can help to disentangle instrumental effects from the physics in an observation.

Simulations of astronomical X-ray observatories have been refined to an astonishing level in recent years. X-ray simulators currently used include[3] MARX for *Chandra* (Davis et al., 2012), NUSIM for *NuSTAR* (e.g., Zoglauer et al., 2011), SOXS for *LEM* and *Lynx*[4], IXPEOBSSIM for *IXPE* (Baldini et al., 2022), COMPTONSOFT for CCD-based instruments (Odaka et al., 2010; Tamba et al., 2022), and the mission-independent simulators SIMX[5] and HEASIM[6]. Often, a *generic* simulator capable of simulating multiple X-ray telescope types is advantageous, for instance, for cross-calibration purposes or the direct comparison how a source looks like with different instruments. Another reason is that proposed X-ray missions are not always funded. Developing a full simulator for each proposed mission is costly and it is often easier to rely on an existing framework where it is possible to simply add the mission specific calibration data. Developing such a framework is the main motivation of the Simulation of X-ray Telescopes (SIXTE) software (Dauser et al., 2019, and references therein), which is used in this dissertation, and which is described in the next section.

[3] There also exist other simulators related to the detection of X-rays, however, these are further away from X-ray astronomy. Examples include synchrotron simulators (Collonge et al., 2022; Johng-ay et al., 2016) or GEANT4, which is a general software toolkit to simulate the physics of particle-matter interactions (Agostinelli et al., 2003). PYXEL is a simulator for CCD- or CMOS-based detectors but is mainly used for optical wavelengths (Lucsanyi et al., 2018). For completeness, I also mention the `fakeit` tool within ISIS/XSPEC with which one can perform basic spectroscopic simulations. It is solely based on the response of the telescope but does not simulate the actual photon detection chain. `fakeit` can only be used for point sources and is inapt to simulate bright or extended sources or variability processes.

[4] https://hea-www.cfa.harvard.edu/soxs/

[5] http://hea-www.harvard.edu/simx/

[6] https://heasarc.gsfc.nasa.gov/docs/hitomi/analysis/ahhelp/heasim.html

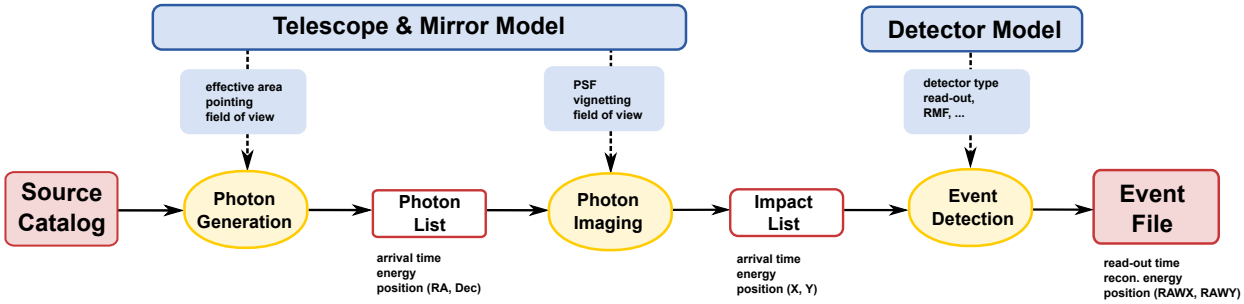

Figure 6.1: Work flow of SIXTE (Credit: Fig. 1 from Dauser et al. 2019, A&A 630, A66, reproduced with permission ©ESO). The three fundamental modules (yellow ellipses) are the photon generation, photon imaging, and event detection. The source catalog encapsulates the astrophysical information of the simulated source in the SIMPUT format. The photon and impact list are intermediate files which can be used to isolate different steps of the simulation.

6.1 The SIXTE Software

The Simulation for X-ray Telescopes SIXTE (Dauser et al., 2019) software package is a generic Monte Carlo toolkit for X-ray astronomical instrumentation. It is an end-to-end simulator, which means that it simulates the full detection chain of a generic X-ray telescope for individual photons, from the astrophysical source through the imaging and detection process to the final data product. It is built to be a mission-independent tool with easy and fast usage (i.e., usable on a standard laptop). At the time of writing, SIXTE is the official simulator of *Athena* (Nandra et al., 2013), *eROSITA* (Predehl et al., 2021), and the proposed NASA probe missions *AXIS* (Mushotzky, 2018), *HEX-P* (Madsen et al., 2018), and *Arcus* (Smith et al., 2017). It also supports *XRISM* (XRISM Science Team, 2020), *Suzaku* (Mitsuda et al., 2007), *STROBE-X* (Ray et al., 2019), *eXTP* (Zhang et al., 2016), *XMM-Newton* (Strüder et al., 2001; Turner et al., 2001), and *NuSTAR* (Harrison et al., 2013). Details on the SIXTE software can be found in Schmid (2012), Dauser et al. (2019), and the SIXTE manual[7]. In the following, I will summarize the main working steps of the simulator. According to Dauser et al. (2019), the astrophysical information of the source(s) to be simulated are encapsulated in the simulation input file (SIMPUT; Schmid et al. 2013). The SIMPUT format is flexible and all relevant observables (except for polarization, which is planned to be implemented) can be defined in this format. For example, the source can have a spectral energy distribution, variability behavior, can be spatially extended and have regionally different spectral properties, or can even be 3-dimensional. This source description is instrument-independent, which has the major advantage that, once a SIMPUT file has been produced, it can be simulated with all missions integrated in SIXTE or other simulators, such as SIMX.

SIXTE uses a modular approach for the source definition, the effects of the optics, and the description of the detector (Fig. 6.1). In the first step, the *photon generation*, individual photons are sampled from the source catalog of the SIMPUT file, depending on the ARF, the pointing of the telescope, and how large the field of view is. Thus, SIXTE ensures to only simulate photons which enter the

[7] https://www.sternwarte.uni-erlangen.de/sixte/

field-of-view. The resulting photon list encodes the arrival time of the photon, its energy, and the sky position in right ascension and declination. This is the input for the second step, the *photon imaging*, where the photons are propagated through the optics. SIXTE uses the vignetting and PSF calibration files to describe the optics. This approach significantly speeds up the simulation compared to ray-tracing (which is also planned for implementation). At the end of the photon imaging, the impact times and positions of the photons on the detector are recorded in the *impact file*.

The next step is the *event detection* where the deposited signal in the detector is calculated through randomization from the RMF. Currently, multiple different detector types can be simulated with SIXTE, which can be broadly distinguished by event- and time-triggered detectors. Event-triggered means that the impact of an X-ray leads to an immediate measurement. Examples for such detectors implemented in SIXTE are microcalorimeters and SDDs. As they are not used in the simulations shown in this thesis, I refer the reader to Wilms et al. (2016), Lorenz et al. (2020), and Kirsch et al. (2022) for details on the simulation of transition edge sensors. Time-triggered means that the detector integrates over a certain time until it measures the signal. This type of detector includes CCDs and DePFETs where the impact of a photon creates an electron charge cloud (see Sect. 3.2). SIXTE models the charge cloud as a 2D rotationally symmetric Gaussian distribution, where the charge fraction in the detector pixel (n, m) is

$$c_{n,m} = \frac{c_{\mathrm{total}}}{2\pi\sigma^2} \cdot \int_{x_n}^{x_{n+1}} \int_{y_m}^{y_{m+1}} e^{-\frac{(x-x_\mathrm{i})^2+(y-y_\mathrm{i})^2}{2\sigma^2}} \,\mathrm{d}x\,\mathrm{d}y \quad . \tag{6.1}$$

$(x_\mathrm{i}, y_\mathrm{i})$ is the impact position of the photon, c_{total} the total generated charge, and σ the standard deviation of the Gaussian charge cloud (Dauser et al., 2019). It has the value

$$\sigma = a + b\sqrt{E} \quad , \tag{6.2}$$

where a and b can be adjusted in a file describing the instrument[8]. For time-triggered detectors, the charge is then shifted line-wise to the read-out (for CCDs), or can be directly read-out at the pixel (for DePFETs). In the final event reconstruction, the pattern types are calculated, and a possible calibration step can be applied (see Dauser et al. 2019, Sect. 2.6.3, for details). Finally, the reconstructed event information, such as pixel position, time, energy and pattern type, is written to an output file in the standard event file format used in X-ray astronomy (George et al., 1994).

In general, SIXTE strives to find a compromise between runtime and accuracy. The main objective that sets the SIXTE software apart from other generic X-ray simulators is its modular approach. Logically separated blocks can be exchanged by more sophisticated models. An example is the simulation of electron loss effects in the detector, which lead to escape peaks and a weak continuum below the photon energy. In SIXTE, this can be either simulated using the appropriate RMF, which is fast, or by actually simulating the radiative transfer in the absorber (Lorenz et al., 2022), which results in slower but more physical simulations. In addition, simulators like SIMX and HEASIM use a rather top-level representation of the charge cloud and the read-out process, which is simulated in much more detail in SIXTE. An exception is COMPTONSOFT, which utilizes GEANT4 in order

[8] a and b are named `par1` and `par2` in the SIXTE code.

to simulate the photon-matter interactions (Tamba et al., 2022). Another advantage is the strict separation between the instrument model (e.g., CCD) and the instrument parameters (e.g., pixel size), which makes it very easy to change the latter.
Following the three application cases outlined in the introduction of this chapter, development, calibration, and proposal planning, I will show-case a set of SIXTE simulations next. Section 6.2 studies the filter thickness of the *Athena* WFI Fast Detector in order to illustrate the necessity of simulations for detector development. In Sect. 6.3, I use SIXTE to calibrate the electron charge cloud distribution of the *eROSITA* detectors. In Sect. 6.4, I give an example of a feasibility study for observations of high-redshift galaxy clusters.

6.2 Filter Thickness of the *Athena* WFI Fast Detector

The thick filter of the *Athena* WFI Fast Detector (see Sect. 3.3.3) is designed to enable observations of the brightest extrasolar X-ray sources. As explained in Sect. 3.2.2, bright sources produce pile-up in a DePFET detector above a certain flux limit, leading to spectral distortions and immediate complications of the analysis. In this section, we present simulations of bright black hole X-ray binaries to address the question whether the current baseline of 100 μm beryllium is the ideal choice[9]. In particular, we focus on the influence of the spectrum on the flux limit for which the WFI Fast Detector can still observe sources without major distortions. Accreting neutron stars, such as Sco X-1, or other X-ray emitting objects, are not included in this study.
Determining the optimal filter thickness requires studying sources which show a variety of spectral shapes. Section 4.1 introduced the states of black hole X-ray binaries and showed that their spectra look vastly different in the hard and soft state, respectively. Therefore, this type of object is ideally suited for this study. We simulate the sources Cyg X-1, GX 339−4, and GRO J1655−40 in the hard state with typical values of the equivalent hydrogen column density[10]. The soft state is simulated using a multi-temperature accretion disk (`diskbb`) of 400 eV and a continuum reflection model (`kerrbb`). Figure 6.2 shows these input spectra.
Before we begin with the analysis, we emphasize that the fluxes shown throughout this study assume sources of constant flux. As shown in Sect. 4.1, black hole X-ray binaries in outburst typically show strong variability on short timescales with up to 40% RMS. Since observations have to cover the full dynamic range of instantaneous source flux, the fluxes discussed in the following are to be interpreted as peak fluxes and not as the average fluxes.
The flux limit where spectral distortion becomes problematic can be characterized by the fraction of piled-up with respect to non piled-up events, called the *pile-up fraction*. Figure 6.3 shows a set of simulations of black hole X-ray binaries in the soft state for a range of input fluxes, characterized by the pile-up fraction. A higher source flux leads to a larger pile-up fraction. We investigate how well the input parameters can be reconstructed as a function of pile-up fraction and find that the spectrum is too distorted at $\gtrsim$1% pile-up to allow a reconstruction of the input parameters. Observations below 1% pile-up still allow a reasonable reconstruction of the spectral parameters.

[9]This analysis is also presented in an internal report by the SIXTE team, called `WFI-ECAP-TNO-13-010_i1.0_FD_Thick_Filter`.
[10]The SIMPUT files were provided by Jörn Wilms based on *Chandra*/HETG observations.

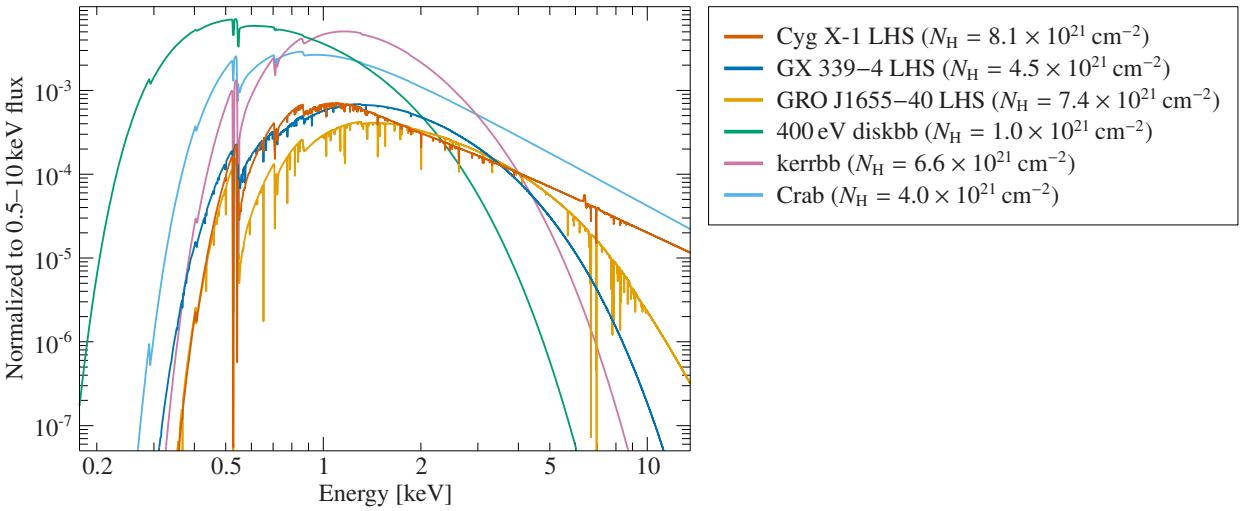

Figure 6.2: Normalized source spectra for the Fast Detector filter thickness study. The spectra of Cyg X-1, GX 339−4, and GRO J1655−40 represent the low hard state. In addition, two spectra in the high soft state are simulated, modeled by a multi-temperature (green) and relativistic disk black body (pink). For reference, also the Crab spectrum is simulated (light blue).

This threshold has also been deduced based on further simulations performed by the SIXTE team (see *Bright Source Report*; BSR[11]).

Each source is simulated for a varying thickness of the beryllium filter using the baseline setup of the *Athena* WFI Fast Detector as of September 2021 (instrument version 1.9.8, SIXTE version 2.6.3, SIMPUT version 2.4.10). An on-chip optical blocking filter (OBF) is always included, and additionally an OBF from the filter wheel in the case of no beryllium filter. A thicker filter reduces the amount of soft photons impacting the detector. At a flux of $1.2 \times 10^{-8}\,\mathrm{erg\,cm^{-2}\,s^{-1}}$, a $50\,\mu$m filter still enables a count rate of several 100 counts s^{-1} at 1 keV, while only few photons pass a $>100\,\mu$m filter. In order to investigate how the spectral shape influences the performance of the Fast Detector, with and without filter, each spectrum is simulated for a range of fluxes $(1\text{–}1000) \times 10^{-9}\,\mathrm{erg\,cm^{-2}\,s^{-1}}$. The exposure time is scaled such that each observation has 10^6 counts in order to ensure the same statistics.

The performance of the filter can be characterized by the ratio of the detected valid events and the total number of photons entering the telescope, called the *throughput*. Figure 6.4 (*left*) shows that the throughput is highest at low flux where no pile-up is present and almost all photons are detected. With increasing source flux the pattern pile-up increases and more invalid patterns emerge, leading to a reduction in throughput. Since *Athena* has most effective area at low energies, sources with a harder spectrum produce less pile-up. Therefore, they are detected with higher throughput compared to a soft source of the same flux.

The second parameter that we use to characterize the filter is the pile-up faction (Fig. 6.4, *right*). The curves of the hard state sources that have relatively few photons at low energies show a similar

[11] `WFI-ECAP-TNO-10-001_i1.11_Bright_Source_Report`

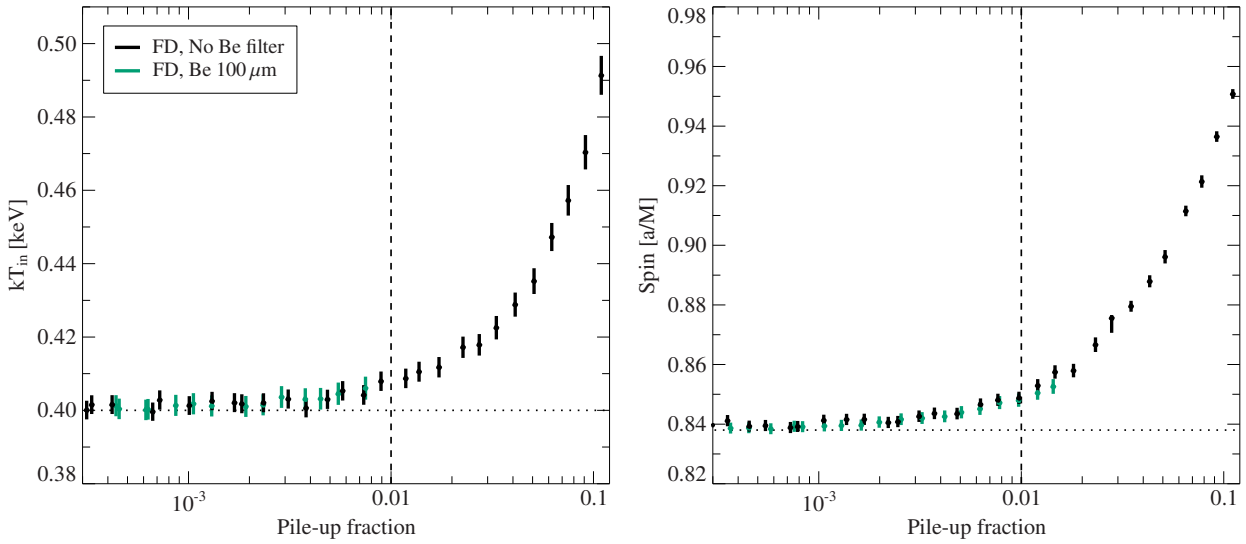

Figure 6.3: Spectral stability of an accretion disk spectrum simulated for the WFI Fast Detector with and without Be filter. *Left:* Temperature reconstruction of a `diskbb` spectrum. *Right:* Spin reconstruction from the continuum shape of a `kerrbb` spectrum. Horizontal dotted lines represent the input values and vertical dashed lines denote the 1% pile-up limit. Above this threshold, the spectral fits systematically deviate from the input values.

behavior to each other. Without a filter, the sources become piled-up at the 1% level at a 0.5–10 keV flux of roughly $10^{-7}\,\mathrm{erg\,cm^{-2}\,s^{-1}}$. In contrast, a 100 μm filter increases the observation limit by a factor of four. The effect of the filter is much more pronounced for soft spectra, which is easy to explain. A 100 μm Be filter significantly reduces the amount of soft photons in the spectrum. As the filter reduces the flux only below 1 keV, the resulting flux gain is most pronounced for soft sources. While an observation without filter is piled-up already at a few $10^{-8}\,\mathrm{erg\,cm^{-2}\,s^{-1}}$, the 100 μm filter increases the observation limit by over an order of magnitude. Thus, soft sources can be observed with low pile-up fraction (and high throughput) at larger fluxes.

For each of the simulations with different filter thicknesses and source spectra, we determine the flux limit according to the 1% pile-up criterion. The results are shown in Fig. 6.5. As expected, increasing the filter thickness allows us to observe brighter sources. Again, this behavior strongly depends on the spectral shape. In the case of harder spectra (like GRO J1655−40), an increase of the filter thickness from 50 μm to 150 μm yields only a 50% improvement of the flux limit. For a soft spectrum, the filter has a much larger influence on the performance. This result can be readily explained as for a softer spectrum the filter blocks a larger fraction of the emitted spectrum. It is also interesting to note that in the flux regime tested here, Fig. 6.5 shows the observation flux limit to scale approximately linearly with the filter thickness (note, however, that at very high fluxes pattern pile-up leads to a loss of signal, which changes the pile-up fraction in a more complex way).

One essential outcome of this study is that a filter of at least 50 μm thickness is absolutely necessary, as otherwise the sources would only be observable at up to $10^{-7}\,\mathrm{erg\,cm^{-2}\,s^{-1}}$. Even in the case of

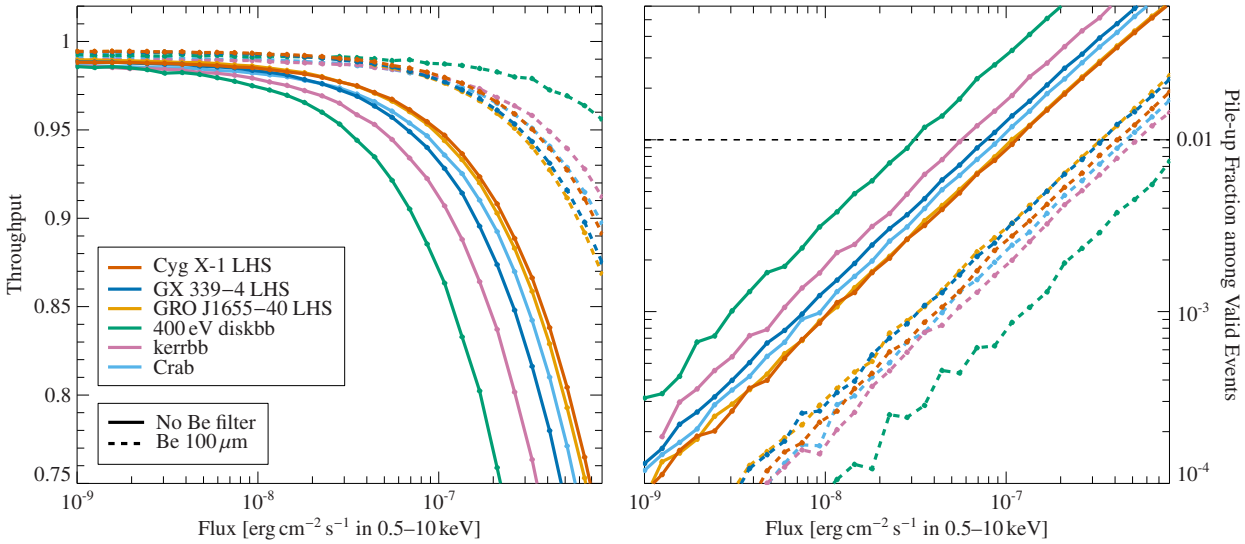

Figure 6.4: Performance of the *Athena* WFI Fast Detector at high count rates. Each dot represents one simulation with 10^6 photons. *Left:* The throughput as a function of flux decreases with increasing flux as more pattern pile-up is present. The point where the throughput is reduced highly depends on the spectral shape of the source and the presence of a filter. *Right:* Fraction of piled-up events as a function of source flux. At roughly 1% pile-up events (dashed horizontal line) the spectral shape is significantly distorted. When no filter is used, soft sources reach this limit at lower flux due to the larger effective area at low energies. When a filter is used, the 1% pile-up threshold can be significantly increased, depending on the spectral shape of the source.

the hardest spectrum, a 50 μm thick Be-filter already improves the flux limit by more than a factor of two.

The goal of this study is to recommend an optimal filter thickness. Due to the different performance depending on the spectral shape, no strict criterion can be formulated at this stage, as the WFI should be able to observe all types of bright X-ray sources studied here, and because *Athena* is currently in a re-definition phase where mirror and detector specifications might change (see Sect. 3.3.3). Figure 6.5 shows that using a filter thickness of 100 μm allows observations of all investigated spectra up to a 0.5–10 keV peak flux of roughly 3×10^{-7} erg cm^{-2} s^{-1} (around 10 Crab). This result implies that, including the typical variability in these sources, they can be comfortably observed at a mean flux of a few Crab. In summary, we do not see a strong argument to change the filter thickness from the current baseline value of 100 μm.

6.3 Calibrating the Charge Cloud of *eROSITA* CCDs

Parts of the content of this section have been taken in verbatim from König et al., *X-ray detection of a nova in the fireball phase*, first published in Nature, Volume 605, Issue 7909, p. 248–250, 2022 by Springer Nature and reproduced with permission from Springer Nature. These parts are reproduced

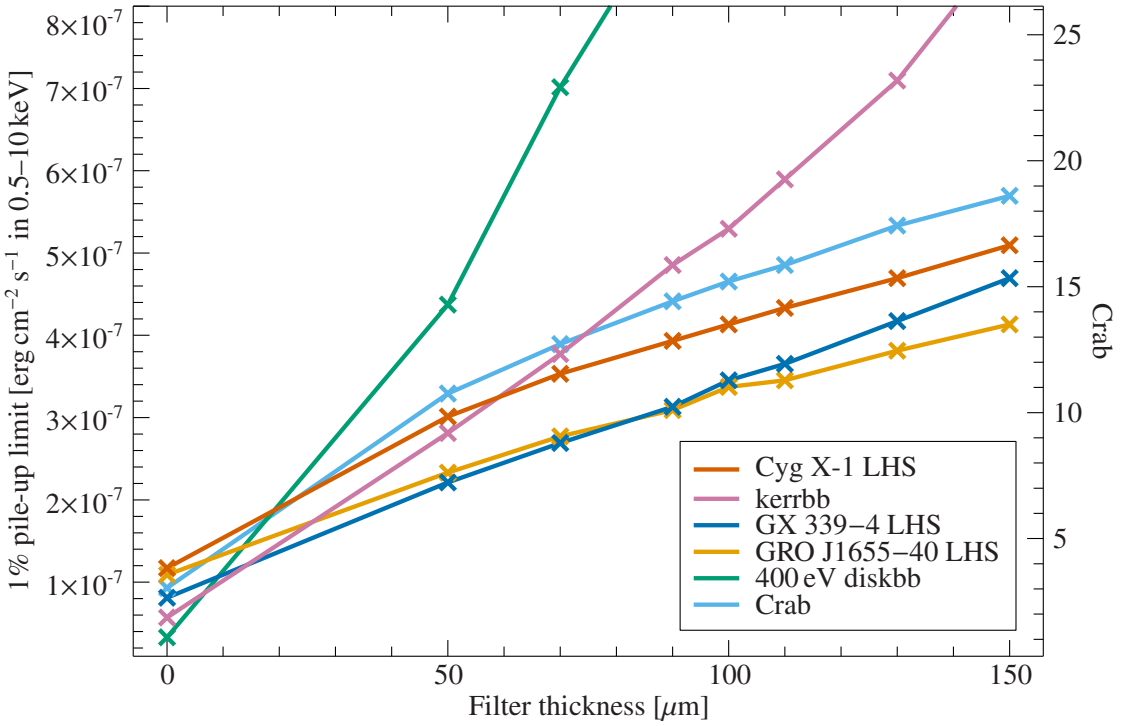

Figure 6.5: Flux limit (at 1% pile-up) as a function of the Fast Detector filter thickness for black hole X-ray binary spectra in the soft and hard state. The pile-up behaves approximately linearly with filter thickness and the spectral shape determines the slope. The conversion of the 0.5–10 keV flux into Crab units is based on the spectrum as defined in the BSR.

without direct reference.

In this section, I substantiate the second claim of this chapter's introduction: simulations play a key role in the calibration of X-ray instruments. The charge cloud created from an X-ray photon in the *eROSITA* CCDs (see Sect. 3.3.1) is a priori not known. This uncertainty is particularly problematic for the observation of bright sources. A high flux of photons illuminates many pixels and a slightly underestimated charge cloud size can lead to the situation that more charge than thought is located in neighboring pixels (see Sect. 3.2.2). In the pile-up regime, many more pixels can be illuminated if this underestimated charge in neighboring pixels surpasses the low-energy threshold, leading to more energy distortions in the spectrum and potentially invalid patterns. Understanding the charge cloud is, therefore, important to analyze observations which suffer from pile-up.

Because pile-up is strongly dependent on the source flux and spectral shape, the typical forward-fitting approach of X-ray astronomy where detector effects are modeled solely through a linear response matrix (Lampton et al., 1976) is not applicable. An additional problem in the case of *eROSITA*'s slew observations is that the pile-up is time-dependent. Vignetting reduces the count rate at the edge of the field-of-view (FoV) and the astigmatism of the Wolter mirrors distorts the PSF (see Predehl et al., 2021, their Sect. 4.2). This effect is also illustrated in Fig. 3.7 of the

eROSITA description in Sect. 3.3.1. As a result, photons are distributed over a larger number of pixels when the source enters and leaves the FOV, resulting in less pile-up at the beginning and end of the slew observation. This complexity also makes an excising of the PSF core, which is a common mitigation approach for moderate pile-up in pointed observations (e.g., Done & Diaz Trigo, 2010), unpractical for the *eROSITA* slew.

As discussed in Sect. 6.1, SIXTE can model the charge cloud, vignetting, and event reconstruction during slew observations (see Townsley et al. 2002 and Tamba et al. 2022 for similar approaches). Comparison between existing on-ground and in-flight *eROSITA* calibration measurements shows that the pre-flight PSF and vignetting data reproduce the observations well. Since the pile-up behavior of the detector is sensitively dependent on the charge cloud size, the largest uncertainty in our simulation lies in the charge cloud model (Eq. 6.1–6.2).

One of the best ways to quantify the size of the charge cloud from observational data is to measure the fraction of single, double, triple and quadruple events as a function of energy (called *pattern fractions* or *split patterns*, see Dennerl et al. 2012). Because the distribution of events in the real detector is energy-dependent, σ can be determined from the measured pattern fractions. To this end, we need to determine a reference curve for the in-orbit pattern fractions. These are derived from a large number of *eROSITA* slew observations of brighter AGN, which are, however, faint enough not to be piled up. Roughly 35 600 events from 3C 273, MCG−6-30-15, 4FGL J1223.0+1100, 3FGL J0658.6+0636, PKS 0537−286, PKS 1256+0136, and PKS 2005−489 are used to construct this calibration curve, which is displayed in Fig. 6.6. Only events from the source regions are included, as the particle background affects the low and high energies (due to the abrupt reduction in effective area above the Au M-edge of *eROSITA*'s mirror system).

Thus, we can empirically determine σ by minimizing the simulation against the calibration curve in the 0.2–2 keV range. The parameter b is constrained to be larger or equal to zero. This choice limits the charge cloud to either stay constant in size, independent of the photon energy, or increase in size with increasing energy (see Eq. 6.2). We simulate a grid of 20×10 points in the a versus b plane where each grid point represents a 10 Ms SIXTE slew simulation of the RASS catalog (Boller et al., 2016), excluding potentially piled-up sources with 0.11–2.3 keV fluxes brighter than $10^{-11}\,\mathrm{erg\,cm^{-2}\,s^{-1}}$. We then calculate the $\Delta\chi^2$ with respect to the reference calibration curve derived above, which is shown in Fig. 6.7. The best-fit of the single patterns can be found at $b = 0$ and $\sigma = a = 9.8\,\mu$m (see red cross in Fig. 6.7). The resulting pattern fractions are shown as the blue curves in Fig. 6.6, indicating that SIXTE can reproduce the *eROSITA* in-flight pattern fractions at an accuracy of a few percent in the energy range relevant here (see also König et al., 2022).

I note here that it is not necessarily unphysical to have a negative energy-dependency of the charge cloud size. Janesick et al. (1986, Fig. 2) show that the initial charge cloud is on the order of 0.1–1 μm, depending on the energy (see also Pavlov & Nousek, 1999, Eq. 3). The initial charge cloud is at least a factor of 10 smaller than the size of 9.8 μm chosen for the *eROSITA* charge cloud in SIXTE. The initial charge cloud then drifts to the read-out (e.g., Rodney & Tonry 2006, Eq. 3, and Pavlov & Nousek 1999, Eq. 7 and 17) and broadens. As low-energy photons penetrate less deep into the semiconductor material, the diffusion length can be longer. This effect could lead to high-energy photons causing a smaller effective charge cloud size compared to low-energy photons (although this also depends on whether the detector is front- or back-illuminated).

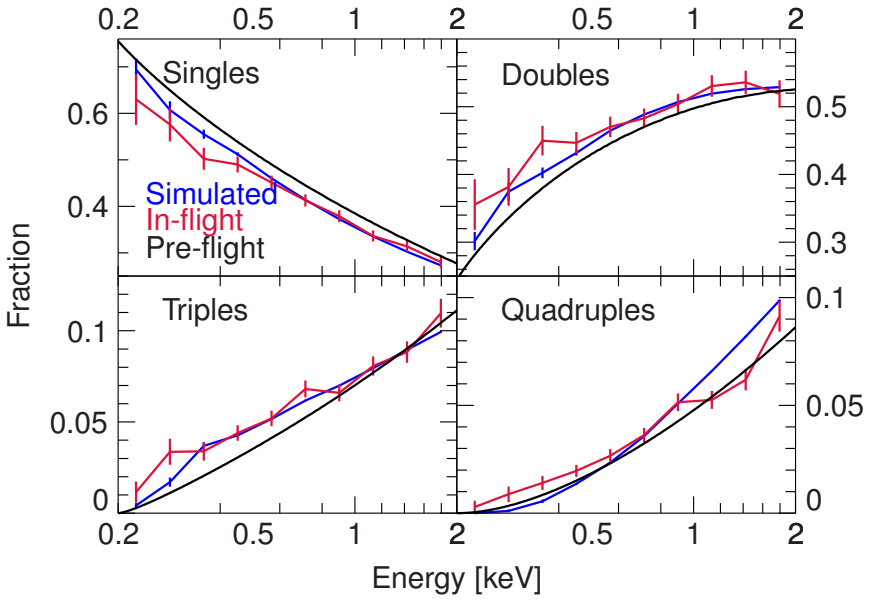

Figure 6.6: Comparison of simulated and measured pattern fractions in order to verify the pile-up model of SIXTE. The pre-flight pattern fractions from the TRoPIC prototype camera are shown for comparison (Dennerl et al., 2012). Error bars are at the 1σ level. Figure reproduced from König et al. (2022, Extended Data Fig. 3) with permission from Springer Nature.

6.4 *Athena* WFI Simulations of Galaxy Clusters at high Redshift

The final set of simulations presented in this section emphasizes the importance of simulators for proposal planning. Studying large scale structures is one of the prime scientific goals of *Athena*'s WFI detector (Rau et al., 2016). A particular target class comprises galaxy clusters as they allow scientists to study AGN feedback or cooling time scales of the intra-cluster gas, which impacts galaxy evolution theories and, ultimately, cosmology (Nandra et al., 2013, and references therein). Motivated by this science case, simulations are needed to answer the question up to which redshift the WFI will be able to resolve spatial features in these galaxy clusters.

We use the archetypical Perseus cluster as an example for this study[12]. The simulation input is an exposure corrected composite *Chandra* image[13]. Spectra of galaxy clusters can be approximated by an optically thin collisional plasma (APEC; Smith et al. 2001). As the center of galaxy clusters loses energy through radiative cooling, the center typically has a lower plasma temperature and metallicity than the outskirts (Sanders & Fabian, 2007). This gradient in metallicity and temperature can be incorporated in the SIMPUT definition by varying the parameters of the APEC across the image using a temperature and abundance map. We set the total spatial flux to $7.5 \times 10^{-10}\,\mathrm{erg\,cm^{-2}\,s^{-1}}$ (2–10 keV; Edge et al. 1990, Table 1).

[12]This study is also reported in the document `WFI-ECAP-TNO-10-008_i1.2_Galaxy_Cluster_Simulations` by the SIXTE team.

[13]All input images were provided by Jeremy Sanders, MPE.

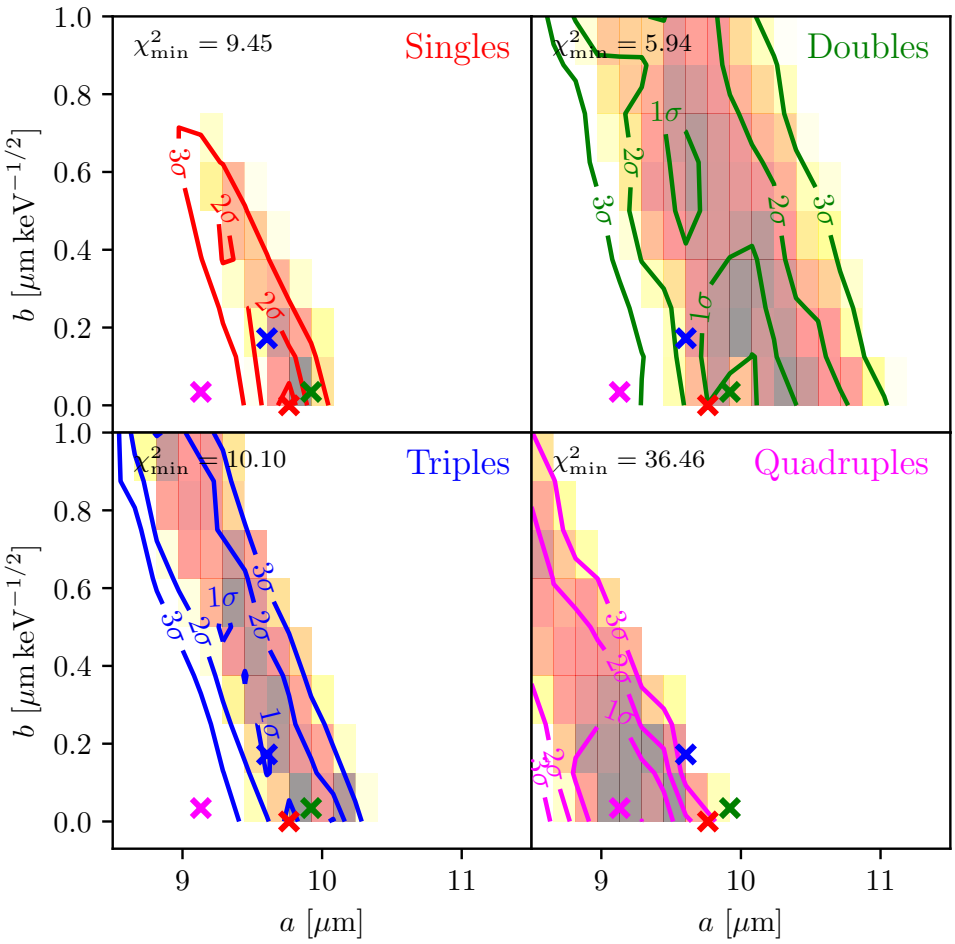

Figure 6.7: χ^2-landscape of the charge cloud optimization for *eROSITA*. The pattern fractions of single events (top left) give the tightest constraints. We adopt the best fit value of $a = 9.8\,\mu$m and $b = 0$ for the *eROSITA* charge cloud standard deviation.

The Perseus cluster is then shifted to higher and higher redshifts in order to determine the threshold where surface brightness fluctuations from cavities in the galaxy cluster remain visible. The cluster can be made more *compact* by adjusting the size of the image pixels on the sky. If the image has a smaller angular size it appears more distant. In FITS images, this is can be done by changing the `CDELT` keyword[14]. However, this consideration is not purely geometrical as the Universe is expanding. For objects at cosmological distances, the *luminosity distance* D_L can be calculated from the redshift[15]. The Perseus cluster has a luminosity distance of roughly 77.7 Mpc, while a

[14] `CDELT`n is the rate of change of the physical coordinate (here: degrees) along axis n per unit change in the counting index, evaluated at the reference point `CRPIX`n (`fits.gsfc.nasa.gov/users_guide` and Wells et al. 1981).
[15] The luminosity distance is calculated using the `lumdist` function in the ISISSCRIPTS.

$z = 0.05$ cluster has a distance of approximately 222 Mpc. The luminosity distance is related to the *angular diameter distance* D_A, which gives the distance in terms of the object's physical size as viewed from Earth, by $D_A = D_L/(1+z)^2$. One factor $1/(1+z)$ is due to the expansion of the Universe, the second $1/(1+z)$ term is due to time dilation. Taking this into account, we can infer the pixel increment of the shifted cluster image by

$$\texttt{CDELT}(z) = \texttt{CDELT}_{\text{Perseus}} \cdot \frac{D_{L,\,\text{Perseus}}/(1+z_{\text{Perseus}})^2}{D_L(z)/(1+z)^2} \quad , \tag{6.3}$$

where z denotes the redshift of the shifted cluster. Keeping the luminosity constant at $1.1 \times 10^{45}\,\text{h}_{50}^{-2}\,\text{erg}\,\text{s}^{-1}$ (Edge et al., 1990), the flux decreases quadratically when looking at a higher redshift cluster. Thus, the flux is calculated as

$$F(z) = F_{\text{Perseus}} \cdot \left(\frac{D_{L,\,\text{Perseus}}}{D_L(z)}\right)^2 \quad . \tag{6.4}$$

Lastly, the spectrum of the shifted cluster has to be adjusted for the farther redshift in the `apec` model.

The cluster core has a spatial extend of about $5'$ and can be placed on only one of the four chips of the *Athena* WFI. Therefore, we perform the simulations with only one chip and no dithering for redshifts up to $z = 0.2$. In order to accentuate structures, such as cavities, we apply an unsharp masking filter. Figure 6.8 shows 50 ks *Athena* WFI simulations for different redshifts. Note that this is the old *Athena* setup as of April 2020 before the mission re-formulation phase (instrument version 1.8.4). The detection threshold for identifying clear and distinct features in the image is roughly $z = 0.1$. As expected, at higher redshifts $z \sim 0.175$ the features blur out and are not distinguishable from an extended point source any more.

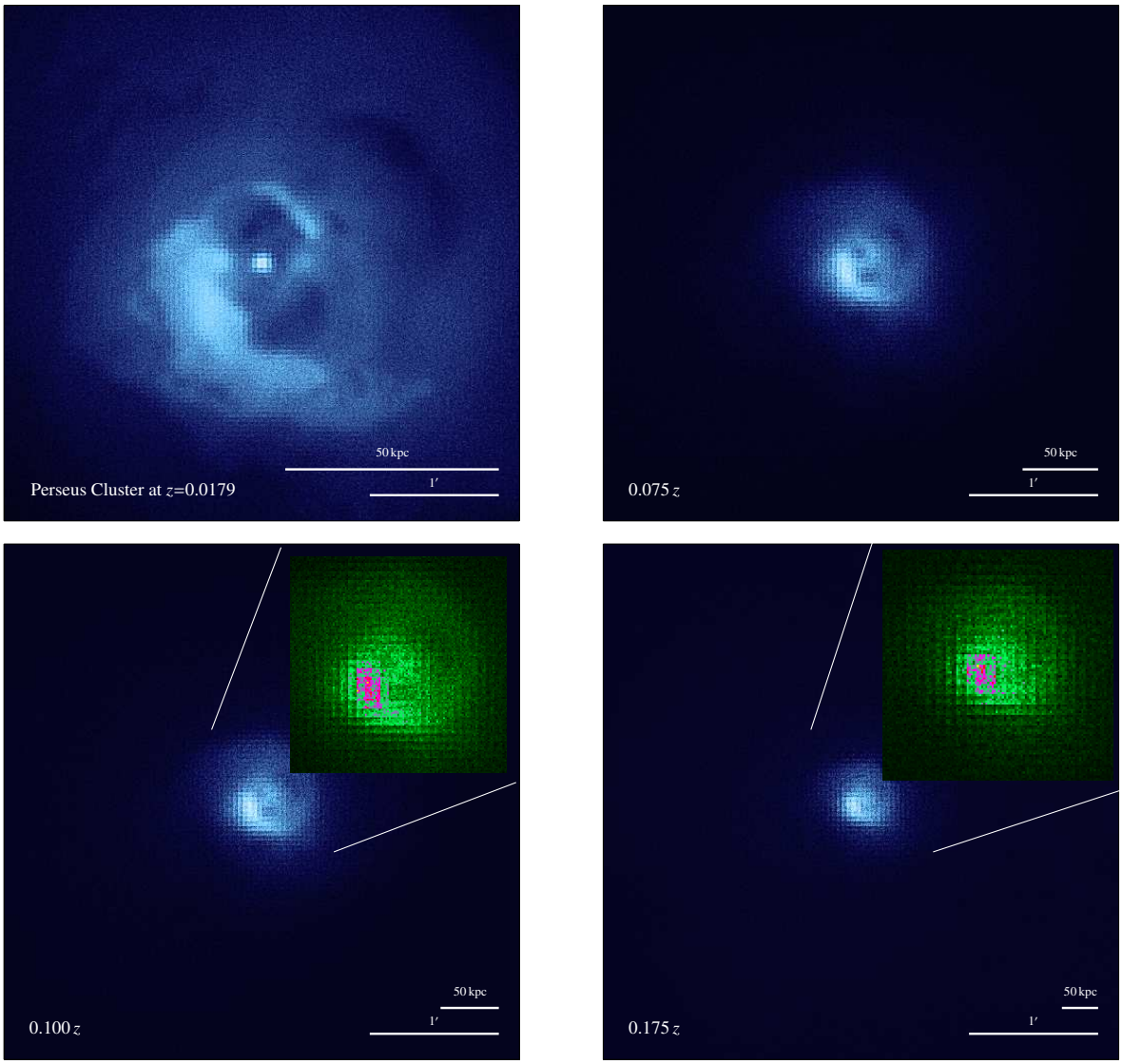

Figure 6.8: *Athena* WFI simulations of clusters at different redshifts. The Perseus-like cluster is placed on one WFI chip and simulated with a 50 ks exposure in full frame mode. The top left simulation shows the Perseus cluster at its actual distance. In the other images the cluster is shifted to higher redshifts. An unsharp masking filter is applied to enhance surface brightness gradients. The insets show zoom-ins to the central region. One can see that the surface brightness fluctuations (cavities) become too smeared out for a significant detection at around 0.175 z.

Chapter 7

X-ray Detection of a Nova in the Fireball Phase

Als Paul viele Jahre nachdem er den Weißen Zwerg verlassen hat, in das Sonnensystem hineinfliegt, sieht er, dass er auf ein großes Weltraumteleskop zufliegt. Das Teleskop dreht sich und die Öffnung ist für Paul nur für wenige Sekunden zu sehen. Doch er hat Glück, schlüpft hinein und prasselt zusammen mit dutzenden anderen Röntgenteilchen[vii], die mit ihm gereist sind, auf den Detektor. Fast wäre er noch von dem Türsteher aussortiert worden, der sich ihm als Pattern vorstellt. „Hier sind zu viele von euch, ich schmeiße euch raus!", sagt Pattern[viii]. „Aber wollt ihr denn nicht wissen, wo ich herkomme? Ich komme direkt von einem Weißen Zwerg", erwidert Paul, lächelt und winkt freundlich, und wird von dem Türsteher durchgelassen.

To be continued in Ch. 7.1.

Section 2.6 gave an introduction to the physics of novae and described the predicted X-ray flash arising directly after the thermonuclear runaway. In this chapter, I report on the discovery of this X-ray ignition flash in the Galactic nova YZ Reticuli with the *eROSITA* telescope. This detection confirms the theoretical prediction of the fireball phase, first described more than three decades ago by Starrfield et al. (1990). I describe the chronology of the detection (Sect. 7.1), followed by the data reduction (Sect. 7.2). In Sect. 7.3, a simulation-based spectral analysis is performed to arrive at the physical interpretation of what happens in the vicinity of the white dwarf (Sect. 7.4). Conclusions are drawn in Sect. 7.5 with some remarks on the implications of this detection.

Large parts of the content of this chapter have been taken in verbatim from König et al., *X-ray detection of a nova in the fireball phase*, first published in Nature, Volume 605, Issue 7909, p. 248–250, 2022 by Springer Nature and reproduced with permission from Springer Nature. These parts are reproduced without direct reference. The "Methods" section of the original paper has been integrated into the bulk text.

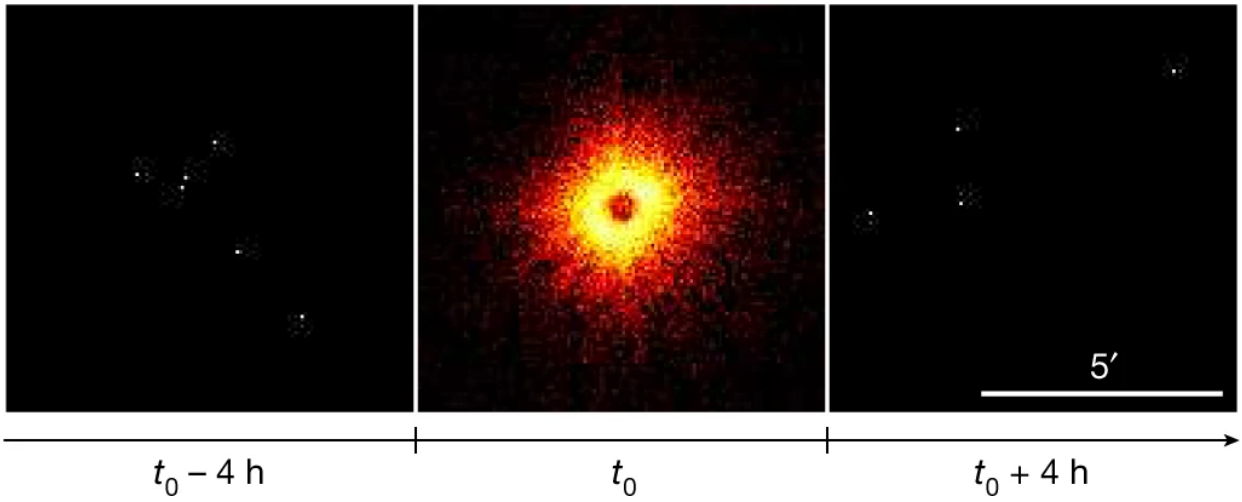

Figure 7.1: Sky images of all seven *eROSITA* cameras combined (0.2–0.6 keV). On t_0 = 2020 July 7, 16 h 47 min 20.64 s TT, during the second all-sky survey, *eROSITA* detected a bright, new, soft X-ray flash that was severely affected by pile-up. No source can be seen in the scans four hours before and after the event. Figure reproduced from König et al. (2022, Fig. 1) with permission from Springer Nature.

7.1 *eROSITA* Detection of YZ Reticuli

Emilia, das optische Lichtteilchen, konnte den Weißen Zwerg erst nach einigem Herumgestreue verlassen. Einen halben Tag ist Paul nun schon vor ihr. Sie kommt von unten in das Sonnensystem gesaust, doch ist zu spät, um noch das Weltraumteleskop zu erreichen, es liegt bereits 1,3 Millionen Kilometer entfernt von ihr[ix]*. Stattdessen landet sie auf der Südhalbkugel des Planeten Erde. „Wow, was blinkt denn dort für ein neuer Stern auf?“, fragt sich ein Mensch namens Robert. „Das muss ich direkt berichten*[x]*.“*

The End.

During its second all-sky survey (2020 June 26 to 2020 December 15), the *eROSITA* instrument (Predehl et al., 2021, and Sect. 3.3.1) on board Spectrum-Roentgen-Gamma (SRG; Sunyaev et al. 2021) scanned the field around $\alpha_{\mathrm{J2000.0}} = 03\mathrm{h}\,58\mathrm{min}\,30\mathrm{s}$, $\delta_{\mathrm{J2000.0}} = -54^\circ\,46'\,41''$ 28 times, with each scan separated by 4 hours. No source was detected for the first 22 scans. During the 23rd passage over the position, which started on t_0 = 2020 July 7, 16 h 47 min 20 s Terrestrial Time (TT), a new and extremely bright source was detected (Fig. 7.1). No source was visible in the subsequent scans, constraining the event's duration to less than 8 h. The position coincides with the location of Nova YZ Reticuli (= EC 03572−5455 = Nova Reticuli 2020), for which an optical outburst was discovered (McNaught, 2020a) on 2020 July 15, 14 h 09 min UT. Subsequently, the object was classified as a classical He/N Galactic nova (Aydi et al., 2020a; Carr et al., 2020) with a geometric distance of $2.53^{+0.25}_{-0.26}$ kpc.

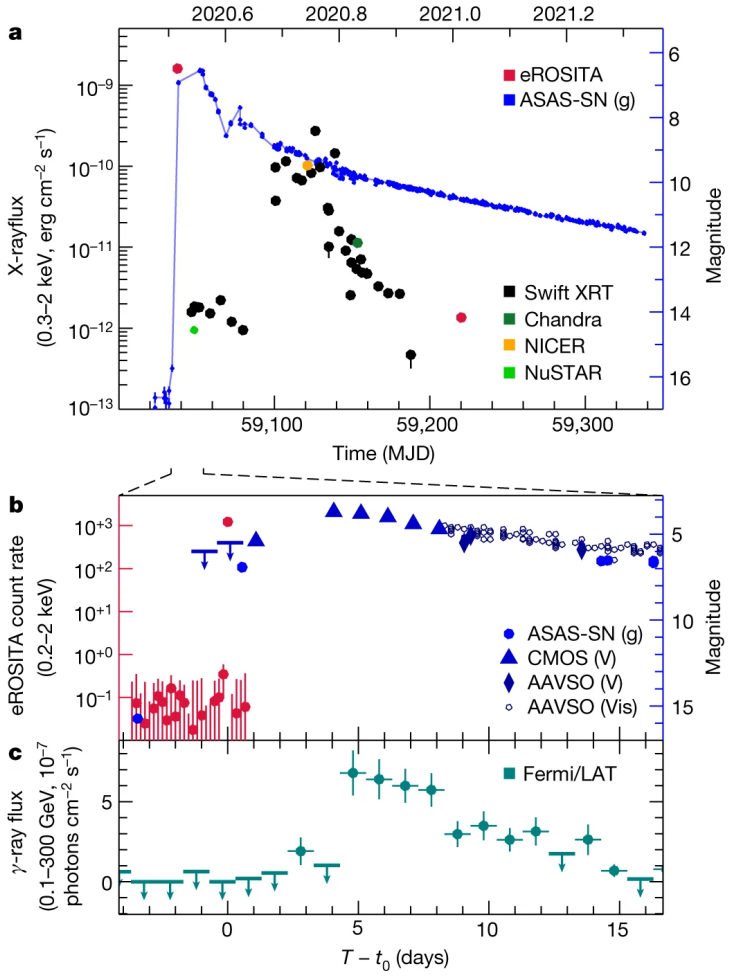

Figure 7.2: Multi-wavelength lightcurve of YZ Ret. Error bars denote 1σ confidence levels. The top x-axis shows the fractional time of the year. **a** Long-term evolution tracing the absorbed X-ray flux and the optical flux from the flash through the supersoft state using *eROSITA*, *Swift*, *NICER*, and *Chandra* data. The extrapolated *NuSTAR* flux (Sokolovsky et al., 2020b) is multiplied by 100 for visibility. **b** Short-term lightcurve before and after the X-ray flash showing the *eROSITA* count rate and the subsequent optical brightening. **c** Fermi/LAT lightcurve showing the γ-ray activity starting a few days after the flash. Figure reproduced from König et al. (2022, Fig. 2) with permission from Springer Nature.

Figure 7.2 shows the combined multi-wavelength lightcurve of YZ Ret. At $t_0 - 3.5\,\mathrm{d}$, ASAS-SN monitoring indicates the source close to the 16.4 mag detection limit at 15.8 mag. At $t_0 + 2.2\,\mathrm{h}$ an optical (V-band) non-detection with a lower limit of 5.5 mag was reported (McNaught, 2020b; Sokolovsky et al., 2020b), followed by a fast brightening at $t_0 + 11.3\,\mathrm{h}$ (2020 July 8, 04 h 05 min 58 s UT). The nova reached a peak V-band brightness of 3.7 mag (McNaught, 2020b) at $t_0 + 4.1\,\mathrm{d}$, making it visible to the naked eye and the second brightest nova of the decade. The first X-ray measurement following the *eROSITA* observations was taken only at $t_0 + 9\,\mathrm{d}$ with *Swift* XRT, when the nova entered the supersoft state. At $t_0 + 9\,\mathrm{d}$ the X-ray flux of YZ Ret was $1.6^{+2.1}_{-1.3} \times 10^{-12}\,\mathrm{erg\,cm^{-2}\,s^{-1}}$ (0.3–10 keV) shown in Fig. 7.2, which also includes complementary data from *NICER* (Pei et al., 2020), *Chandra* (Drake et al., 2020) and *NuSTAR* (Sokolovsky et al., 2020b). The subsequent outburst behavior is fully consistent with the picture of a nova in the supersoft source state. From this chronology of the events we conclude that *eROSITA* has detected the X-ray ignition flash of a nova and that the X-ray flash happened a few hours before the optical rise, as theoretically predicted (Krautter, 2008; Kato et al., 2016; Chomiuk et al., 2021).

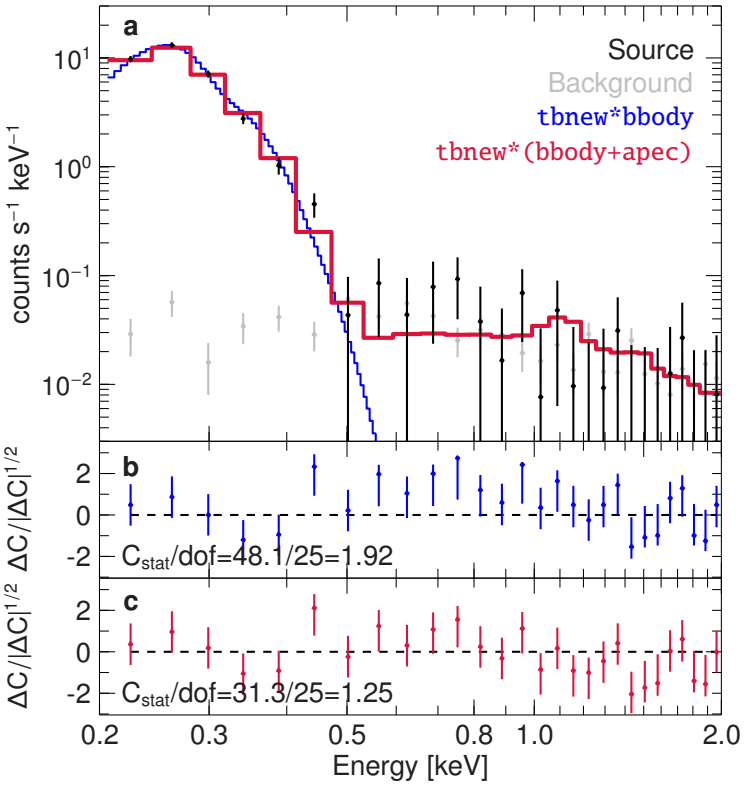

Figure 7.3: *eROSITA* spectrum of YZ Reticuli taken during the supersoft state between $t_0+176.3\,\mathrm{d}$ and $t_0+186.3\,\mathrm{d}$. The total exposure time is 640 s, the spectrum is background subtracted. The spectrum can be described by a $20.7^{+0.7}_{-0.4}$ eV black body under an equivalent hydrogen column density of $7.1^{+0.3}_{-0.9}\times10^{20}\,\mathrm{cm}^{-2}$ and a 0.3–2 keV absorbed flux of $1.35(9)\times10^{-12}\,\mathrm{erg\,cm}^{-2}\,\mathrm{s}^{-1}$. The reconstructed source position is 1.2″ from the optical position, which makes source confusion very unlikely. The fit is based on Cash statistics (see Sect. 3.4.1), error bars are given at the 1σ confidence level. Panel **b** shows the residuals using only an absorbed black body model. While the statistics are formally better when including an additional APEC model, as shown in **c**, the data are consistent with the background level at energies >0.6 keV. Figure reproduced from König et al. (2022, Extended Data Fig. 1) with permission from Springer Nature.

In other wavelengths, Fermi/LAT detected significant γ-ray emission starting at $t_0+2.8\,\mathrm{d}$ (Li et al., 2020), and a *NuSTAR* observation detected hard X-rays at $t_0+10.3\,\mathrm{d}$ (Sokolovsky et al., 2022). The hard emission is due to internal shocks within the expanding shell. Starting approximately two months after the X-ray flash, multiple missions (Sokolovsky et al., 2022), including *eROSITA* (Fig. 7.3), showed that YZ Ret had entered the supersoft state.

The progenitor of YZ Ret is the known white dwarf system MGAB-V207 (Kilkenny et al., 2015), which had a pre-eruption orbital period of 0.1324539(98) days (Schaefer, 2021). Irregular variations

in the optical before the nova event suggest the system to be a VY Scl type cataclysmic variable[1] (Sokolovsky et al., 2022). While the mass accretion rate of VY Scl type CVs is typically small, this classification does not constrain the chemical abundances of the white dwarf and, thus, the nature and composition of the white dwarf in YZ Ret is still unclear (Sokolovsky et al., 2022).

7.2 Data Reduction

In the following, I will describe the data reduction methods used in this paper. This section can be found in the "Methods" part of the original paper (König et al., 2022).

The *eROSITA* (see Sect. 3.3.1) data analysis was performed with eSASS v201009, the official analysis software of *eROSITA*. We exclude data of telescope modules 5 and 7 that are contaminated by a light-leak. Images were extracted using `evtool` and lightcurves and spectra using `srctool`, selecting all valid patterns and a symmetric PSF with no further event flagging. The data products of the flash are extracted for the time range with a fractional exposure >0.2. We use a source radius of 4.8′ for the extraction of the X-ray flash data, and 2′ for the data taken during the supersoft phase half a year later. In both cases we subtract a background spectrum, accumulated from an annulus of radii 6′ and 9′ around the source position. Throughout this paper, absorption modeling assumes the `wilm` abundances for the interstellar medium (Wilms et al., 2000) and `vern` cross-sections (Verner et al., 1996).

For the optical lightcurve of YZ Ret, we use V-band (wavelength $\lambda_{\rm eff} = 5,448$ Å, $\Delta\lambda = 890$ Å) and g-band ($\lambda_{\rm eff} = 4,639$ Å, $\Delta\lambda = 1,280$ Å) data from the All-Sky Automated Survey for Supernovae (ASAS-SN; Kochanek et al. 2017), V-band complementary metal-oxide semiconductor (CMOS) and visual (Vis, human eye, around 5,500 Å) CCD data from the American Association of Variable Star Observers (AAVSO).

We reduced the XRT spectra with HEASOFT v6.26, using `xselect` v2.4k. A source extraction radius of 1′ for data taken in the photon counting (PC) mode and the same background region as for *eROSITA* was used. We limited the PC and windowed timing mode spectra to the 0.35–10 keV energy range and modeled the spectra with an absorbed black body of ∼30–40 eV and, when applicable, a thermal plasma model of ∼4 keV (see also Sokolovsky et al. 2020a).

We extracted the 0.1–300 GeV Fermi/LAT (Atwood et al., 2009) daily binned lightcurve using the Sciencetools (v1.2.23) and fermipy (v0.20.0) (Wood et al., 2017). The 15° region of interest is centered on the *eROSITA* position of YZ Ret, with `SOURCE` class events being selected and quality cuts being applied (`DATA_QUAL>0 && LAT_CONFIG==1`). Events with zenith angles ≥ 90° were discarded. We used the `P8R3_SOURCE_V2` response for the extraction and `gll_iem_v07` and `iso_P8R3_SOURCE_V2_v1` to model the Galactic diffusion and the isotropic diffusion emission, respectively. Data points with a test statistic < 9 are given as upper limits.

[1] VY Sculptoris stars show occasional drops in the lightcurve by 1–5 mag to transition from a steady high state into a low state. These transitions are likely triggered when starspots pass underneath the inner Lagrangian point (Leach et al., 1999; Honeycutt & Kafka, 2004).

7.3 Spectral Analysis

During the *eROSITA* detection of the flash, YZ Ret was in the field-of-view for 35.8 s, with a count rate in excess of 1 000 counts s^{-1} (see Fig. 7.2b). Although the strong signal makes the detection of the flash unambiguous, it complicates a more detailed analysis of the properties of the nova: *eROSITA*'s detectors are severely affected by photon pile-up at such high count rates. The nonlinear distortion of the spectral information requires careful modeling of the response of the instrument to such a bright source. Our approach includes simulations using the same observing strategy as in the real observation. SIXTE (Dauser et al. 2019 and Sect. 6.1) has been particularly tailored to model pile-up in the *eROSITA* detectors. The simulations allow us to perform a quantitative analysis and robustly recover the basic properties of the source even when considering the remaining systematic uncertainties. In the following, unless mentioned otherwise, all uncertainties denote 3σ confidence levels.

For a given spectral model, which is characterized by a constant flux and parameters such as the temperature, and modeling the foreground absorption using interstellar medium abundances (Wilms et al., 2000), a sufficiently large number of Monte Carlo realizations is averaged to minimize the statistical noise in the simulated piled-up spectra. We compute such model observations on a dense grid of spectral parameters using SIMPUT v2.5.0, SIXTE v2.7.0, and the *eROSITA* instrument files v1.9.1. For each grid point we simulate 1 000 slews (corresponding to an effective exposure time of 31.5 ks) using the attitude file of the SRG spacecraft and the optical position of the source ($\alpha_{\mathrm{J2000.0}} = 03\mathrm{h}\,58\mathrm{min}\,29.55\mathrm{s}, \delta_{\mathrm{J2000.0}} = -54^\circ\,46'\,41.23''$). We then compare the simulated spectra against the measured data, varying the parameters to minimize the χ^2-statistics. This approach allows us to derive the parameter uncertainties from the $\Delta\chi^2$-contours (Fig. 7.4). We estimate that due to the uncertainties inherent to the charge cloud modeling (see Sect. 6.3), systematic errors of $\sim$10% will dominate the final error budget. This systematic uncertainty is incorporated into the error propagation.

We investigate the data using three different models representative for the range of expected spectral shapes, an empirical black body, an optically thin collisional plasma (APEC; Smith et al. 2001), and a white dwarf atmosphere model (Suleimanov et al., 2013, 2014). The best-fitting models are shown in Fig. 7.5 and in the Table 7.1. For the black body model we find that the spectrum can be best described at a 0.2–10 keV absorbed flux of $1.86^{+0.38}_{-0.23} \times 10^{-8}\,\mathrm{erg\,cm^{-2}\,s^{-1}}$ with a temperature of $kT_{\mathrm{BB}} = 28.2^{+0.9}_{-2.8}\,\mathrm{eV}$ ($3.27^{+0.11}_{-0.33} \times 10^5\,\mathrm{K}$), where k is the Boltzmann constant. The foreground and internal absorption column to the source is not very well known and the latter can also vary throughout the outburst. Estimates of the Galactic equivalent hydrogen column are $1 \times 10^{19}\,\mathrm{cm^{-2}} \lesssim N_{\mathrm{H}} \lesssim 1.86 \times 10^{20}\,\mathrm{cm^{-2}}$, and intrinsic absorption has been estimated to be $\lesssim 1.5 \times 10^{23}\,\mathrm{cm^{-2}}$ at $t_0 + 10\,\mathrm{d}$ (Izzo et al., 2020; Sokolovsky et al., 2022). Our black body fit constrains the equivalent hydrogen column density to $N_{\mathrm{H}} < 1.4 \times 10^{20}\,\mathrm{cm^{-2}}$, indicating no major intrinsic absorption during the X-ray flash. A comparison of the measured and simulated lightcurve shows a possible decline during the last few seconds of the observation (Fig. 7.6).

The best-fit atmosphere model has a 0.2–10 keV absorbed flux of $1.82^{+0.22}_{-0.28} \times 10^{-8}\,\mathrm{erg\,cm^{-2}\,s^{-1}}$ and a temperature of $27.1^{+1.2}_{-0.5}\,\mathrm{eV}$, consistent with the parameters of the black body model. In the fits we fixed $N_{\mathrm{H}} = 1 \times 10^{19}\,\mathrm{cm^{-2}}$, i.e., we set N_{H} to the lower limit of Galactic equivalent hydrogen

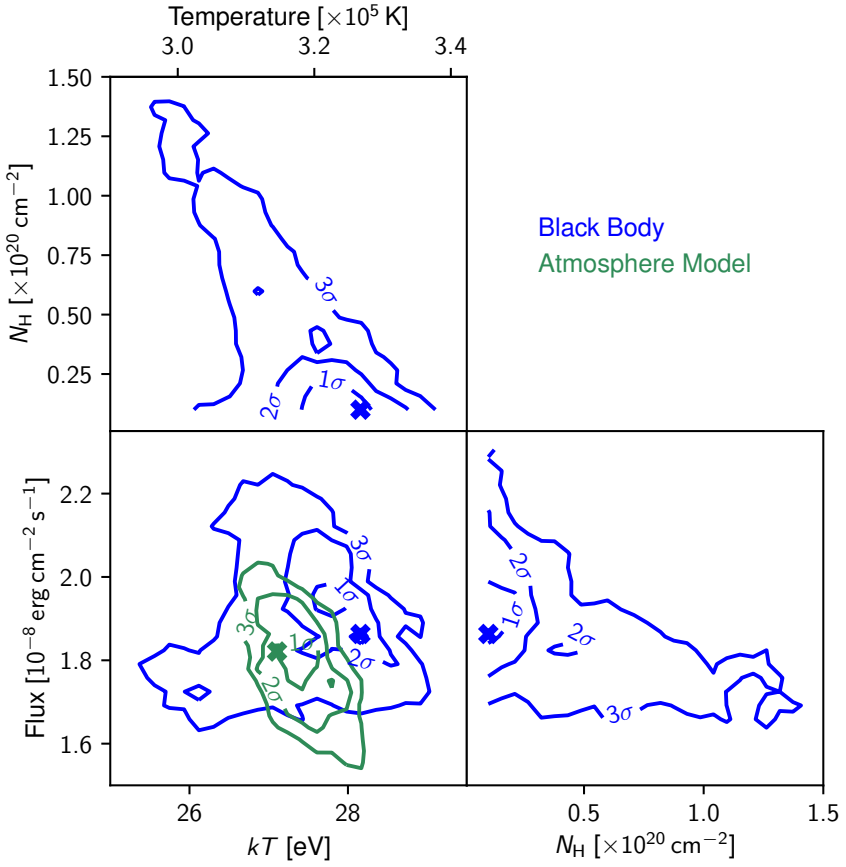

Figure 7.4: Parameter contours of the black body and atmosphere model fits. The contours show the $\Delta\chi^2$ between the averaged simulated spectra with respect to the observed spectrum. A systematic uncertainty of 10% is assigned to each simulated spectrum. Contour lines give the $\Delta\chi^2$ values for 2 degrees of freedom. The crosses denote the best-fit values, which are used in Fig. 7.5. Figure reproduced from König et al. (2022, Extended Data Fig. 4) with permission from Springer Nature.

column estimates (Izzo et al., 2020). Within the systematic uncertainties of the pile-up modeling, the black body and atmosphere models cannot be further distinguished.
The residuals of the APEC fit are significantly worse, especially at low energies, consistent with results that emission lines, presumably due to shocks, typically emerge in the X-rays only days to months after the eruption (Chomiuk et al., 2021). Similar to the later supersoft phase, any shocked plasma emission is likely orders of magnitude fainter than the supersoft emission. Therefore, we conclude that *eROSITA* detected an optically thick thermal spectrum from the photosphere.
The simulation is accurate enough to determine the black body or atmosphere temperature to a relative uncertainty of ∼10% and the flux to ∼20% (see Table 7.1). We emphasize that due to our fitting approach and remaining uncertainties in the SIXTE pile-up model and other calibration data,

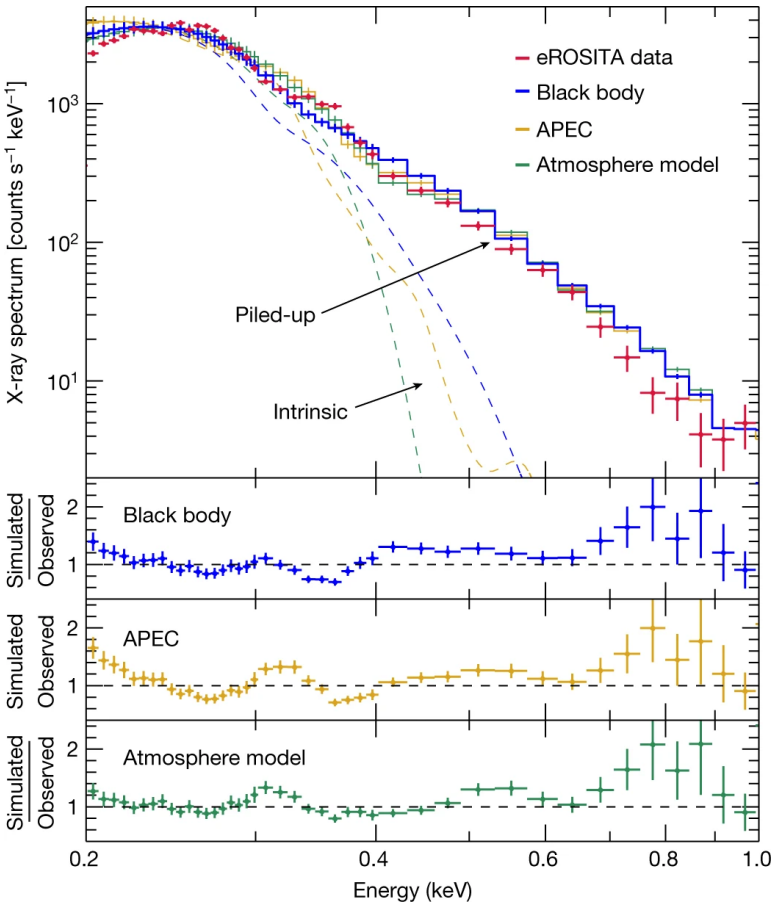

Figure 7.5: Comparison of measured and simulated spectra of the X-ray flash and the ratios between the best-fit models and the data. Solid lines show the piled-up model data, while dashed lines show the spectral shape for an observation without pile-up. Error bars are at the 1σ level and are shown assuming systematic uncertainties of 10%. Model parameters are given in Table 7.1. Figure reproduced from König et al. (2022, Fig. 3) with permission from Springer Nature.

Table 7.1: Best-fit models of the X-ray flash of YZ Ret. Table reproduced from König et al. (2022, Extended Data Table 1) with permission from Springer Nature.

Model	`tbnew*bbody`	`tbnew*atmos`	`tbnew*apec`
kT [eV]	$28.2^{+0.9}_{-2.8}$	$27.1^{+1.2}_{-0.5}$	25.9
Absorption[1]	< 1.4	0.1 (fixed)	1.7
Absorbed flux[2]	$1.86^{+0.38}_{-0.23} \times 10^{-8}$	$1.82^{+0.22}_{-0.28} \times 10^{-8}$	2.5×10^{-8}
$\chi^2_{\mathrm{red.}}$	$228.3/(130-3) = 1.80$	$179.1/(130-2) = 1.40$	$255.0/(130-3) = 2.01$
Luminosity [erg s^{-1}]	$2.0(1.2) \times 10^{38}$	$0.98(22) \times 10^{38}$	
Radius [km]	$50\,000 \pm 18\,000$	$37\,000 \pm 2\,900$	
Notes		$\log g = 6.97 \pm 0.17$	Solar abundances

Uncertainties are given at the 3σ confidence level for one parameter of interest.

[a] Equivalent hydrogen column density in units of 10^{20} cm^{-2}.
[b] Absorbed flux in units of erg cm^{-2} s^{-1} in 0.2–10 keV.

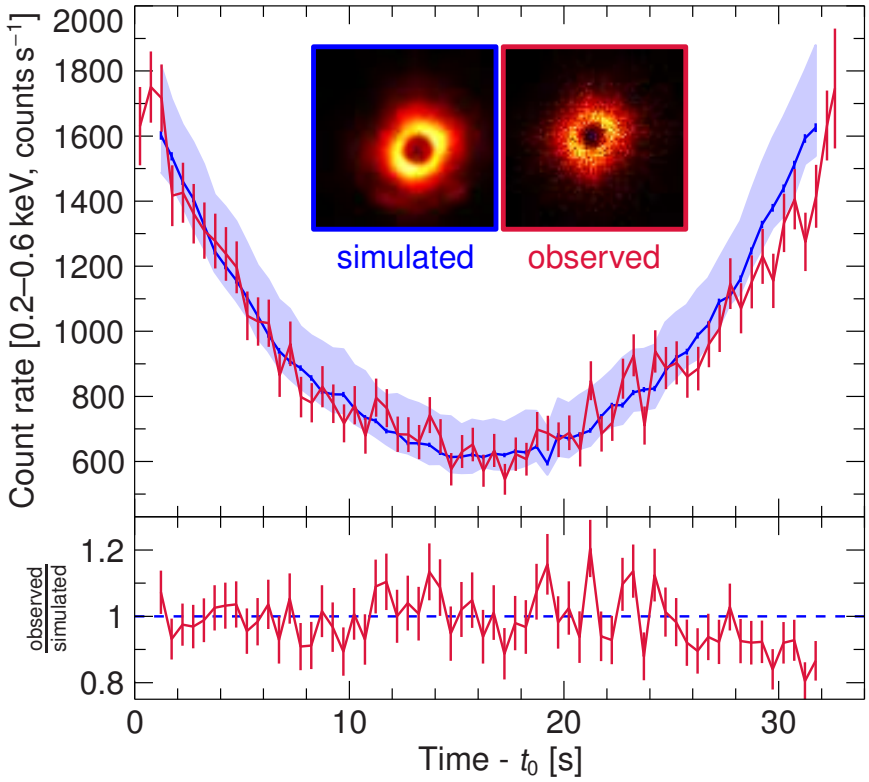

Figure 7.6: Comparison of the observed *eROSITA* slew lightcurve of the X-ray flash and the (averaged) simulation of a constant source with the best-fit black body parameters. The trough shape is due to pattern pile-up when the source passes the center of the FOV and vignetting. The last few seconds of the lightcurve show a possible decline in brightness. Error bars are at the 1σ level, the blue shaded region indicates the 3σ flux uncertainty. The inset shows the observed source and (averaged) simulated image. Figure reproduced from König et al. (2022, Extended Data Fig. 2) with permission from Springer Nature.

the modeling is dominated by systematic uncertainties. Our approach also allows us to simulate the piled-up lightcurve and sky image, which are both very similar to the measurement (Fig. 7.6). The fact that we can reproduce the piled-up image, lightcurve, and spectrum with a reasonable set of parameters shows that SIXTE is indeed capable of adequately modeling the very strong pile-up of this source.

7.4 The Photosphere of YZ Reticuli during the Flash

Assuming spherical emission and the Gaia distance of 2.53 ± 0.26 kpc, the unabsorbed bolometric flux of the black body model, $2.6^{+1.4}_{-0.6} \times 10^{-7}$ erg cm^{-2} s^{-1}, corresponds to a bolometric luminosity of $(2.0 \pm 1.2) \times 10^{38}$ erg s^{-1}. This luminosity is consistent with the theoretical prediction that the source radiates at the Eddington luminosity during the "fireball" phase (2×10^{38} erg s^{-1} for a canonical

white dwarf, Kato et al. 2015, 2016; see also Sect. 2.6.1 for details on the predictions of the fireball phase). At $t_0 + 4.1\,\mathrm{d}$ Nova YZ Ret was estimated (Sokolovsky et al., 2022) to have a peak optical bolometric luminosity of $6.6 \times 10^{38}\,\mathrm{erg\,s^{-1}}$ (correcting the distance from Gaia DR2 to Gaia EDR3). Since the high-energy luminosity at that time is a factor of $\sim$2,500 fainter (Sokolovsky et al., 2022), we can assume that this luminosity is representative of the total bolometric luminosity. The nova is expected to evolve at approximately constant, Eddington-limited bolometric luminosity, with the spectral peak moving from the X-rays during the initial flash, to a peak in the optical at the maximum expansion of the photosphere. Our derived luminosity is on the same order of magnitude as at $t_0 + 4.1\,\mathrm{d}$, implying that the total nova energetics are approximately conserved throughout the outburst. The bolometric luminosity from the black body model during the flash corresponds to a photospheric radius of $50\,000 \pm 18\,000\,\mathrm{km}$. The atmosphere model yields a consistent radius of $37\,000 \pm 2\,900\,\mathrm{km}$.

Theoretical work on nova outbursts shows that in the minutes after the thermonuclear runaway the rise in bolometric luminosity occurs at approximately constant radius (José & Hernanz, 1998; Hillman et al., 2014). Once the energy has diffused from the bottom of the envelope to the photosphere (about 5–10 minutes after the onset of the runaway) expansion starts immediately, and the envelope is ejected (Aydi et al., 2020b) with velocities that can eventually reach up to $6\,000\,\mathrm{km\,s^{-1}}$. Thus, the photosphere will become orders of magnitude larger than a white dwarf in a matter of minutes to hours. Given that our derived photospheric radius is only a few times larger than a typical white dwarf radius ($3\,500 \lesssim \mathrm{R_{WD}} \lesssim 18\,000\,\mathrm{km}$, Bédard et al. 2017), *eROSITA* detected the "naked" photosphere just after the released energy reached the surface of the photosphere, before the main expansion of the envelope. At $t_0 + 10.3\,\mathrm{d}$ the shocked region of YZ Ret had expanded to an estimated < 1.6 astronomical units (Sokolovsky et al., 2022).

The *eROSITA* detection provides further constraints on the temperature evolution of the photosphere during a complete nova outburst. The effective temperature during the flash is expected to peak in the range $40\,\mathrm{eV} \lesssim kT \lesssim 100\,\mathrm{eV}$ and then gradually decline to $\sim$5 eV as the envelope expands over a period of a few hours to days and the peak emission shifts to the optical (Hillman et al., 2014; Kato et al., 2016). When the photosphere recedes back closer to the white dwarf surface during the supersoft state, the temperature is expected to take a similar value as during the flash. The detailed temperature profile depends on the core temperature, accretion rate, and mass of the white dwarf, but this overall pattern is ubiquitous for typical novae (Hillman et al., 2014). The temperature during the *eROSITA* observation, $kT \sim 28\,\mathrm{eV}$, is slightly below the expected peak temperature, suggesting that the observation was in the gradual decay phase of the flash. This interpretation is consistent with the possible flux decrease in the last approximately 6 s of the observation. During the supersoft state the temperature was around 30 eV (Fig. 7.3 and Sokolovsky et al. 2020a), which confirms that similar temperatures are measured during the flash and the supersoft phase.

Theoretical studies also predict that the existence and duration of the ignition flash correlates with the white dwarf mass (Hillman et al., 2014; Kato et al., 2017). Low-mass white dwarfs with approximately $0.65\,M_\odot$ are predicted to show only near-UV flashes, with durations of 5–10 d, while X-ray flashes are expected in moderate to high-mass white dwarfs with durations of 6–12 h for a mass of $1.0\,M_\odot$ (Hillman et al., 2014). The existence of the X-ray flash seen in YZ Ret therefore implies a relatively massive white dwarf, which is confirmed by the short duration of the flash, and consistent with the mass inferred from the atmosphere model fits, $M_{\mathrm{WD}} = (0.98 \pm 0.23)\,M_\odot$,

although this model does not include the effects of the expansion of the atmosphere.
With the successful detection of the flash of YZ Ret by SRG/*eROSITA*, the existence of X-ray flashes has now been observationally confirmed. On the basis of estimates for the Galactic nova rate (De et al., 2021), *eROSITA* is expected to detect at most one to two such events during its four year survey phase. This detection of the expanding white dwarf photosphere before the ejection of the envelope provides the last link of the predicted photospheric light curve evolution, as the initial UV flashes and all post-maximum phases have been detected. Therefore, our detection also adds the missing piece to measure the total nova energetics and completes the whole picture of the photospheric evolution of the thermonuclear runaway.

7.5 Summary and Conclusion

Novae are caused by runaway thermonuclear burning in the hydrogen-rich envelopes of accreting white dwarfs, which results in the envelope to expand rapidly and to eject most of its mass (Chomiuk et al., 2021; Starrfield et al., 2016). For more than 30 years, nova theory has predicted the existence of a "fireball" phase following directly the runaway fusion, which should be observable as a short, bright, and soft X-ray flash before the nova becomes visible in the optical (Hillman et al., 2014; Starrfield et al., 1990; Krautter, 2008).
In this chapter I presented the unequivocal detection of an extremely bright and very soft X-ray flash of the classical Galactic nova YZ Reticuli 11 hours prior to its 9 mag optical brightening. No X-ray source was detected 4 hours before and after the event, constraining the duration of the flash to shorter than 8 hours. In agreement with theoretical predictions (Starrfield et al., 1990; Kato et al., 2015, 2016; Morii et al., 2016), the source's spectral shape is consistent with a black body of $3.27^{+0.11}_{-0.33} \times 10^5$ K ($28.2^{+0.9}_{-2.8}$ eV), or a white dwarf atmosphere, radiating at the Eddington luminosity, with a photosphere that is only slightly larger than a typical white dwarf. This detection of the expanding white dwarf photosphere before the ejection of the envelope provides the last link of the predicted photospheric lightcurve evolution and opens a new window to measure the total nova energetics.
After publication of this result in König et al. (2022), a few follow-up papers were published (Walter, 2022; Kato et al., 2022a,c; Hachisu & Kato, 2023), in particular on the implications of this detection for theoretical models. Kato et al. (2022a) used the data presented here to calculated theoretical lightcurves for various white dwarf masses, mass-accretion rates, and mass loss rates from an optically thick wind. By comparing the duration, spectral properties and luminosity of the *eROSITA* observation to their models, they were able to further constrain the physical properties of nova YZ Ret. An essential point for their analysis are the *eROSITA* non-detections at $t_0 \pm 4$ h, which could exclude many of the theoretical models (Fig. 7.7).
Kato et al. (2022a) confirm that the temperature and luminosity derived here is consistent with their hydrostatic evolution model of a massive white dwarf. They constrain the white dwarf mass in YZ Ret to $\sim$1.3 $M_\odot$, close to the Chandrasekhar limit[2]. The short duration of the flash also

[2]Kato et al. (2022a) state that, without the timing constraints, they deduce a mass of $M_{\rm WD} \gtrsim 1.2\,{\rm M}_\odot$, barely consistent with the value derived in this thesis, $(0.98 \pm 0.23)\,{\rm M}_\odot$. The discrepancy can be explained by our assumption of local thermodynamic equilibrium in the atmosphere (see Suleimanov et al. 2013), that is, the model applied in

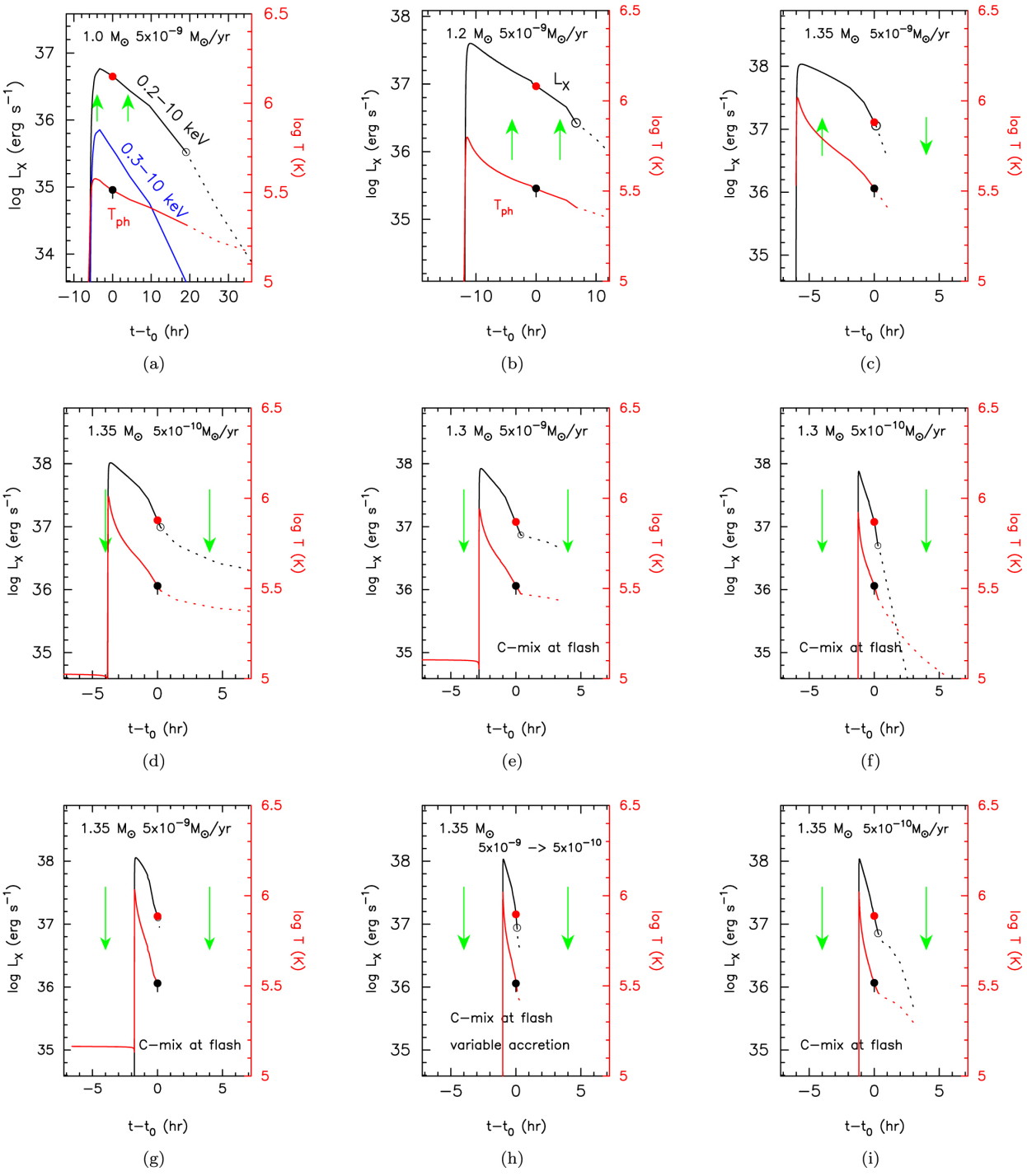

Figure 7.7: Theoretical X-ray flash lightcurves compared to the constraints of the YZ Ret flash (Fig. 3 from Kato et al., 2022a). Each panel denotes a model with different white dwarf mass, mass accretion rate, and carbon mixture. The red line denotes the predicted temporal variation of the photospheric temperature (right-side vertical axis). The black lines show the 0.2–10 keV X-ray flux (left-side vertical axis). The black and red points denote the measurement values of the *eROSITA* detection. Open circles denote the time where the optically thick wind starts and the dotted line marks the wind phase. The green arrows shows the times of the *eROSITA* non-detections. If the arrow faces upwards, the model is incompatible with the *eROSITA* non-detections.

constrains the mass accretion rate to $M_{\rm acc} \sim (5\text{–}50) \times 10^{-10}\,M_\odot\,{\rm yr}^{-1}$ and suggests a slight carbon contamination of core material in the envelope.
Furthermore, Kato et al. (2022a) argue that the launching of optically thick winds causes strong absorption of X-rays at values as high as $10^{24}\,{\rm cm}^{-2}$ (Hachisu & Kato, 2022). The absorpion possibly terminated the X-ray flash in YZ Ret when the photosphere reached ∼70 000 km. This value is only slightly higher than what we derived from the spectral modeling, indicating that the flash was extinguished soon after the *eROSITA* detection. This means that, with the detection of the X-ray flash, one can constrain the starting time of the wind. Lastly, Hachisu & Kato (2023) used the data presented here to develop a multi-wavelength lightcurve model that can reproduce the optical, X-ray, and γ-ray properties of YZ Ret. Their modeling narrows down the value of the white dwarf mass in YZ Ret to approximately $1.33\,{\rm M}_\odot$.

this thesis does not take the expansion of the photosphere into account.

Chapter 8

Conclusions and Outlook

In the outline of this thesis (Ch. 1), I formulated my first central question as

1. What is the structure of the accretion flow in the vicinity of a stellar-mass black hole?

One fundamental step in understanding the accretion flow is to comprehend the physical processes constituting its rapid X-ray variability. Part I of my thesis reported on the timing phenomenology of the black hole X-ray binary Cygnus X-1. By extending previous timing studies to soft X-ray energies with *NICER*, we showed that the well-known low- and high-frequency variability components likely represent individual physical processes. The low-frequency component can be associated with the emission of the accretion disk, being modulated by Comptonization. The high-frequency component can be interpreted to come solely from the Comptonized medium ("corona"). We detected a high coherence between the soft and hard X-rays and concluded that the accretion disk and corona are causally physically related in the hard and intermediate states. This connection fundamentally changes in the soft state as the coherence between soft X-rays, which are completely dominated by disk emission, and the coronal red noise variability drops. If one interprets the variability in the hard and intermediate state to be produced by propagating fluctuations, which causally connect the disk and corona, the drop in coherence could mean that the propagation of variability information is absent in the soft state, or at least does not reach the emitted radiation. Thus, this indicates that the process producing the coronal red noise washes out the main variability information that comes from the disk seed photons.
The second major result of Part I is the discovery of a previously unknown timing phenomenon, which only emerges when soft X-rays are considered. The feature is intrinsically correlated to the broad Lorentzian components, and coincides with an abrupt change of the time lag and a coherence drop. It can be seen significantly only in hard state observations where the power spectrum exhibits a double-humped shape. The occurrence in the overlap region of the Lorentzians indicates a fundamental connection to the underlying variability processes. We showed that the feature can be modeled as a relatively narrow Lorentzian located at the difference frequency of the broad components, which may indicate that the feature is due to a beat between the processes producing the broad band noise.

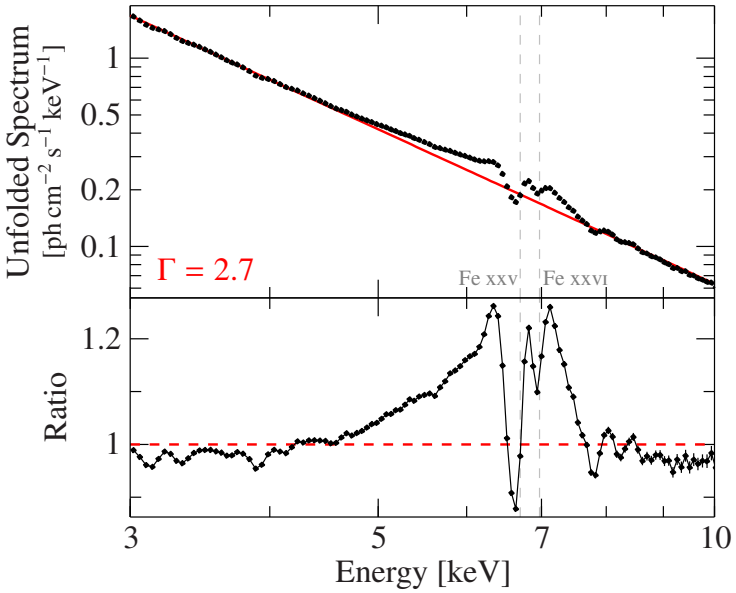

Figure 8.1: *NICER* spectrum of Cyg X-1 in the soft state (observation ID 1100320121). In addition to a relativistically broadened iron line, strong absorption lines are detected below the line energies of ionized iron. A power law with a photon index of 2.7 was used to unfold the spectrum.

We showed that this feature also occurs in the low hard state of low-mass X-ray binary black holes. It is, therefore, a general phenomenon in accreting black hole binaries, which motivates a more detailed characterization of the effect. A population study to infer whether the phenomenon shows up only on the lower branch of the q-diagram, as suggested by our preliminary comparison, is a logical next step.

Another potential follow-up project is to study the color-color diagram of low-mass X-ray binary black holes to investigate whether the zig-zag shape seen at low energies is solely an effect due to the accretion disk (see also Miyamoto et al. 1991, their Fig. 5), or whether it is a property intrinsic to Cyg X-1, for instance, due to ionization and absorption effects in the stellar wind. I also emphasize that Part I focused primarily on the variability aspect of the Cyg X-1 data. The spectroscopic information of these publicly available data has not yet been analyzed. As an outlook, I show a spectrum taken in the soft state (Fig. 8.1), which features strong absorption lines from ionized iron. Considering the large equivalent width of the line and its redshift, this detection indicates that fast moving ionized material is present in the system, potentially from a disk wind (e.g., Ponti et al., 2012), or due to intersecting clumps from the stellar wind (Nowak et al., 2011). Without doubt, it can be said that there are more exciting results hidden in these data.

In Part II, I presented the observational discovery of an X-ray flash of a nova, which has been predicted more than 30 years ago (Starrfield et al., 1990). The classical Galactic nova YZ Reticuli was serendipitously observed with the *eROSITA* telescope during the onset of its outbreak, roughly half a day before the source brightened by 9 magnitudes in the optical. At a peak brightness of 3.7 mag, the source was visible by the naked eye in the southern sky constellation Reticulum for several days. The X-ray data taken with the CCD instrument on-board *eROSITA* were affected by severe pile-up, which prohibited a straightforward modeling of the spectrum. In order to properly account for the pile-up distortions in the spectrum, it proved essential to understand the physics of the measurement process. By modeling the detector response with the SIXTE simulator, it was

Figure 8.2: Artists impression of a nova fireball. *Left:* Expansion of the photosphere during the initial X-ray flash (courtesy by Annika Kreikenbohm). *Right:* Cover page of Nature volume 605, issue 7909 (© Springer Nature).

possible to infer the physical parameters of the nova, show-casing the synergy of observations and simulations. The second central question formulated at the beginning was

2. What are the physical properties of the photosphere during the fireball phase of a nova?

We could show that the X-ray data are consistent with an approximately 327 000 K hot and roughly 50 000 km large spherical photosphere that emits as a black body at the Eddington luminosity (this was named a "nova fireball" on the cover of the publishing journal[1]; Fig. 8.2). These parameters and the outburst evolution are in excellent agreement with theoretical predictions and the general picture of a nova outburst. As the radius of a white dwarf is smaller than the derived photospheric radius by a factor of roughly 10, we concluded that the envelope of the nova at the time of the X-ray flash has already started expanding but has not yet been ejected into the interstellar medium. Furthermore, the *eROSITA* non-detections in the subsequent scan after the event place an upper limit of 8 h on the flash duration. These detections could constrain the white dwarf mass to be at around 1.3 $M_\odot$ (Kato et al., 2022a; Hachisu & Kato, 2023), which is close to the Chandrasekhar limit.

[1] https://www.nature.com/nature/volumes/605/issues/7909

What are the prospects and opportunities for the science of novae that come with this newly discovered class of events? Capturing the decay of the X-ray flash gives constraints on the early acceleration of the shell (see also Lépine et al., 1999), how it cools, and how the thermal radiation is shifted to lower energies (e.g., Pottasch, 1959, Fig. 1). A full observation of the decay phase can possibly also yield information about the asymmetry of the expanding shell (see also O'Brien et al., 2006). Furthermore, the X-ray flash facilitates studying the launching mechanism of optically thick winds from deep inside the photosphere (Kato & Hachisu, 1994) and their connection to γ-ray emission seen in later stages of the outburst (Abdo et al., 2010). Indeed, Hachisu & Kato (2023) used the data presented in this thesis to develop a comprehensive model that describes the optical, X-ray, and γ-ray properties of YZ Ret, taking the wind phase into account.
The *eROSITA* observation of YZ Ret was only 36 s long and it was not possible to constrain the decay timescale with these data. Probing the temporal expansion of the photosphere requires a longer, ideally uninterrupted observation of an X-ray flash. Due to the uncertainty of the source location before an outbreak, the chances of finding another X-ray flash in a classical nova in the Milky Way with a small field-of-view telescope are very small (see König et al. 2022 for an estimate of nova X-ray flashes in the 4 year *eROSITA* all-sky survey). It is important to observe as much sky area as possible to catch the onset of the nova in the X-rays. With the launch of the planned Chinese mission *Einstein Probe* (Yuan et al., 2018), serendipitous observations of classical novae could be feasible. A path-finder mission with an energy range of 0.5–4 keV has already demonstrated the feasibility of a new *lobster-eye* technology in orbit, which enables a field-of-view of $18.6° \times 18.6°$ (Zhang et al., 2022). The *Einstein Probe* will contain a follow-up telescope capable of starting observations 3–5 minutes after a trigger, and which also has the necessary soft response (0.3–10 keV) to observe the very soft X-ray flash (Chen et al., 2020). Other promising targets are recurrent novae in nearby galaxies with well-known recurrency periods. The best candidate is probably M31N 2008-12a in the Andromeda galaxy, whose one year recurrency period can be predicted to within one month (Kato et al., 2016).

Bibliography

Abbott B.P., Abbott R., Abbott T.D., et al., 2016, Observation of Gravitational Waves from a Binary Black Hole Merger., Phys. Rev. Lett. 116, 061102

Abbott B.P., Abbott R., Abbott T.D., et al., 2017a, GW170817: Observation of Gravitational Waves from a Binary Neutron Star Inspiral., Phys. Rev. Lett. 119, 161101

Abbott B.P., Abbott R., Abbott T.D., et al., 2017b, Multi-messenger Observations of a Binary Neutron Star Merger., ApJL 848, L12

Abbott R., Abbott T.D., Abraham S., et al., 2020a, GW190521: A Binary Black Hole Merger with a Total Mass of 150 $M_{\odot}$., Phys. Rev. Lett. 125, 101102

Abbott R., Abbott T.D., Abraham S., et al., 2020b, GW190814: Gravitational Waves from the Coalescence of a 23 Solar Mass Black Hole with a 2.6 Solar Mass Compact Object., ApJL 896, L44

Abdo A.A., Ackermann M., Ajello M., et al., 2010, Gamma-Ray Emission Concurrent with the Nova in the Symbiotic Binary V407 Cygni., Science 329, 817

Agostinelli S., Allison J., Amako K., et al., 2003, G EANT4—a simulation toolkit., Nucl. Instrum. Methods Phys. Res., Sect. A 506, 250

Alpar M.A., Shaham J., 1985, Is GX5 - 1 a millisecond pulsar?, Nature 316, 239

Altamirano D., Belloni T., Linares M., et al., 2011, The Faint "Heartbeats" of IGR J17091-3624: An Exceptional Black Hole Candidate., ApJL 742, L17

Altamirano D., Méndez M., 2015, The evolution of the X-ray phase lags during the outbursts of the black hole candidate GX 339-4., MNRAS 449, 4027

Althaus L.G., Benvenuto O.G., 1997, Evolution of Helium White Dwarfs of Low and Intermediate Masses., ApJ 477, 313

Amaro-Seoane P., Audley H., Babak S., et al., 2017, Laser Interferometer Space Antenna, White paper (arXiv:1702.00786)

Amenomori M., Bao Y.W., Bi X.J., et al., 2019, First Detection of Photons with Energy beyond 100 TeV from an Astrophysical Source., Phys. Rev. Lett. 123, 051101

Andrews J.J., Kalogera V., 2022, Constraining Black Hole Natal Kicks with Astrometric Microlensing., ApJ 930, 159

Arévalo P., Uttley P., 2006, Investigating a fluctuating-accretion model for the spectral-timing properties of accreting black hole systems., MNRAS 367, 801

Arnaud K., Smith R., Siemiginowska A., 2011, Handbook of X-ray Astronomy, Cambridge University Press, Cambridge, UK

Arnett W.D., 1977, Neutrino trapping during gravitational collapse of stars., ApJ 218, 815

Atalla M.M., Tannenbaum E., Scheibner E.J., 1959, Stabilization of silicon surfaces by thermally grown oxides., The Bell System Technical Journal 38, 749

Atwood W.B., Abdo A.A., Ackermann M., et al., 2009, The Large Area Telescope on the Fermi Gamma-Ray Space Telescope Mission., ApJ 697, 1071

Axelsson M., Borgonovo L., Larsson S., 2005, Evolution of the 0.01-25 Hz power spectral components in

Cygnus X-1., A&A 438, 999
Axelsson M., Borgonovo L., Larsson S., 2006, Probing the temporal variability of Cygnus X-1 into the soft state., A&A 452, 975
Axelsson M., Veledina A., 2021, Accretion geometry of the black hole binary MAXI J1820+070 probed by frequency-resolved spectroscopy., MNRAS 507, 2744
Aydi E., Buckley D.A.H., Chomiuk L., et al., 2020a, SALT spectroscopic classification of MGAB-V207 as a classical nova., Astronomer's Telegram 13867
Aydi E., Chomiuk L., Izzo L., et al., 2020b, Early Spectral Evolution of Classical Novae: Consistent Evidence for Multiple Distinct Outflows., ApJ 905, 62
Aydi E., Page K.L., Kuin N.P.M., et al., 2018, Multiwavelength observations of nova SMCN 2016-10a - one of the brightest novae ever observed., MNRAS 474, 2679
Baade W., Zwicky F., 1934, Remarks on Super-Novae and Cosmic Rays., Phys. Rev. 46, 76
Bachetti M., Harrison F.A., Cook R., et al., 2015, No Time for Dead Time: Timing Analysis of Bright Black Hole Binaries with NuSTAR., ApJ 800, 109
Bachetti M., Huppenkothen D., 2023, Fourier Domain. In: Bambi C., Santangelo A. (eds.) Handbook of X-ray and Gamma-ray Astrophysics. Springer, Singapore (arXiv:2209.07954)
Bahramian A., Degenaar N., 2022, Low-Mass X-ray Binaries. In: Bambi C., Santangelo A. (eds.) Handbook of X-ray and Gamma-ray Astrophysics. Springer, Singapore (arXiv:2206.10053)
Balbus S.A., Hawley J.F., 1991, A Powerful Local Shear Instability in Weakly Magnetized Disks. I. Linear Analysis., ApJ 376, 214
Baldini L., Bucciantini N., Lalla N.D., et al., 2022, ixpeobssim: A simulation and analysis framework for the imaging X-ray polarimetry explorer., SoftwareX 19, 101194
Ballet J., 1999, Pile-up on X-ray CCD instruments., A&AS 135, 371
Bałucińska-Church M., Church M.J., Charles P.A., et al., 2000, The Distribution of X-ray Dips with Orbital Phase in Cygnus X-1., MNRAS 311, 861
Bambi C., Brenneman L.W., Dauser T., et al., 2021, Towards Precision Measurements of Accreting Black Holes Using X-Ray Reflection Spectroscopy., SSRv 217, 65
Bardeen J.M., Press W.H., Teukolsky S.A., 1972, Rotating Black Holes: Locally Nonrotating Frames, Energy Extraction, and Scalar Synchrotron Radiation., ApJ 178, 347
Barillier E., Grinberg V., Horn D., et al., 2023, NICER/NuSTAR Characterization of 4U 1957+11: A Near Maximally Spinning Black Hole Potentially in the Mass Gap., ApJ 944, 165
Barret D., Albouys V., Herder J.W.d., et al., 2023, The Athena X-ray Integral Field Unit: a consolidated design for the system requirement review of the preliminary definition phase., Experimental Astronomy 55, 373
Barret D., Cappi M., 2019, Inferring black hole spins and probing accretion/ejection flows in AGNs with the Athena X-ray Integral Field Unit., A&A 628, A5
Barret D., Trong T.L., den Herder J.W., et al., 2018, The ATHENA X-ray Integral Field Unit (X-IFU)., In: den Herder J.W.A., Nikzad S., Nakazawa K. (eds.) Proc. SPIE., Vol. 10699. Space Telescopes and Instrumentation 2018: Ultraviolet to Gamma Ray, Austin, Texas, United States, p. 106991G
Baschek B., Scholz M., Wehrse R., 1991, The parameters R and Teff in stellar models and observations., A&A 246, 374
Bath G.T., Shaviv G., 1976, Classical novae - a steady state, constant luminosity, continuous ejection model., MNRAS 175, 305
Becker W., Hurley-Walker N., Weinberger C., et al., 2021, Hoinga: a supernova remnant discovered in the SRG/eROSITA All-Sky Survey eRASS1., A&A 648, A30
Bédard A., Bergeron P., Fontaine G., 2017, Measurements of Physical Parameters of White Dwarfs: A Test of the Mass-Radius Relation., ApJ 848, 11
Belczynski K., Ziolkowski J., 2009, On the Apparent Lack of Be X-Ray Binaries with Black Holes., ApJ 707,

870
Belloni D., Schreiber M.R., 2023, Formation and Evolution of Accreting Compact Objects. In: Bambi C., Santangelo A. (eds.) Handbook of X-ray and Gamma-ray Astrophysics. Springer, Singapore (arXiv:2303.08997)
Belloni T., Klein-Wolt M., Méndez M., et al., 2000, A model-independent analysis of the variability of GRS 1915+105., A&A 355, 271
Belloni T., Psaltis D., van der Klis M., 2002, A Unified Description of the Timing Features of Accreting X-Ray Binaries., ApJ 572, 392
Belloni T.M., 2010, States and Transitions in Black Hole Binaries. In: Belloni T. (ed.) The Jet Paradigm, Vol. 794. Lecture Notes in Physics Springer, Berlin, p. 53
Belloni T.M., Bhattacharya D., 2022, Basics of Fourier Analysis for High-Energy Astronomy. In: Bambi C., Santangelo A. (eds.) Handbook of X-ray and Gamma-ray Astrophysics. Springer, Singapore (arXiv:2203.04106)
Belloni T.M., Hasinger G., 1990, Variability in the noise properties of Cygnus X-1., A&A 227, L33
Belloni T.M., Homan J., Casella P., et al., 2005, The evolution of the timing properties of the black-hole transient GX 339-4 during its 2002/2003 outburst., A&A 440, 207
Belloni T.M., Méndez M., Zhang C., 2020, Timing Neutron Stars: Pulsations, Oscillations and Explosions, Astrophysics and Space Science Library, Springer Berlin Heidelberg
Belloni T.M., Motta S.E., 2016, Transient Black Hole Binaries., In: Bambi C. (ed.) Astrophysics of Black Holes: From Fundamental Aspects to Latest Developments, Vol. 440. Astrophysics and Space Science Library, p. 61
Beloborodov A.M., 1999, Plasma Ejection from Magnetic Flares and the X-Ray Spectrum of Cygnus X-1., ApJL 510, L123
Bendat J., Piersol A., 2010, Random Data: Analysis and Measurement Procedures, Wiley Series in Probability and Statistics, Wiley, 4 edition
Bendat J.S., Piersol A.G., 1986, Decomposition of wave forces into linear and non-linear components., J. Sound & Vibration 106, 391
Bethe H.A., 1939, Energy Production in Stars., Phys. Rev. 55, 434
Bethe H.A., Wilson J.R., 1985, Revival of a Stalled Supernova Shock by Neutrino Heating., ApJ 295, 14
Blaauw A., 1961, On the origin of the O- and B-type stars with high velocities (the "run-away" stars), and some related problems., Bulletin of the Astronomical Institutes of the Netherlands 15, 265
Blackett P.M.S., Occhialini G.P.S., 1933, Some Photographs of the Tracks of Penetrating Radiation., Proc. R. Soc. London, Ser. A 139, 699
Blandford R.D., Payne D.G., 1982, Hydromagnetic flows from accretion disks and the production of radio jets., MNRAS 199, 883
Blandford R.D., Znajek R.L., 1977, Electromagnetic extraction of energy from Kerr black holes., MNRAS 179, 433
Böck M., Grinberg V., Pottschmidt K., et al., 2011, Spectro-timing analysis of Cygnus X-1 during a fast state transition., A&A 533, A8
Boller T., Freyberg M.J., Trümper J., et al., 2016, Second ROSAT all-sky survey (2RXS) source catalogue., A&A 588, A103
Boller T., Liu T., Weber P., et al., 2021, Extreme ultra-soft X-ray variability in an eROSITA observation of the narrow-line Seyfert 1 galaxy 1H 0707-495., A&A 647, A6
Bolton C.T., 1972, Identification of Cygnus X-1 with HDE 226868., Nature 235, 271
Bondi H., Hoyle F., 1944, On the mechanism of accretion by stars., MNRAS 104, 273
Bowyer S., Byram E.T., Chubb T.A., Friedman H., 1965, Cosmic X-ray Sources., Sci 147, 394
Boyle W.S., Smith G.E., 1970, Charge coupled semiconductor devices., The Bell System Technical Journal 49, 587
Brandi E., Quiroga C., Mikołajewska J., et al., 2009, Spectroscopic orbits and variations of RS Ophiuchi.,

A&A 497, 815
Bright J.S., Fender R.P., Motta S.E., et al., 2020, An extremely powerful long-lived superluminal ejection from the black hole MAXI J1820+070., Nature Astronomy 4, 697
Brunner H., Liu T., Lamer G., et al., 2022, The eROSITA Final Equatorial Depth Survey (eFEDS). X-ray catalogue., A&A 661, A1
Buisson D.J.K., Fabian A.C., Barret D., et al., 2019, MAXI J1820+070 with NuSTAR I. An increase in variability frequency but a stable reflection spectrum: coronal properties and implications for the inner disc in black hole binaries., MNRAS 490, 1350
Burbidge E.M., Burbidge G.R., Fowler W.A., Hoyle F., 1957, Synthesis of the Elements in Stars., Rev. Mod. Phys. 29, 547
Burrows A., Vartanyan D., 2021, Core-collapse supernova explosion theory., Nature 589, 29
Caballero I., Wilms J., 2012, X-ray pulsars: a review., Memorie della Societa Astronomica Italiana 83, 230
Cabanac C., Henri G., Petrucci P.O., et al., 2010, Variability of X-ray binaries from an oscillating hot corona., MNRAS 404, 738
Campana S., Stella L., 1995, Reverberation by a relativistic accretion disc., MNRAS 272, 585
Cao Y., Kasliwal M.M., Neill J.D., et al., 2012, Classical Novae in Andromeda: Light Curves from the Palomar Transient Factory and GALEX., ApJ 752, 133
Carpano S., Pollock A.M.T., Wilms J., et al., 2007, A Wolf-Rayet/black-hole X-ray binary candidate in NGC 300., A&A 461, L9
Carr A., Said K., Davis T.M., et al., 2020, WiFeS follow-up observations of the naked-eye nova associated to MGAB-V207., Astronomer's Telegram 13874
Carroll B., Ostlie D., 2017, An Introduction to Modern Astrophysics, Cambridge University Press, Cambridge, second edition
Casares J., Negueruela I., Ribó M., et al., 2014, A Be-type star with a black-hole companion., Nature 505, 378
Cash W., 1979, Parameter estimation in astronomy through application of the likelihood ratio., ApJ 228, 939
Castor J.I., Abbott D.C., Klein R.I., 1975, Radiation-driven winds in Of stars., ApJ 195, 157
Celotti A., Miller J.C., Sciama D.W., 1999, Astrophysical evidence for the existence of black holes., Classical and Quantum Gravity 16, A3
Chabrier G., Brassard P., Fontaine G., Saumon D., 2000, Cooling Sequences and Color-Magnitude Diagrams for Cool White Dwarfs with Hydrogen Atmospheres., ApJ 543, 216
Chandrasekhar S., 1931, The Maximum Mass of Ideal White Dwarfs., ApJ 74, 81
Chen Y., Cui W., Han D., et al., 2020, Status of the follow-up x-ray telescope onboard the Einstein Probe satellite., In: Proc. SPIE., Vol. 11444. Space Telescopes and Instrumentation 2020: Ultraviolet to Gamma Ray, Online Only, p. 114445B
Chiu H.Y., 1964, Supernovae, neutrinos, and neutron stars., Annals of Physics 26, 364
Chiu H.Y., Stabler R.C., 1961, Emission of Photoneutrinos and Pair Annihilation Neutrinos from Stars., Phys. Rev. 122, 1317
Chomiuk L., Linford J.D., Yang J., et al., 2014, Binary orbits as the driver of γ-ray emission and mass ejection in classical novae., Nature 514, 339
Chomiuk L., Metzger B.D., Shen K.J., 2021, New Insights into Classical Novae., ARA&A 59, 391
Churazov E., Gilfanov M., Revnivtsev M., 2001, Soft state of Cygnus X-1: stable disc and unstable corona., MNRAS 321, 759
Colgate S.A., White R.H., 1966, The Hydrodynamic Behavior of Supernovae Explosions., ApJ 143, 626
Collonge M., Busca P., Fajardo P., Williams M., 2022, Monte Carlo simulations for XIDer, a novel digital integration X-ray detector for the next generation of synchrotron radiation sources., Journal of Instrumentation 17, C01037

Compton A.H., 1923, A Quantum Theory of the Scattering of X-rays by Light Elements., Phys. Rev. 21, 483
Corbel S., Coriat M., Brocksopp C., et al., 2013, The 'universal' radio/X-ray flux correlation: the case study of the black hole GX 339-4., MNRAS 428, 2500
Corral-Santana J.M., Casares J., Muñoz-Darias T., et al., 2016, BlackCAT: A catalogue of stellar-mass black holes in X-ray transients., A&A 587, A61
Crawford J.A., Kraft R.P., 1956, An Intrepretation of AE Aquarii., ApJ 123, 44
Crowther P.A., 2007, Physical Properties of Wolf-Rayet Stars., ARA&A 45, 177
Cui W., Heindl W.A., Rothschild R.E., et al., 1997a, Rossi X-Ray Timing Explorer Observation of Cygnus X-1 in Its High State., ApJL 474, L57
Cui W., Zhang S.N., Focke W., Swank J.H., 1997b, Temporal Properties of Cygnus X-1 during the Spectral Transitions., ApJ 484, 383
Darnley M.J., Henze M., Bode M.F., et al., 2016, M31N 2008-12a - The Remarkable Recurrent Nova in M31: Panchromatic Observations of the 2015 Eruption., ApJ 833, 149
Darnley M.J., Ribeiro V.A.R.M., Bode M.F., et al., 2012, On the Progenitors of Galactic Novae., ApJ 746, 61
Dauser T., Falkner S., Lorenz M., et al., 2019, SIXTE: a generic X-ray instrument simulation toolkit., A&A 630, A66
Dauser T., Garcia J., Wilms J., et al., 2013, Irradiation of an accretion disc by a jet: general properties and implications for spin measurements of black holes., MNRAS 430, 1694
Davis J.E., 2001, Event Pileup in Charge-coupled Devices., ApJ 562, 575
Davis J.E., Bautz M.W., Dewey D., et al., 2012, Raytracing with MARX: x-ray observatory design, calibration, and support., In: Takahashi T., Murray S.S., den Herder J.W.A. (eds.) Proc. SPIE., Vol. 8443. Space Telescopes and Instrumentation 2012: Ultraviolet to Gamma Ray, Amsterdam, Netherlands, p. 84431A
De K., Kasliwal M.M., Hankins M.J., et al., 2021, A Population of Heavily Reddened, Optically Missed Novae from Palomar Gattini-IR: Constraints on the Galactic Nova Rate., ApJ 912, 19
De Marco B., Ponti G., Cappi M., et al., 2013, Discovery of a relation between black hole mass and soft X-ray time lags in active galactic nuclei., MNRAS 431, 2441
De Marco B., Ponti G., Muñoz-Darias T., Nandra K., 2015, Tracing the Reverberation Lag in the Hard State of Black Hole X-Ray Binaries., ApJ 814, 50
De Marco B., Zdziarski A.A., Ponti G., et al., 2021, The inner flow geometry in MAXI J1820+070 during hard and hard-intermediate states., A&A 654, A14
Debnath D., Chakrabarti S.K., Nandi A., Mandal S., 2008, Spectral and timing evolution of GRO J1655-40 during its outburst of 2005., Bull. Astron. Soc. India 36, 151
Dennerl K., Burkert W., Burwitz V., et al., 2012, Determination of the eROSITA mirror half energy width (HEW) with subpixel resolution., In: Takahashi T., Murray S.S., den Herder J.W.A. (eds.) Proc. SPIE., Vol. 8443. Space Telescopes and Instrumentation 2012: Ultraviolet to Gamma Ray, Amsterdam, Netherlands, p. 844350
Diefendorff K., 1999, Pentium III = Pentium II + SSE., Microprocessor Report 13, 1
Döhring T., Stollenwerk M., Gong Q., et al., 2015, The challenge of developing thin mirror shells for future x-ray telescopes., In: Duparr A.V., Geyl R. (eds.) Proc. SPIE., Vol. 9628. Optical Systems Design 2015: Optical Fabrication, Testing, and Metrology V, Jena, Germany, p. 962809
Done C., Diaz Trigo M., 2010, A re-analysis of the iron line in the XMM-Newton data from the low/hard state in GX339-4., MNRAS 407, 2287
Done C., Gierliński M., 2003, Observing the effects of the event horizon in black holes., MNRAS 342, 1041
Done C., Gierliński M., Kubota A., 2007, Modelling the behaviour of accretion flows in X-ray binaries. Everything you always wanted to know about accretion but were afraid to ask., Astron. Astrophys. Rev. 15, 1

Done C., Mulchaey J.S., Mushotzky R.F., Arnaud K.A., 1992, An Ionized Accretion Disk in Cygnus X-1., ApJ 395, 275
Doroshenko V., Suleimanov V., Pühlhofer G., Santangelo A., 2022, A strangely light neutron star within a supernova remnant., Nature Astronomy 6, 1444
Dove J.B., Wilms J., Maisack M., Begelman M.C., 1997, Self-consistent Thermal Accretion Disk Corona Models for Compact Objects. II. Application to Cygnus X-1., ApJ 487, 759
Drake J.J., Orio M., Bearmore A., et al., 2020, Chandra high resolution X-ray spectroscopy of Nova Ret 2020., Astronomer's Telegram 14214
Dubus G., Guillard N., Petrucci P.O., Martin P., 2017, Sizing up the population of gamma-ray binaries., A&A 608, A59
Duchêne G., Kraus A., 2013, Stellar Multiplicity., ARA&A 51, 269
Duerbeck H.W., 1981, Light curve types, absolute magnitudes, and physical properties of galactic novae., PASP 93, 165
Duerbeck H.W., 2008, Novae: an historical perspective. In: Bode M.F., Evans A. (eds.) Classical Novae. Cambridge Astrophysics Cambridge University Press, second edition, p. 1–15
Duquennoy A., Mayor M., 1991, Multiplicity among Solar Type Stars in the Solar Neighbourhood - Part Two - Distribution of the Orbital Elements in an Unbiased Sample., A&A 248, 485
Duro R., Dauser T., Wilms J., et al., 2011, The broad iron Kα line of Cygnus X-1 as seen by XMM-Newton in the EPIC-pn modified timing mode., A&A 533, L3
Dziewonski A.M., Anderson D.L., 1981, Preliminary reference Earth model., Physics of the Earth and Planetary Interiors 25, 297
Eddington A.S., 1920, The Internal Constitution of the Stars., Nature 106, 14
Edgar R., 2004, A review of Bondi-Hoyle-Lyttleton accretion., New Astron. Rev. 48, 843
Edge A.C., Stewart G.C., Fabian A.C., Arnaud K.A., 1990, An X-ray flux-limited sample of clusters of galaxies : evidence for evolution of the luminosity function., MNRAS 245, 559
Einstein A., 1905, Über einen die Erzeugung und Verwandlung des Lichtes betreffenden heuristischen Gesichtspunkt., Annalen der Physik 322, 132
Einstein A., 1916, Die Grundlage der allgemeinen Relativitätstheorie., Annalen der Physik 354, 769
El-Badry K., Rix H.W., Cendes Y., et al., 2023a, A red giant orbiting a black hole., MNRAS 521, 4323
El-Badry K., Rix H.W., Quataert E., et al., 2023b, A Sun-like star orbiting a black hole., MNRAS 518, 1057
El Mellah I., Sundqvist J.O., Keppens R., 2018, Accretion from a clumpy massive-star wind in supergiant X-ray binaries., MNRAS 475, 3240
Elvis M., Page C.G., Pounds K.A., et al., 1975, Discovery of powerful transient X-ray source A0620-00 with Ariel V Sky Survey Experiment., Nature 257, 656
Esin A.A., McClintock J.E., Narayan R., 1997, Advection-Dominated Accretion and the Spectral States of Black Hole X-Ray Binaries: Application to Nova Muscae 1991., ApJ 489, 865
Event Horizon Telescope CollaborationAkiyama K., Alberdi A., et al., 2019, First M87 Event Horizon Telescope Results. I. The Shadow of the Supermassive Black Hole., ApJL 875, L1
Fabian A.C., Buisson D.J., Kosec P., et al., 2020, The soft state of the black hole transient source MAXI J1820+070: emission from the edge of the plunge region?, MNRAS 493, 5389
Fabian A.C., Rees M.J., Stella L., White N.E., 1989, X-ray fluorescence from the inner disc in Cygnus X-1., MNRAS 238, 729
Fabian A.C., Zoghbi A., Ross R.R., et al., 2009, Broad line emission from iron K- and L-shell transitions in the active galaxy 1H0707-495., Nature 459, 540
Fabrika S., 2004, The jets and supercritical accretion disk in SS433., Astrophysics and Space Physics Reviews 12, 1
Fano U., 1947, Ionization Yield of Radiations. II. The Fluctuations of the Number of Ions., Phys. Rev. 72, 26

Farmer R., Renzo M., de Mink S.E., et al., 2019, Mind the Gap: The Location of the Lower Edge of the Pair-instability Supernova Black Hole Mass Gap., ApJ 887, 53
Fender R.P., Belloni T.M., Gallo E., 2004, Towards a unified model for black hole X-ray binary jets., MNRAS 355, 1105
Fender R.P., Gallo E., Jonker P.G., 2003, Jet-dominated states: an alternative to advection across black hole event horizons in 'quiescent' X-ray binaries., MNRAS 343, L99
Feng M.Z., Kong L.D., Wang P.J., et al., 2022, Evolution of Accretion Modes between Spectral States Inferred from Spectral and Timing Analysis of Cygnus X-1 with Insight-HXMT Observations., ApJ 934, 47
Ferrarese L., Merritt D., 2000, A Fundamental Relation between Supermassive Black Holes and Their Host Galaxies., ApJL 539, L9
Finlay C.C., Maus S., Beggan C.D., et al., 2010, International Geomagnetic Reference Field: the eleventh generation., Geophysical Journal International 183, 1216
Fontaine G., Brassard P., Bergeron P., 2001, The Potential of White Dwarf Cosmochronology., PASP 113, 409
Formaggio J.A., Zeller G.P., 2012, From eV to EeV: Neutrino cross sections across energy scales., Rev. Mod. Phys. 84, 1307
Fornasini F.M., Antoniou V., Dubus G., 2023, High-mass X-ray Binaries. In: Bambi C., Santangelo A. (eds.) Handbook of X-ray and Gamma-ray Astrophysics. Springer, Singapore (arXiv:2308.02645)
Fowler R.H., 1926, On dense matter., MNRAS 87, 114
Fraley G.S., 1968, Supernovae Explosions Induced by Pair-Production Instability., Ap&SS 2, 96
Frampton P.H., Kawasaki M., Takahashi F., Yanagida T.T., 2010, Primordial black holes as all dark matter., Journal of Cosmology and Astroparticle Physics 2010, 023
Frank J., King A., Raine D., 2002, Accretion Power in Astrophysics, Cambridge University Press, 3 edition
Frew D.J., Parker Q.A., 2010, Planetary Nebulae: Observational Properties, Mimics and Diagnostics., Proc. Astron. Soc. Aust. 27, 129
Freyberg M.J., Bräuninger H., Burkert W., et al., 2005, The MPE X-ray test facility PANTER: Calibration of hard X-ray (15-50 kev) optics., Experimental Astronomy 20, 405
Friedman H., Lichtman S.W., Byram E.T., 1951, Photon Counter Measurements of Solar X-Rays and Extreme Ultraviolet Light., Phys. Rev. 83, 1025
Fryer C.L., Woosley S.E., Heger A., 2001, Pair-Instability Supernovae, Gravity Waves, and Gamma-Ray Transients., ApJ 550, 372
Fujimoto M., Iben, Icko J., 1992, Constraints on Element Mixing in Classical Novae., ApJ 399, 646
Gallo E., Fender R.P., Pooley G.G., 2003, A universal radio-X-ray correlation in low/hard state black hole binaries., MNRAS 344, 60
García J., Dauser T., Reynolds C.S., et al., 2013, X-Ray Reflected Spectra from Accretion Disk Models. III. A Complete Grid of Ionized Reflection Calculations., ApJ 768, 146
García J., Kallman T.R., 2010, X-ray Reflected Spectra from Accretion Disk Models. I. Constant Density Atmospheres., ApJ 718, 695
García J.A., McClintock J.E., Steiner J.F., et al., 2014, An Empirical Method for Improving the Quality of RXTE PCA Spectra., ApJ 794, 73
García J.A., Steiner J.F., McClintock J.E., et al., 2015, X-Ray Reflection Spectroscopy of the Black Hole GX 339–4: Exploring the Hard State with Unprecedented Sensitivity., ApJ 813, 84
Gatti E., Rehak P., 1984, Semiconductor drift chamber — An application of a novel charge transport scheme., Nuclear Instruments and Methods in Physics Research 225, 608
Gehrz R.D., Truran J.W., Williams R.E., Starrfield S., 1998, Nucleosynthesis in Classical Novae and Its Contribution to the Interstellar Medium., PASP 110, 3
Gendreau K.C., Arzoumanian Z., Adkins P.W., et al., 2016, The Neutron star Interior Composition Explorer

(NICER): design and development., In: den Herder J.W.A., Takahashi T., Bautz M. (eds.) Proc. SPIE., Vol. 9905. Space Telescopes and Instrumentation 2016: Ultraviolet to Gamma Ray, Edinburgh, United Kingdom, p. 99051H
George I.M., Fabian A.C., 1991, X-ray reflection from cold matter in Active Galactic Nuclei and X-ray binaries., MNRAS 249, 352
George I.M., Rots A., Mukai K., 1994, Guidelines for defining FITS formats for event lists, OGIP Memo OGIP/94-003, Code 668, NASA/GSFC, Greenbelt, MD 20771
Giacconi R., 2009, History of X-ray telescopes and astronomy., Experimental Astronomy 25, 143
Giacconi R., Branduardi G., Briel U., et al., 1979, The Einstein (HEAO 2) X-ray Observatory., ApJ 230, 540
Giacconi R., Gursky H., Kellogg E., et al., 1971, Discovery of Periodic X-Ray Pulsations in Centaurus X-3 from UHURU., ApJL 167, L67
Giacconi R., Gursky H., Paolini F.R., Rossi B.B., 1962, Evidence for x Rays From Sources Outside the Solar System., Phys. Rev. Lett. 9, 439
Giacconi R., Rossi B., 1960, A 'Telescope' for Soft X-Ray Astronomy., J. Geophys. Res. 65, 773
Gierliński M., Done C., 2004, Black hole accretion discs: reality confronts theory., MNRAS 347, 885
Gilfanov M., 2010, X-Ray Emission from Black-Hole Binaries. In: Belloni T. (ed.) Lecture Notes in Physics, Vol. 794. Springer-Verlag Berlin Heidelberg, p. 17
Gilfanov M., Churazov E., Revnivtsev M., 2000, Frequency-resolved spectroscopy of Cyg X-1: fast variability of the reflected emission in the soft state., MNRAS 316, 923
Gleissner T., Wilms J., Pooley G.G., et al., 2004a, Long term variability of Cygnus X-1. III. Radio-X-ray correlations., A&A 425, 1061
Gleissner T., Wilms J., Pottschmidt K., et al., 2004b, Long term variability of Cyg X-1. II. The rms-flux relation., A&A 414, 1091
Gorenstein P., Gursky H., Garmire G., 1968, The Analysis of X-Ray Spectra., ApJ 153, 885
Grinberg V., Hell N., Pottschmidt K., et al., 2013, Long term variability of Cygnus X-1. V. State definitions with all sky monitors., A&A 554, A88
Grinberg V., Leutenegger M.A., Hell N., et al., 2015, Long term variability of Cygnus X-1. VII. Orbital variability of the focussed wind in Cyg X-1/HDE 226868 system., A&A 576, A117
Grinberg V., Nowak M.A., Hell N., 2020, Color-color diagrams as tools for assessment of the variable absorption in high mass X-ray binaries., A&A 643, A109
Grinberg V., Pottschmidt K., Böck M., et al., 2014, Long term variability of Cygnus X-1. VI. Energy-resolved X-ray variability 1999-2011., A&A 565, A1
Guilbert P.W., Rees M.J., 1988, 'Cold' material in non-thermal sources., MNRAS 233, 475
Gutierrez J., Garcia-Berro E., Iben, Icko J., et al., 1996, The Final Evolution of ONeMg Electron-Degenerate Cores., ApJ 459, 701
H. E. S. S. Collaboration, Aharonian F., Ait Benkhali F., et al., 2022, Time-resolved hadronic particle acceleration in the recurrent nova RS Ophiuchi., Science 376, 77
Haardt F., Maraschi L., 1991, A Two-Phase Model for the X-Ray Emission from Seyfert Galaxies., ApJL 380, L51
Haberl F., Maitra C., Carpano S., et al., 2022, eROSITA calibration and performance verification phase: High-mass X-ray binaries in the Magellanic Clouds., A&A 661, A25
Hachisu I., Kato M., 2006, A Universal Decline Law of Classical Novae., ApJS 167, 59
Hachisu I., Kato M., 2022, A Strong Shock During a Nova Outburst: An Origin of Multiple Velocity Systems in Optical Spectra and of High-energy Emissions., ApJ 939, 1
Hachisu I., Kato M., 2023, A Multiwavelength Light-curve Analysis of the Classical Nova YZ Ret: An Extension of the Universal Decline Law to the Nebular Phase., ApJ 953, 78
Hachisu I., Kato M., Luna G.J.M., 2007, Supersoft X-Ray Light Curve of RS Ophiuchi (2006)., ApJL 659, L153

Haensel P., Potekhin A.Y., Yakovlev D.G., 2007, Neutron Stars 1 : Equation of State and Structure, Vol. 326, Springer, New York
Haensel P., Zdunik J.L., Schaefer R., 1986, Strange quark stars., A&A 160, 121
Hanke M., 2007, High-resolution X-ray Spectroscopy of the Black Hole Cygnus X-1 with the Chandra X-ray Observatory., *Master's thesis*, Friedrich Alexander Universität of Erlangen-Nürnberg
Hanke M., 2011, Probing the Environment of Accreting Compact Objects, PhD thesis, Friedrich Alexander Universität of Erlangen-Nürnberg
Hanuschik R.W., 1996, On the structure of Be star disks., A&A 308, 170
Harding A.K., Lai D., 2006, Physics of strongly magnetized neutron stars., Reports on Progress in Physics 69, 2631
Harrison F.A., Craig W.W., Christensen F.E., et al., 2013, The Nuclear Spectroscopic Telescope Array (NuSTAR) High-energy X-Ray Mission., ApJ 770, 103
Hawking S., 1971, Gravitationally collapsed objects of very low mass., MNRAS 152, 75
Hawking S.W., 1975, Particle creation by black holes., Communications in Mathematical Physics 43, 199
Hawking S.W., 1976, Breakdown of predictability in gravitational collapse., Phys. Rev. D 14, 2460
Hawking S.W., Ellis G.F.R., 1973, The Large Scale Structure of Space-Time, Cambridge Monographs on Mathematical Physics, Cambridge University Press
Heber U., 2009, Hot Subdwarf Stars., ARA&A 47, 211
Heil O., 1935, Improvements in or relating to electrical amplifiers and other control arrangements and devices, British Patent No. 439,457 (filed 5 March 1935. Issued 6 December 1935)
Heise J., 1985, X-Ray Emission from Isolated Hot White Dwarfs., SSRv 40, 79
Heisenberg W., 1927, Über den anschaulichen Inhalt der quantentheoretischen Kinematik und Mechanik., Zeitschrift für Physik 43, 172
Henze M., Ness J.U., Darnley M.J., et al., 2015, A remarkable recurrent nova in M 31: The predicted 2014 outburst in X-rays with Swift., A&A 580, A46
Hernanz M., Gómez-Gomar J., José J., 2002, The prompt gamma-ray emission of novae., New Astron. Rev. 46, 559
Hernanz M., José J., Coc A., et al., 1999, Gamma-Ray Emission from Novae Related to Positron Annihilation: Constraints on its Observability Posed by New Experimental Nuclear Data., ApJL 526, L97
Hessels J.W.T., Ransom S.M., Stairs I.H., et al., 2006, A Radio Pulsar Spinning at 716 Hz., Science 311, 1901
Hewish A., Bell S.J., Pilkington J.D.H., et al., 1968, Observation of a Rapidly Pulsating Radio Source., Nature 217, 709
Hillebrandt W., Niemeyer J.C., 2000, Type IA Supernova Explosion Models., ARA&A 38, 191
Hillman Y., Prialnik D., Kovetz A., et al., 2014, Nova multiwavelength light curves: predicting UV precursor flashes and pre-maximum halts., MNRAS 437, 1962
Hiramatsu D., Howell D.A., Van Dyk S.D., et al., 2021, The electron-capture origin of supernova 2018zd., Nature Astronomy 5, 903
Hirsch M., Hell N., Grinberg V., et al., 2019, Chandra X-ray spectroscopy of the focused wind in the Cygnus X-1 system. III. Dipping in the low/hard state., A&A 626, A64
Hjellming R.M., Rupen M.P., 1995, Episodic ejection of relativistic jets by the X-ray transient GRO J1655 - 40., Nature 375, 464
Homan J., Bright J., Motta S.E., et al., 2020, A Rapid Change in X-Ray Variability and a Jet Ejection in the Black Hole Transient MAXI J1820+070., ApJL 891, L29
Homan J., Wijnands R., van der Klis M., et al., 2001, Correlated X-Ray Spectral and Timing Behavior of the Black Hole Candidate XTE J1550-564: A New Interpretation of Black Hole States., ApJS 132, 377
Honeycutt R.K., Kafka S., 2004, Characteristics of High-State/Low-State Transitions in VY Sculptoris Stars., AJ 128, 1279

Hoogerwerf R., de Bruijne J.H.J., de Zeeuw P.T., 2000, The Origin of Runaway Stars., ApJL 544, L133
Horn D., 2022, Analysing spectra of X-ray active black hole binaries using empirical models., Bachelor's thesis, Friedrich Alexander Universität of Erlangen-Nürnberg
Houck J.C., 2002, ISIS: The Interactive Spectral Interpretation System., In: Branduardi-Raymont G. (ed.) High Resolution X-ray Spectroscopy with XMM-Newton and Chandra., Mullard Space Science Laboratory, p. 17
Hoyle F., 1946, The synthesis of the elements from hydrogen., MNRAS 106, 343
Hoyle F., 1954, On Nuclear Reactions Occuring in Very Hot STARS.I. the Synthesis of Elements from Carbon to Nickel., ApJS 1, 121
Hoyle F., Lyttleton R.A., 1939, The effect of interstellar matter on climatic variation., Proceedings of the Cambridge Philosophical Society 35, 405
Iben I., 2012a, Stellar Evolution Physics, Vol. 1, Cambridge University Press
Iben I., 2012b, Stellar Evolution Physics, Vol. 2, Cambridge University Press
Iben, I. J., Renzini A., 1983, Asymptotic giant branch evolution and beyond., ARA&A 21, 271
Iben, Icko J., Livio M., 1993, Common Envelopes in Binary Star Evolution., PASP 105, 1373
Ingram A., 2023, Fourier spectral-timing techniques for the study of accreting black holes., Astron. Nachr. 344, e20230002
Ingram A., Done C., Fragile P.C., 2009, Low-frequency quasi-periodic oscillations spectra and Lense-Thirring precession., MNRAS 397, L101
Ingram A., Mastroserio G., Dauser T., et al., 2019, A public relativistic transfer function model for X-ray reverberation mapping of accreting black holes., MNRAS 488, 324
Ingram A., van der Klis M., 2013, An exact analytic treatment of propagating mass accretion rate fluctuations in X-ray binaries., MNRAS 434, 1476
Ingram A.R., Motta S.E., 2019, A review of quasi-periodic oscillations from black hole X-ray binaries: Observation and theory., New Astron. Rev. 85, 101524
Ivanova N., Justham S., Chen X., et al., 2013, Common envelope evolution: where we stand and how we can move forward., Astron. Astrophys. Rev. 21, 59
Izzo L., Molaro P., Aydi E., et al., 2020, UVES observations of Nova Reticuli 2020 during Minimal Science Operations show it is entering the nebular phase., Astronomer's Telegram 14048
Jahoda K., Markwardt C.B., Radeva Y., et al., 2006, Calibration of the Rossi X-Ray Timing Explorer Proportional Counter Array., ApJS 163, 401
Janesick J., 2001, Scientific Charge-coupled Devices, Press Monographs, Society of Photo Optical
Janesick J., Elliott T., Bredthauer R., et al., 1988, Fano-noise-limited CCDs., In: Golub L. (ed.) Proc. SPIE., Vol. 982. X-ray instrumentation in astronomy II, San Diego, CA, United States, p.70
Janesick J., Elliott T., Collins S., et al., 1986, CCD advances for X-ray scientific measurements in 1985., In: Culhane J.L. (ed.) Proc. SPIE., Vol. 597. X-ray instrumentation in astronomy, Cannes, France, p.364
Janka H.T., 2011, Supernovae und kosmische Gammablitze, Astrophysik aktuell, Spektrum Akademischer Verlag (Springer), Heidelberg
Janka H.T., Hanke F., Hüdepohl L., et al., 2012, Core-collapse supernovae: Reflections and directions., Progress of Theoretical and Experimental Physics 2012, 01A309
Jeffreys H., 1929, The Earth: its origin, history and physical constitution, Cambridge University Press, 2nd edition
Johng-ay T., Fajardo P., Martin T., et al., 2016, DECIMO: A simulation tool to explore next generation of detectors for synchrotron radiation applications., In: 2016 IEEE Nuclear Science Symposium, Medical Imaging Conference and Room-Temperature Semiconductor Detector Workshop (NSS/MIC/RTSD)., Strasbourg, France, p.1
José J., Hernanz M., 1998, Nucleosynthesis in Classical Novae: CO versus ONe White Dwarfs., ApJ 494, 680
Kahabka P., van den Heuvel E.P.J., 1997, Luminous Supersoft X-Ray Sources., ARA&A 35, 69

Kahn S.M., Blissett R.J., 1980, The direct deconvolution of X-ray spectra., ApJ 238, 417
Kahng D., 1960, Electric Field Controlled Semiconductor Device, US Patent No. 3,102,230 (filed 31 May 1960, issued 27 August 1963)
Kalemci E., Kara E., Tomsick J.A., 2022, Black Holes: Timing and Spectral Properties and Evolution. In: Bambi C., Santangelo A. (eds.) Handbook of X-ray and Gamma-ray Astrophysics. Springer, Singapore, p.1 (arXiv:2307.06652)
Kallman T.R., McCray R., Voit G.M., 1987, Rapid Variability of P Cygni Lines in Massive X-Ray Binaries., ApJ 317, 746
Kalogera V., Baym G., 1996, The Maximum Mass of a Neutron Star., ApJL 470, L61
Kara E., Fabian A.C., Cackett E.M., et al., 2013a, The closest look at 1H0707-495: X-ray reverberation lags with 1.3 Ms of data., MNRAS 428, 2795
Kara E., Fabian A.C., Cackett E.M., et al., 2013b, Discovery of high-frequency iron K lags in Ark 564 and Mrk 335., MNRAS 434, 1129
Kara E., Steiner J.F., Fabian A.C., et al., 2019, The corona contracts in a black-hole transient., Nature 565, 198
Kaspi V.M., Beloborodov A.M., 2017, Magnetars., ARA&A 55, 261
Kato M., Hachisu I., 1994, Optically Thick Winds in Nova Outbursts., ApJ 437, 802
Kato M., Saio H., Hachisu I., 2015, Multi-wavelength Light Curve Model of the One-year Recurrence Period Nova M31N 2008-12A., ApJ 808, 52
Kato M., Saio H., Hachisu I., 2017, A Self-consistent Model for a Full Cycle of Recurrent Novae—Wind Mass-Loss Rate and X-Ray Luminosity., ApJ 838, 153
Kato M., Saio H., Hachisu I., 2022a, A Light-curve Analysis of the X-Ray Flash First Observed in Classical Novae., ApJL 935, L15
Kato M., Saio H., Hachisu I., 2022b, Physics of nova outbursts: A theoretical model of classical nova outbursts with self-consistent wind mass loss., PASJ 74, 1005
Kato M., Saio H., Hachisu I., 2022c, Pre-maximum Evolution of the Classical Nova YZ Reticuli., Research Notes of the American Astronomical Society 6, 258
Kato M., Saio H., Henze M., et al., 2016, X-ray Flashes in Recurrent Novae: M31N 2008-12a and the Implications of the Swift Nondetection., ApJ 830, 40
Kawamura T., Axelsson M., Done C., Takahashi T., 2022, A full spectral-timing model to map the accretion flow in black hole binaries: the low/hard state of MAXI J1820+070., MNRAS 511, 536
Kawamuro T., Ueda Y., Shidatsu M., et al., 2018, The 7-year MAXI/GSC X-Ray Source Catalog in the High Galactic Latitude Sky (3MAXI)., ApJS 238, 32
Keil M.T., Raffelt G.G., Janka H.T., 2003, Monte Carlo Study of Supernova Neutrino Spectra Formation., ApJ 590, 971
Kemmer J., Lutz G., 1987, New detector concepts., Nucl. Instrum. Methods Phys. Res., Sect. A 253, 365
Kenyon S.J., 1986, The Symbiotic Stars, Cambridge Astrophysics, Cambridge University Press
Kepler S.O., Koester D., Romero A.D., et al., 2017, White Dwarf Mass Distribution., In: Tremblay P.E., Gaensicke B., Marsh T. (eds.) 20th European White Dwarf Workshop, Vol. 509. Astronomical Society of the Pacific Conference Series, p. 421
Kepler S.O., Pelisoli I., Koester D., et al., 2016, New white dwarf and subdwarf stars in the Sloan Digital Sky Survey Data Release 12., MNRAS 455, 3413
Kerr R.P., 1963, Gravitational Field of a Spinning Mass as an Example of Algebraically Special Metrics., Phys. Rev. Lett. 11, 237
Kilic M., Allende Prieto C., Brown W.R., Koester D., 2007, The Lowest Mass White Dwarf., ApJ 660, 1451
Kilkenny D., O'Donoghue D., Worters H.L., et al., 2015, The Edinburgh-Cape Blue Object Survey - IV. Zone 3: Galactic latitudes $-40° > b > -50°$., MNRAS 453, 1879
King A., Lasota J.P., Middleton M., 2023, Ultraluminous X-ray sources., New Astron. Rev. 96, 101672

Kirsch C., Lorenz M., Peille P., et al., 2022, The Athena X-IFU Instrument Simulator xifusim., J. Low Temp. Phys.
Kirsch M.G., Briel U.G., Burrows D., et al., 2005, Crab: the standard x-ray candle with all (modern) x-ray satellites., In: Siegmund O.H.W. (ed.) Proc. SPIE., Vol. 5898. UV, X-Ray, and Gamma-Ray Space Instrumentation for Astronomy XIV, San Diego, California, United States, p.22
Knoll G., 2010, Radiation Detection and Measurement, Wiley
Kochanek C.S., Shappee B.J., Stanek K.Z., et al., 2017, The All-Sky Automated Survey for Supernovae (ASAS-SN) Light Curve Server v1.0., PASP 129, 104502
Kong A.K.H., McClintock J.E., Garcia M.R., et al., 2002, The X-Ray Spectra of Black Hole X-Ray Novae in Quiescence as Measured by Chandra., ApJ 570, 277
König O., Rau A., Haberl F., et al., 2020a, SRG/eROSITA detection of Nova V1708 Scorpii in its super-soft phase., Astronomer's Telegram 14057
König O., Wilms J., Arcodia R., et al., 2022, X-ray detection of a nova in the fireball phase., Nature 605, 248
König O., Wilms J., Kreykenbohm I., et al., 2020b, SRG/eROSITA detection of a bright flare of the millisecond pulsar PSR J1023+0038., Astronomer's Telegram 13765
Kopal Z., 1955, The classification of close binary systems., Annales d'Astrophysique 18, 379
Körding E., Falcke H., 2004, X-ray time lags from a pivoting power law in black holes., A&A 414, 795
Kormendy J., Richstone D., 1995, Inward Bound—The Search For Supermassive Black Holes In Galactic Nuclei., ARA&A 33, 581
Kotov O., Churazov E., Gilfanov M., 2001, On the X-ray time-lags in the black hole candidates., MNRAS 327, 799
Kovács Z., Cheng K.S., Harko T., 2009, Can stellar mass black holes be quark stars?, MNRAS 400, 1632
Kraft R.P., 1959, The Binary System Nova DQ Herculis. II. an Interpretation of the Spectrum during the Eclipse Cycle., ApJ 130, 110
Krautter J., 2008, The Super-soft Phase in Novae., In: Evans A., Bode M.F., O'Brien T.J., Darnley M.J. (eds.) RS Ophiuchi (2006) and the Recurrent Nova Phenomenon, Vol. 401. Astron. Soc. Pacific Conf. Ser., Astron. Soc. Pacific, San Francisco, p. 139
Kritcher A.L., Swift D.C., Döppner T., et al., 2020, A measurement of the equation of state of carbon envelopes of white dwarfs., Nature 584, 51
Kruskal M.D., 1960, Maximal Extension of Schwarzschild Metric., Phys. Rev. 119, 1743
Kuiper G.P., 1941, On the Interpretation of β Lyrae and Other Close Binaries., ApJ 93, 133
Kupfer T., Bauer E.B., Burdge K.B., et al., 2020, A New Class of Roche Lobe-filling Hot Subdwarf Binaries., ApJL 898, L25
Lada C.J., 2006, Stellar Multiplicity and the Initial Mass Function: Most Stars Are Single., ApJL 640, L63
Lai E.V., De Marco B., Zdziarski A.A., et al., 2022, The X-ray spectral-timing contribution of the stellar wind in the hard state of Cyg X-1., MNRAS 512, 2671
LaMarr B., Prigozhin G., Remillard R., et al., 2016, Ground calibration of the Silicon Drift Detectors for NICER., In: den Herder J.W.A., Takahashi T., Bautz M. (eds.) Space Telescopes and Instrumentation 2016: Ultraviolet to Gamma Ray, Vol. 9905. Society of Photo-Optical Instrumentation Engineers (SPIE) Conference Series, p. 99054W
Lamb F.K., Shibazaki N., Alpar M.A., Shaham J., 1985, Quasi-periodic oscillations in bright galactic-bulge X-ray sources., Nature 317, 681
Lampton M., Margon B., Bowyer S., 1976, Parameter estimation in X-ray astronomy., ApJ 208, 177
Laplace P.S., 1796, Exposition du Système du Monde, (Translated by Rev. H. Harte, Dublin, 1830)
Laplace P.S., 1799, Beweis des Satzes, dass die anziehende Kraft bey einem Weltkörper so groß seyn könne, dass das Licht davon nicht ausströmen kann., Allgemeine Geographische Ephemeriden 4, 1
Lasota J.P., 2001, The disc instability model of dwarf novae and low-mass X-ray binary transients., New

Astron. Rev. 45, 449
Lattimer J.M., Prakash M., 2004, The Physics of Neutron Stars., Science 304, 536
Leach R., Hessman F.V., King A.R., et al., 1999, The light curves of VY Scl stars., MNRAS 305, 225
Leahy D.A., Darbro W., Elsner R.F., et al., 1983, On searches for pulsed emission with application to four globular cluster X-ray sources : NGC 1851, 6441, 6624 and 6712., ApJ 266, 160
Lechner P., Fiorini C., Hartmann R., et al., 2001, Silicon drift detectors for high count rate X-ray spectroscopy at room temperature., Nucl. Instrum. Methods Phys. Res., Sect. A 458, 281
Lépine S., Shara M.M., Livio M., Zurek D., 1999, First Direct Measurement of Acceleration in the Outflow of a Nova: U Scorpii (1999)., ApJL 522, L121
Lewin W.H.G., van Paradijs J., Taam R.E., 1993, X-Ray Bursts., SSRv 62, 223
Li K.L., Kong A., Aydi E., et al., 2020, Fermi-LAT detection of the naked-eye classical nova MGAB-V207., Astronomer's Telegram 13868
Li K.L., Kong A.K.H., Charles P.A., et al., 2012, A Luminous Be+White Dwarf Supersoft Source in the Wing of the SMC: MAXI J0158-744., ApJ 761, 99
Li K.L., Metzger B.D., Chomiuk L., et al., 2017, A nova outburst powered by shocks., Nature Astronomy 1, 697
Liang E.P.T., Price R.H., 1977, Accretion disk coronae and Cygnus X-1., ApJ 218, 247
Lightman A.P., White T.R., 1988, Effects of Cold Matter in Active Galactic Nuclei: A Broad Hump in the X-Ray Spectra., ApJ 335, 57
Lilienfeld E.J., 1926, Method and apparatus for controlling electric currents, US Patent No. 1,745,175 (filed: 8 October 1926; issued: 28 January 1930)
Liska M., Hesp C., Tchekhovskoy A., et al., 2018, Formation of precessing jets by tilted black hole discs in 3D general relativistic MHD simulations., MNRAS 474, L81
Liu Q.Z., van Paradijs J., van den Heuvel E.P.J., 2006, Catalogue of high-mass X-ray binaries in the Galaxy (4th edition)., A&A 455, 1165
Lorenz M., Kirsch C., Merino-Alonso P.E., et al., 2020, GPU Supported Simulation of Transition-Edge Sensor Arrays., J. Low Temp. Phys. 200, 277
Lorenz M., Kirsch C., Peille P., et al., 2022, Simulation of Radiative Transfer Within X-ray Microcalorimeter Absorbers., J. Low Temp. Phys. 209, 464
Lucsanyi D., Prod'homme T., Smit H., et al., 2018, Pyxel: a novel and multi-purpose Python-based framework for imaging detector simulation., In: Holland A.D., Beletic J. (eds.) Proc. SPIE., Vol. 10709. High Energy, Optical, and Infrared Detectors for Astronomy VIII, Austin, Texas, United States, p. 107091A
Lyubarskii Y.E., 1997, Flicker noise in accretion discs., MNRAS 292, 679
Maccarone T.J., 2003, Do X-ray binary spectral state transition luminosities vary?, A&A 409, 697
Maccarone T.J., 2005, Using radio emission to detect isolated and quiescent accreting black holes., MNRAS 360, L30
Maccarone T.J., Coppi P.S., Poutanen J., 2000, Time Domain Analysis of Variability in Cygnus X-1: Constraints on the Emission Models., ApJL 537, L107
MacDonald R.K.D., Bailyn C.D., Buxton M., et al., 2014, The Black Hole Binary V4641 Sagitarii: Activity in Quiescence and Improved Mass Determinations., ApJ 784, 2
Madsen K.K., Harrison F., Broadway D., et al., 2018, Optical instrument design of the high-energy x-ray probe (HEX-P)., In: den Herder J.W.A., Nikzad S., Nakazawa K. (eds.) Proc. SPIE., Vol. 10699. Space Telescopes and Instrumentation 2018: Ultraviolet to Gamma Ray, Austin, Texas, United States, p. 106996M
Magorrian J., Tremaine S., Richstone D., et al., 1998, The Demography of Massive Dark Objects in Galaxy Centers., AJ 115, 2285
Mahmoud R.D., Done C., De Marco B., 2019, Reverberation reveals the truncated disc in the hard state of

GX 339-4., MNRAS 486, 2137
Maqbool B., Mudambi S.P., Misra R., et al., 2019, A stochastic propagation model to the energy dependent rapid temporal behaviour of Cygnus X-1 as observed by AstroSat in the hard state., MNRAS 486, 2964
Marcel G., Ferreira J., Clavel M., et al., 2019, A unified accretion-ejection paradigm for black hole X-ray binaries. IV. Replication of the 2010-2011 activity cycle of GX 339-4., A&A 626, A115
Marino A., Barnier S., Petrucci P.O., et al., 2021, Tracking the evolution of the accretion flow in MAXI J1820+070 during its hard state with the JED-SAD model., A&A 656, A63
Markoff S., Nowak M.A., Wilms J., 2005, Going with the Flow: Can the Base of Jets Subsume the Role of Compact Accretion Disk Coronae?, ApJ 635, 1203
Martínez-Núñez S., Kretschmar P., Bozzo E., et al., 2017, Towards a Unified View of Inhomogeneous Stellar Winds in Isolated Supergiant Stars and Supergiant High Mass X-Ray Binaries., SSRv 212, 59
Martocchia A., Matt G., 1996, Iron Kalpha line intensity from accretion discs around rotating black holes., MNRAS 282, L53
Massey P., 2003, MASSIVE STARS IN THE LOCAL GROUP: Implications for Stellar Evolution and Star Formation., ARA&A 41, 15
Mastroserio G., Ingram A., van der Klis M., 2019, An X-ray reverberation mass measurement of Cygnus X-1., MNRAS 488, 348
Mastroserio G., Ingram A., Wang J., et al., 2021, Modelling correlated variability in accreting black holes: the effect of high density and variable ionization on reverberation lags., MNRAS 507, 55
Matt G., Perola G.C., Piro L., 1991, The iron line and high energy bump as X-ray signatures of cold matter in Seyfert 1 galaxies., A&A 247, 25
McHardy I.M., Arévalo P., Uttley P., et al., 2007, Discovery of multiple Lorentzian components in the X-ray timing properties of the Narrow Line Seyfert 1 Ark 564., MNRAS 382, 985
McHardy I.M., Koerding E., Knigge C., et al., 2006, Active galactic nuclei as scaled-up Galactic black holes., Nature 444, 730
McNaught R.H., 2020a, Apparent Nova in Reticulum., Central Bureau for Astronomical Telegrams CBET 4811
McNaught R.H., 2020b, Nova Reticuli 2020., Central Bureau for Astronomical Telegrams CBET 4812
Medvedev P., Sazonov S., Gilfanov M., et al., 2020, SRG/eROSITA uncovers the most X-ray luminous quasar at z $>$ 6., MNRAS 497, 1842
Meidinger N., Müller-Seidlitz J., 2022, DEPFET Active Pixel Sensors. In: Bambi C., Santangelo A. (eds.) Handbook of X-ray and Gamma-ray Astrophysics. Springer, Singapore, p.1 (arXiv:2307.06652)
Méndez M., Peirano V., García F., et al., 2023, Unveiling hidden variability components in accreting X-ray binaries using both the Fourier power and cross spectra., MNRAS in press (arXiv:2312.03476)
Merloni A., Predehl P., Becker W., et al., 2012, eROSITA Science Book: Mapping the Structure of the Energetic Universe, White paper (arXiv:1209.3114)
Mestel L., 1952, On the theory of white dwarf stars. I. The energy sources of white dwarfs., MNRAS 112, 583
Metzger B.D., Finzell T., Vurm I., et al., 2015, Gamma-ray novae as probes of relativistic particle acceleration at non-relativistic shocks., MNRAS 450, 2739
Michell J., 1784, On the Means of Discovering the Distance, Magnitude, &c. of the Fixed Stars, in Consequence of the Diminution of the Velocity of Their Light, in Case Such a Diminution Should be Found to Take Place in any of Them, and Such Other Data Should be Procured from Observations, as Would be Farther Necessary for That Purpose. By the Rev. John Michell, B. D. F. R. S. In a Letter to Henry Cavendish, Esq. F. R. S. and A. S., Philosophical Transactions of the Royal Society of London 74, 35
Miller J.M., Homan J., Steeghs D., et al., 2006, A Long, Hard Look at the Low/Hard State in Accreting Black Holes., ApJ 653, 525

Miller J.M., Zoghbi A., Raymond J., et al., 2020, An Obscured, Seyfert 2-like State of the Stellar-mass Black Hole GRS 1915+105 Caused by Failed Disk Winds., ApJ 904, 30
Miller M.C., Lamb F.K., Dittmann A.J., et al., 2019, PSR J0030+0451 Mass and Radius from NICER Data and Implications for the Properties of Neutron Star Matter., ApJL 887, L24
Miller Bertolami M.M., 2016, New models for the evolution of post-asymptotic giant branch stars and central stars of planetary nebulae., A&A 588, A25
Miller-Jones J.C.A., Bahramian A., Orosz J.A., et al., 2021, Cygnus X-1 contains a 21-solar mass black hole—Implications for massive star winds., Sci 371, 1046
Mirabel I.F., Rodríguez L.F., 1994, A superluminal source in the Galaxy., Nature 371, 46
Mirabel I.F., Rodríguez L.F., 1998, Microquasars in our Galaxy., Nature 392, 673
Misner, Thorne, Wheeler 1973, Gravitation, Princeton University Press
Misra R., Yadav J.S., Verdhan Chauhan J., et al., 2017, AstroSat/LAXPC Observation of Cygnus X-1 in the Hard State., ApJ 835, 195
Mitsuda K., Bautz M., Inoue H., et al., 2007, The X-Ray Observatory Suzaku., PASJ 59, S1
Miyaji S., Nomoto K., Yokoi K., Sugimoto D., 1980, Supernova triggered by electron captures., PASJ 32, 303
Miyamoto S., Iga S., Kitamoto S., Kamado Y., 1993, Another Canonical Time Variation of X-Rays from Black Hole Candidates in the Very High Flare State?, ApJL 403, L39
Miyamoto S., Kimura K., Kitamoto S., et al., 1991, X-Ray Variability of GX 339-4 in Its Very High State., ApJ 383, 784
Miyamoto S., Kitamoto S., 1989, X-Ray Time Variations from Cygnus X-1 and Implications for the Accretion Process., Nature 342, 773
Miyamoto S., Kitamoto S., 1991, A Jet Model for a Very High State of GX 339-4., ApJ 374, 741
Miyamoto S., Kitamoto S., Hayashida K., Egoshi W., 1995, Large Hysteretic Behavior of Stellar Black Hole Candidate X-Ray Binaries., ApJL 442, L13
Miyamoto S., Kitamoto S., Iga S., et al., 1992, Canonical Time Variations of X-Rays from Black Hole Candidates in the Low-Intensity State., ApJL 391, L21
Miyamoto S., Kitamoto S., Mitsuda K., Dotani T., 1988, Delayed hard X-rays from Cygnus X-l., Nature 336, 450
Momeni M., 2021, Feldeffekttransistor (Grundlagen der Mikroelektronik 1), p.195, Springer, Berlin, Heidelberg
Montgomery C., Orchiston W., Whittingham I., 2009, Michell, Laplace and the origin of the black hole concept., Journal of Astronomical History and Heritage 12, 90
Moore G.E., 1965, Cramming more components onto integrated circuits., Electronics 38, 114 (reprinted in IEEE Solid-State Circuits Society Newsletter 11, 3, p. 33–35, 2006)
Morii M., Tomida H., Kimura M., et al., 2013, Extraordinary Luminous Soft X-Ray Transient MAXI J0158-744 as an Ignition of a Nova on a Very Massive O-Ne White Dwarf., ApJ 779, 118
Morii M., Yamaoka H., Mihara T., et al., 2016, Search for soft X-ray flashes at the fireball phase of classical/recurrent novae using MAXI/GSC data., PASJ 68, S11
Moseley S.H., Mather J.C., McCammon D., 1984, Thermal detectors as x-ray spectrometers., J. Appl. Phys. 56, 1257
Mukai K., 2017, X-Ray Emissions from Accreting White Dwarfs: A Review., PASP 129, 062001
Müller-Seidlitz J., Andritschke R., Bähr A., et al., 2016, Spectroscopic performance of DEPFET active pixel sensor prototypes suitable for the high count rate Athena WFI detector., In: den Herder J.W.A., Takahashi T., Bautz M. (eds.) Proc. SPIE., Vol. 9905. Space Telescopes and Instrumentation 2016: Ultraviolet to Gamma Ray, Edinburgh, United Kingdom, p. 990567
Mushotzky R., 2018, AXIS: a probe class next generation high angular resolution x-ray imaging satellite., In: den Herder J.W.A., Nikzad S., Nakazawa K. (eds.) Proc. SPIE., Vol. 10699. Space Telescopes and

Instrumentation 2018: Ultraviolet to Gamma Ray, Austin, Texas, United States, p. 1069929
Nandra K., Barret D., Barcons X., et al., 2013, The Hot and Energetic Universe: A White Paper presenting the science theme motivating the Athena+ mission, White paper (arXiv:1306.2307)
Napiwotzki R., Karl C.A., Lisker T., et al., 2020, The ESO supernovae type Ia progenitor survey (SPY). The radial velocities of 643 DA white dwarfs., A&A 638, A131
Narayan R., Yi I., 1995, Advection-dominated Accretion: Underfed Black Holes and Neutron Stars., ApJ 452, 710
Negueruela I., Smith D.M., Reig P., et al., 2006, Supergiant Fast X-ray Transients: A New Class of High Mass X-ray Binaries Unveiled by INTEGRAL., In: Wilson A. (ed.) The X-ray Universe 2005, Vol. 604. ESA Special Publication, p. 165
Nelemans G., Jonker P.G., 2010, Ultra-compact (X-ray) binaries., New Astron. Rev. 54, 87
Nelemans G., Portegies Zwart S.F., Verbunt F., Yungelson L.R., 2001a, Population synthesis for double white dwarfs. II. Semi-detached systems: AM CVn stars., A&A 368, 939
Nelemans G., Yungelson L.R., Portegies Zwart S.F., Verbunt F., 2001b, Population synthesis for double white dwarfs . I. Close detached systems., A&A 365, 491
Ness J.U., Starrfield S., Beardmore A.P., et al., 2007, The SSS Phase of RS Ophiuchi Observed with Chandra and XMM-Newton. I. Data and Preliminary Modeling., ApJ 665, 1334
Ness J.U., Starrfield S., Burwitz V., et al., 2003, A Chandra Low Energy Transmission Grating Spectrometer Observation of V4743 Sagittarii: A Supersoft X-Ray Source and a Violently Variable Light Curve., ApJL 594, L127
Newton I., 1704, Opticks: or, A Treatise of the Reflexions, Refractions, Inflexions and Colours of Light
Nomoto K., 1984, Evolution of 8-10 solar mass stars toward electron capture supernovae. I - Formation of electron-degenerate O + NE + MG cores., ApJ 277, 791
Nomoto K., 1987, Evolution of 8–10 M_{sun} Stars toward Electron Capture Supernovae. II. Collapse of an O + NE + MG Core., ApJ 322, 206
Novikov I.D., Thorne K.S., 1973, Astrophysics of black holes. In: DeWitt C., DeWitt B. (eds.) Black Holes (Les Astres Occlus). Gordon and Breach, New York, p.343
Nowak M.A., 1995, Toward a Unified View of Black-Hole High-Energy States., PASP 107, 1207
Nowak M.A., 2000, Are there three peaks in the power spectra of GX 339-4 and Cyg X-1?, MNRAS 318, 361
Nowak M.A., Hanke M., Trowbridge S.N., et al., 2011, Corona, Jet, and Relativistic Line Models for Suzaku/RXTE/Chandra-HETG Observations of the Cygnus X-1 Hard State., ApJ 728, 13
Nowak M.A., Juett A., Homan J., et al., 2008, Disk-dominated States of 4U 1957+11: Chandra, XMM-Newton, and RXTE Observations of Ostensibly the Most Rapidly Spinning Galactic Black Hole., ApJ 689, 1199
Nowak M.A., Vaughan B.A., Wilms J., et al., 1999a, Rossi X-Ray Timing Explorer Observation of Cygnus X-1. II. Timing Analysis., ApJ 510, 874
Nowak M.A., Wilms J., Dove J.B., 1999b, Low-Luminosity States of the Black Hole Candidate GX 339-4. II. Timing Analysis., ApJ 517, 355
Nowak M.A., Wilms J., Hanke M., et al., 2012, The microquasar Cyg X-1: a short review., Mem. S.A. It. 83, 202
Nowak M.A., Wilms J., Heindl W.A., et al., 2001, A good long look at the black hole candidates LMC X-1 and LMC X-3., MNRAS 320, 316
Nowak M.A., Wilms J., Vaughan B.A., et al., 1999c, Rossi X-Ray Timing Explorer Observation of Cygnus X-1. III. Implications for Compton Corona and Advection-dominated Accretion Flow Models., ApJ 515, 726
O'Brien T.J., Bode M.F., Porcas R.W., et al., 2006, An asymmetric shock wave in the 2006 outburst of the recurrent nova RS Ophiuchi., Nature 442, 279
Oda M., Gorenstein P., Gursky H., et al., 1971, X-Ray Pulsations from Cygnus X-1 Observed from UHURU.,

ApJL 166, L1
Odaka H., Sugimoto S., Ishikawa S.n., et al., 2010, Development of an integrated response generator for Si/CdTe semiconductor Compton cameras., Nucl. Instrum. Methods Phys. Res., Sect. A 624, 303
Oegelman H., Beuermann K., Krautter J., 1984, The detection of X-rays from nova MUSCAE 1983 with the EXOSAT satellite., ApJL 287, L31
Ohlmann S.T., Röpke F.K., Pakmor R., Springel V., 2016, Hydrodynamic Moving-mesh Simulations of the Common Envelope Phase in Binary Stellar Systems., ApJL 816, L9
Okajima T., Soong Y., Balsamo E.R., et al., 2016, Performance of NICER flight x-ray concentrator., In: den Herder J.W.A., Takahashi T., Bautz M. (eds.) Proc. SPIE., Vol. 9905. Space Telescopes and Instrumentation 2016: Ultraviolet to Gamma Ray, Edinburgh, United Kingdom, p. 99054X
Omama T., Tsujimoto M., Ebisawa K., Mizumoto M., 2023, X-ray Time Lag Evaluation of MAXI J1820+070 with a Differential Cross-correlation Analysis., ApJ 945, 92
Oppenheimer J.R., Snyder H., 1939, On Continued Gravitational Contraction., Phys. Rev. 56, 455
Oppenheimer J.R., Volkoff G.M., 1939, On Massive Neutron Cores., Phys. Rev. 55, 374
Orosz J.A., Bailyn C.D., 1997, Optical Observations of GRO J1655-40 in Quiescence. I. A Precise Mass for the Black Hole Primary., ApJ 477, 876
Orosz J.A., McClintock J.E., Narayan R., et al., 2007, A 15.65-solar-mass black hole in an eclipsing binary in the nearby spiral galaxy M 33., Nature 449, 872
Owocki S.P., Castor J.I., Rybicki G.B., 1988, Time-dependent Models of Radiatively Driven Stellar Winds. I. Nonlinear Evolution of Instabilities for a Pure Absorption Model., ApJ 335, 914
Özel F., Freire P., 2016, Masses, Radii, and the Equation of State of Neutron Stars., ARA&A 54, 401
Paczyński B., 1971, Evolutionary Processes in Close Binary Systems., ARA&A 9, 183
Paczyński B., 1976, Common Envelope Binaries., Symposium - International Astronomical Union 73, 75
Parratt L.G., 1954, Surface Studies of Solids by Total Reflection of X-Rays., Phys. Rev. 95, 359
Parseval M.A., 1806, Mémoire sur les séries et sur l'intégration complète d'une équation aux différences partielles linéaires du second ordre, à coefficients constants., Mém. prés. par divers savants, Acad. des Sciences, Paris 1, 638
Patterson J., Raymond J.C., 1985a, X-ray emission from cataclysmic variables with accretion disks. I. Hard X-rays., ApJ 292, 535
Patterson J., Raymond J.C., 1985b, X-ray emission from cataclysmic variables with accretion disks. II. EUV/soft X-ray radiation., ApJ 292, 550
Pauli W., 1925, Über den Zusammenhang des Abschlusses der Elektronengruppen im Atom mit der Komplexstruktur der Spektren., Zeitschrift für Physik 31, 765
Pavlov G.G., Nousek J.A., 1999, Charge diffusion in CCD X-ray detectors., Nucl. Instrum. Methods Phys. Res., Sect. A 428, 348
Paxton B., Bildsten L., Dotter A., et al., 2011, Modules for Experiments in Stellar Astrophysics (MESA)., ApJS 192, 3
Paxton B., Marchant P., Schwab J., et al., 2015, Modules for Experiments in Stellar Astrophysics (MESA): Binaries, Pulsations, and Explosions., ApJS 220, 15
Pei S., Orio M., Gendreau K., et al., 2020, NICER observations of Nova Ret 2020., Astronomer's Telegram 14067
Peterson B.M., Ferrarese L., Gilbert K.M., et al., 2004, Central Masses and Broad-Line Region Sizes of Active Galactic Nuclei. II. A Homogeneous Analysis of a Large Reverberation-Mapping Database., ApJ 613, 682
Pfeffermann E., Briel U.G., Hippmann H., et al., 1987, The focal plane instrumentation of the ROSAT Telescope., In: Proc. SPIE., Vol. 733. Soft X-ray optics and technology, Bellingham, WA, USA, p. 519
Pietsch W., Sala G., Haberl F., Greiner J., 2007, Detection of nova M31N 2007-07c with Swift UVOT in the UVW2 filter., Astronomer's Telegram 1149

Pivovaroff M.J., Okajima T., 2022, Geometries for Grazing Incidence Mirrors. In: Bambi C., Santangelo A. (eds.) Handbook of X-ray and Gamma-ray Astrophysics. Springer, Singapore
Plotkin R.M., Gallo E., Jonker P.G., 2013, The X-Ray Spectral Evolution of Galactic Black Hole X-Ray Binaries toward Quiescence., ApJ 773, 59
Plucinsky P.P., Beardmore A.P., Foster A., et al., 2017, SNR 1E 0102.2-7219 as an X-ray calibration standard in the 0.5-1.0 keV bandpass and its application to the CCD instruments aboard Chandra, Suzaku, Swift and XMM-Newton., A&A 597, A35
Ponti G., Fender R.P., Begelman M.C., et al., 2012, Ubiquitous equatorial accretion disc winds in black hole soft states., MNRAS 422, L11
Portegies Zwart S.F., Verbunt F., Ergma E., 1997, The formation of black-holes in low-mass X-ray binaries., A&A 321, 207
Postnov K.A., Yungelson L.R., 2014, The Evolution of Compact Binary Star Systems., Living Reviews in Relativity 17, 3
Pottasch S., 1959, The nova outburst: II. The radiative cooling of an expanding shell., Annales d'Astrophysique 22, 310
Pottschmidt K., 2002, Accretion Disk Weather of Black Hole X-Ray Binaries - The Case of Cygnus X-1, PhD thesis, Eberhard Karls Universität Tübingen
Pottschmidt K., Wilms J., Nowak M.A., et al., 2000, Temporal evolution of X-ray lags in Cygnus X-1., A&A 357, L17
Pottschmidt K., Wilms J., Nowak M.A., et al., 2006, INTEGRAL and RXTE power spectra of Cygnus X-1., Adv. Space Res. 38, 1350
Pottschmidt K., Wilms J., Nowak M.A., et al., 2003, Long term variability of Cygnus X-1. I. X-ray spectral-temporal correlations in the hard state., A&A 407, 1039
Poutanen J., Fabian A.C., 1999, Spectral evolution of magnetic flares and time lags in accreting black hole sources., MNRAS 306, L31
Predehl P., Andritschke R., Arefiev V., et al., 2021, The eROSITA X-ray telescope on SRG., A&A 647, A1
Predehl P., Sunyaev R.A., Becker W., et al., 2020, Detection of large-scale X-ray bubbles in the Milky Way halo., Nature 588, 227
Press W.H., 1978, Flicker noises in astronomy and elsewhere., Comments on Astrophysics 7, 103
Prestwich A.H., Kilgard R., Crowther P.A., et al., 2007, The Orbital Period of the Wolf-Rayet Binary IC 10 X-1: Dynamic Evidence that the Compact Object Is a Black Hole., ApJL 669, L21
Prialnik D., Kovetz A., 1992, Classical Nova Models with Accretion Heating at Accretion Rates of 10 -9 and 10 -10 M_{sun} per Year., ApJ 385, 665
Prialnik D., Shara M.M., Shaviv G., 1978, The evolution of a slow nova model with a Z = 0.03 envelope from pre-explosion to extinction., A&A 62, 339
Priedhorsky W., Garmire G.P., Rothschild R., et al., 1979, Extended-bandwidth X-ray observations of Cygnus X-1., ApJ 233, 350
Prigozhin G., Gendreau K., Doty J.P., et al., 2016, NICER instrument detector subsystem: description and performance., In: den Herder J.W.A., Takahashi T., Bautz M. (eds.) Proc. SPIE., Vol. 9905. Space Telescopes and Instrumentation 2016: Ultraviolet to Gamma Ray, Edinburgh, United Kingdom, p. 99051I
Pringle J.E., 1981, Accretion discs in astrophysics., ARA&A 19, 137
Pringle J.E., Rees M.J., 1972, Accretion Disc Models for Compact X-Ray Sources., A&A 21, 1
Psaltis D., Belloni T., van der Klis M., 1999, Correlations in Quasi-periodic Oscillation and Noise Frequencies among Neutron Star and Black Hole X-Ray Binaries., ApJ 520, 262
Psaltis D., Norman C., 2000, On the Origin of Quasi-Periodic Oscillations and Broad-band Noise in Accreting Neutron Stars and Black Holes., submitted to ApJ on 8/6/99 (arXiv.astro-ph/0001391)
Rapisarda S., Ingram A., van der Klis M., 2017, Modelling hard and soft states of Cygnus X-1 with propagating mass accretion rate fluctuations., MNRAS 472, 3821

Rappaport S., Clark G.W., Cominsky L., et al., 1978, Orbital elements of 4U 0115+63 and the nature of the hard X-ray transients., ApJL 224, L1
Rappaport S., Verbunt F., Joss P.C., 1983, A new technique for calculations of binary stellar evolution application to magnetic braking., ApJ 275, 713
Rau A., Meidinger N., Nandra K., et al., 2013, The Hot and Energetic Universe: The Wide Field Imager (WFI) for Athena+, White paper (arXiv:1308.6785)
Rau A., Nandra K., Aird J., et al., 2016, Athena Wide Field Imager key science drivers., In: den Herder J.W.A., Takahashi T., Bautz M. (eds.) Proc. SPIE., Vol. 9905. Space Telescopes and Instrumentation 2016: Ultraviolet to Gamma Ray, Edinburgh, United Kingdom, p. 99052B
Ray P.S., Arzoumanian Z., Ballantyne D., et al., 2019, STROBE-X: X-ray Timing and Spectroscopy on Dynamical Timescales from Microseconds to Years, White paper (arXiv:1903.03035)
Reig P., 2011, Be/X-ray binaries., Ap&SS 332, 1
Remillard R.A., Loewenstein M., Steiner J.F., et al., 2022, An Empirical Background Model for the NICER X-Ray Timing Instrument., AJ 163, 130
Remillard R.A., McClintock J.E., 2006, X-Ray Properties of Black-Hole Binaries., ARA&A 44, 49
Revnivtsev M., Gilfanov M., Churazov E., 2000, High frequencies in the power spectrum of Cyg X-1 in the hard and soft spectral states., A&A 363, 1013
Reynolds C.S., Young A.J., Begelman M.C., Fabian A.C., 1999, X-Ray Iron Line Reverberation from Black Hole Accretion Disks., ApJ 514, 164
Riley T.E., Watts A.L., Bogdanov S., et al., 2019, A NICER View of PSR J0030+0451: Millisecond Pulsar Parameter Estimation., ApJL 887, L21
Rivinius T., Carciofi A.C., Martayan C., 2013, Classical Be stars. Rapidly rotating B stars with viscous Keplerian decretion disks., Astron. Astrophys. Rev. 21, 69
Rodney S.A., Tonry J.L., 2006, Characterizing Charge Diffusion in CCDs with X-Rays., PASP 118, 866
Roelofs G.H.A., Rau A., Marsh T.R., et al., 2010, Spectroscopic Evidence for a 5.4 Minute Orbital Period in HM Cancri., ApJL 711, L138
Romani R.W., Kandel D., Filippenko A.V., et al., 2022, PSR J0952-0607: The Fastest and Heaviest Known Galactic Neutron Star., ApJL 934, L17
Ross R.R., Fabian A.C., 2005, A comprehensive range of X-ray ionized-reflection models., MNRAS 358, 211
Rosseland S., 1946, Some Remarks on the Nova Phenomenon., ApJ 104, 324
Rothschild R.E., Boldt E.A., Holt S.S., Serlemitsos P.J., 1974, Millisecond Temporal Structure in Cygnus X-1., ApJL 189, L13
Rotondo M., Rueda J.A., Ruffini R., Xue S.S., 2011, Relativistic Feynman-Metropolis-Teller theory for white dwarfs in general relativity., Phys. Rev. D 84, 084007
Russell R.M., 1978, The CRAY-1 Computer System., Commun. ACM 21, 63–72
Rutledge R.E., Lewin W.H.G., van der Klis M., et al., 1999, Quasi-periodic Oscillations in Black Hole Candidates as an Indicator of Transition between Low and High States., ApJS 124, 265
Sahu K.C., Anderson J., Casertano S., et al., 2022, An Isolated Stellar-mass Black Hole Detected through Astrometric Microlensing., ApJ 933, 83
Salpeter E.E., 1952, Nuclear Reactions in Stars Without Hydrogen., ApJ 115, 326
Sanders J.S., Fabian A.C., 2007, A deeper X-ray study of the core of the Perseus galaxy cluster: the power of sound waves and the distribution of metals and cosmic rays., MNRAS 381, 1381
Santangelo A., Madonia R., Piraino S., 2023, A Chronological History of X-Ray Astronomy Missions. In: Bambi C., Santangelo A. (eds.) Handbook of X-ray and Gamma-ray Astrophysics. Springer, Singapore (arXiv:2307.06652)
Sazonov S., Gilfanov M., Medvedev P., et al., 2021, First tidal disruption events discovered by SRG/eROSITA: X-ray/optical properties and X-ray luminosity function at z $<$ 0.6., MNRAS 508, 3820
Schaefer B.E., 2021, Discovery of 13 New Orbital Periods for Classical Novae., Res. Notes American Astron.

Soc. 5, 150
Schmid C., 2012, X-ray telescopes in the digital lab: Instrument performance simulations, PhD thesis, Friedrich Alexander Universität of Erlangen-Nürnberg
Schmid C., Randall S., Wilms J., 2013, SIMPUT – A File Format for SIMulation inPUT, Technical report http://hea-www.harvard.edu/heasarc/formats/simput-1.1.0.pdf
Schneider P.C., Freund S., Czesla S., et al., 2022, The eROSITA Final Equatorial-Depth Survey (eFEDS). The Stellar Counterparts of eROSITA sources identified by machine learning and Bayesian algorithms., A&A 661, A6
Schödel R., Ott T., Genzel R., et al., 2002, A star in a 15.2-year orbit around the supermassive black hole at the centre of the Milky Way., Nature 419, 694
Schönberg M., Chandrasekhar S., 1942, On the Evolution of the Main-Sequence Stars., ApJ 96, 161
Schwarzschild K., 1916, Über das Gravitationsfeld eines Massenpunktes nach der Einsteinschen Theorie., Sitzungsberichte der Königlich Preußischen Akademie der Wissenschaften 189–196
Schwope A., Buckley D.A.H., Malyali A., et al., 2022, Discovery of eRASSt J192932.9-560346: A bright, two-pole accreting, eclipsing polar., A&A 661, A43
Segreto A., Del Santo M., D'Aí A., et al., 2015, A giant flare of V404 Cyg observed with Swift/BAT., Astronomer's Telegram 7755
Shafter A.W., 2017, The Galactic Nova Rate Revisited., ApJ 834, 196
Shakura N.I., Sunyaev R.A., 1973, Black holes in binary systems. Observational appearance., A&A 24, 337
Shapiro S.L., Teukolsky S.A., 1983, Black Holes, White Dwarfs, and Neutron Stars. The physics of compact objects, John Wiley & Sons, Ltd
Shaposhnikov N., Jahoda K., Markwardt C., et al., 2012, Advances in the RXTE Proportional Counter Array Calibration: Nearing the Statistical Limit., ApJ 757, 159
Shklovsky I.S., 1967, On the Nature of the Source of X-Ray Emission of Sco XR-1., ApJL 148, L1
Sion E.M., Holberg J.B., Oswalt T.D., et al., 2014, The White Dwarfs within 25 pc of the Sun: Kinematics and Spectroscopic Subtypes., AJ 147, 129
Skenderis K., Taylor M., 2008, The fuzzball proposal for black holes., Phys. Rep. 467, 117
Slane P.O., Helfand D.J., Murray S.S., 2002, New Constraints on Neutron Star Cooling from Chandra Observations of 3C 58., ApJL 571, L45
Smith D.M., Heindl W.A., Swank J., et al., 1997, X-Ray Timing in 1E 1740.7-2942 and GRS 1758-258., ApJL 489, L51
Smith R.K., Abraham M., Allured R., et al., 2017, Arcus: exploring the formation and evolution of clusters, galaxies, and stars., In: Siegmund O.H. (ed.) Proc. SPIE., Vol. 10397. UV, X-Ray, and Gamma-Ray Space Instrumentation for Astronomy XX, San Diego, California, United States, p. 103970Q
Smith R.K., Brickhouse N.S., Liedahl D.A., Raymond J.C., 2001, Collisional Plasma Models with APEC/APED: Emission-Line Diagnostics of Hydrogen-like and Helium-like Ions., ApJ 556, L91
Smith S.J., Adams J.S., Bandler S.R., et al., 2016, Transition-edge sensor pixel parameter design of the microcalorimeter array for the x-ray integral field unit on Athena., In: den Herder J.W.A., Takahashi T., Bautz M. (eds.) Proc. SPIE., Vol. 9905. Space Telescopes and Instrumentation 2016: Ultraviolet to Gamma Ray, Edinburgh, United Kingdom, p. 99052H
Sokolova-Lapa E., 2023, , PhD thesis, Friedrich Alexander Universität of Erlangen-Nürnberg
Sokolovsky K., Aydi E., Chomiuk L., et al., 2020a, Super-soft X-ray emission of Nova Reticuli 2020., Astronomer's Telegram 14043
Sokolovsky K.V., Aydi E., Chomiuk L., et al., 2020b, NuSTAR detection of Nova Reticuli 2020 = MGAB-V207., Astronomer's Telegram 13900
Sokolovsky K.V., Li K.L., Lopes de Oliveira R., et al., 2022, The first nova eruption in a novalike variable: YZ Ret as seen in X-rays and γ-rays., MNRAS 514, 2239
Solheim J.E., 2010, AM CVn Stars: Status and Challenges., PASP 122, 1133

Spiller E., 2015, X-Rays: Optical Elements, Ch. 270, CRC Press
Starrfield S., Iliadis C., Hix W.R., 2016, The Thermonuclear Runaway and the Classical Nova Outburst., PASP 128, 051001
Starrfield S., Truran J.W., Sparks W.M., et al., 1990, Soft x-ray emission from classical novae in outburst., In: Cassatella A., Viotti R. (eds.) Physics of Classical Novae., Springer Verlag, Berlin, Heidelberg, p.306
Starrfield S., Truran J.W., Sparks W.M., Kutter G.S., 1972, CNO Abundances and Hydrodynamic Models of the Nova Outburst., ApJ 176, 169
Staubert R., Trümper J., Kendziorra E., et al., 2019, Cyclotron lines in highly magnetized neutron stars., A&A 622, A61
Steiner J.F., McClintock J.E., Remillard R.A., et al., 2010, The Constant Inner-disk Radius of LMC X-3: A Basis for Measuring Black Hole Spin., ApJL 718, L117
Steiner J.F., Narayan R., McClintock J.E., Ebisawa K., 2009, A Simple Comptonization Model., PASP 121, 1279
Steiner J.F., Remillard R.A., García J.A., McClintock J.E., 2016, Stronger Reflection from Black Hole Accretion Disks in Soft X-Ray States., ApJL 829, L22
Stevens A.L., Uttley P., Altamirano D., et al., 2018, A NICER Discovery of a Low-frequency Quasi-periodic Oscillation in the Soft-intermediate State of MAXI J1535-571., ApJL 865, L15
Stiele H., Kong A.K.H., 2018, A Spectral and Timing Study of MAXI J1535-571, Based on Swift/XRT, XMM-Newton, and NICER Observations Obtained in Fall 2017., ApJ 868, 71
Stiele H., Kong A.K.H., 2020, A Timing Study of MAXI J1820+070 Based on Swift/XRT and NICER Monitoring in 2018/19., ApJ 889, 142
Strüder L., Briel U., Dennerl K., et al., 2001, The European Photon Imaging Camera on XMM-Newton: The pn-CCD camera., A&A 365, L18
Struve O., 1931, On the Origin of Bright Lines in Spectra of Stars of Class B., ApJ 73, 94
Sugimoto J., Mihara T., Kitamoto S., et al., 2016, MAXI observations of long-term variations of Cygnus X-1 in the low/hard and the high/soft states., PASJ 68, S17
Suleimanov V., Hertfelder M., Werner K., Kley W., 2014, Modeling the EUV spectra of optically thick boundary layers of dwarf novae in outburst., A&A 571, A55
Suleimanov V.F., Mauche C.W., Zhuchkov R.Y., Werner K., 2013, Fitting the Chandra LETG Spectrum of SS Cygni in Outburst with Model Atmosphere Spectra., In: Krzesiński J., Stachowski G., Moskalik P., Bajan K. (eds.) 18th European White Dwarf Workshop., Vol. 469. Astron. Soc. Pacific Conf. Ser., Astron. Soc. Pacific, San Francisco, p. 349
Sundqvist J.O., Owocki S.P., Puls J., 2018, 2D wind clumping in hot, massive stars from hydrodynamical line-driven instability simulations using a pseudo-planar approach., A&A 611, A17
Sunyaev R., Arefiev V., Babyshkin V., et al., 2021, SRG X-ray orbital observatory. Its telescopes and first scientific results., A&A 656, A132
Sunyaev R.A., Titarchuk L.G., 1980, Comptonization of X-rays in plasma clouds. Typical radiation spectra., A&A 500, 167
Sunyaev R.A., Trümper J., 1979, Hard X-ray spectrum of Cyg X-1., Nature 279, 506
Susskind L., Uglum J., 1994, Black hole entropy in canonical quantum gravity and superstring theory., Phys. Rev. D 50, 2700
Tamba T., Odaka H., Bamba A., et al., 2022, Simulation-based spectral analysis of X-ray CCD data affected by photon pile-up., PASJ 74, 364
Tanabé T., Nishida S., Matsumoto S., et al., 1997, Duration of the superwind phase of asymptotic giant branch stars., Nature 385, 509
Tanaka Y., Inoue H., Holt S.S., 1994, The X-Ray Astronomy Satellite ASCA., PASJ 46, L37
Tananbaum H., Gursky H., Kellogg E., et al., 1972, Observation of a Correlated X-Ray Transition in Cygnus X-1., ApJL 177, L5

Terrell, N. James J., 1972, Shot-Noise Character of Cygnus X-1 Pulsations., ApJL 174, L35
Tetarenko B.E., Sivakoff G.R., Heinke C.O., Gladstone J.C., 2016, WATCHDOG: A Comprehensive All-sky Database of Galactic Black Hole X-ray Binaries., ApJS 222, 15
Thompson T.A., Kochanek C.S., Stanek K.Z., et al., 2019, A noninteracting low-mass black hole-giant star binary system., Science 366, 637
Thorne K.S., Price R.H., 1975, Cygnus X-1: an interpretation of the spectrum and its variability., ApJL 195, L101
Timmer J., Koenig M., 1995, On generating power law noise., A&A 300, 707
Tolman R.C., 1939, Static Solutions of Einstein's Field Equations for Spheres of Fluid., Phys. Rev. 55, 364
Tomsick J.A., Nowak M.A., Parker M., et al., 2014, The Reflection Component from Cygnus X-1 in the Soft State Measured by NuSTAR and Suzaku., ApJ 780, 78
Tomsick J.A., Yamaoka K., Corbel S., et al., 2009, Truncation of the Inner Accretion Disk Around a Black Hole at Low Luminosity., ApJL 707, L87
Torres M.A.P., Casares J., Jiménez-Ibarra F., et al., 2019, Dynamical Confirmation of a Black Hole in MAXI J1820+070., ApJL 882, L21
Townsley D.M., Bildsten L., 2004, Theoretical Modeling of the Thermal State of Accreting White Dwarfs Undergoing Classical Nova Cycles., ApJ 600, 390
Townsley L.K., Broos P.S., Chartas G., et al., 2002, Simulating CCDs for the Chandra Advanced CCD Imaging Spectrometer., Nucl. Instrum. Methods Phys. Res., Sect. A 486, 716
Trümper J., Pietsch W., Reppin C., et al., 1978, Evidence for strong cyclotron line emission in the hard X-ray spectrum of Hercules X-1., ApJL 219, L105
Truran J.W., Livio M., 1986, On the Frequency of Occurrence of Oxygen-Neon-Magnesium White Dwarfs in Classical Nova Systems., ApJ 308, 721
Turner M.J.L., Abbey A., Arnaud M., et al., 2001, The European Photon Imaging Camera on XMM-Newton: The MOS cameras., A&A 365, L27
Usman S., Patil A., 2018, Radiation detector deadtime and pile up: A review of the status of science., Nuclear Engineering and Technology 50, 1006
Uttley P., Cackett E.M., Fabian A.C., et al., 2014, X-ray reverberation around accreting black holes., Astron. Astrophys. Rev. 22, 72
Uttley P., Hartog R.d., Bambi C., et al., 2021, The high energy Universe at ultra-high resolution: the power and promise of X-ray interferometry., Experimental Astronomy 51, 1081
Uttley P., McHardy I.M., 2001, The flux-dependent amplitude of broadband noise variability in X-ray binaries and active galaxies., MNRAS 323, L26
Uttley P., McHardy I.M., Papadakis I.E., 2002, Measuring the broad-band power spectra of active galactic nuclei with RXTE., MNRAS 332, 231
Uttley P., Wilkinson T., Cassatella P., et al., 2011, The causal connection between disc and power-law variability in hard state black hole X-ray binaries., MNRAS 414, L60
Vadawale S.V., Rao A.R., Naik S., et al., 2003, On the Origin of the Various Types of Radio Emission in GRS 1915+105., ApJ 597, 1023
van den Heuvel E.P.J., Bhattacharya D., Nomoto K., Rappaport S.A., 1992, Accreting white dwarf models for CAL 83, CAL 87 and other ultrasoft X-ray sources in the LMC., A&A 262, 97
van der Klis M., 1989, Fourier techniques in X-ray timing., In: Ögelman H., van den Heuvel E.P.J. (eds.) Timing Neutron Stars, Vol. 262. NATO Advanced Study Institute (ASI) Series C, p. 27
van der Klis M., 1997, Quantifying Rapid Variability in Accreting Compact Objects., In: Babu G.J., Feigelson E.D. (eds.) Statistical Challenges in Modern Astronomy, Vol. II., Springer-Verlag, New York, p. 321
van Maanen A., 1917, Two Faint Stars with Large Proper Motion., PASP 29, 258
van Paradijs J., McClintock J.E., 1994, Absolute visual magnitudes of low-mass X-ray binaries., A&A 290,

133
Vanbeveren D., De Loore C., Van Rensbergen W., 1998, Massive stars., Astron. Astrophys. Rev. 9, 63
Vanlandingham K.M., Starrfield S., Wagner R.M., et al., 1996, Optical and ultraviolet spectrophotometry of the ONeMg Nova V838 Herculis 1991., MNRAS 282, 563
Vaughan B.A., Nowak M.A., 1997, X-Ray Variability Coherence: How to Compute It, What It Means, and How It Constrains Models of GX 339-4 and Cygnus X-1., ApJL 474, L43
Vaughan S., 2010, A Bayesian test for periodic signals in red noise., MNRAS 402, 307
Vaughan S., Edelson R., Warwick R.S., Uttley P., 2003, On characterizing the variability properties of X-ray light curves from active galaxies., MNRAS 345, 1271
Veledina A., Muleri F., Poutanen J., et al., 2023, Astronomical puzzle Cyg X-3 is a hidden Galactic ultraluminous X-ray source., submitted to Nature arXiv:2303.01174
Verner D.A., Ferland G.J., Korista K.T., Yakovlev D.G., 1996, Atomic Data for Astrophysics. II. New Analytic FITS for Photoionization Cross Sections of Atoms and Ions., ApJ 465, 487
Voges W., Aschenbach B., Boller T., et al., 1999, The ROSAT all-sky survey bright source catalogue., A&A 349, 389
von Weizsäcker C.F.F., 1937, Über Elementumwandlungen im Inneren der Sterne. I, S. Hirzel
Vrtilek S.D., Boroson B.S., Hunacek A., et al., 2008, Ultraviolet Observations of the X-Ray Photoionized Wind of Cygnus X-1 during X-Ray Soft/High State., ApJ 678, 1248
Walborn N.R., 1973, The Spectrum of HDE 226868 (=CYGNUS X-1)., ApJL 179, L123
Walker M.F., 1954, Nova DQ Herculis (1934): an Eclipsing Binary with Very Short Period., PASP 66, 230
Walter F.M., 2022, Chance discovery sheds light on exploding stars., Nature 605, 230
Wang J., Kara E., Lucchini M., et al., 2022, The NICER "Reverberation Machine": A Systematic Study of Time Lags in Black Hole X-Ray Binaries., ApJ 930, 18
Wang J., Kara E., Steiner J.F., et al., 2020a, Relativistic Reflection and Reverberation in GX 339-4 with NICER and NuSTAR., ApJ 899, 44
Wang J., Mastroserio G., Kara E., et al., 2021, Disk, Corona, Jet Connection in the Intermediate State of MAXI J1820+070 Revealed by NICER Spectral-timing Analysis., ApJL 910, L3
Wang Y., Ji L., Zhang S.N., et al., 2020b, The Evolution of the Broadband Temporal Features Observed in the Black-hole Transient MAXI J1820+070 with Insight-HXMT., ApJ 896, 33
Webster B.L., Murdin P., 1972, Cygnus X-1-a Spectroscopic Binary with a Heavy Companion ?, Nature 235, 37
Weisskopf M.C., Brinkman B., Canizares C., et al., 2002, An Overview of the Performance and Scientific Results from the Chandra X-Ray Observatory., PASP 114, 1
Wells D.C., Greisen E.W., Harten R.H., 1981, FITS - a Flexible Image Transport System., A&AS 44, 363
Werner K., Dreizler S., Rauch T., 2012, TMAP: Tübingen NLTE Model-Atmosphere Package, Astrophysics Source Code Library, record ascl:1212.015
White T.R., Lightman A.P., Zdziarski A.A., 1988, Compton Reflection of Gamma Rays by Cold Electrons., ApJ 331, 939
Wiescher M., Görres J., Uberseder E., et al., 2010, The Cold and Hot CNO Cycles., Annual Review of Nuclear and Particle Science 60, 381
Wijnands R., Homan J., van der Klis M., 1999, The Complex Phase-Lag Behavior of the 3-12 HZ Quasi-Periodic Oscillations during the Very High State of XTE J1550-564., ApJL 526, L33
Wilkinson T., Uttley P., 2009, Accretion disc variability in the hard state of black hole X-ray binaries., MNRAS 397, 666
Wilms J., Allen A., McCray R., 2000, On the Absorption of X-Rays in the Interstellar Medium., ApJ 542, 914
Wilms J., Kreykenbohm I., Weber P., et al., 2020, SRG/eROSITA detection of the bright, transient X-ray flare SRGt J123822.3-253206., Astronomer's Telegram 13416

Wilms J., Nowak M.A., Pottschmidt K., et al., 2001, Discovery of recurring soft-to-hard state transitions in LMC X-3., MNRAS 320, 327
Wilms J., Nowak M.A., Pottschmidt K., et al., 2006, Long term variability of Cygnus X-1. IV. Spectral evolution 1999-2004., A&A 447, 245
Wilms J., Pottschmidt K., Pooley G.G., et al., 2007, Correlated Radio-X-Ray Variability of Galactic Black Holes: A Radio-X-Ray Flare in Cygnus X-1., ApJL 663, L97
Wilms J., Smith S.J., Peille P., et al., 2016, TESSIM: a simulator for the Athena-X-IFU., In: den Herder J.W.A., Takahashi T., Bautz M. (eds.) Proc. SPIE., Vol. 9905. Space Telescopes and Instrumentation 2016: Ultraviolet to Gamma Ray, Edinburgh, United Kingdom, p. 990564
Wolter H., 1952a, Spiegelsysteme streifenden Einfalls als abbildende Optiken für Röntgenstrahlen., Annalen der Physik 445, 94
Wolter H., 1952b, Verallgemeinerte Schwarzschildsche Spiegelsysteme streifender Reflexion als Optiken für Röntgenstrahlen., Annalen der Physik 445, 286
Wood M., Caputo R., Charles E., et al., 2017, Fermipy: An open-source Python package for analysis of Fermi-LAT Data., In: 35th International Cosmic Ray Conference (ICRC2017), Vol. 301. International Cosmic Ray Conference, p. 824
Woosley S.E., Heger A., 2015, The Remarkable Deaths of 9-11 Solar Mass Stars., ApJ 810, 34
Woosley S.E., Heger A., Weaver T.A., 2002, The evolution and explosion of massive stars., Rev. Mod. Phys. 74, 1015
XRISM Science Team 2020, Science with the X-ray Imaging and Spectroscopy Mission (XRISM), White paper (arXiv:2003.04962)
Yao Y., Lu W., Guolo M., et al., 2022, The Tidal Disruption Event AT2021ehb: Evidence of Relativistic Disk Reflection, and Rapid Evolution of the Disk-Corona System., ApJ 937, 8
Yuan W., Zhang C., Ling Z., et al., 2018, Einstein Probe: a lobster-eye telescope for monitoring the x-ray sky., In: den Herder J.W.A., Nikzad S., Nakazawa K. (eds.) Proc. SPIE., Vol. 10699. Space Telescopes and Instrumentation 2018: Ultraviolet to Gamma Ray, Austin, Texas, United States, p. 1069925
Zdziarski A.A., Dziełak M.A., De Marco B., et al., 2021, Accretion Geometry in the Hard State of the Black Hole X-Ray Binary MAXI J1820+070., ApJL 909, L9
Zdziarski A.A., Mikolajewska J., Belczynski K., 2013, Cyg X-3: a low-mass black hole or a neutron star., MNRAS 429, L104
Zdziarski A.A., Segreto A., Pooley G.G., 2016, The radio/X-ray correlation in Cyg X-3 and the nature of its hard spectral state., MNRAS 456, 775
Zel'dovich Y.B., Novikov I.D., 1966, The Hypothesis of Cores Retarded during Expansion and the Hot Cosmological Model., Astronomicheskii Zhurnal 43, 758
Zhang C., Ling Z.X., Sun X.J., et al., 2022, First Wide Field-of-view X-Ray Observations by a Lobster-eye Focusing Telescope in Orbit., ApJL 941, L2
Zhang L., Altamirano D., Cúneo V.A., et al., 2020, NICER observations reveal that the X-ray transient MAXI J1348-630 is a black hole X-ray binary., MNRAS 499, 851
Zhang S.N., Feroci M., Santangelo A., et al., 2016, eXTP: Enhanced X-ray Timing and Polarization mission., In: den Herder J.W.A., Takahashi T., Bautz M. (eds.) Proc. SPIE., Vol. 9905. Space Telescopes and Instrumentation 2016: Ultraviolet to Gamma Ray, Edinburgh, United Kingdom, p. 99051Q
Zhang W., Jahoda K., Swank J.H., et al., 1995, Dead-Time Modifications to Fast Fourier Transform Power Spectra., ApJ 449, 930
Zhou M., Grinberg V., Bu Q.C., et al., 2022, The spectral-timing analysis of Cygnus X-1 with Insight-HXMT., A&A 666, A172
Zoghbi A., Fabian A.C., Reynolds C.S., Cackett E.M., 2012, Relativistic iron K X-ray reverberation in NGC 4151., MNRAS 422, 129
Zoglauer A., Kruse-Madsen K., Kitaguchi T., et al., 2011, Simulating Extended Galactic Sources with

the NuSTAR Simulator NuSIM., In: AAS/High Energy Astrophysics Division #12, Vol. 12. AAS/High Energy Astrophysics Division, p. 43.07

Appendix A

Supplementary Data on the Cygnus X-1 Analysis

In this section, we provide supplementary information on the analysis of Cyg X-1 presented in Ch. 5. Table A.1 contains the observation log of the data analyzed in this paper. Table A.2 provides the parameters of the fit model used in Sect. 5.5.3. Figures A.1–A.52 show the timing products of each observation in the *NICER* archive of Cyg X-1 up to Cycle 4. Each collection of figures is arranged as follows. The top row shows overview figures of the lightcurve, the PSD in 0.5–10 keV, and the location of the observation in the hardness-intensity, orbital phase, and color-color diagrams. The data in the top rows are colored as in the main text: red is the soft, green the intermediate, and blue the hard state. The bottom panel shows timing properties for low and high energies. The left column shows PSDs computed in three energy bands. The center column shows the lag-frequency spectrum for two correlated bands: Blue uses 0.5–1 keV and 2–4 keV, and red uses 2–4 keV and 5–8 keV. Dashed lines denote the phase-wrapping limit. The right column shows the coherence between these energy bands.

Table A.1: Overview of the Cyg X-1 observations in the *NICER* archive up to Cycle 4. Photon indices are derived from diskbb+power law fits, described in Sect. 5.3.1. The last column lists observations with a confident visual detection of a timing feature.

Obs. ID	Start date	Exposure [s]	Γ	ϕ_{orb}	timing feature
0100320101	2017-06-30T15:55:11	719	1.8	0.02–0.03	
0100320102	2017-07-02T12:41:37	1580	2.2	0.36–0.38	–
0100320103	2017-07-03T01:27:00	668	2.1	0.45–0.61	–
0100320104	2017-07-04T00:00:28	10682	1.9	0.62–0.80	✓
0100320105	2017-07-05T00:49:32	14153	1.9	0.80–0.96	✓
0100320106	2017-07-06T01:21:25	7945	1.8	0.00–0.14	✓
0100320107	2017-07-07T08:23:28	4369	2.0	0.22–0.24	✓
0100320108	2017-07-10T23:19:38	415	2.1	0.86–0.87	–
0100320109	2017-07-11T00:19:49	7304	2.1	0.87–0.04	

0100320110	2017-07-12T00:03:49	6584	2.3	0.05–0.21	–
1100320101	2017-10-28T06:53:58	3709	3.3	0.39–0.42	–
1100320102	2017-10-28T23:53:17	3054	3.0	0.51–0.55	–
1100320103	2017-10-30T00:35:37	1406	3.4	0.70–0.70	–
1100320104	2017-11-01T11:05:00	626	3.0	0.13–0.17	–
1100320106	2017-12-01T22:13:28	501	3.0	0.57–0.57	–
1100320107	2017-12-02T03:07:00	483	2.9	0.61–0.66	–
1100320108	2017-12-03T23:37:15	106	3.5	0.94–0.94	–
1100320109	2017-12-04T21:15:20	221	3.3	0.10–0.11	–
1100320110	2018-02-08T20:16:33	3970	1.6	0.88–0.90	
1100320111	2018-02-08T23:21:40	10251	1.8	0.90–0.95	✓
1100320112	2018-02-17T14:29:47	400	1.8	0.44–0.49	
1100320113	2018-02-18T05:51:40	1044	1.7	0.56–0.67	
1100320114	2018-02-19T00:21:00	390	1.8	0.69–0.87	–
1100320115	2018-02-20T02:38:00	386	1.7	0.89–0.93	
1100320116	2018-02-21T00:10:00	678	1.7	0.05–0.13	
1100320117	2018-03-26T18:41:40	6203	2.2	0.08–0.12	–
1100320118	2018-03-27T00:52:40	4612	2.3	0.13–0.15	–
1100320119	2018-04-15T14:55:08	11373	2.7	0.63–0.69	–
1100320121	2018-05-27T07:38:00	17450	2.7	0.07–0.16	–
1100320122	2018-08-11T03:12:34	17954	3.1	0.61–0.69	–
2100320101	2019-04-04T18:14:20	5801	1.8	0.87–0.90	✓
2636010101	2019-08-06T09:01:20	14207	1.8	0.94–0.04	✓
2636010102	2019-11-13T10:32:00	12355	3.1	0.63–0.71	–
2636010201	2019-09-18T23:42:59	4272	2.4	0.73–0.80	–
4690010103	2022-02-15T12:10:45	274	1.7	0.97–0.04	–
4690010104	2022-03-04T09:46:04	1176	1.5	0.99–1.00	
4690010105	2022-03-10T00:29:20	1564	1.6	0.99–0.00	–
4690010106	2022-03-15T12:07:00	4759	1.6	0.97–0.01	shelf
4690010107	2022-03-20T09:48:00	4795	1.7	0.85–0.90	shelf
4690010109	2022-04-12T15:50:21	4386	1.6	1.00–0.01	–
4690010110	2022-04-17T09:04:37	3798	1.7	0.84–0.95	
4690010111	2022-04-18T00:44:17	6180	1.6	0.96–0.06	–
4690020101	2022-02-12T19:01:14	879	1.6	0.48–0.51	–
4690020102	2022-02-18T10:05:41	235	1.6	0.49–0.50	–
4690020103	2022-03-07T04:20:20	715	1.7	0.48–0.48	
4690020104	2022-03-12T19:04:58	912	1.7	0.48–0.49	
4690020105	2022-03-18T03:35:50	2320	1.7	0.44–0.46	shelf
4690020107	2022-04-04T03:37:06	1865	1.6	0.48–0.49	–
4690020108	2022-04-06T23:41:40	239	1.5	0.98–0.01	–
4690020109	2022-04-09T21:20:00	2063	1.6	0.50–0.51	–
4690020110	2022-04-15T09:14:00	2441	1.7	0.48–0.50	

Table A.2: Lorentzian model parameters of the simultaneous fit of observation 2636010101 (Fig. 5.21). Each non-zero-centered Lorentzian adds 6 free parameters: Frequency, width, and two normalizations for the low- and high-energy PSD plus the lag and modulus of the cross vector. The norm of the real/imaginary part is the modulus of the cross vector times the cosine/sine of the phase lag, respectively. The frequency of the zeroth Lorentzian (L_0) is fixed to 0 Hz and phase zero is anchored to the strongest component (L_1). L_n denotes the narrow component at the frequency of the timing feature. Uncertainties denote 90% confidence limits.

Parameter	Value
ν_{L_0} [Hz]	0 (frozen)
ν_{L_1} [Hz]	0.186 ± 0.010
ν_{L_2} [Hz]	1.76 ± 0.12
ν_{L_n} [Hz]	1.57 ± 0.04
Δ_{L_0} [Hz]	$(8 \pm 6) \times 10^{-3}$
Δ_{L_1} [Hz]	0.703 ± 0.018
Δ_{L_2} [Hz]	4.79 ± 0.10
Δ_{L_n} [Hz]	$0.62^{+0.14}_{-0.12}$
$\Delta\phi_{L_0}$ [rad]	$-0.13^{+0.09}_{-0.13}$
$\Delta\phi_{L_1}$ [rad]	0 (frozen)
$\Delta\phi_{L_2}$ [rad]	$0.197^{+0.021}_{-0.022}$
$\Delta\phi_{L_n}$ [rad]	$1.01^{+0.16}_{-0.14}$
$N(L_0, \text{CPD})$	$\left(6.1^{+4.0\,(\text{p})}_{-2.3}\right) \times 10^{-4}$
$N(L_0, 0.5\text{–}1\,\text{keV})$	$\left(6.6^{+3.5\,(\text{p})}_{-2.0}\right) \times 10^{-4}$
$N(L_0, 2\text{–}4\,\text{keV})$	$(6 \pm 4) \times 10^{-4\,(\text{p})}$
$N(L_1, \text{CPD})$	0.0448 ± 0.0009
$N(L_1, 0.5\text{–}1\,\text{keV})$	0.0307 ± 0.0006
$N(L_1, 2\text{–}4\,\text{keV})$	$0.0665^{+0.0016}_{-0.0017}$
$N(L_2, \text{CPD})$	0.0129 ± 0.0007
$N(L_2, 0.5\text{–}1\,\text{keV})$	$(3.7 \pm 0.4) \times 10^{-3}$
$N(L_2, 2\text{–}4\,\text{keV})$	0.0428 ± 0.0016
$N(L_n, \text{CPD})$	$\left(1.59^{+0.34}_{-0.28}\right) \times 10^{-3}$
$N(L_n, 0.5\text{–}1\,\text{keV})$	$\left(9.6^{+2.3}_{-2.0}\right) \times 10^{-4}$
$N(L_n, 2\text{–}4\,\text{keV})$	$\left(10^{+8}_{-7}\right) \times 10^{-4}$

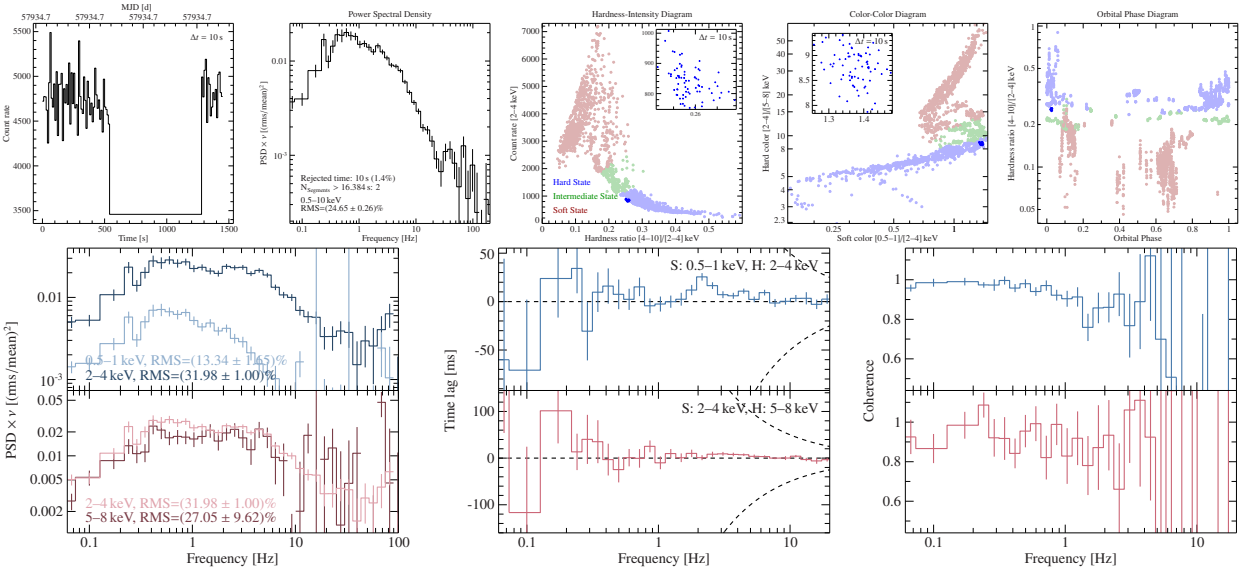

Figure A.1: Observation 0100320101. $\Gamma \approx 1.8$.

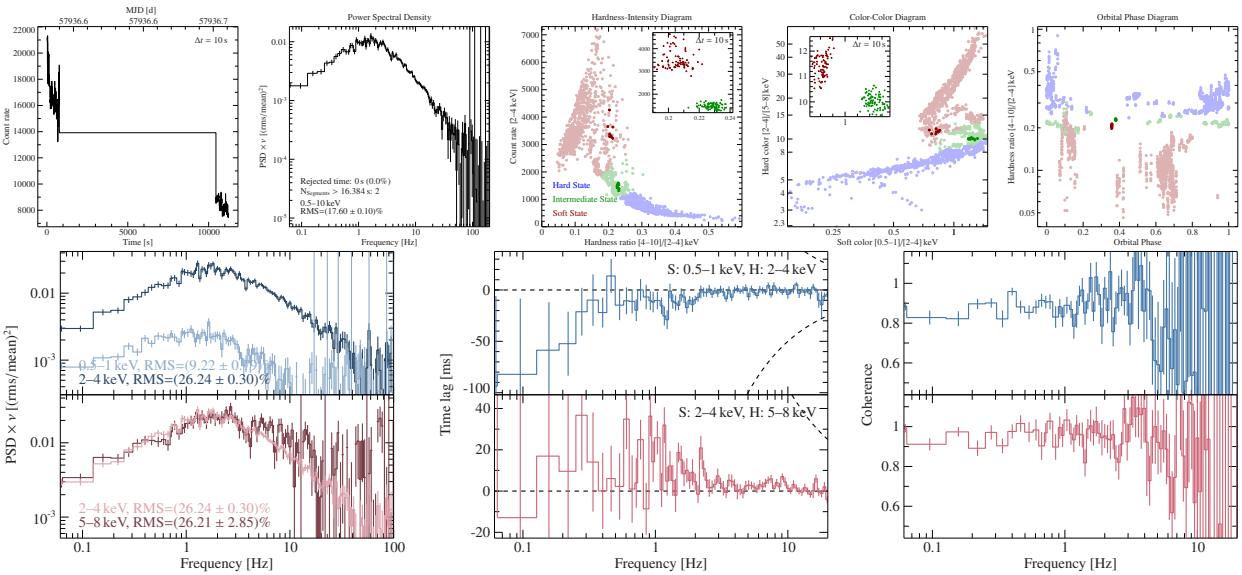

Figure A.2: Observation 0100320102. $\Gamma \approx 2.2$.

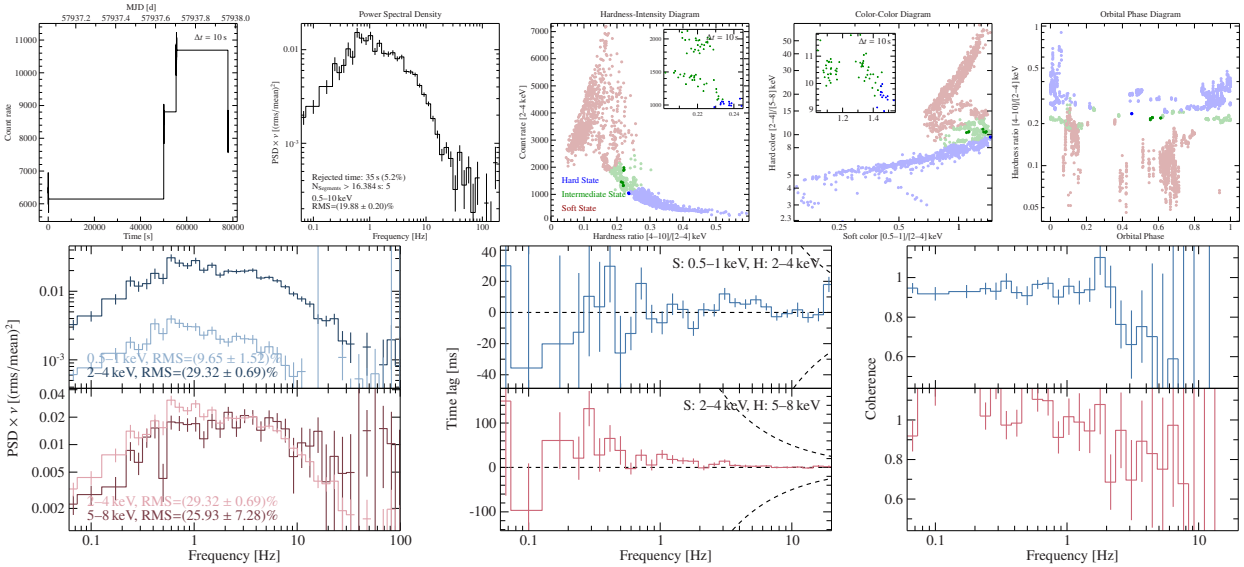

Figure A.3: Observation 0100320103. $\Gamma \approx 2.1$.

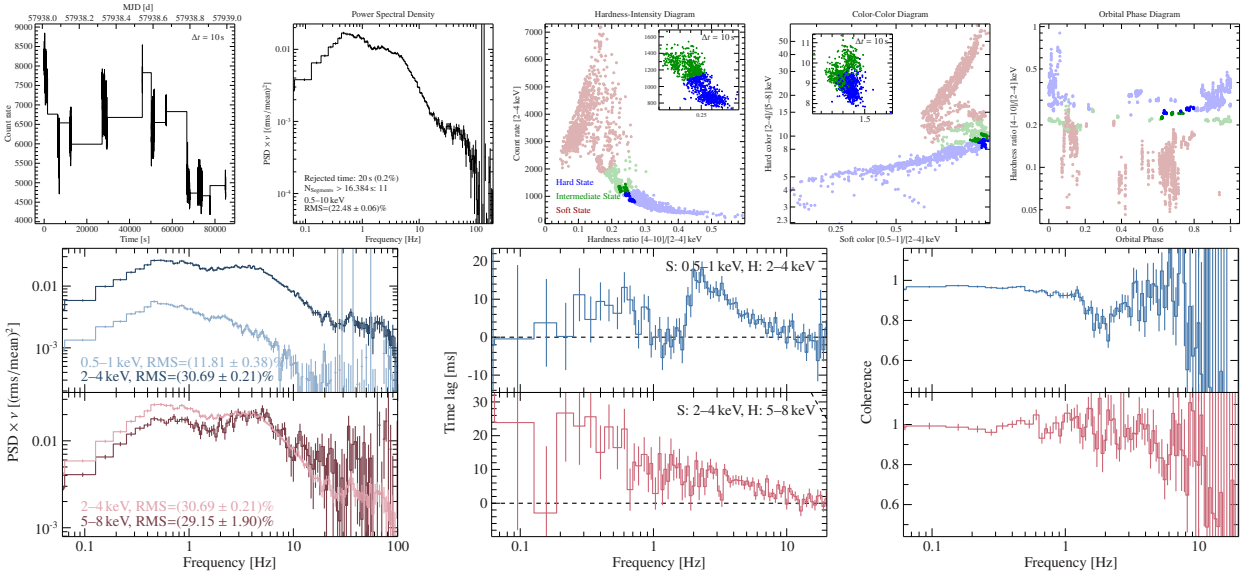

Figure A.4: Observation 0100320104. $\Gamma \approx 1.9$.

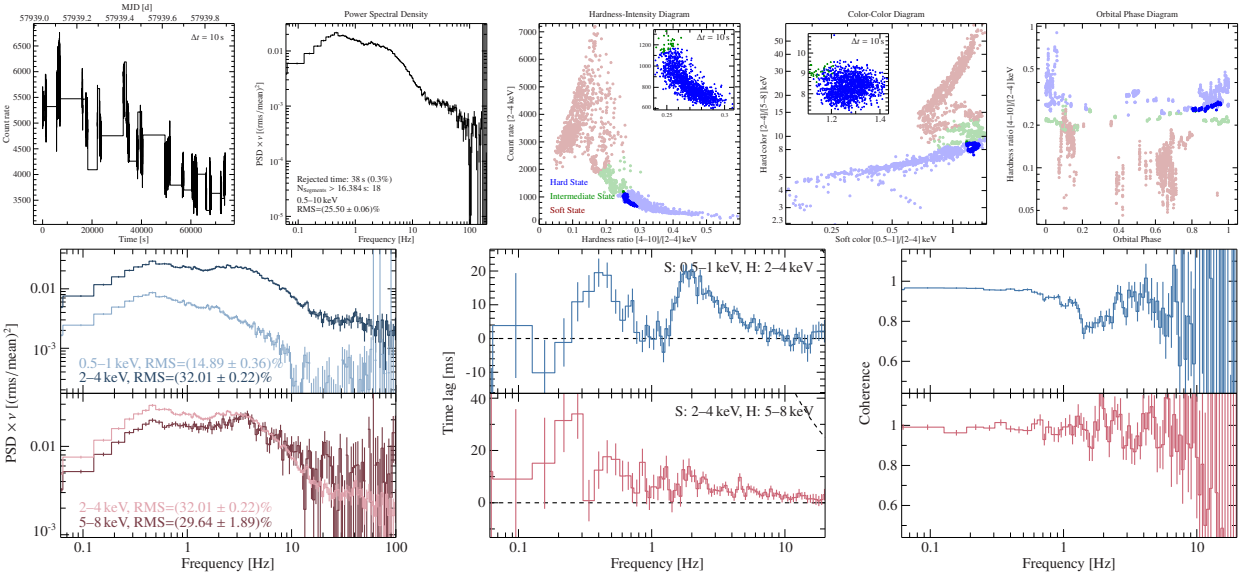

Figure A.5: Observation 0100320105. $\Gamma \approx 1.9$.

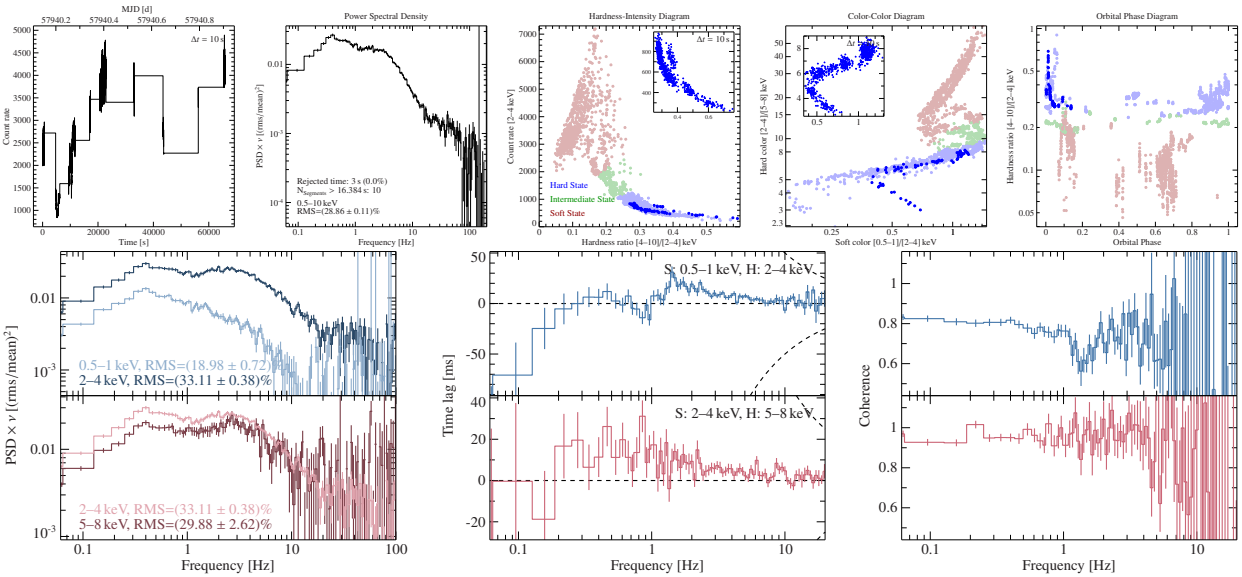

Figure A.6: Observation 0100320106. $\Gamma \approx 1.8$.

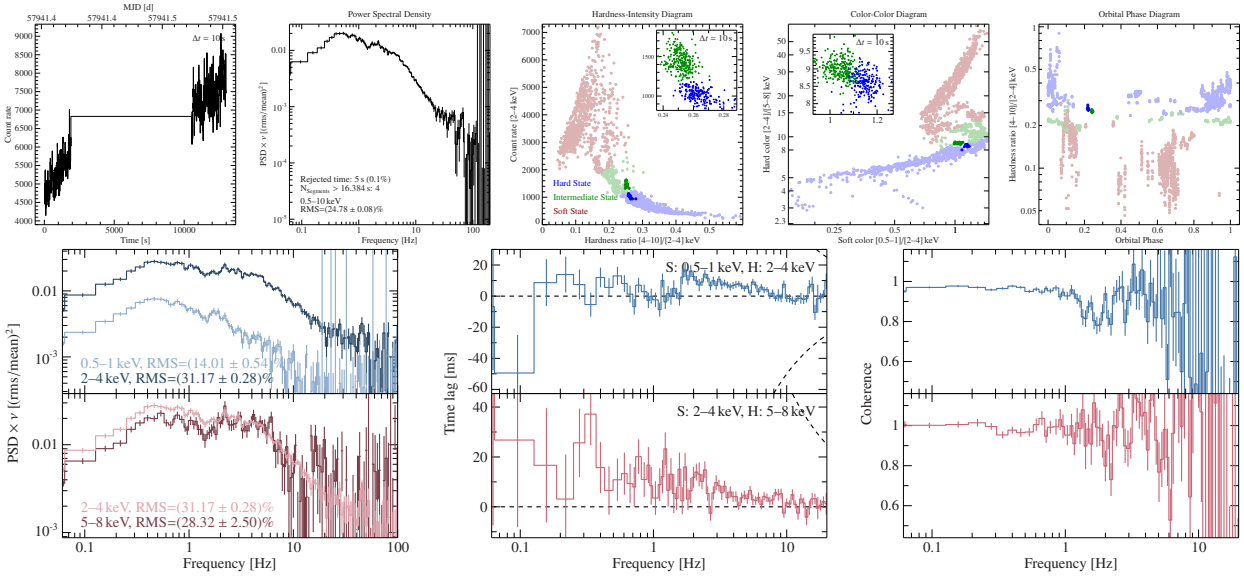

Figure A.7: Observation 0100320107. $\Gamma \approx 2.0$.

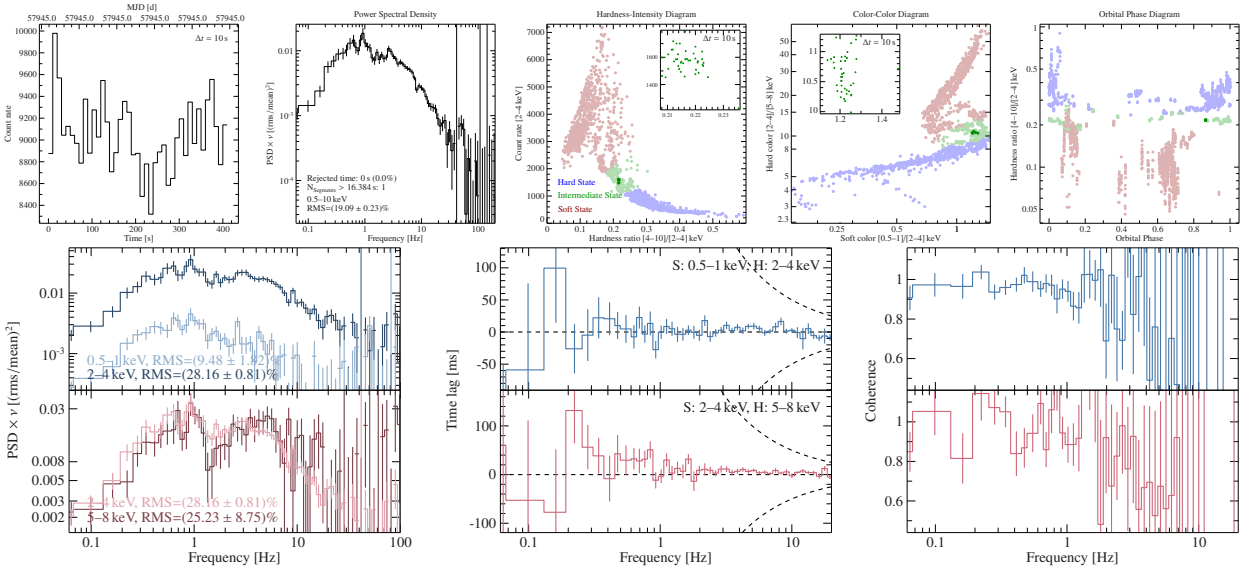

Figure A.8: Observation 0100320108. $\Gamma \approx 2.1$.

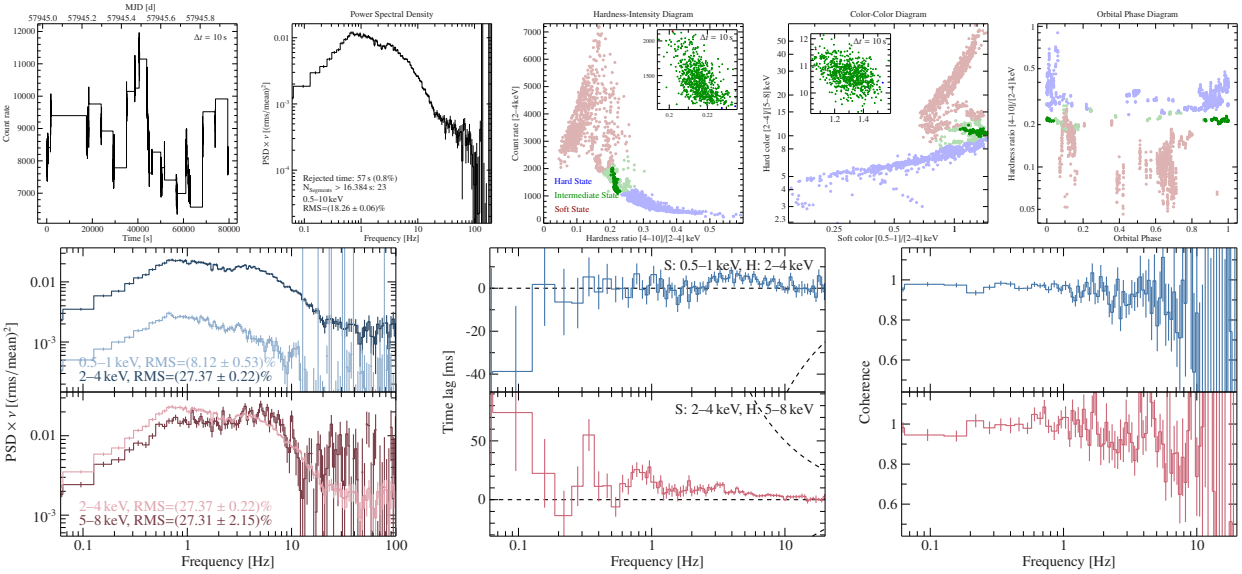

Figure A.9: Observation 0100320109. $\Gamma \approx 2.1$.

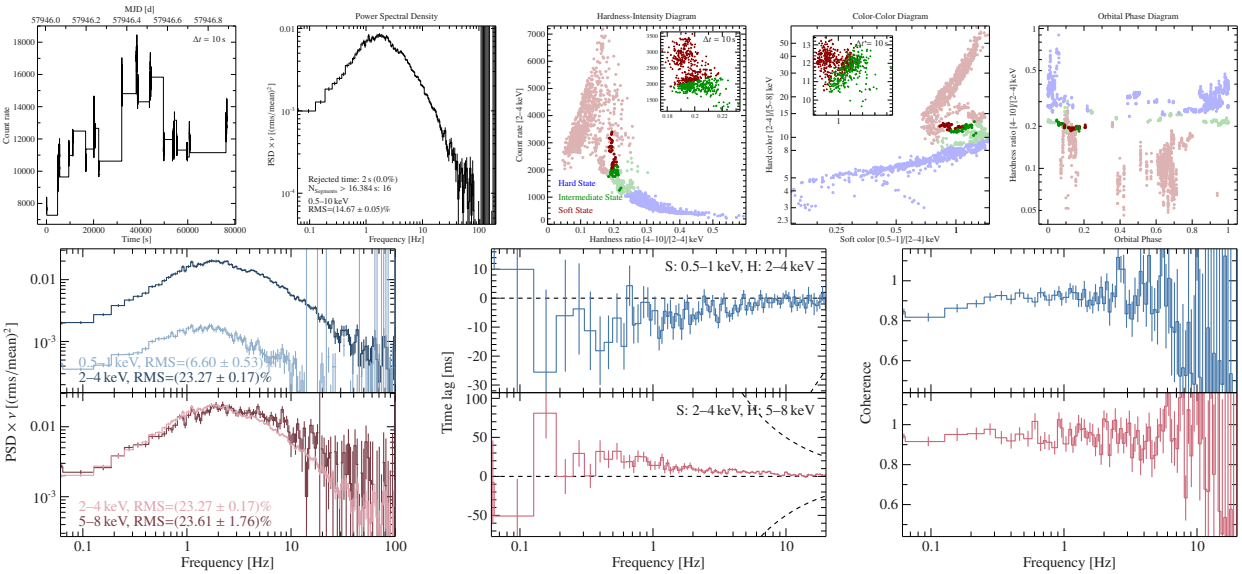

Figure A.10: Observation 0100320110. $\Gamma \approx 2.3$.

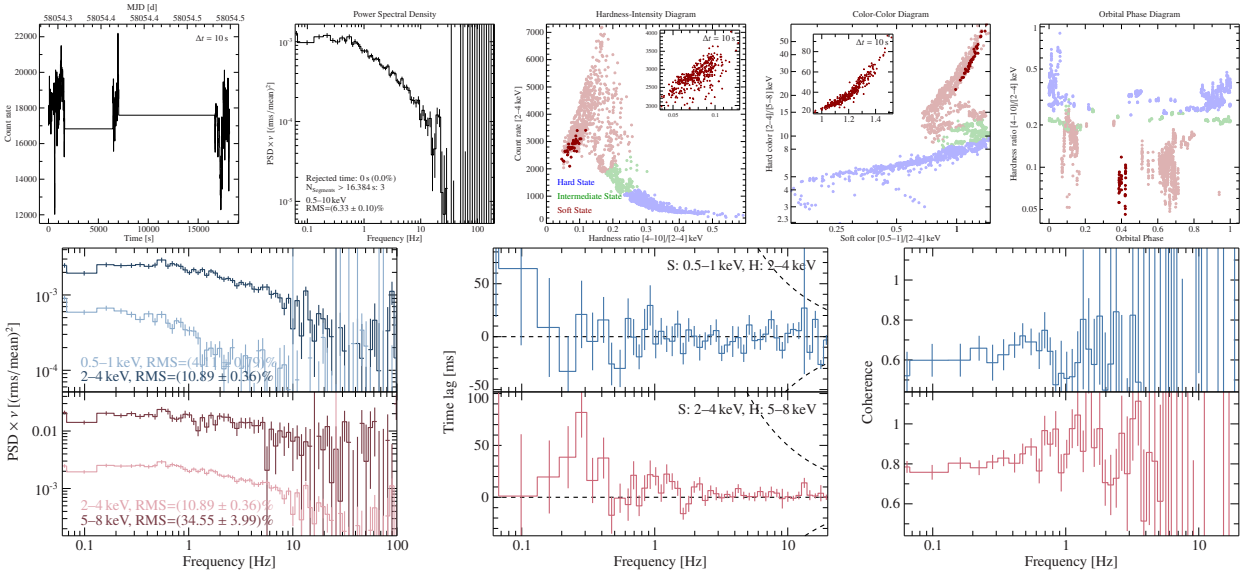

Figure A.11: Observation 1100320101. $\Gamma \approx 3.3$.

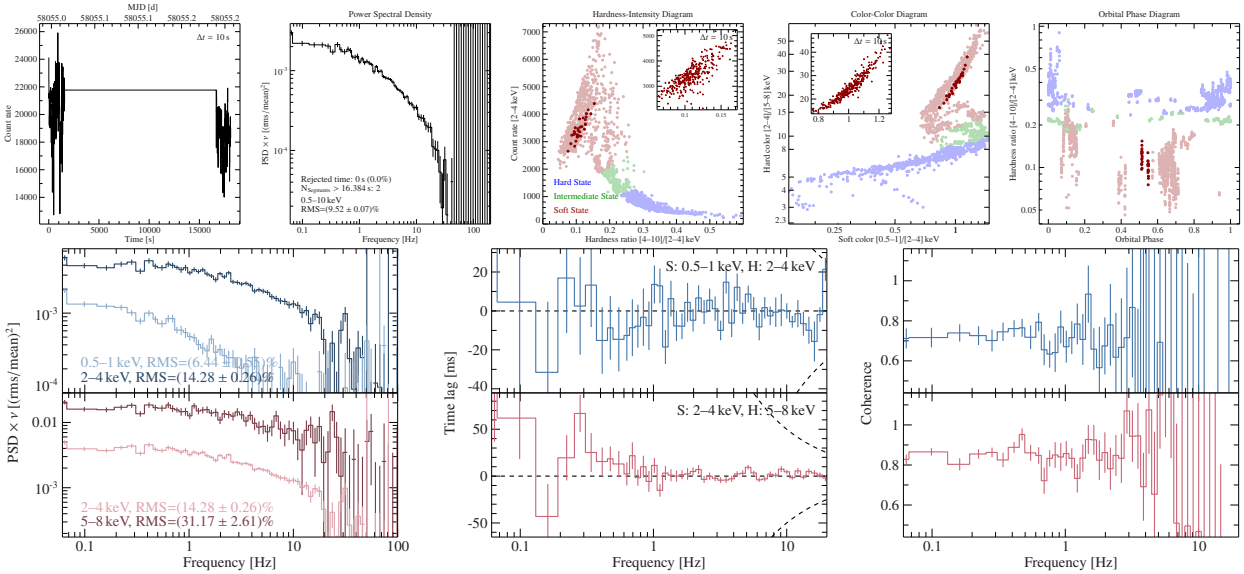

Figure A.12: Observation 1100320102. $\Gamma \approx 3.0$.

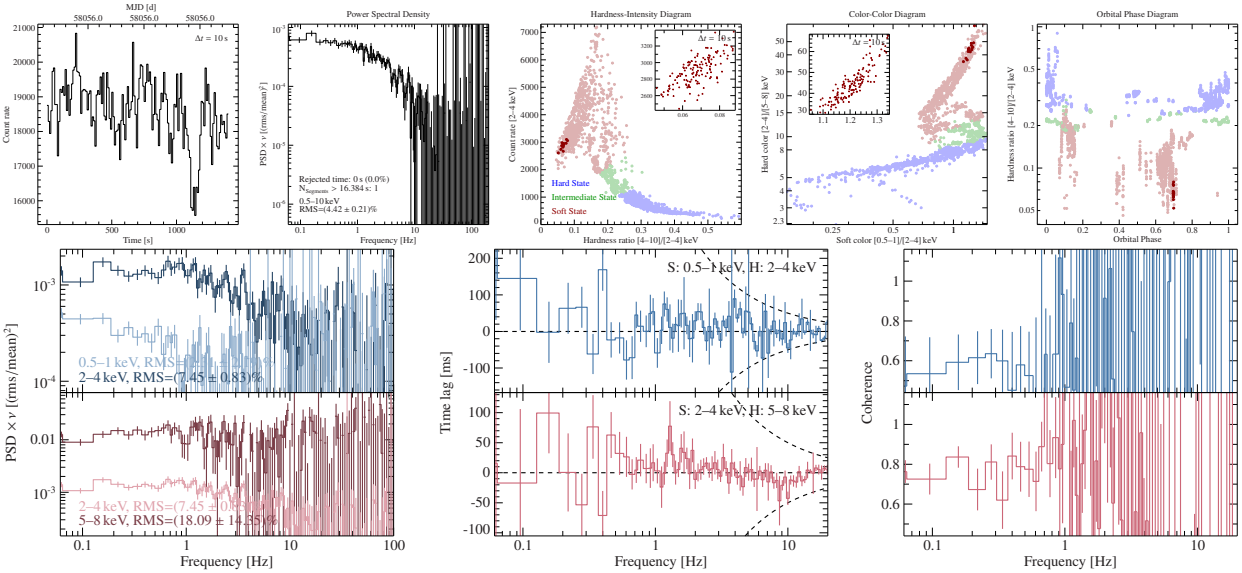

Figure A.13: Observation 1100320103. $\Gamma \approx 3.4$.

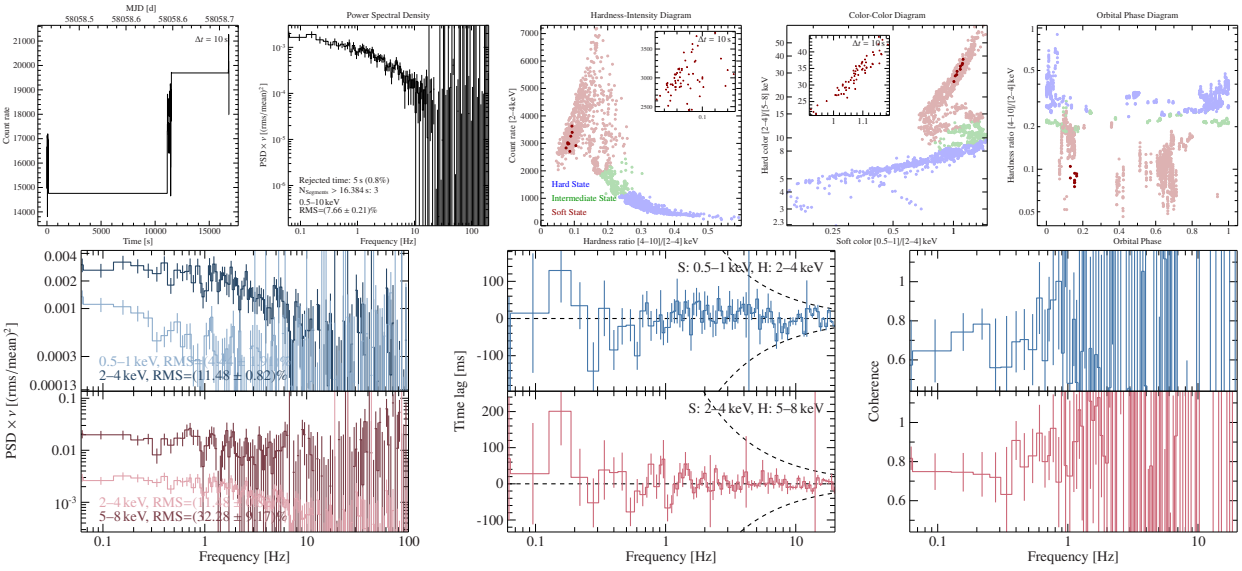

Figure A.14: Observation 1100320104. $\Gamma \approx 3.0$.

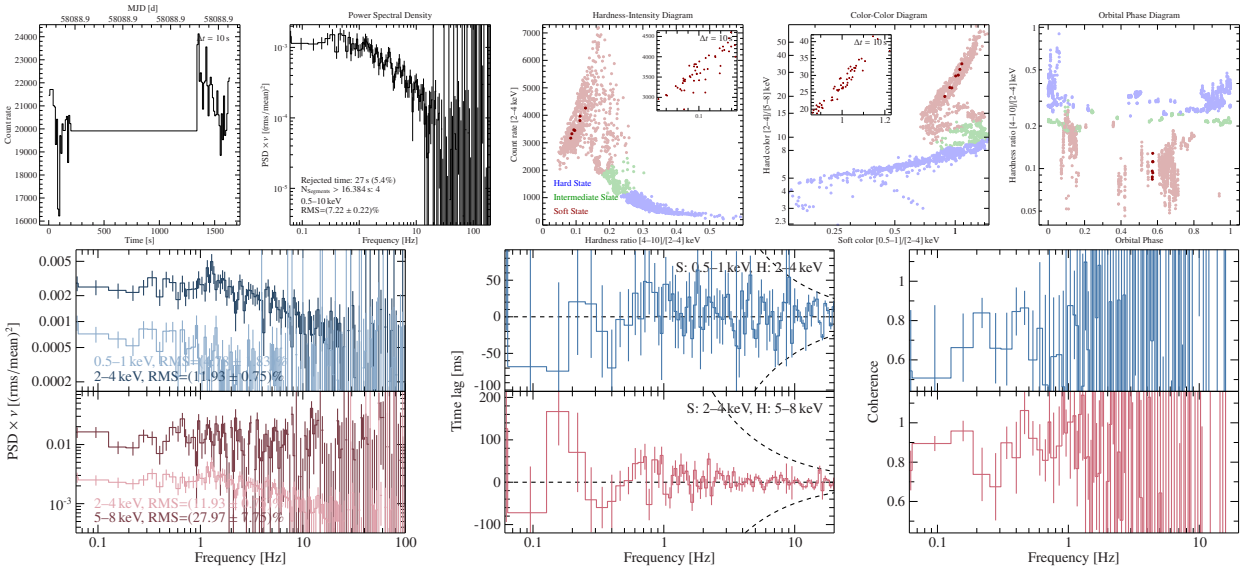

Figure A.15: Observation 1100320106. $\Gamma \approx 3.0$.

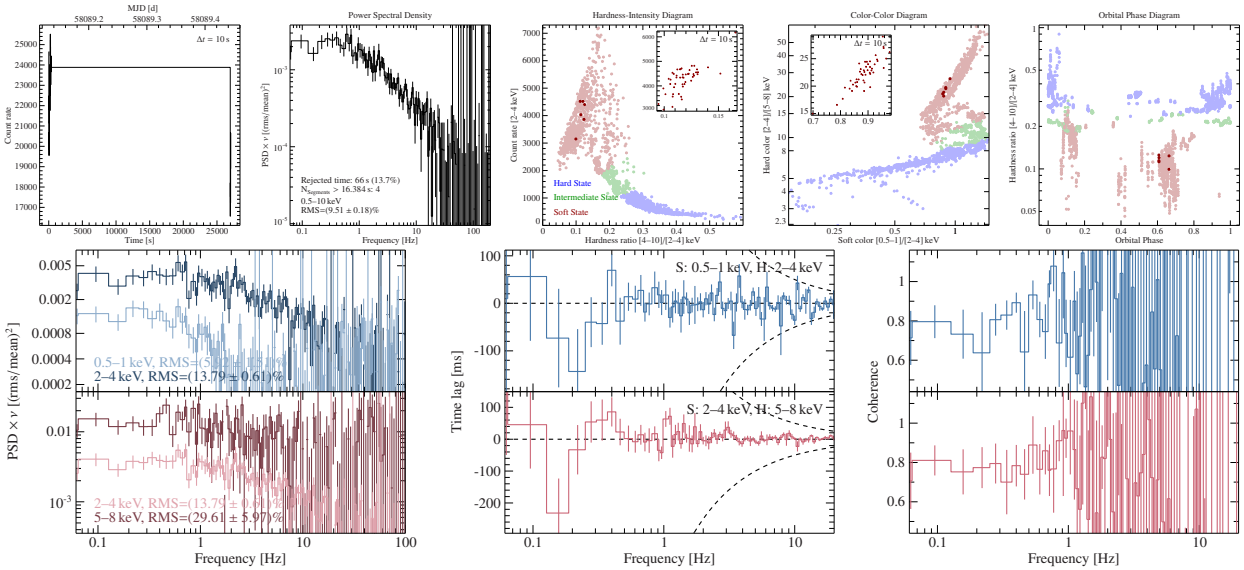

Figure A.16: Observation 1100320107. $\Gamma \approx 2.9$.

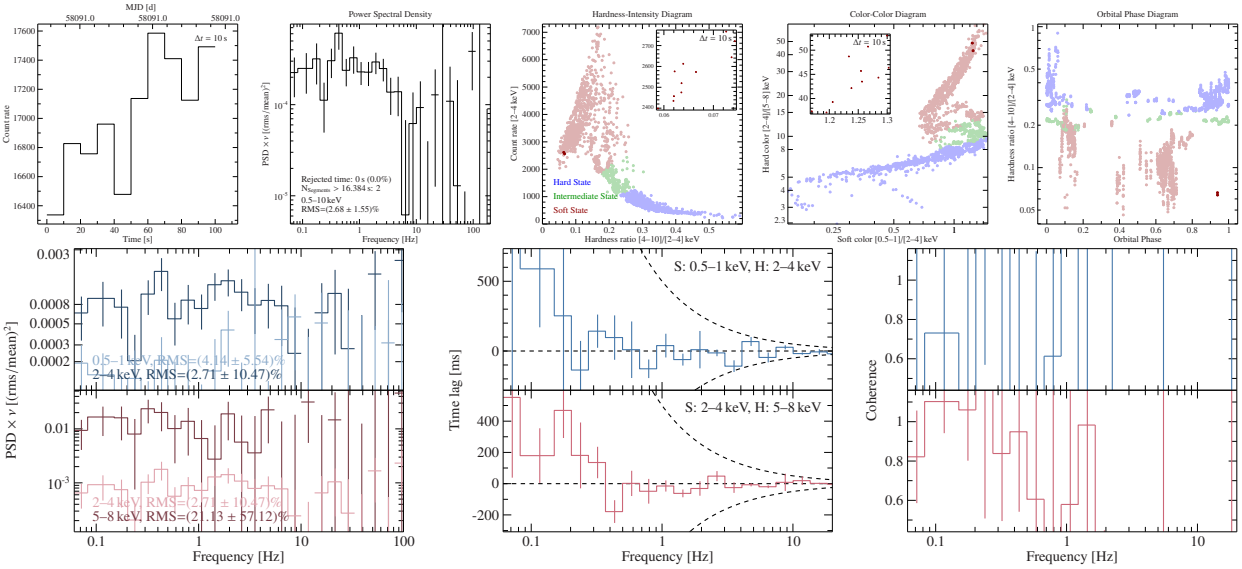

Figure A.17: Observation 1100320108. $\Gamma \approx 3.5$.

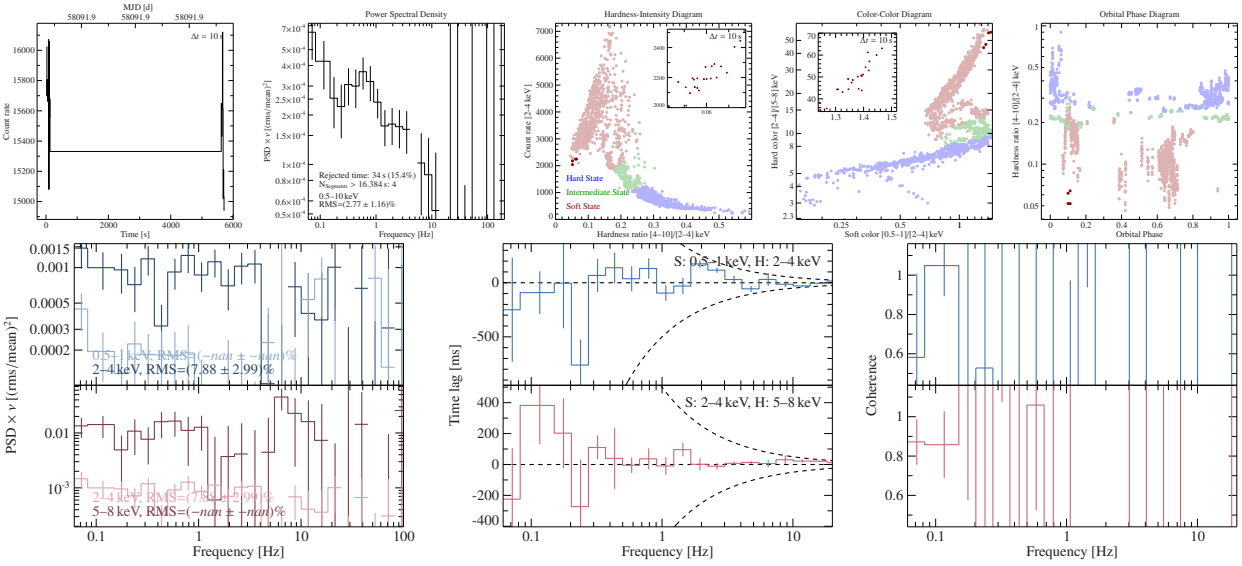

Figure A.18: Observation 1100320109. $\Gamma \approx 3.3$.

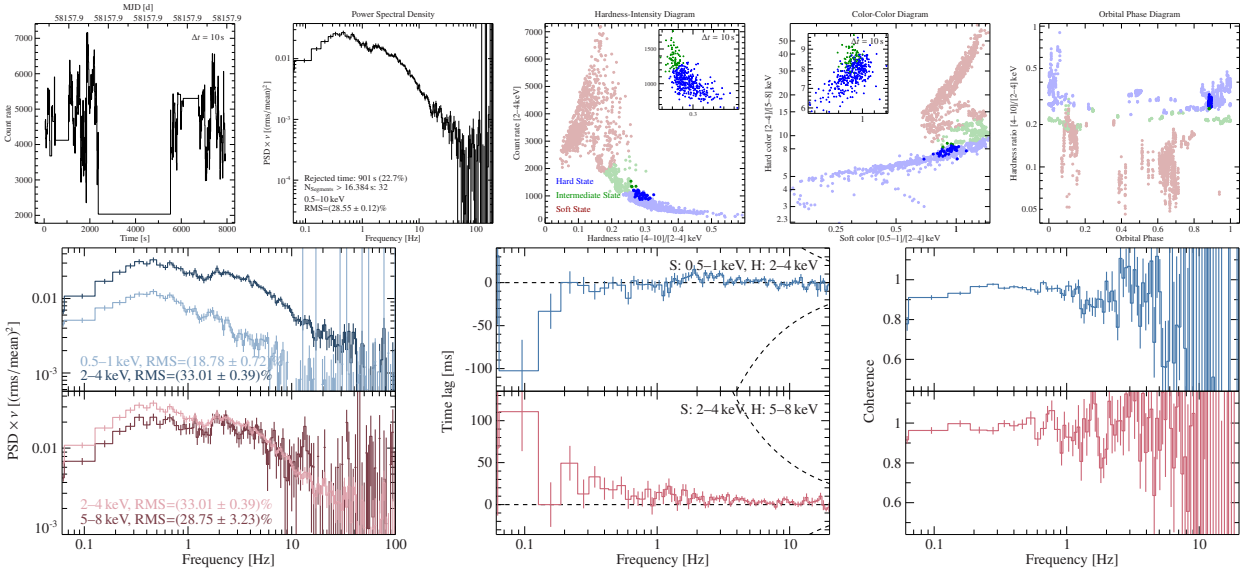

Figure A.19: Observation 1100320110. $\Gamma \approx 1.6$.

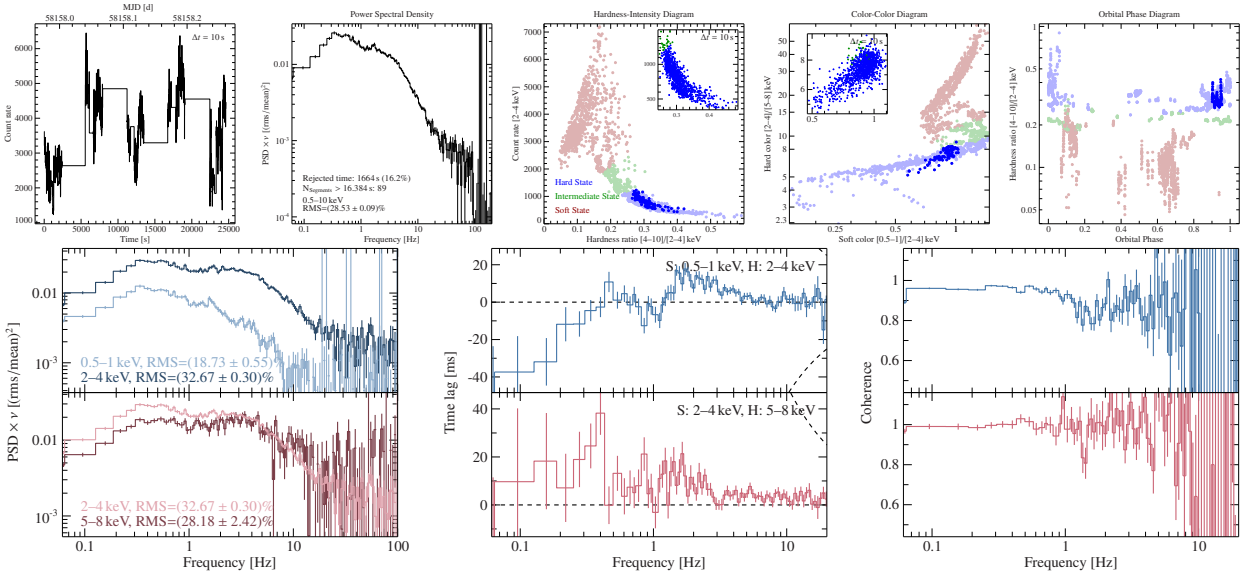

Figure A.20: Observation 1100320111. $\Gamma \approx 1.8$.

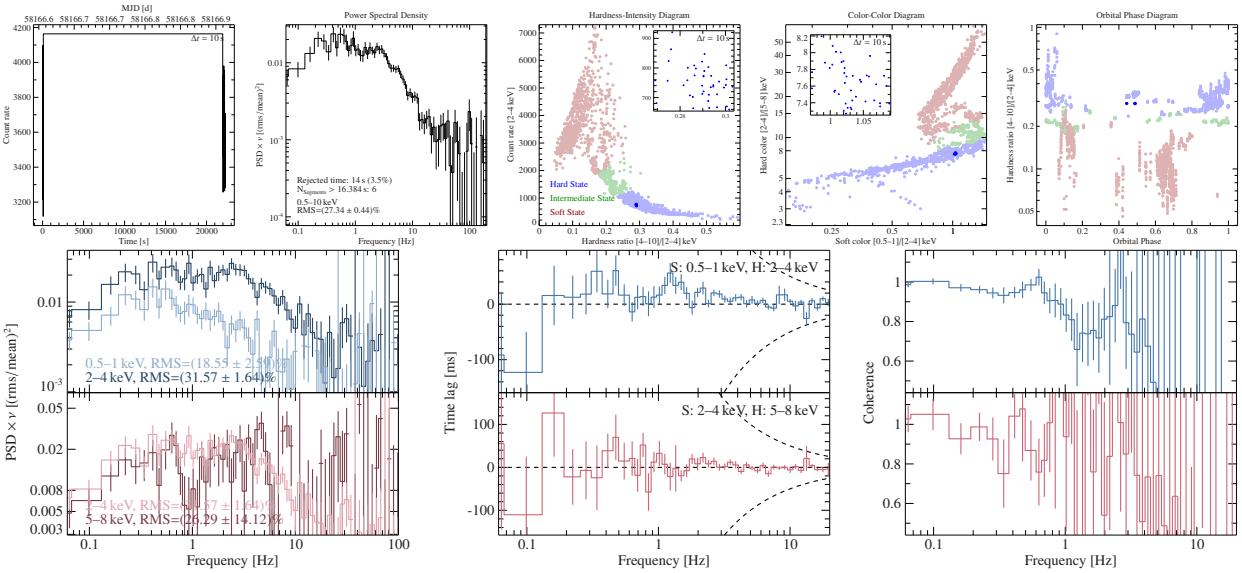

Figure A.21: Observation 1100320112. $\Gamma \approx 1.8$.

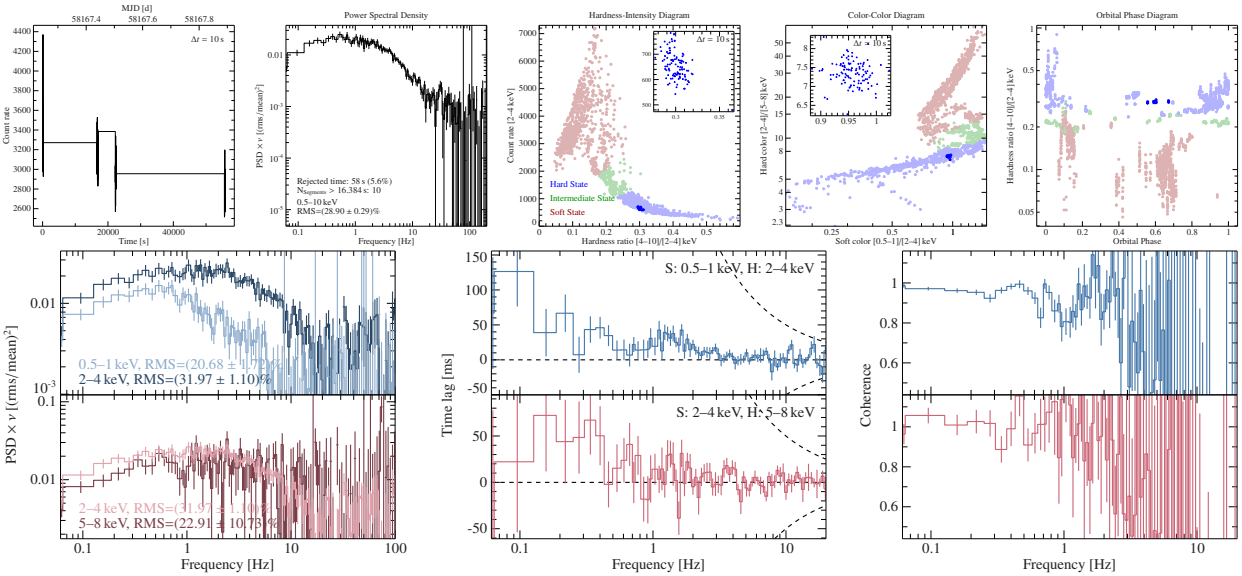

Figure A.22: Observation 1100320113. $\Gamma \approx 1.7$.

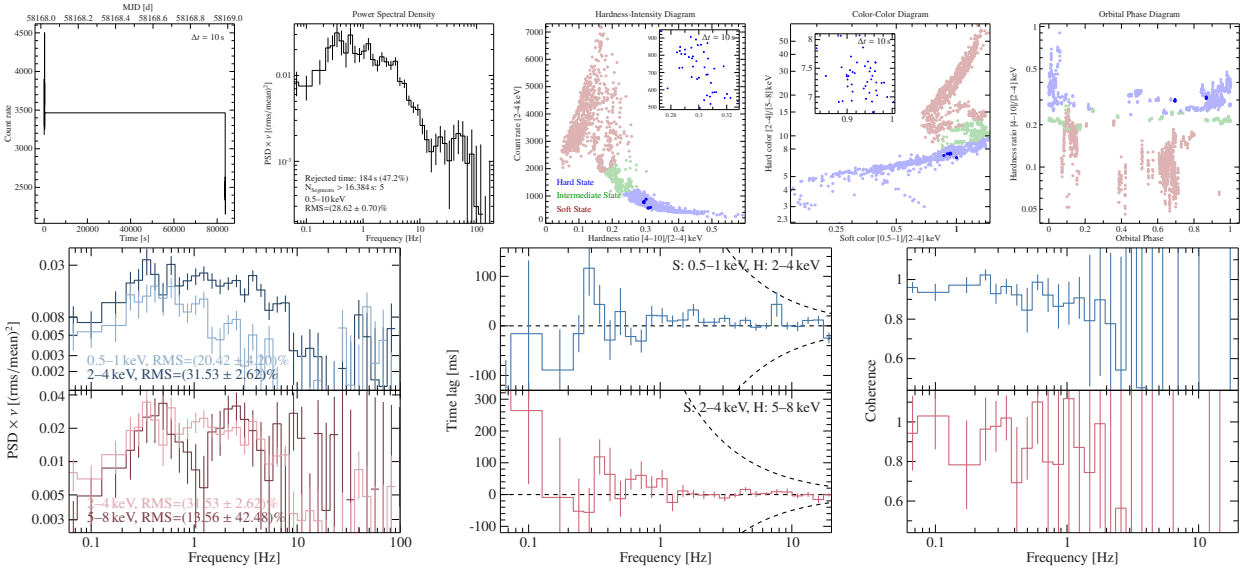

Figure A.23: Observation 1100320114. $\Gamma \approx 1.8$.

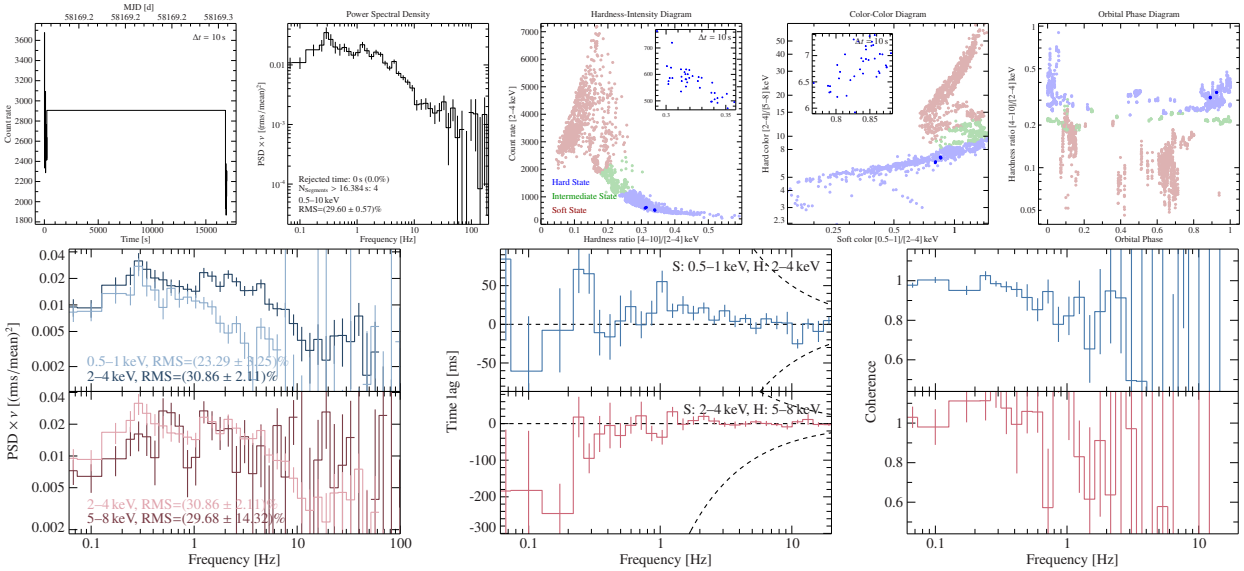

Figure A.24: Observation 1100320115. $\Gamma \approx 1.7$.

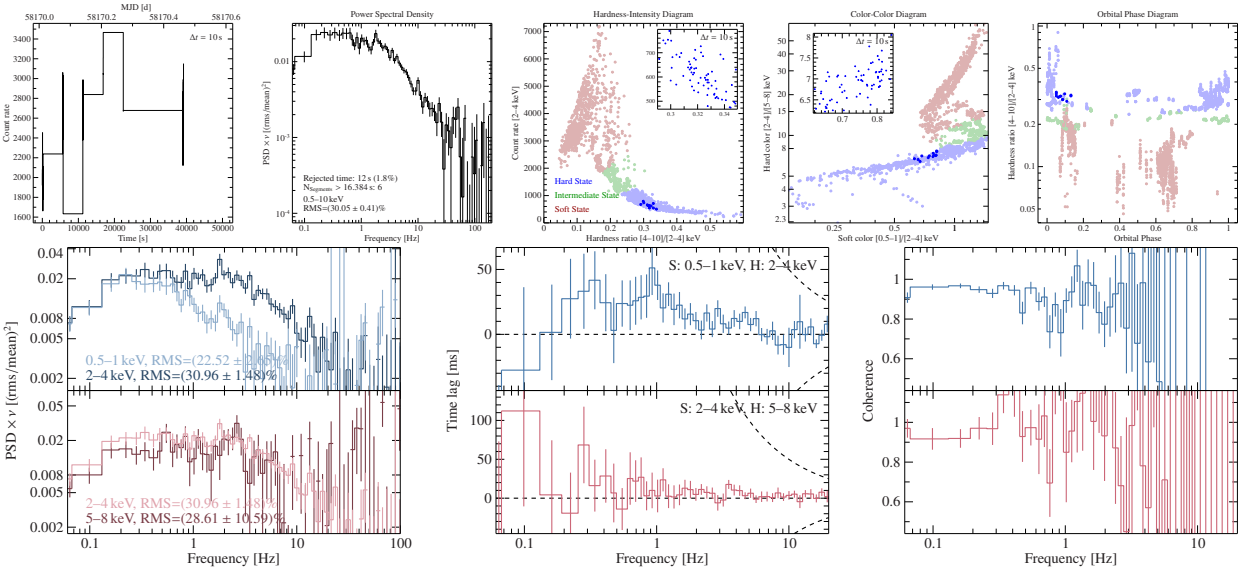

Figure A.25: Observation 1100320116. $\Gamma \approx 1.7$.

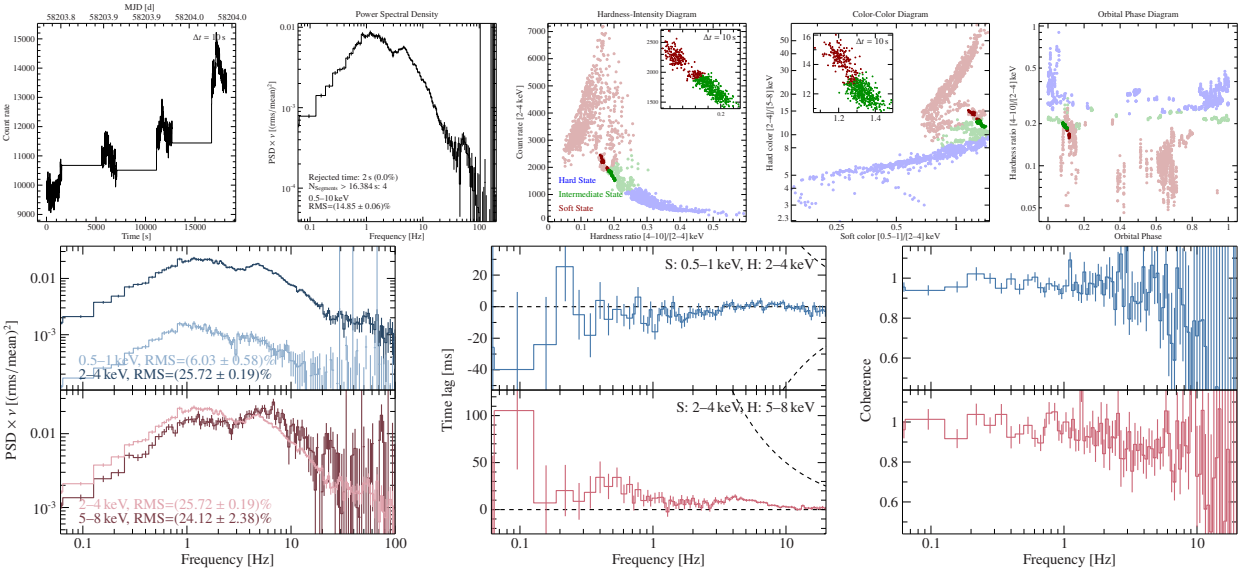

Figure A.26: Observation 1100320117. $\Gamma \approx 2.2$.

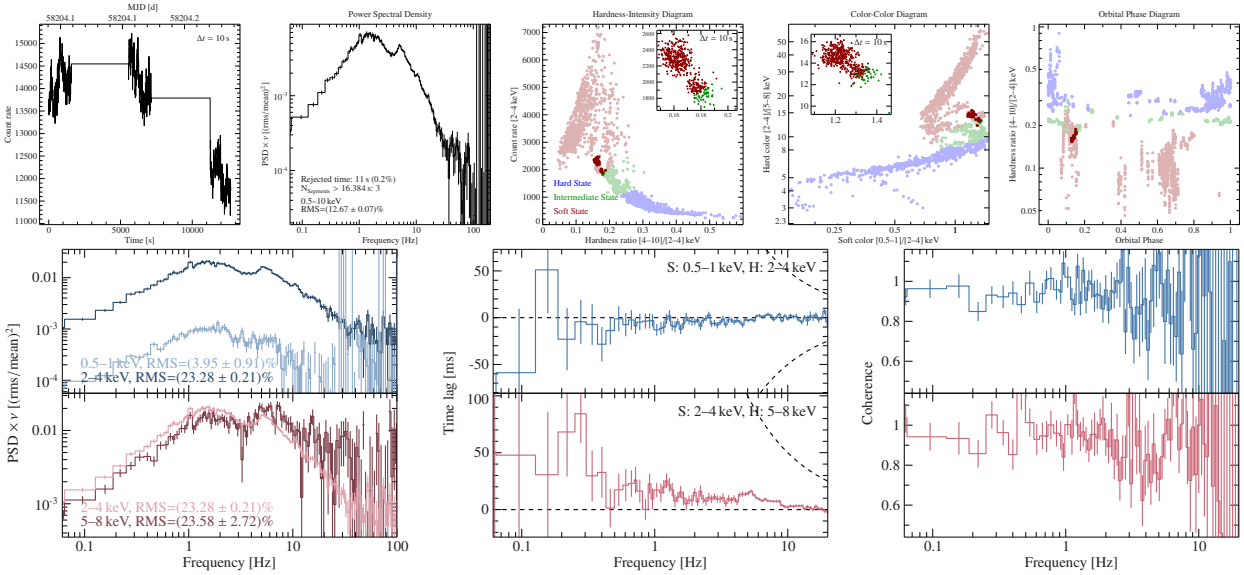

Figure A.27: Observation 1100320118. $\Gamma \approx 2.3$.

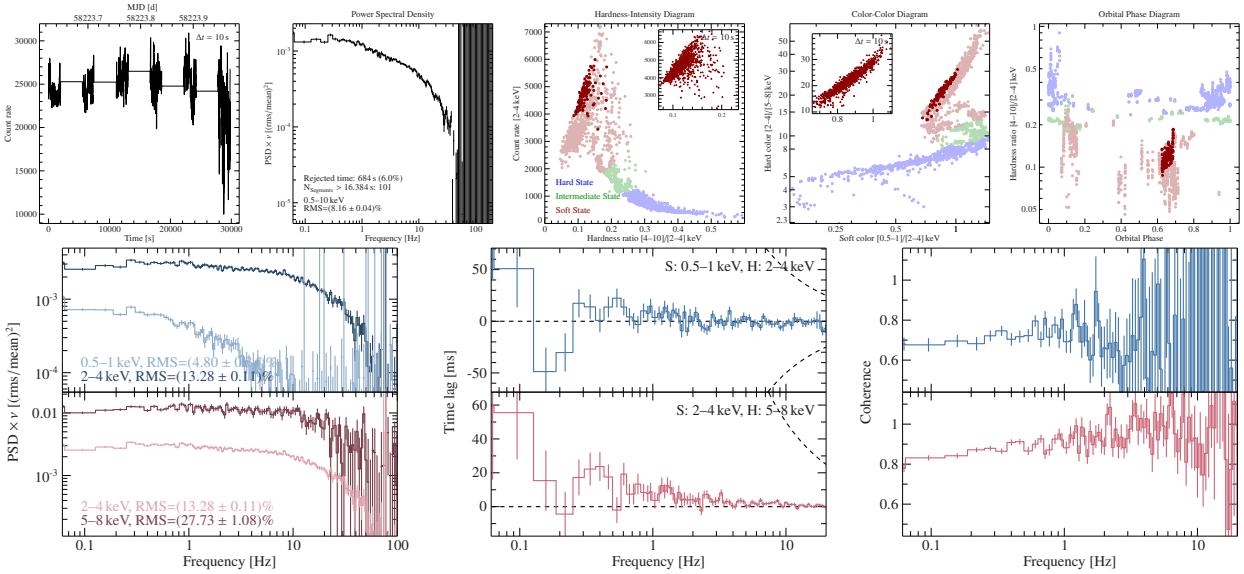

Figure A.28: Observation 1100320119. $\Gamma \approx 2.7$.

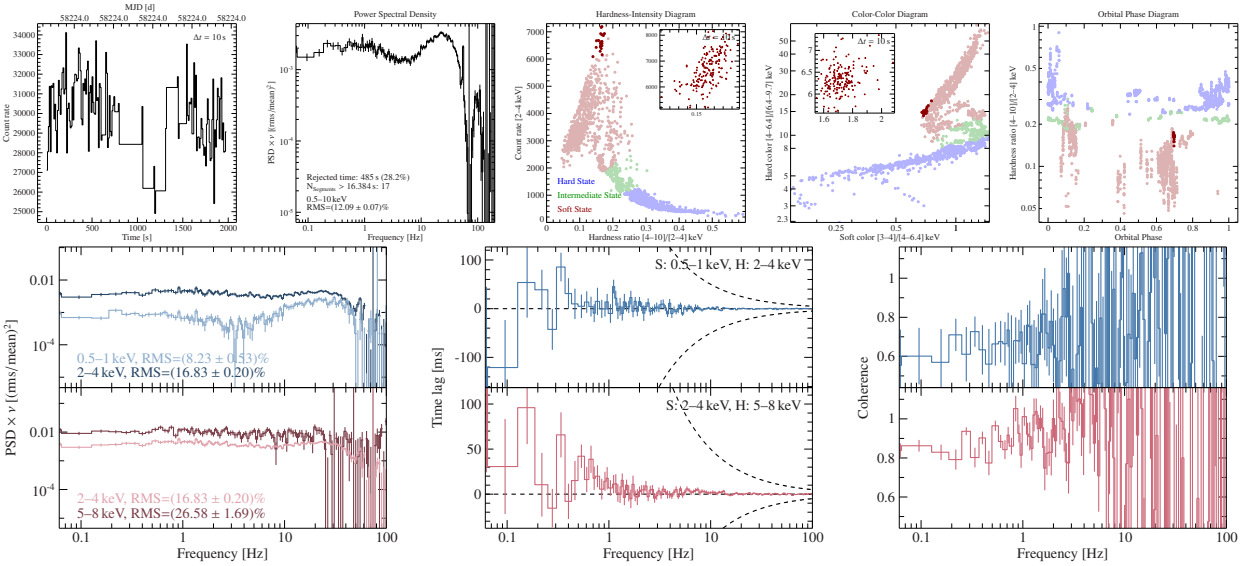

Figure A.29: Observation 1100320120. $\Gamma \approx 2.7$.

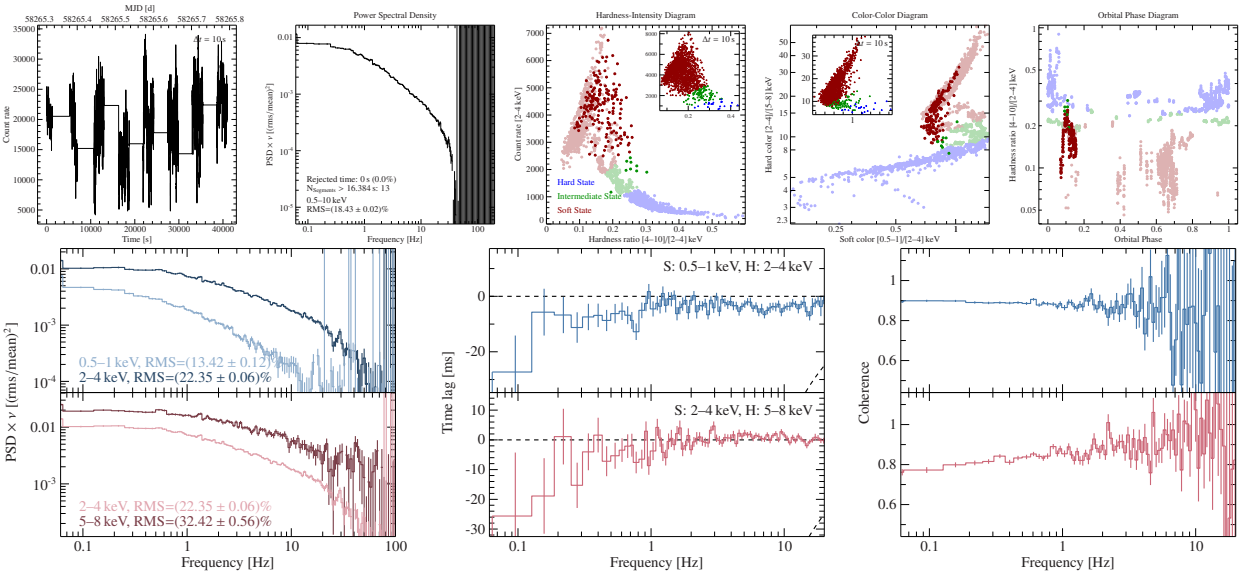

Figure A.30: Observation 1100320121. $\Gamma \approx 2.7$.

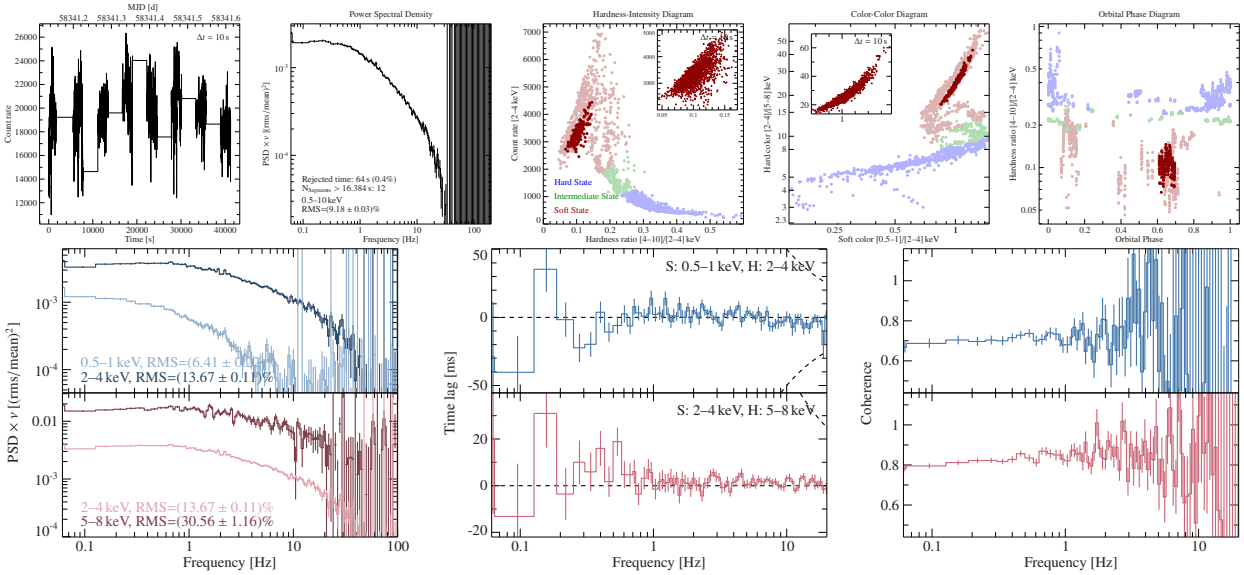

Figure A.31: Observation 1100320122. $\Gamma \approx 3.1$.

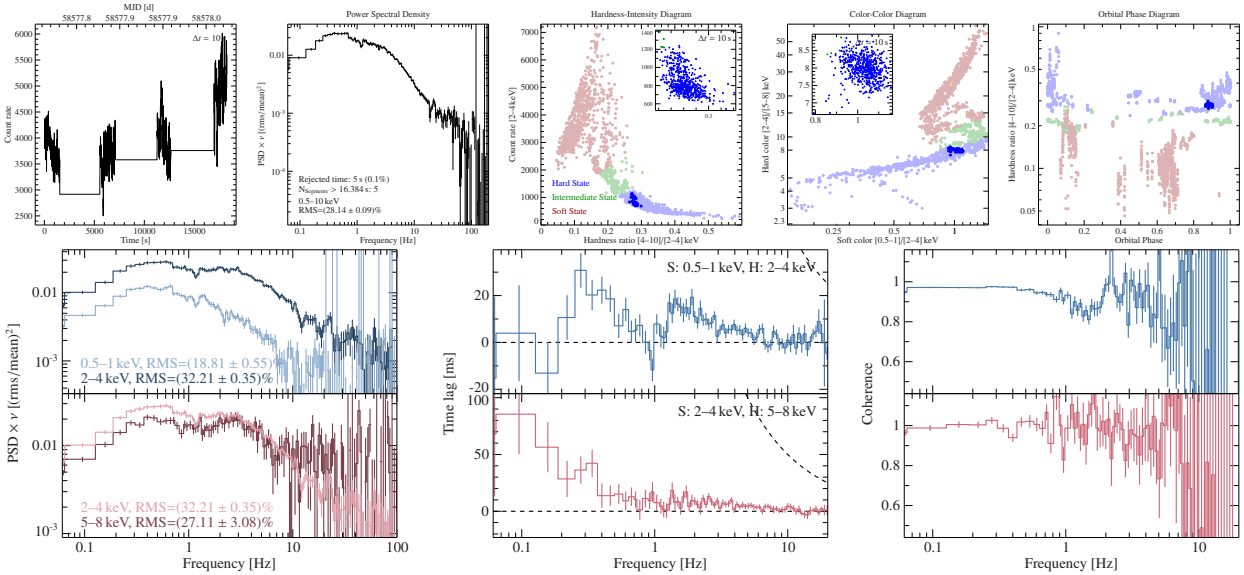

Figure A.32: Observation 2100320101. $\Gamma \approx 1.8$.

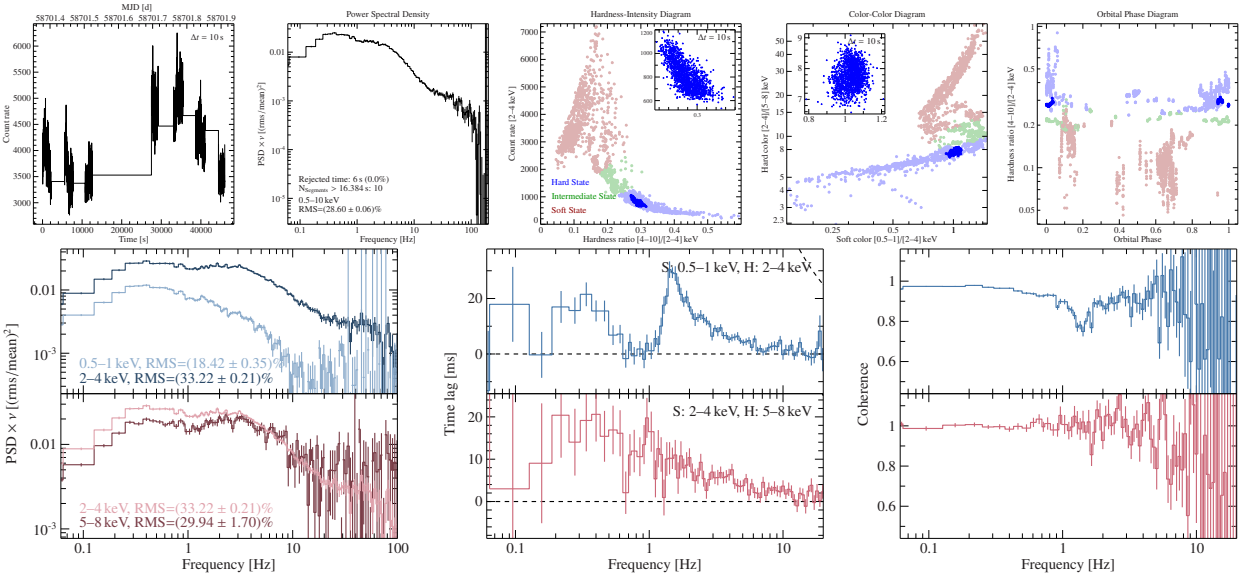

Figure A.33: Observation 2636010101. $\Gamma \approx 1.8$.

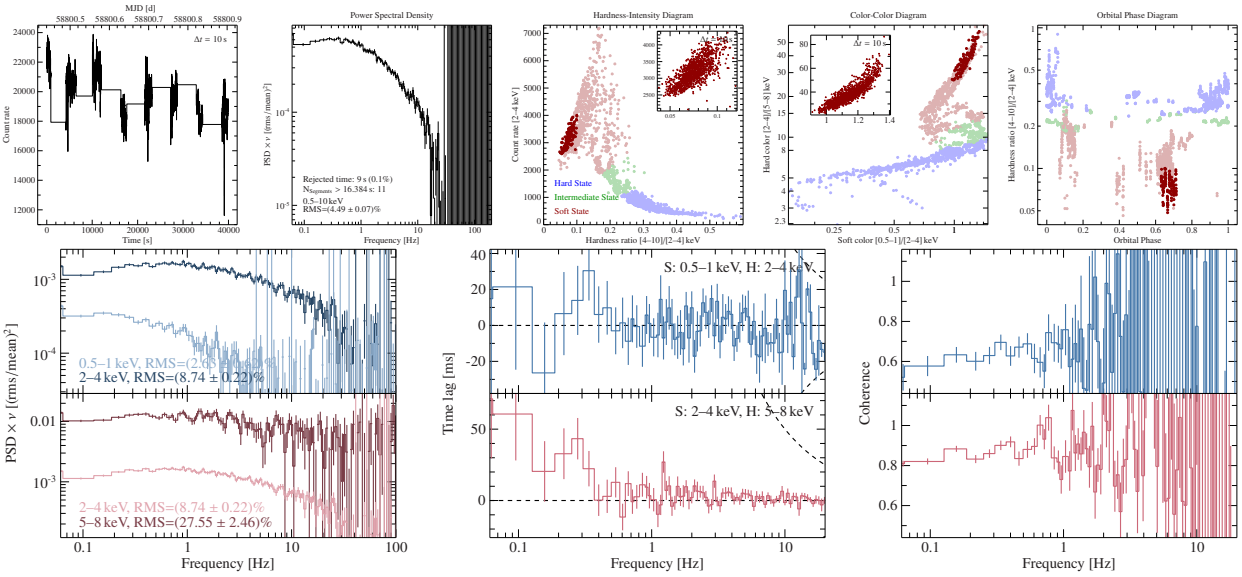

Figure A.34: Observation 2636010102. $\Gamma \approx 3.1$.

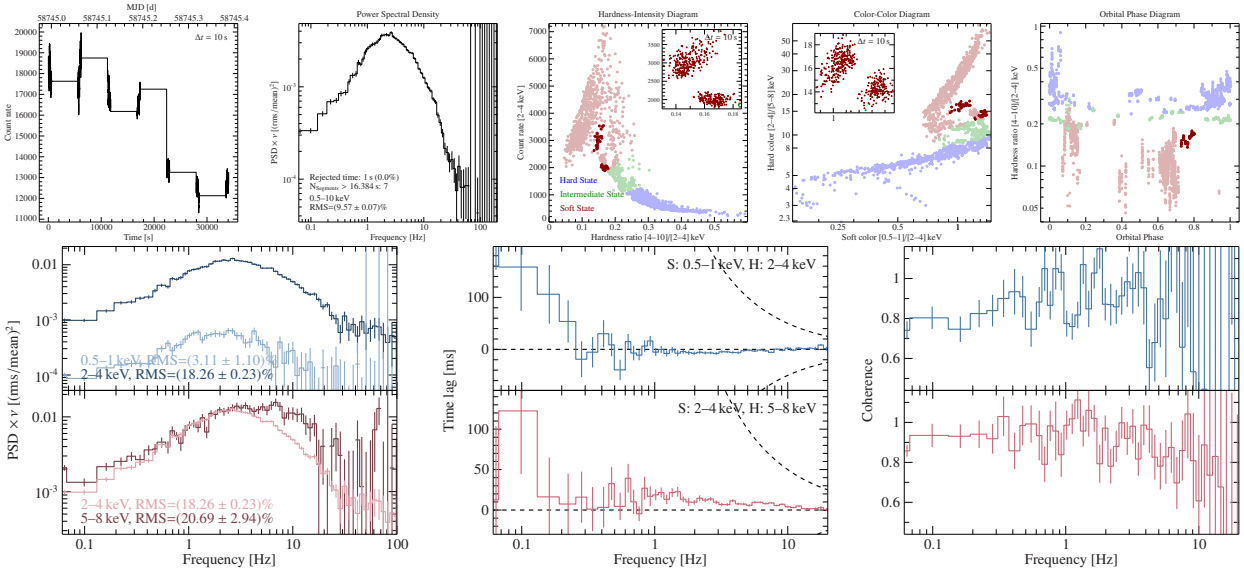

Figure A.35: Observation 2636010201. $\Gamma \approx 2.4$.

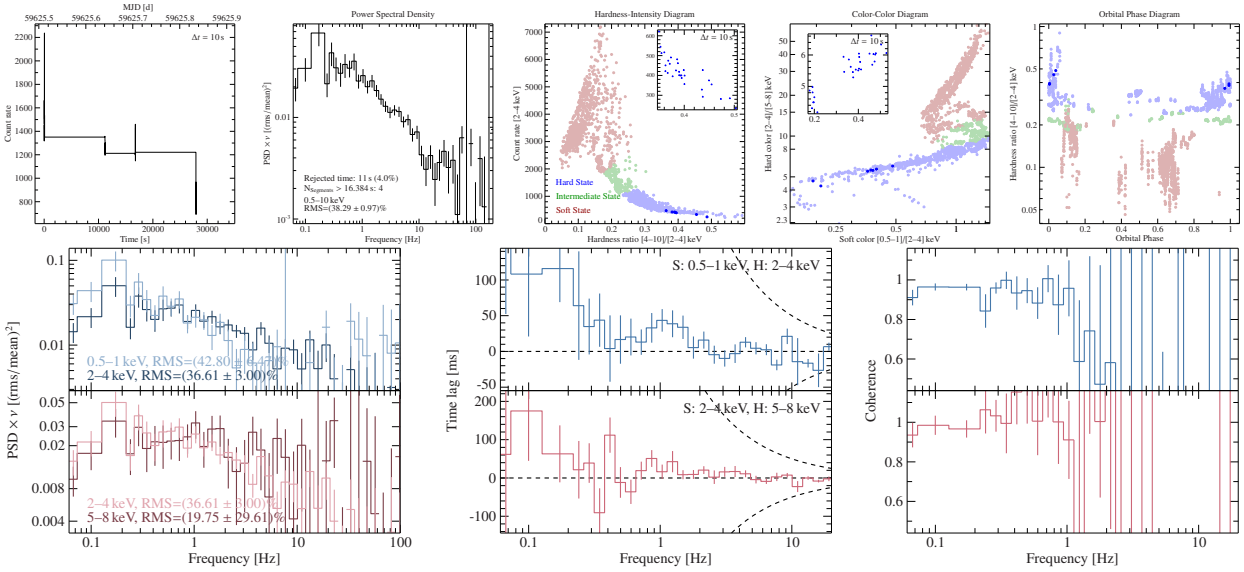

Figure A.36: Observation 4690010103. $\Gamma \approx 1.7$.

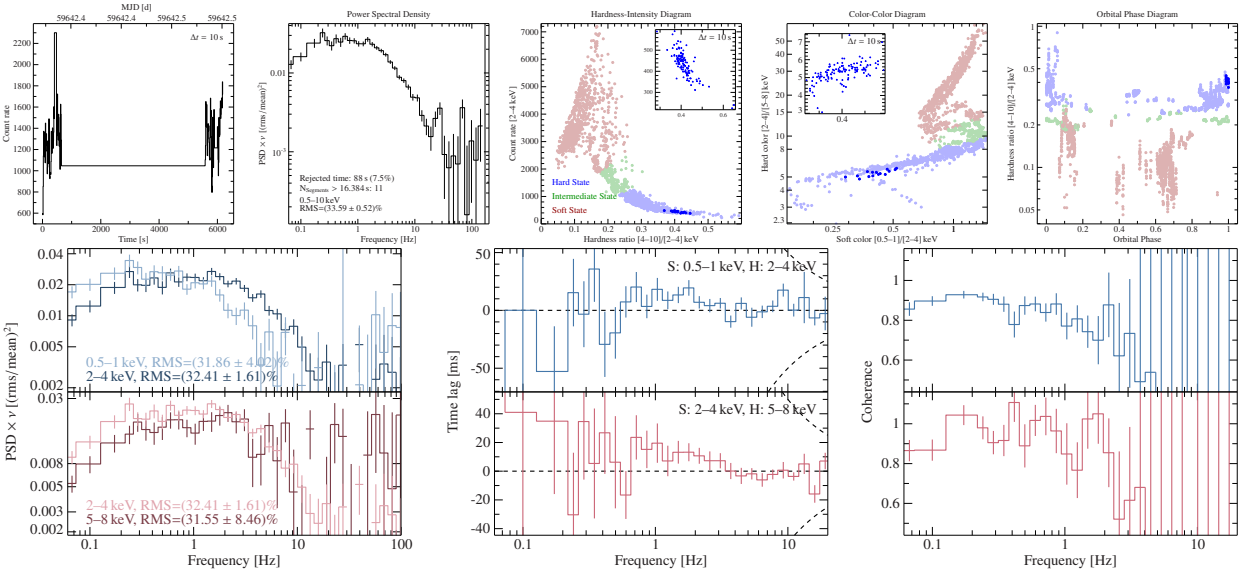

Figure A.37: Observation 4690010104. $\Gamma \approx 1.5$.

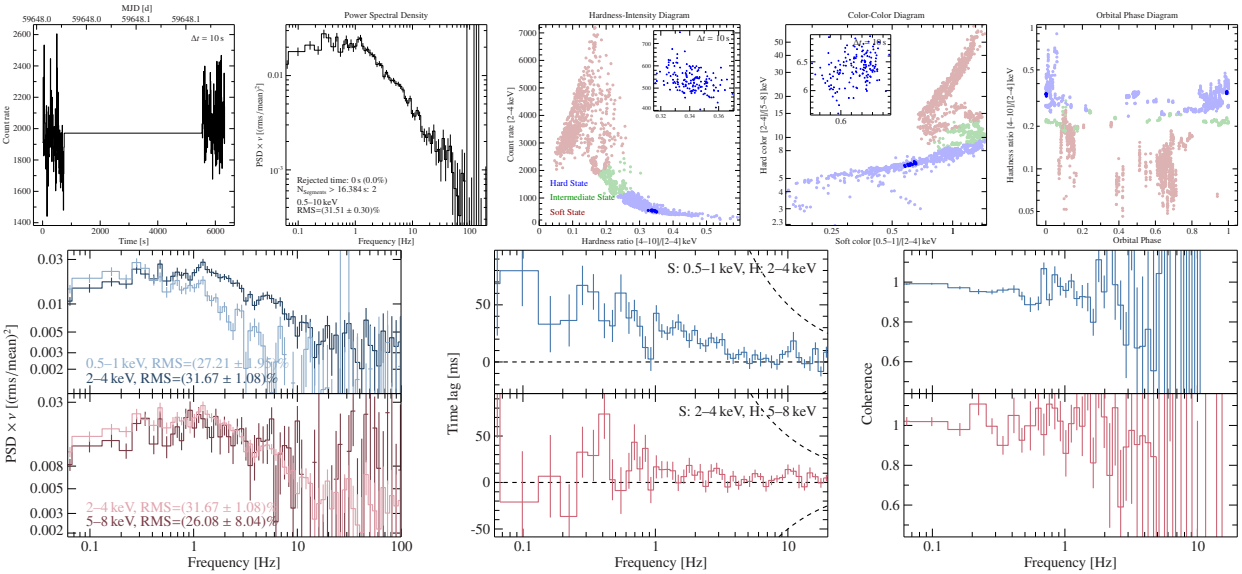

Figure A.38: Observation 4690010105. $\Gamma \approx 1.6$.

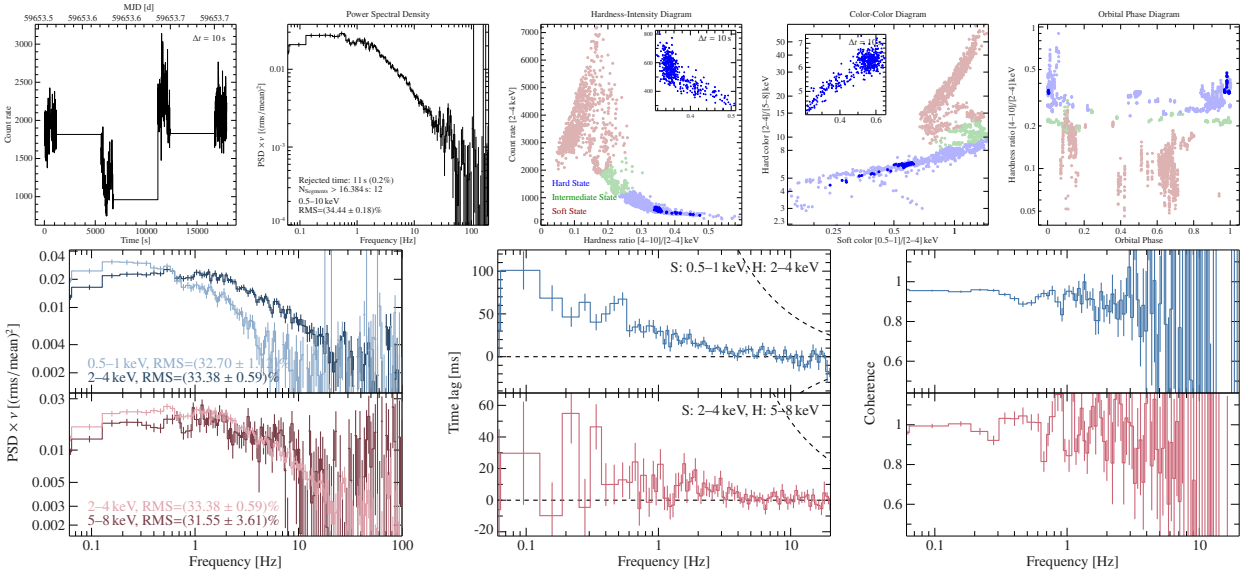

Figure A.39: Observation 4690010106. $\Gamma \approx 1.6$.

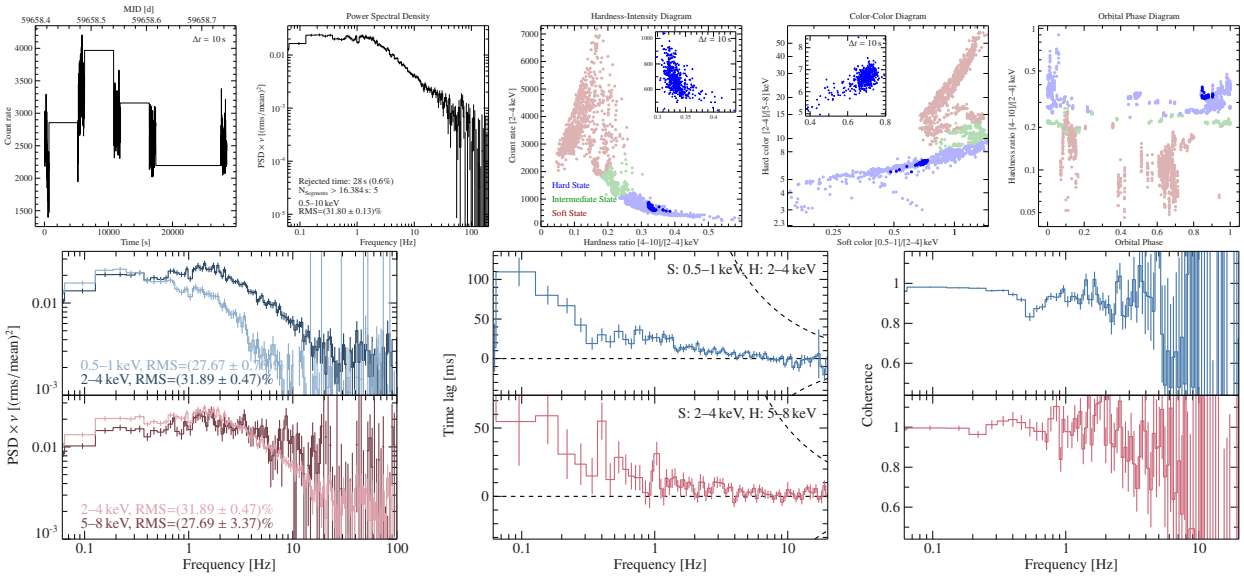

Figure A.40: Observation 4690010107. $\Gamma \approx 1.7$.

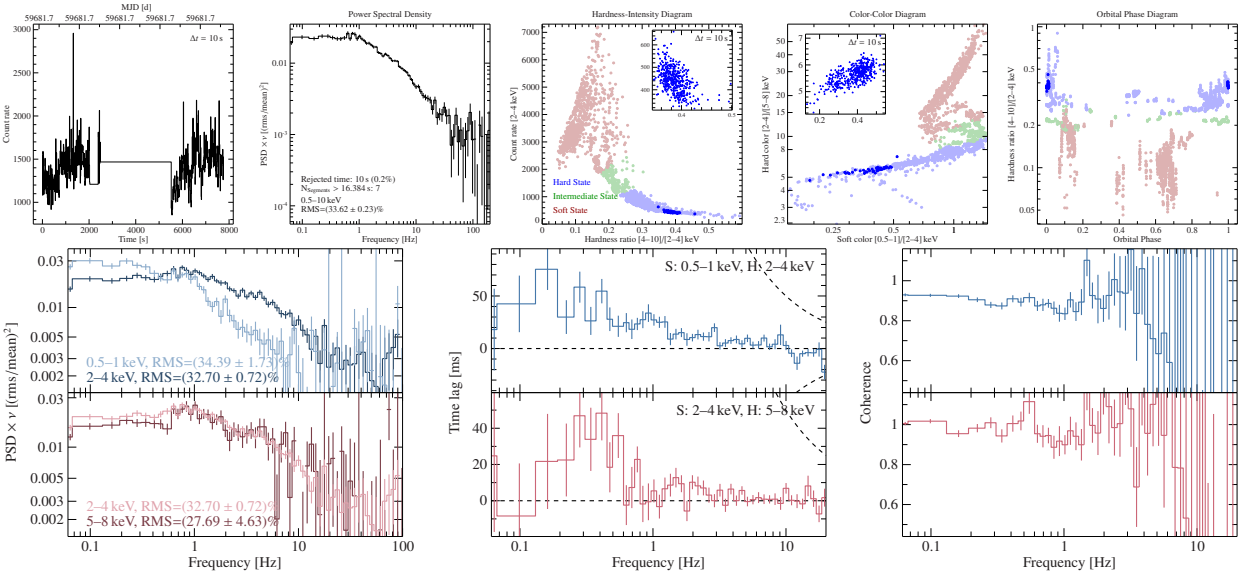

Figure A.41: Observation 4690010109. $\Gamma \approx 1.6$.

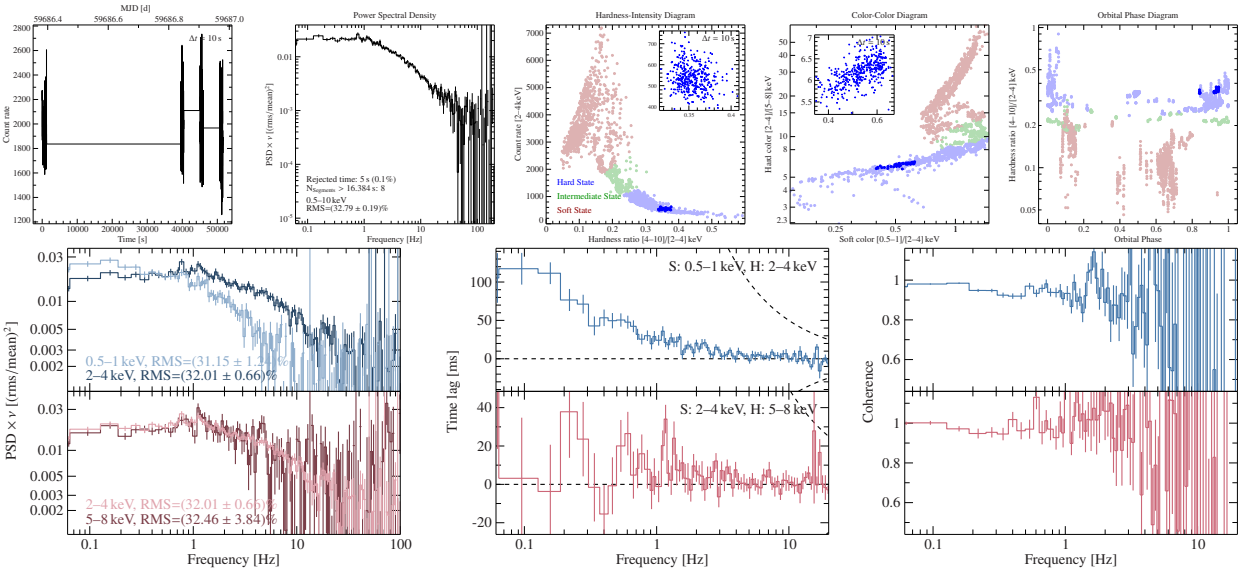

Figure A.42: Observation 4690010110. $\Gamma \approx 1.7$.

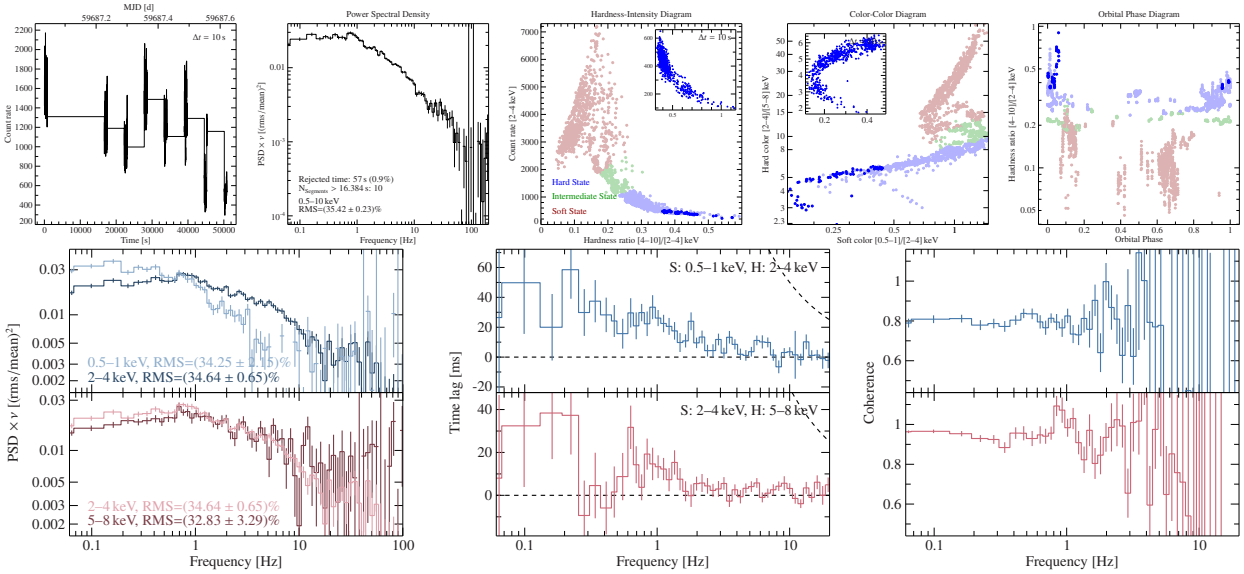

Figure A.43: Observation 4690010111. $\Gamma \approx 1.6$.

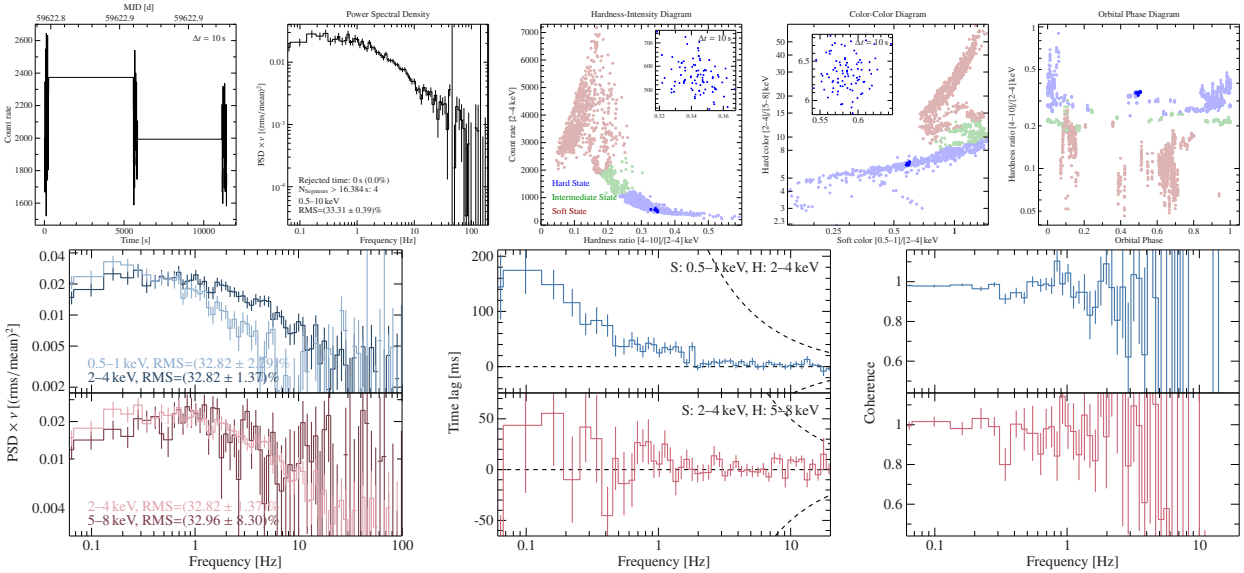

Figure A.44: Observation 4690020101. $\Gamma \approx 1.6$.

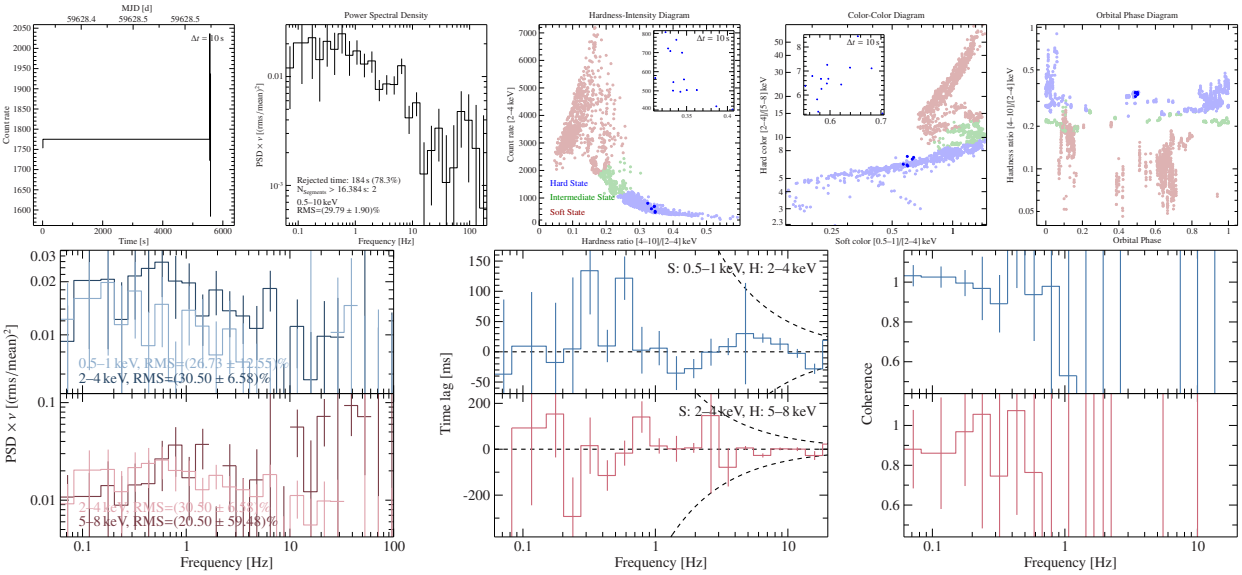

Figure A.45: Observation 4690020102. $\Gamma \approx 1.6$.

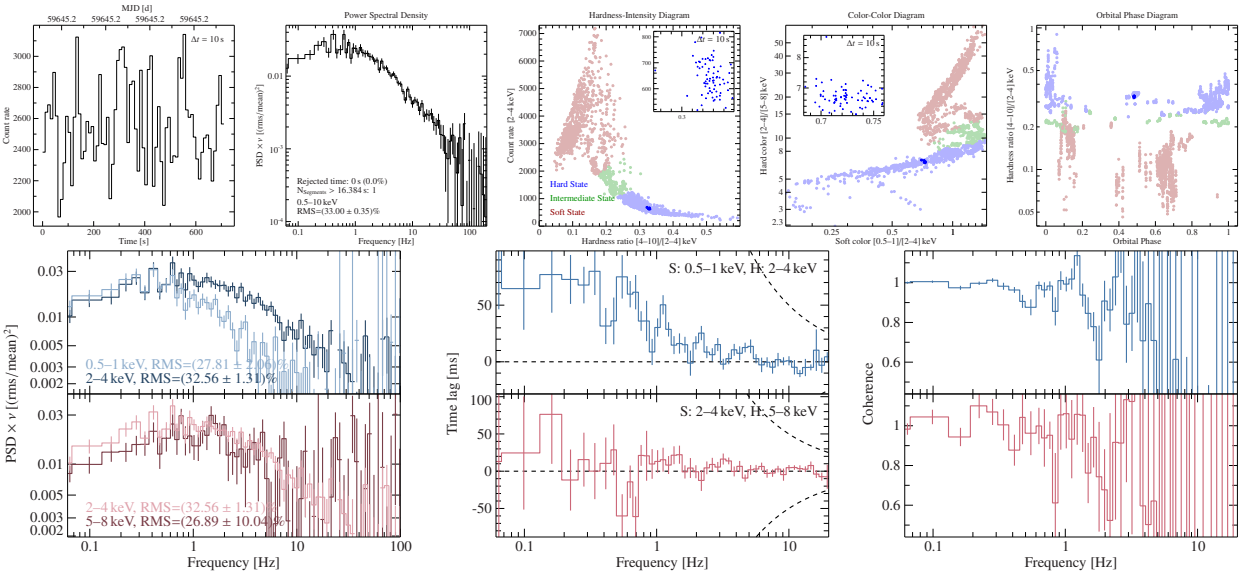

Figure A.46: Observation 4690020103. $\Gamma \approx 1.7$.

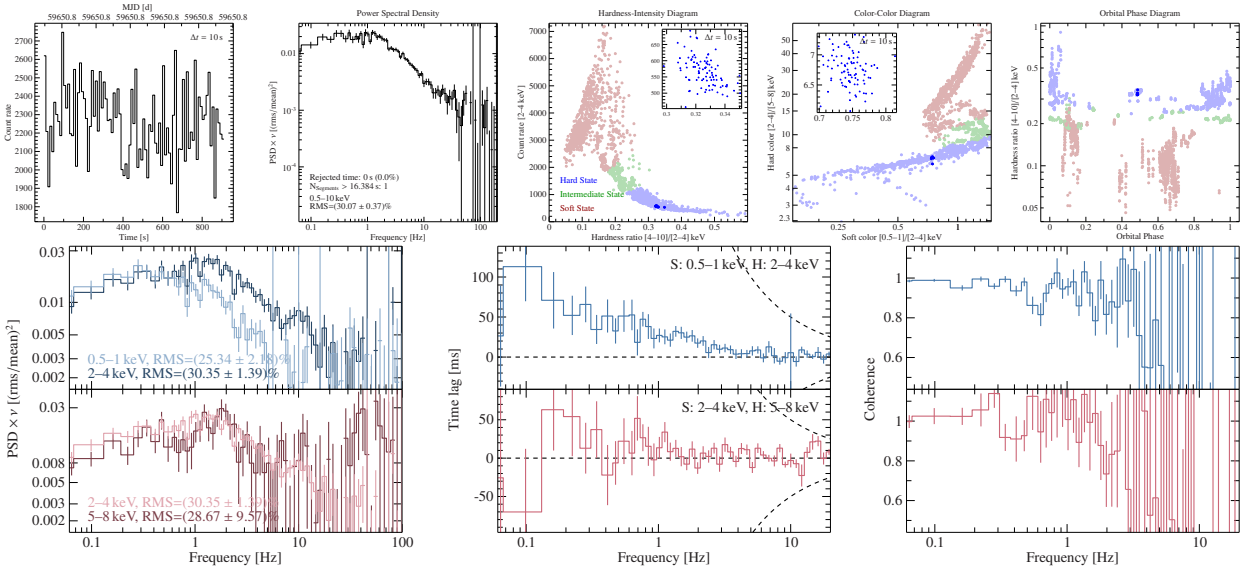

Figure A.47: Observation 4690020104. $\Gamma \approx 1.7$.

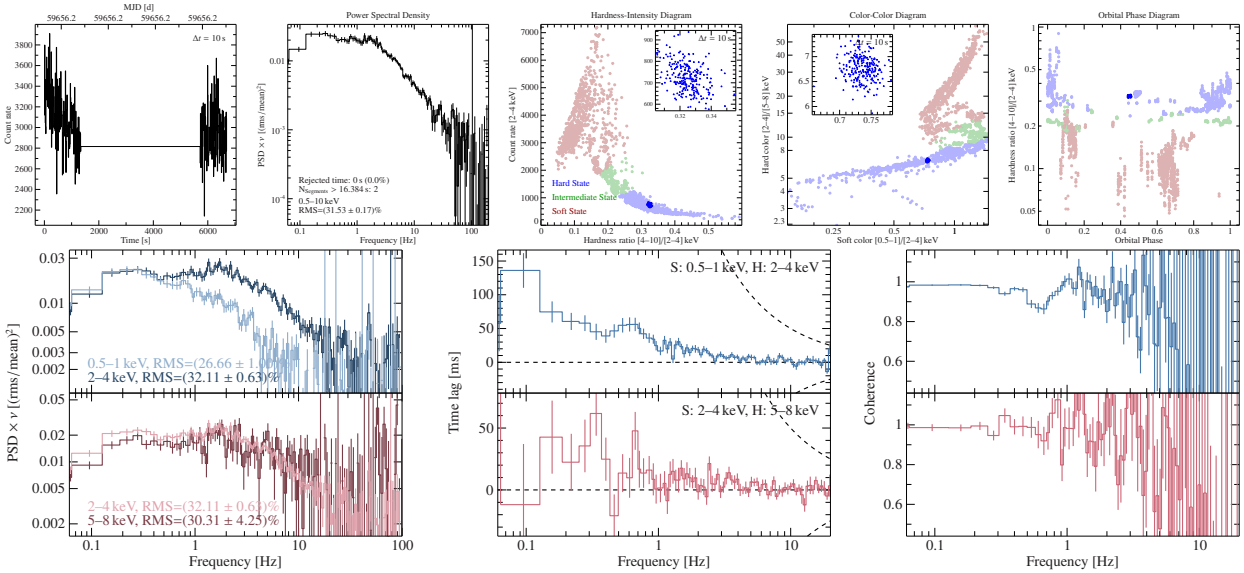

Figure A.48: Observation 4690020105. $\Gamma \approx 1.7$.

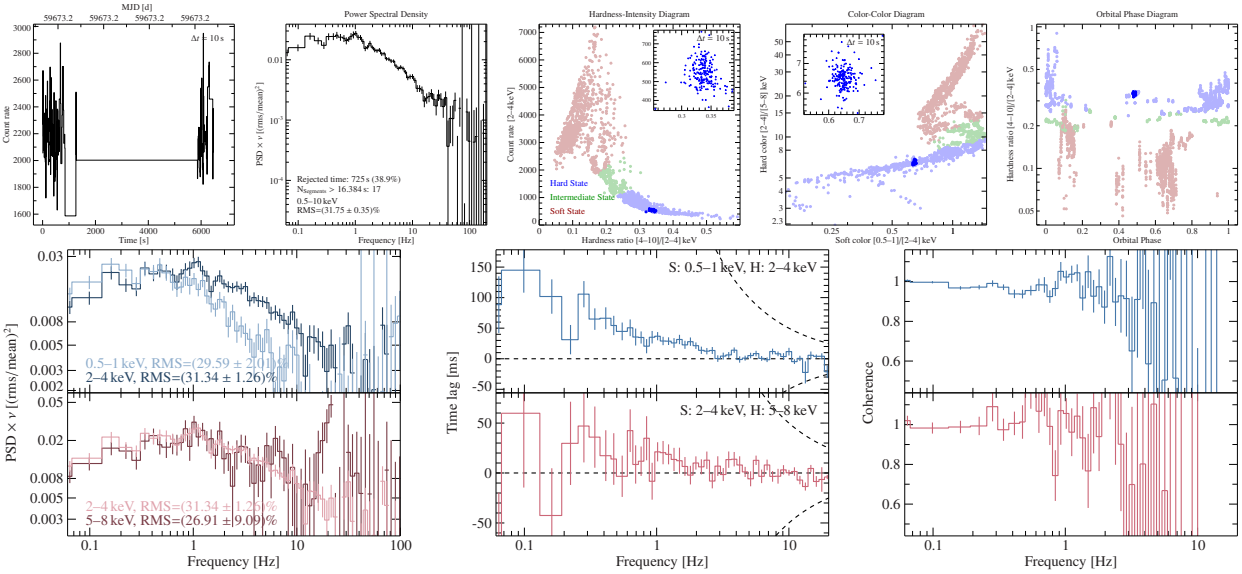

Figure A.49: Observation 4690020107. $\Gamma \approx 1.6$.

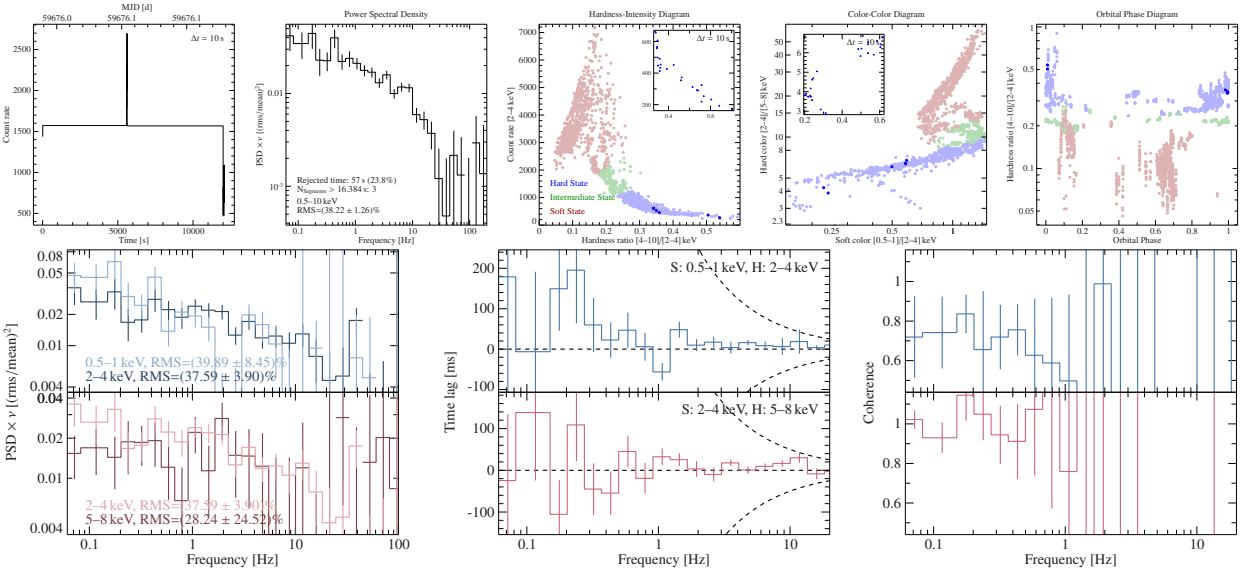

Figure A.50: Observation 4690020108. $\Gamma \approx 1.5$.

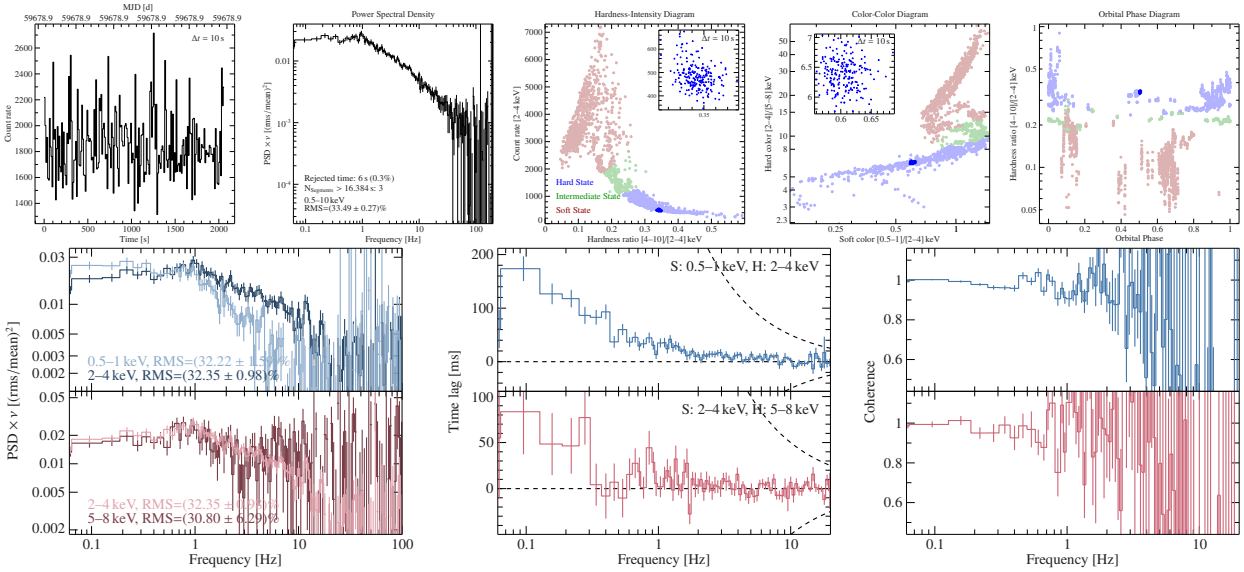

Figure A.51: Observation 4690020109. $\Gamma \approx 1.6$.

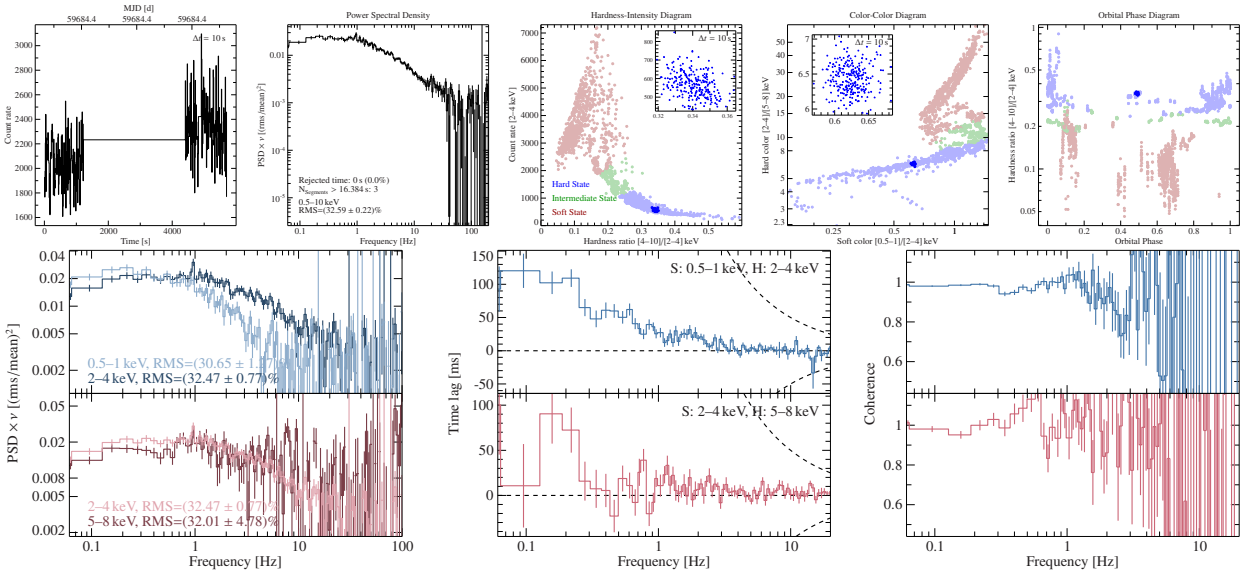

Figure A.52: Observation 4690020110. $\Gamma \approx 1.7$.

Appendix B

Comments and Scientific Considerations on Paul's Adventures

i. The CNO cycle fuses four protons to one alpha particle $^4_2$He and two electron neutrinos, using carbon, nitrogen, and oxygen as a catalyst. The binding energy of $^4_2$He, 26.7 MeV, is radiated away as energy (Wiescher et al., 2010).

ii. The distance to Cygnus X-1 can be derived, for instance, from radio astrometry measurements and is estimated to be $2.22^{+0.18}_{-0.17}$ kpc $= 7200 \pm 600$ ly (Miller-Jones et al., 2021).

iii. The reader may forgive the cheeky analogy to Jörn referring to the *NICER* replica next to his "desk" at NASA's Goddard Space Flight Center as the "laundry machine".

iv. X-ray photons in grazing incidence optics impact the mirrors at shallow angles and undergo total internal reflection. The penetration depth of the evanescent wave depends on the coating material, the incidence angle, surface roughness, and the energy of the photon. To give an example, the penetration depth of a 10 keV photon in copper under an incidence angle of 1° is roughly 660 nm (Parratt, 1954, their Table 1 and Fig. 5).

v. The initial charge cloud size of a 6.7 keV photon is roughly 0.5 μm according to Janesick et al. (1986, their Fig. 2).

vi. As a charge cloud, Paul is located in the bulk of *NICER*'s silicon drift detectors. In SDDs, the charge drifts to the collecting anodes parallel to the surface (in a CCD, Paul would drift into the potential well of the pixels and one can only speculate what happens to him in case of a split event...).

vii. In Sect. 7.3, I show that the *eROSITA* observation can be simulated using the Sixte simulator. In the simulator, one can trace the number of photons impacting the detector and compare it to the number of events that are actually detected after the pattern recognition step (see Sect. 6.1). By analyzing the impact file using the best fit parameters of the nova X-ray flash, I estimate an impact rate of 522 ± 23 photons s^{-1} on telescope module 1. *eROSITA* detectors have a frame time of 50 ms, meaning that roughly 25 photons per frame impacted the detector. A large number of these events are discarded during the pattern recognition step – the final event file contains only roughly one forth of these events.

viii. Pattern is a tool within the *eROSITA* Science Analysis Software System (eSASS), which is responsible for the pattern recognition. Patterns other than singles, doubles, triples, or quadruples (Sect. 3.2.2) are rejected by this algorithm. The sky image of the nova during Paul's arrival can be seen in Fig. 7.1. Severe pattern pile-up in the center of the image leads to many invalid patterns, which are "thrown out" by Pattern.

ix. Assuming *eROSITA* is placed exactly at the second Lagrange point and orbits the Sun with the same angular velocity as Earth at a distance of 1.01 astronomical units ($R \approx 151.5 \times 10^6$ km), results in an orbital velocity of $2\pi R/365.256$ days $\approx 2.61 \times 10^6$ km days^{-1} (note that the length of one Earth revolution around the Sun is given by

the siderial year, and not by the topical year).

x. Robert H. McNaught discovered nova YZ Reticuli at 5th magnitude in Coonabarabran, New South Wales, Australia on 2020 July 15 using a Canon 6D camera. He "notes that the variable is an easy naked-eye object" (McNaught, 2020a) and he provided very valuable and the only available optical data with which the peak of the optical outburst could be constrained (McNaught, 2020b).

Acknowledgements

I find it rather remarkable what a multi-layered scientific, professional, but also emotional connection one develops during a PhD – to the scientific topic of the thesis, the community around it, the colleagues and friends, and, in particular, to the supervisor. The German term *Doktorvater* probably entails just as many layers and, surely, every PhD student has a subtly different understanding of this word. Summarizing how much I learnt from *my* Doktorvater, Jörn Wilms, is near impossible. Certainly, I caught up a few astrophysical bits here and there but there are other skills, perseverance, consistency, or knowledge of the historic background, which drive science and I cannot imagine a supervisor being more skilled in representing these qualities, as well as being dedicated to convey them, in particular in situations where this responsibility may be challenging to fulfill. I appreciate Jörn's excellent lectures, our challenging, yet enriching, scientific discussions, and his relentless effort to teach me proper scientific writing. I am particularly grateful for his lesson that good science needs its time and one should not feel pressured by an unreasonable urge to publish papers. Jörn, I want to whole-heartedly thank you for your mentoring.

I am truly grateful to Thomas Dauser for being a dear friend, climbing partner, an incredibly nice and humble person, and a fantastic 2$^{\text{nd}}$ supervisor. Thank you for all the scientific and non-scientific advice, the many days spent on the walls, cliffs and boulders of the Alps, Yosemite, and the Frankenjura. I am relatively certain that, without your inspiration, my life would have taken some different turns, perhaps even without doing a PhD in astrophysics.

I want to whole-heartily thank the Remeis family for six years of fun and friendship. Thank you Aafia Zainab for being an amazing listener and friend. Amy Joyce, thanks for the great time in Madrid and be aware that your puns are always appreciated. Andrea Gokus, thank you for relieving walks with Amos during Covid. Ekaterina Sokolova-Lapa, your enthusiasm for science, literature, and organizing pub quizzes is awe-inspiring (I'm still waiting for that group name that is supposed to knock our socks off!). Ingo Kreykenbohm, thank you for managing the observatory and organizing the LitClub. Jakob Stierhof, thanks for thinking outside the box, your S-LANG advice, and for being an amazing person to hang out with. Philipp Thalhammer, thank you for being the best roomy on conferences. Sebastian Falkner, your early night exits are absolutely legendary. Steven Hämmerich, thank you for your super hero-like organizational and coffee drinking skills. Thomas Dauser, thanks for always being there – from the Henkestraße up to now. Thanks, Philipp Weber, for doing an amazing admin job and your impressive space photography. I want to thank my dear office mates Christian Kirsch, for best cooking and coding advice, Lea Dauner, for always providing sweets and cheers, and Maximilian Lorenz, for your patient and incredibly calm, warm-hearted attitude. I want to thank the professors Manami Sasaki, for listening when I

needed to talk, Uli Heber, for making me aware how awesome stars are, and Jörn Wilms for our fun TeX-to-Word conversion adventures. Last but not least, thank you, Edith Day for keeping the whole observatory together. It's difficult to pick occasions from all the exciting things we experienced together, but they include silly pool lunch breaks, pub quizzes, Looping Louie, the (notorious, I wanna say) Remeis skiing, powder days, (Dusch-)beers, board game nights, political discussions, (some) gossiping, freezing during observing nights, and so much more. I'd also like to thank all admins who have made the Remeis cluster run smoothly, which enables so much research! Finally, I want to thank the professors for letting me sleep at the observatory for a few days per week in the last period of my PhD.

I want to thank Jörn and Thomas for letting me join the *eROSITA* and *Athena* consortia and allowing me to contribute my share to these two exciting missions. By what appears as a lucky coincidence to me, I got involved in the *eROSITA* discovery of a bright X-ray flash from a nova. Throughout the following years, staring at these 36 s of data, I want to thank, next to all co-authors, particularly Gloria Sala for giving amazing advice. The serendipitous discovery of a nova fireball involved a huge portion of luck, from the observational perspective but also personally and I feel really grateful for that. Thank you, Annika Kreikenbohm, for producing an amazing animation and for bringing us onto the cover of *Nature*.

I want to thank Javier García for inviting me to Caltech for two months. I want to thank Guglielmo Mastroserio for guiding me while I was there, for his professionalism, his charming character, for being an awesome swimming and running training partner (sub-20-5k, yay), and a dear friend. I would also like to thank Gullo, Riley Conners, and Ilaria Caiazzo for adopting me to their "crew", for fun nights and wild talks in LA. I am grateful for the invitation to Colorado by Javier during this time, a week locked in an apartment talking about science, black holes, and so much other stuff, which was *so* inspirational after many months of Covid lock-down. I'd also like to say thanks to the people from the Caltech alpine club for inviting me to go back-country skiing on my first weekend in California (didn't see that one coming), the surfing club for cold laundry machine rides, and the triathlon club for smashing the Pasadena Tri together. Also many thanks to the LA climbing community, especially to Hunt Cramer for awesome climbing trips to Joshua Tree, Malibu Creek, Stoney Point, and more.

I am very grateful to Katja Pottschmidt for hosting me in Greenbelt, the fun shows in the New Deal Cafe, showing me around at NASA GSFC, and for urging me to wear a bicycle helmet in the skate park. Thanks to Erin Kara and Jingyi Wang for the visit at MIT, and Jack Steiner for the days at CfA/Harvard-Smithsonian. Thanks to all of them for the opportunity to present my research at the GSFC litclub, Chandra HETG group-meeting at MIT and in the CfA/HEAD seminar. I would also like to thank the DAAD for supporting this trip financially.

Thank you, Jan-Uwe Ness for hosting me during the XMM conference and the interesting pool discussions on novae. Thanks to the BlackSTAR collaboration for the stimulating Monday's telecons. Thank you, Mike Nowak for the interesting discussions on low-pass filters and for wrestling through an early draft of a 17 page Cyg X-1 paper. Thanks to all people proof-reading this thesis, Aafia Zainab, Amy Joyce, Ekaterina Sokolova-Lapa, Gloria Sala, Guglielmo Mastroserio, Jakob Stierhof, Jan-Uwe Ness, Jörn Wilms, Julia Häfner, Katja Pottschmidt, Maximilian Lorenz, Philipp Thalhammer, Riley Conners, Steven Hämmerich, Thomas Dauser, and Uli Heber.

I also want to thank all my fellow students during my undergraduate studies, especially Carl

Roßdeutscher, Constantin (Franz) Nauk, Dominik Arold, Katharina Witzmann (our library sessions had a weird mixture of joy and frustration, for sure), Lukas Maderer, Moritz Schulz, Oskar Schuster, Paul Beck, Philipp Stürmer, and Sara Baumann.
Finally, I want to thank my family for their love and support. The story of Paul, the X-ray photon is inspired by numerous hiking vacations with my family and the effort of my father to explain us the water cycle based on "Paul, the water droplet". Paul could be a droplet in a wave, vapor in a cloud, or ice inside a glacier, and it was always there to inspire. Lastly, I want to thank Carla Sure for her positivity, cheerful mood, morale support, and the exciting times that lie behind and ahead.